UNIVERSITY OF COPENHAGEN

Neutrino Flavor Conversion in Dense Astrophysical Environments

DOCTORAL THESIS

by

IAN PADILLA GAY

Supervised by Prof. Irene Tamborra

This thesis has been submitted to the PhD School of the Faculty of Science,

University of Copenhagen

August 30, 2022

ABSTRACT

Neutrinos are among the most abundant particles in the universe. They interact only weakly and can travel great distances unimpeded, offering a window into the interiors of the dense astrophysical sources that otherwise would be invisible to us. However, neutrinos have the peculiar property of converting their flavor content as they propagate. In neutrino-dense environments such as core-collapse supernovae, compact binary merger remnants, and the early universe, the flavor evolution is significantly affected by the interactions of neutrinos with matter and other neutrinos in the medium. Apart from neutrino oscillations and the well-known Mikheyev-Smirnov-Wolfenstein resonance effect, neutrino-neutrino coherent forward scattering can lead, on much shorter time scales, to a plethora of non-linear effects which can collectively convert flavor. This phenomenon is known as collective neutrino conversion, and there are two important regimes depending on the neutrino gas density: slow flavor conversion, whose characteristic frequency is determined by the vacuum oscillation frequency, and fast flavor conversion, whose characteristic frequency is instead determined by the neutrino self-interaction strength and is even possible for vanishing vacuum oscillation frequency. Slow and fast flavor conversion can occur in the proximity of the decoupling regions; however, the time scales over which they operate are orders of magnitude apart. Due to the proximity to the decoupling regions and the short time scales of fast flavor conversion, flavor mixing is expected to have significant consequences on the inner workings of astrophysical sources. State-of-the-art hydrodynamical simulations cannot incorporate neutrino flavor evolution yet, and many conceptual and technical challenges must be addressed first to grasp the physics of neutrino flavor evolution in dense media. There are strong hints that core-collapse supernovae and compact binary merger remnants provide favorable conditions for the development of flavor instabilities. However, whether such fast-growing instabilities lead to a minimal mixing of neutrinos or to complete flavor conversion remains an open question in the field. The work presented in this thesis aims to bridge this knowledge gap. This thesis provides new tools to predict the behavior of fast flavor conversion in dense environments and explores the rich phenomenology that fast flavor conversion offers.

The first part of this thesis presents a broad overview of neutrinos, their Standard Model interactions with matter, other neutrinos, and their impact on the evolution of flavor conversions. Next, the main physics behind neutrino-neutrino interactions is presented to pave the road towards discussing collective neutrino conversions. Finally, relevant sites that can host collective neutrino conversions are presented and discussed with a focus on core-collapse supernovae and compact binary merger remnants.

From the second part of the thesis and onward, we present original results from the publications concluded during the doctoral studies of the PhD candidate. The second part of the thesis focuses on describing the dynamics of fast flavor conversion using the classical analogy with a gyroscopic pendulum. This work shows that for homogeneous and azimuthally symmetric systems, the equations of motion of neutrinos are formally equivalent to those of a gyroscopic pendulum. Such an analogy was known for the case of slow conversions, but its validity in the fast regime had never been mathematically proven. Through the lens of the gyroscopic pendulum analogy, our work can predict the maximum amount of conversion without solving the equations of motion. The latter is achieved by identifying the pendulum parameters from the linearized equations of motion. As a next-to-minimal configuration, we also address how the gyroscopic pendulum analogy is modified in the presence of random quantum fluctuations induced by the medium, which can destroy the coherence among flavors. Nevertheless, our findings suggest that the gyroscopic pendulum still has predictive power and can foresee the final flavor outcome after decoherence.

The third part of the thesis focuses on developing numerical modeling and phenomenology of fast flavor conversions. It improves on previous calculations in the literature by relaxing some assumptions such as homogeneity and isotropy in the equations of motion. As a first step towards understanding the flavor evolution of non-homogeneous media, we implemented for the first time neutrino advection in the equations of motion assuming two spatial coordinates, one angular variable and time. This work showed for the first time that the development of fast flavor conversion is substantially affected by neutrino propagation. In particular, if favorable conditions exist for fast flavor conversions, neutrino advection hinders or prevents flavor development unless

the unstable region is spatially extended, i.e., the conditions are self-sustained and global. Along the same vein and using a similar multi-dimensional framework, we computed the flavor evolution of neutrinos above the disk of compact binary merger remnants and looked for a steady state after the development of flavor instabilities. Although this work assumed a simplified model for the neutrino decoupling regions, it showed for the first time that flavor conversion occurs in very well localized regions above the disk of the merger and that minimal mixing of neutrinos (less than 1%) is possible, albeit the large growth rates of flavor instabilities. Last but not least, in the final work of this thesis, we relax the assumption of isotropy in the matter term and study in detail the consequences on the non-linear evolution of flavor. This work improves on previous studies where the matter background is assumed to be static and therefore isotropic. Furthermore, we studied the unexplored effect of the bulk velocity of matter and demonstrated that the flavor evolution is sensitive to the magnitude and direction of the bulk velocity, which could reach values of a fraction of the speed of light in astrophysical environments.

The work in this thesis shows that the physics of fast flavor conversion is extremely rich. Although many challenges still lie ahead, neutrino flavor conversion physics continuously offers new insights and surprises that contribute to a better understanding of astrophysical sources and our universe.

ABSTRAKT

Neutrinoer er blandt de mest talrige partikler i universet. De vekselvirker kun svagt, og de kan rejse store afstande uhindret, hvorved de kan give et indblik i det indre af kompakte astrofysiske kilder, som ellers ville være usynligt for os. Neutrinoer har imidlertid den særegne egenskab, at de kan konvertere fra én type neutrino til en anden, når de bevæger sig. I miljøer med høj tæthed af neutrinoer, såsom kernekollaps-supernovaer, efterdønninger af kompakte binære sammenstød og det tidlige univers, er konvertering af neutrino-type væsentligt påvirket af neutrinoers vekselvirkninger med stof og andre neutrinoer i mediet. Foruden neutrinooscillationer og den velkendte Mikheyev-Smirnov-Wolfenstein-resonanseffekt, kan kohærent fremadrettet neutrino-neutrino-spredning på meget kortere tidsskalaer føre til et væld af ikke-lineære effekter, som kan konvertere neutrino-type kollektivt. Dette fænomen er kendt som kollektiv neutrino-konvertering, og der er to vigtige regimer afhængigt af neutrino-gassens tæthed: langsom typekonvertering, hvis karakteristiske frekvens bestemmes af vakuumoscillationsfrekvensen og hurtig typekonvertering, hvis karakteristiske frekvens i stedet bestemmes af styrken af neutrino-selvvekselvirkningen og endda er mulig for forsvindende vakuumoscillationsfrekvens. Langsom og hurtig typekonvertering kan forekomme i nærheden af afkoblingsregionerne, men tidsskalaerne, som de opererer over, er størrelsesordener fra hinanden. På grund af nærheden til afkoblingsregionerne og de korte tidsskalaer for hurtig typekonvertering forventes det at have vigtige konsekvenser for astrofysiske kilders indre virkemåde. Moderne hydrodynamiske simuleringer kan endnu ikke tage højde for neutrino-typekonvertering, og mange konceptuelle og tekniske udfordringer skal løses først for at forstå fysikken bag neutrino-typekonvertering i medier med høj neutrinotæthed. Der er stærke indikationer på, at kernekollaps-supernovaer og efterdønninger af kompakte binære sammenstød, giver gunstige betingelser for udvikling af typeustabilitet. Hvorvidt sådanne hurtigt voksende ustabiliteter fører til en minimal blanding af neutrinotyper eller til fuldstændig typekonvertering, er fortsat et åbent spørgsmål. Arbejdet præsenteret i denne afhandling har til formål at slå bro over denne videnskløft. Denne afhandling leverer nye værktøjer til at forudsige adfærden af hurtig

typekonvertering i tætte miljøer og udforsker den rige fænomenologi, som hurtig typekonvertering har at tilbyde.

Den første del af denne afhandling præsenterer et bredt overblik over neutrinoer, deres vekselvirkninger med stof og andre neutrinoer ud fra Standardmodellen og vekselvirkningernes indflydelse på udviklingen af typekonverteringer. Den grundlæggende fysik for neutrino-neutrino-vekselvirkninger præsenteres som grundlag for at diskutere kollektive neutrino-konverteringer. Relevante miljøer, der kan være vært for kollektive neutrino-konverteringer, præsenteres og diskuteres med fokus på kernekollaps-supernovaer og efterdønninger af kompakte binære sammenstød.

Fra anden del af afhandlingen og frem, præsenteres originale resultater fra de publikationer, der er afsluttet under ph.d.-studiet. Anden del af afhandlingen fokuserer på at beskrive dynamikken i hurtig typekonvertering ved hjælp af den klassiske analogi med et gyroskopisk pendul. Dette arbejde viser, at for homogene og azimutalt symmetriske systemer, er bevægelsesligningerne for neutrinoer formelt ækvivalente med dem for et gyroskopisk pendul. En sådan analogi var kendt for tilfældet med langsomme konverteringer, men dens gyldighed for det hurtige regime var aldrig blevet matematisk bevist. Ved at bruge det gyroskopiske pendul, kan vores metode forudsige den maksimale grad af konvertering uden at løse bevægelsesligningerne. Dette opnås ved at identificere pendulparametrene fra de lineariserede bevægelsesligninger. Som den næstsimpleste konfiguration behandledes også, hvordan den gyroskopiske pendulanalogi modificeres i nærværelse af tilfældige kvanteudsving induceret af mediet, som kan ødelægge typekohærensen. Resultaterne tyder på, at det gyroskopiske pendul stadig i nogen grad kan forudse det endelige typeudfald efter dekohærens.

Den tredje del af afhandlingen fokuserer på udviklingen af numerisk modellering og fænomenologi af hurtige typekonverteringer og forbedrer tidligere beregninger i litteraturen ved at slække på nogle af antagelserne, såsom homogenitet og isotropi i bevægelsesligningerne. Som et første skridt til at forstå udviklingen af typekonvertering i ikke-homogene medier implementeredes for første gang neutrino-advektion i bevægelsesligningerne under forudsætning af to rumlige koordinater, en vinkelvariabel og tid. Dette arbejde viste for første gang, at udviklingen af hurtig typekonvertering påvirkes væsentligt af neutrinoernes udbredelse. Særligt hvis der findes gunstige betingelser for hurtige typekonverteringer, hindrer eller forhindrer neutrinoernes udbredelse udviklingen af neutrino-type, medmindre der er en udbredt ustabil region , dvs. betingelserne opretholder sig selv og er globale. På samme måde, og ved brug af en lignende multidimensionel opsætning, beregnedes udviklingen af neutrino-typekonvertering over skiven med rester fra et kompaktt binært sammenstød. Efter typeustbiliteterne havde udviklet sig, blev resultaterne undersøgt for stabile tilstande. Selvom dette arbejde antog en forenklet model for neutrino-afkoblingsregionerne, viste det for første gang, at typekonvertering finder sted i meget vel-lokaliserede områder over skiven med rester fra sammenstødet, og at minimal blanding af neutrinoer (mindre end 1%) er mulig trods de store vækstrater for typeustabiliteter. Sidst men ikke mindst, i det sidste afsnit i denne afhandling blev antagelsen om isotropi i materie-leddet slække og konsekvenserne for den ikke-lineære udvikling af neutrino-type blev undersøgt i detaljer. Dette forbedrer modellen i forhold til tidligere studier, hvor materie-baggrunden antages at være statisk og derfor isotrop. Den uudforskede effekt af stoffets strømningshastighed blev undersøgt og det demonstreres, at typekonvertering er følsom over for størrelsen af og retningen på strømningshastigheden, som kunne opnå værdier på en brøkdel af lysets hastighed i astrofysiske miljøer.

Denne afhandling viser at fysikken for hurtige typekonverteringer er utroligt rig. Selv om der fortsat ligger mange udfordinger foran os, forsætter neutrino typekonvertering med at give anledning til nye indsigter, der giver os en bedre forståelse af astrofysiske kilder og vores univers.

THESIS OUTLINE

The thesis is divided into five parts:

Part i: Introduction.

Part ii: New conceptual developments on the physics of neutrino fast flavor conversion.

Part iii: Numerical modeling and phenomenology of neutrino fast flavor conversion.

Part iv: Summary and conclusions.

Part v: Appendices.

Part i offers a broad introduction to the main physical concepts and phenomena discussed in the thesis. Parts ii and iii of this thesis consist of the reprints of the following published journal articles:

1. Shashank Shalgar, **Ian Padilla-Gay**, Irene Tamborra, *Neutrino propagation hinders fast pairwise flavor conversions*, JCAP06(2020)048, arXiv:1911.09110.
2. **Ian Padilla-Gay**, Shashank Shalgar, Irene Tamborra, *Multi-Dimensional Solution of Fast Neutrino Conversions in Binary Neutron Star Merger Remnants*, JCAP01(2021)017, arXiv:2009.01843.
3. **Ian Padilla-Gay**, Shashank Shalgar, *Fast flavor conversion of neutrinos in presence of matter bulk velocity*, Phys. Rev. D **under review**, arXiv:2108.00012.
4. **Ian Padilla-Gay**, Irene Tamborra, Georg G. Raffelt, *Neutrino flavor pendulum reloaded: The case of fast pairwise conversion*, Phys. Rev. Lett. 128 (2022) 12, 12, arXiv:2109.14627.
5. **Ian Padilla-Gay**, Irene Tamborra, Georg G. Raffelt, *Upshot of Collisional Damping on Neutrino Fast Flavor Conversion*, **to appear soon**.

In every part of the thesis, there is a Chapter called *Critical outlook* which provides a short description of the project, gives the relevant context, and critically discusses the findings of the corresponding publication.

Part ii consists of publications 4 and 5, while Part iii comprehends the remaining publications 1, 2, and 3. The work presented in 5 is a work in progress. However, a preliminary draft of the publication is presented here.

Part iv concludes the main findings and results presented in this body of work, discusses some of the limitations of the field, and offers an outlook for future research. Lastly, part v contains the appendices of the publications not included in the main body of this thesis.

ACKNOWLEDGEMENTS

The past three years have been three of the most challenging. Yet, at the same time, three of the years where I have been able to connect the most and meet extraordinary people I now consider almost family. This Section is dedicated to all the people who were part of my PhD journey and without whom everything I have achieved would be nothing.

First, I would like to express my deepest gratitude to Irene Tamborra for dedicating her time and attention to my PhD supervision and being a great example and inspiration. I am grateful to her for seeing something in me as a young scientist three years ago. I take invaluable lessons with me to continue my scientific career.

I am very grateful to Shashank Shalgar for guiding me and teaching me about the mysteries of collective neutrino oscillations and general topics in particle physics and astrophysics. Wherever I go, I'll miss having quantum mechanics puzzles during coffee breaks, which always left students wondering. I also want to express my gratitude to Rasmus S. L. Hansen, who always discussed his research with me very patiently every time. I am also indebted to Mauricio Bustamante and Markus Ahlers for offering me guidance on postdoctoral applications and other curiosities of the academic world or simply for sharing a coffee with me at NBI. And, of course, no coffee break would be complete without the many laughs with Enrico Peretti and Alejandro Vigna-Gomez. In addition to making me laugh non-stop, they became dear friends and mentors.

Likewise, I would like to express my gratitude to Georg Raffelt, who has been a great inspiration and mentor for the past year. I am fortunate to have been part of the long list of students who have learned from him and had the opportunity to discuss science and a bit about life. To this day, I greatly admire his ability to abstract and ask the right questions at the right time. I am also very grateful for his hospitality at the Max Planck Institute for Physics in Munich. Moreover, I am thankful for the exciting discussions with Sajad Abbar, Manibrata Sen, and Andrea Caputo, from whom I learned much during my academic exchange there.

My work at NBI would have been impossible without the fantastic company of amazing people who have become part of my extended family, as I like to call it. I am incredibly grateful to Laurie Walk, Anna Suliga, Tania Pitik, Kays Haddad, Andrea Cristofoli, and Andreas Helset for their friendship and support; you have made NBI feel like home. In particular, I would like to thank my first office mates, Laurie Walk, Anna Suliga, and Tania Pitik, with whom I became particularly close during the first year of my PhD.

In the second year of my PhD and after a pandemic, I crossed paths with new people. I met people who are now best friends and fellow adventurers. Therefore, I want to express my gratitude to Ersilia Guarini, Victor Valera, Marina De Amicis, Youyou Li, Damiano Fiorillo, Kevin Urquía, Kathrine Mørch Groth, Tyler Corbett, Marie Cornelius Hansen, Arun Krishna Ganesan, Garðar Sigurðarson, Jonathan Bödewadt, Edoardo Vitagliano, Evelyn-Andreea Ester, Bernanda Telalovic and Aysu Arat. I hope we cross paths again very soon.

Finally, I thank my greatest inspiration, family, and friends in México. They have always supported me unconditionally, regardless of the risks and uncertainties involved. Many thanks to my mom, my dad, and my biggest inspiration for as long as I can remember, my brother Adrián. I also want to dedicate this thesis to León, Bety, Mich, Marianne, Lilita and Abuelo Pa. Likewise, I want to thank the wonderful people I have had the chance to share unique experiences. Thanks to Irvin Martinez for your incredible wisdom about life. Also, I am happy to have coincided with Mariana Escobedo and am grateful for having rescued me from a mountain in the Faroe Islands. Last but not least, I thank my dear friend Alonso Malacara for being my best friend since kindergarten (!) and continuing to put up with my crazy ideas years later.

CONTENTS

III NUMERICAL MODELING AND PHENOMENOLOGY OF NEUTRINO FAST FLAVOR CONVERSION

IV SUMMARY AND CONCLUSIONS

V APPENDICES

Part I

INTRODUCTION

1

MOTIVATION

Neutrinos were hypothesized in 1930 by Wolfgang Pauli as a remedy to save energy and momentum conservation in beta decays. The idea was to include a new electrically neutral particle into the picture similar to the neutron but with a much smaller mass, a "little neutral one." With a neutrino in the beta decays, the continuous beta spectrum could be explained, as the neutrino could carry part of the energy in such a process.

Since neutrinos interact very weakly with matter, it took some time to observe them. In 1956, a direct observation was materialized for the first time when reactor $\bar{\nu}_e$ were detected [1] through the inverse beta decay. The existence of a μ lepton [2] suggested the possibility of a neutrino-partner entering the picture. It was only in 1962 that the Brookhaven National Laboratory reported the direct detection of ν_μ [3]. Later on, the existence of τ leptons was confirmed at the Stanford Linear Accelerator Centre [4], and the detection of the corresponding ν_τ in 2001 at Fermilab [5] completed the three families of leptons and neutrinos that we know today.

In 1968, the Homestake experiment led by Raymond Davis detected neutrinos coming from the nitrogen-carbon cycle in the Sun [6] and reported a deficit of ν_e counts; they measured about a $1/3$ of the flux predicted by Bahcall. This discrepancy is known as the solar neutrino problem [7]. Different explanations for this deficit were proposed to explain this discrepancy, including corrections to the solar model and beyond the Standard Model scenarios. Later, a similar discrepancy was confirmed by the Kamiokande detector [8] and by the Irvine-Michigan-Brookhaven experiment [9, 10] which detected fewer atmospheric muon neutrinos than predicted. These anomalies were later explained by a phenomenon known as neutrino flavor conversion [8, 11, 12] which is responsible for a variation of the flavor content of neutrinos between their production and detection location. Neutrino flavor conversion has been observed for atmospheric neutrinos [13, 14], solar neutrinos [15, 16], reactor neutrinos [17, 18], and accelerator neutrinos [19, 20]. See the Gran Unified Neutrino Spectrum at Earth [21] for a global picture of neutrino processes. The solid confirmation of neutrino oscillations implies that neutrinos have non-zero masses and urges for new physics beyond the Standard Model.

Apart from the first detection of neutrinos from the Sun [6], various astrophysical sources have been identified as possible efficient neutrino factories [22–24]. Among these are the famous Supernova 1987A [25–27], cosmic ray neutrinos interacting with Earth's atmosphere [28], and more recently, detections consistent with blazars [29–33], tidal disruption events [34–36] and superluminous supernovae [37].

Also, the recent detection of gravitational waves and photons from a binary neutron star merger event [38], could have been accompanied by neutrinos. The detection of the event GW170817 was followed up by IceCube [39], ANTARES [40], and the Pierre Auger Observatory [41] to search for coincident high-energy neutrinos from the relativistic outflow from the binary neutron star merger. However, IceCube did not identify neutrinos that were directionally coincident with the location of GW170817 [42]. Moreover, Superkamiokande searched for coincident neutrino events in the range MeV–PeV and found no significant neutrino signal. However, upper limits were set on the neutrino fluence for GW170817 [43]. Ongoing efforts are still trying to find coincident neutrino events with gravitational wave events from the latest run (O3) of the LIGO/Virgo collaborations [44].

Neutrinos from astrophysical sources allow us to learn from the behavior of particle interactions in extreme conditions [45], which would otherwise be impossible to create in terrestrial experiments.

For instance, Supernova 1987A [25–27] was the first direct detection of neutrinos from the collapse of a star. Since neutrinos carry away 100 times more energy than the kinetic energy of a typical core-collapse supernova, neutrinos are expected to play a dominant role. Moreover, since neutrinos interactions and neutrino energy deposition is flavor-dependent, the modeling of the evolution of neutrino flavor in a core-collapse supernova is conceptually complex and represents an open issue in astrophysics. Not surprisingly, the situation is also complex for compact binary merger remnants. Even though the detection of neutrinos from merger remnants is unlikely due to a low local merger rate [43], neutrinos can still indirectly affect future observations. For instance, the evolution of the merger disk and the formation of the neutrino-driven wind depend on the balance between neutrino absorption and emission, and thus neutrinos are expected to play an essential role in the cooling of the disk and in the production of elements heavier than iron [46–50].

To better understand the role of neutrino flavor conversions in core-collapse supernovae [51] and the compact binary merger remnants [50], the works contained in this thesis focus on investigating the neutrino flavor evolution in regions where the neutrino densities are incredibly high, with the hope to shed light on the possible impact that neutrino flavor conversion could have on the inner-workings of such fascinating astrophysical sources.

We adopt the following conventions throughout this thesis, unless specified otherwise:

- Natural units: $\hbar = c = 1$.
- Greek indices $\mu, \nu = 0, 1, 2, 3$.
- Neutrino flavor indices in the three-flavor framework $\alpha, \beta = e, \mu, \tau$.
- Neutrino flavor indices in the two-flavor framework $\alpha, \beta = e, x$, where $x = \mu, \tau$ is the admixture of heavy-lepton neutrinos.
- Neutrino mass basis indices $i, j = 1, 2, 3$.
- The Minkowski metric uses the following signature $\eta_{\nu\mu} = \eta^{\mu\nu} = \text{diag}(-1, 1, 1, 1)$.
- The gamma matrices γ^μ satisfy the Clifford algebra $\{\gamma^\mu, \gamma^\nu\} = 2\eta^{\mu\nu}$. The gamma matrix $\gamma^5 \equiv i\gamma^0\gamma^1\gamma^2\gamma^3$.

These are the most common abbreviations used throughout this thesis:

- SM = Standard Model.
- NC, CC = Neutral-Current and Charged-Current, respectively.
- MSW = Mikheyev-Smirnov-Wolfenstein effect.
- NO (NH) = Normal Ordering (Normal Hierarchy).
- IO (IH) = Inverted Ordering (Inverted Hierarchy).
- FFC = Fast Flavor Conversion.
- EOM = Equation of Motion.
- LSA = Linear Stability Analysis.
- ELN = Electron-Lepton-Number.
- MNR = Matter-Neutrino Resonance.
- CCSNe = Core-Collapse Supernovae.
- NS, BH, PNS = Neutron Star, Black Hole and Proto-Neutron Star, respectively.

2

FUNDAMENTALS OF NEUTRINO PHYSICS

Neutrinos are fermions (spin 1/2) and are among the fundamental particles of nature. They participate only in weak and gravitational interactions, and however, due to their very tiny masses and weak coupling to matter, their interactions are difficult to detect. Like quarks and charged-leptons, neutrinos also come in three different flavors: electron (e), muon (μ) and tau (τ). Neutrinos are classified according to their charged-lepton partner that is produced (or destroyed) along with the neutrino via charged-current weak interactions: we call ν_e the neutrino that should follow after the detection of an e, and similar for the μ and τ flavors. In the next Sections, we study neutrino weak interactions as described by the Standard Model and derive, in a standard fashion, phenomenological implications such as neutrino flavor conversion.

2.1 NEUTRINOS IN THE STANDARD MODEL

Three families of neutrinos, ν_e, ν_μ, ν_τ and their antiparticles participate in weak interactions such as charged- and neutral-current interactions via the exchange of weak $W^\pm$ and Z^0 bosons. The contribution from terms containing neutrino fields in the fermion Lagrangian $\mathcal{L}_F$ is given by [52, 53]

$$\begin{aligned}\mathcal{L}_F \quad \supset \quad & \sum_{\alpha=e,\mu,\tau}\left[\bar{\nu}_\alpha i\gamma^\mu\partial_\mu\nu_\alpha + \frac{g}{\sqrt{2}}\left(\bar{\nu}_{\alpha,L}\gamma^\mu e_{\alpha,L}W^+_\mu + h.c.\right) + \frac{g}{2\cos\theta_w}\bar{\nu}_{\alpha,L}\gamma^\mu\nu_{\alpha,L}Z_\mu\right] \\ & - \sum_{\alpha,\beta=e,\mu,\tau}\left(m_{\alpha\beta}\bar{\nu}_{\alpha,L}\nu_{\beta,R} + h.c.\right) . \end{aligned} \tag{2.1}$$

The index runs over the three flavors $\alpha = e, \mu, \tau$. Here, θ_w is the weak mixing angle (Weinberg angle), g is the weak coupling constant, γ^μ are the gamma matrices, and $Z^0, W^\pm$ are the neutral and charged weak bosons. The subscripts L and R refer to left-handed and right-handed neutrino fields, respectively. The charged-current term (second term) couples neutrinos and charged leptons to the $W^\pm$ bosons, while the neutral-current term (third term) couples neutrinos to the neutral

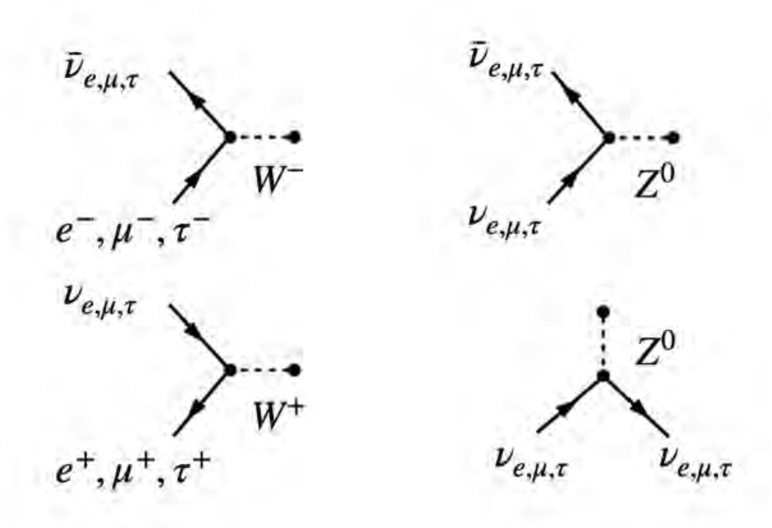

Figure 1: Neutrino interaction vertices. Three families of charged leptons e, μ, τ and neutrinos $\nu_{e,\mu,\tau}$ (and their antiparticles) undergo weak interactions mediated by the gauge bosons $W^{\pm}$ and Z^0.

Z^0 boson. See Fig. 1 for the weak interaction vertices. One peculiar characteristic of the weak interaction is the maximal violation of parity, i.e., only left-handed neutrinos couple to the weak gauge bosons $W^{\pm}$ and Z^0.

The mass term in Eq. 2.1 is generally not diagonal. In other words, there can be non-vanishing $m_{\alpha\beta}$ for $\alpha \neq \beta$. As a result, the *flavor eigenstates* $\nu_{e,\mu,\tau}$ do not have a well-defined mass. To go to a basis where the mass term is diagonal (the mass basis), the unitary matrices U and V are introduced:

$$m = U m_D V^{\dagger} \,, \tag{2.2}$$

where $m_D = \mathrm{diag}(m_1, m_2, m_3)$ has only diagonal entries. The *mass eigenstates* are then defined accordingly

$$\nu_{j,L} \equiv \sum_{\alpha=e,\mu,\tau} U^*_{\alpha,j} \nu_{\alpha,L} \tag{2.3}$$

$$\nu_{j,R} \equiv \sum_{\alpha=e,\mu,\tau} V^*_{\alpha,j} \nu_{\alpha,R} \tag{2.4}$$

where the index j runs over the mass eigenstates $j = 1, 2, 3$. Since only left-handed neutrinos couple to the weak gauge bosons, the matrix $V^*_{\alpha,j}$ cannot be measured, only $U^*_{\alpha,j}$. For left-handed neutrinos however, this rotation has important implications for the charged current interactions

$$\begin{aligned}\mathcal{L}_F \supset & \sum_{j=1,2,3} \left[\bar{\nu}_j i\gamma^\mu \partial_\mu \nu_j + \frac{g}{\sqrt{2}} \left(\bar{\nu}_{j,L} U^*_{\alpha,j} \gamma^\mu e_{\alpha,L} W^+_\mu + h.c. \right) + \frac{g}{2\cos\theta_w} \bar{\nu}_{j,L} \gamma^\mu \nu_{j,L} Z_\mu \right] \\ & - \sum_{j=1,2,3} \left(m_j \bar{\nu}_{j,L} \nu_{j,R} + h.c. \right) . \end{aligned} \tag{2.5}$$

Therefore, charge current neutrino interactions give rise to a superposition of mass eigenstates. The fact that the mass eigenstates do not coincide with the interaction eigenstates leads to neutrino flavor transitions. In the next Section, we discuss neutrino oscillations in more detail.

2.2 NEUTRINO OSCILLATIONS

Neutrino oscillation is a quantum mechanical phenomenon that allows neutrinos created in a specific flavor to be detected later in a different flavor. Historically, Pontecorvo was the first to realize that the presence of two or more neutrino flavors allows for very small neutrino masses to emerge in observations [54]. Pontecorvo's original work referred to $\nu \leftrightarrow \bar{\nu}$ oscillations similar to those of kaons [55, 56]. At present, we understand that neutrino oscillation in vacuum arises because the neutrino propagation eigenstates, the states with definite momentum, are not the same as their interaction eigenstates. The latter means that neutrinos produced in a particular flavor (coherent superposition of mass eigenstates) through weak interaction processes will propagate in vacuum and, in doing so, their wavefunction evolves as a result of phase differences. In practice, there is a well-defined probability of detecting a neutrino flavor other than originally produced, referred to as neutrino oscillations [8, 57].

2.2.1 *Neutrino oscillations in vacuum*

As described by the weak-interaction Lagrangian in Eq. 2.5, a weak-interaction eigenstate produced, for instance, in the decay of a neutron $n \to p + e^- + \bar{\nu}_e$ comes as a superposition of neutrino mass eigenstates

$$|\nu_\alpha\rangle = \sum_j U^*_{\alpha j} |v_j\rangle \ . \tag{2.6}$$

Even though the fields transform as $\nu_{\alpha,L} = \sum_j U_{\alpha j} \nu_{\alpha,L}$ from the mass- to the flavor basis, the ket states transform with $U^\dagger$ and not U. More in detail, the ket states are produced via the creation operator $\sum_j U^*_{\alpha j} \bar{\nu}_{j,L}$ and not the annihilation operator $\sum_j U_{\alpha j} \nu_{j,L}$. By representing the neutrino state as an expansion in plane waves, the wave function as a function of the production source L and the time after production reads as

$$|\nu_\alpha(T, L)\rangle = \sum_j U^*_{\alpha j} e^{-iE_j T + i p_j L} |\nu_j\rangle \, , \tag{2.7}$$

where E_j and p_j are the energy and the momentum for each of the i-th mass eigenstates. In general, due to their different kinematics, E_j and p_j are different for each of the mass eigenstates.

Once the wave function is known, the amplitude can be computed. For a neutrino produced as $|\nu_\alpha\rangle$ and detected as a $\langle\nu_\beta|$, the amplitude is given by

$$\langle\nu_\beta|\nu_\alpha(T, L)\rangle = \sum_{j,k} U^*_{\alpha j} U_{\beta k} e^{-iE_j T + i p_j L} \underbrace{\langle\nu_k|\nu_j\rangle}_{=1} . \tag{2.8}$$

By squaring the amplitude, one obtains the oscillation probability as a function of T and L

$$P_{\alpha\beta}(T, L) = |\,\langle\nu_\beta|\nu_\alpha(T, L)\rangle\,|^2 = \sum_{j,k} U^*_{\alpha j} U_{\beta j} U_{\alpha k} U^*_{\beta k} e^{-i(E_j - E_k)T + i(p_j - p_k)L} . \tag{2.9}$$

In neutrino oscillation experiments and astrophysical sources, one does not know when each neutrino is produced, i.e., the uncertainty in the production time is far larger than the uncertainty of the neutrino energy. Thus, what we see is a time-averaged effect on the oscillation probability

$$\begin{aligned} P_{\alpha\beta}(L) &= \frac{1}{N} \int dT P_{\alpha\beta}(T, L) \\ &= \frac{1}{N} \sum_{j,k} U^*_{\alpha j} U_{\beta j} U_{\alpha k} U^*_{\beta k} \exp\left[i \left(\sqrt{E_j^2 - m_j^2} - \sqrt{E_k^2 - m_k^2} \right) L \right] \delta(E_j - E_k) \qquad (2.10) \end{aligned}$$

where the constant N ensures that $\sum_\beta P_{\alpha\beta}(L) = 1$. Also, the Dirac delta resulted from $\int dT e^{-i(E_j - E_k)T} = \delta(E_j - E_k)$ which forces the energies to be equal to each other $E = E_j = E_k$. Moreover, since the masses are much smaller than the energy, the oscillation probability $P_{\alpha\beta}(L)$ can be Taylor expanded in m_j^2/E^2 (and m_k^2/E^2) to obtain the general three flavor oscillation probabilities

$$P_{\alpha\beta}(L) \simeq \sum_{j,k} U^*_{\alpha j} U_{\beta j} U_{\alpha k} U^*_{\beta k} \exp\Big[-i\frac{\Delta m^2_{jk}}{2E} L\Big]. \tag{2.11}$$

A subtle point is in place regarding the time averaging leading to Eq. 2.11. Alternatively, one could have imposed that all neutrino mass eigenstates are created with the same momentum p but different energies. Qualitatively, this would have given the same result after assuming that neutrinos travel nearly at the speed of light, implying $L = T$. In reality, neutrino sources are, more or less, constant in time, and the elapsed time between production and detection is not measured. The interference between two components of a neutrino beam with E_j and E_k will involve a phase factor $\exp[-i(E_j - E_k)T]$ which vanishes after time-averaging unless $E_j = E_k$, as show in Eq. 2.10. Therefore, the different components of the mass eigenstates of a beam that contribute *coherently* to flavor oscillations have the same energy E.

2.2.1.1 *Three-flavor framework*

The unitary mixing matrix U has 9 angles and 9 complex phases for three active neutrino flavors. Due to unitarity conditions and re-definitions of the neutrino fields, a total of three angles and one complex phase remain the independent physical observables: three mixing angles $\theta_{12}, \theta_{13}, \theta_{23}$ and one complex Dirac phase $\delta_{\rm CP}$ that results in CP violation. The mixing matrix U is parametrized as follows

$$\begin{aligned} U &= \begin{pmatrix} 1 & & \\ & c_{23} & s_{23} \\ & -s_{23} & c_{23} \end{pmatrix} \begin{pmatrix} c_{13} & & s_{13}e^{-i\delta_{\rm CP}} \\ & 1 & \\ -s_{13}e^{i\delta_{\rm CP}} & & c_{13} \end{pmatrix} \begin{pmatrix} c_{12} & s_{12} & \\ -s_{12} & c_{12} & \\ & & 1 \end{pmatrix} \\ &= \begin{pmatrix} c_{12}c_{13} & s_{12}c_{13} & s_{13}e^{-i\delta_{\rm CP}} \\ -s_{12}c_{23} - c_{12}s_{23}s_{13}e^{i\delta_{\rm CP}} & c_{12}c_{23} - s_{12}s_{23}s_{13}e^{i\delta_{\rm CP}} & s_{23}c_{13} \\ s_{13}s_{23} - c_{12}c_{23}s_{13}e^{i\delta_{\rm CP}} & -c_{12}s_{23} - s_{12}c_{23}s_{13}e^{i\delta_{\rm CP}} & c_{23}c_{13}, \end{pmatrix} \end{aligned} \tag{2.12}$$

where $c_{ij} \equiv \cos\theta_{ij}$ and $s_{ij} \equiv \sin\theta_{ij}$. This matrix is the Pontecorvo-Maki-Nakagawa-Sakata (PMNS) matrix [56, 58]. The mixing of three neutrino flavors $\nu_{e,\mu,\tau}$ are described by the three mixing angles $\theta_{12}, \theta_{13}, \theta_{23}$ conventionally taken to lie in the first quadrant $\theta \in [0, \pi/2]$, two mass squared differences that parametrize the variation in mass among the mass eigenstates $\Delta m^2_{12} = m^2_2 - m^2_1 \equiv$

δm^2 and $\Delta m^2_{31} = m^2_3 - m^2_1 \simeq \Delta m^2_{32} \equiv \Delta m^2$, and the Dirac CP-violating phase δ_{CP} conventionally taken to lie in $\delta_{\mathrm{CP}} \in [0, 2\pi]$. Neutrinos may be Majorana particles, in which case two extra phases $\eta_{1,2}$ enter the PMNS matrix. Nevertheless, $\eta_{1,2}$ are unobservable because they can be absorbed in the neutrino states.

In Table 1 we show the best fit values of the mixing parameters with their uncertainties. Since neutrino oscillations are only sensitive to the difference of the neutrino masses, there is no information about their absolute value coming from neutrino oscillation experiments. The latter means that at least two neutrinos are massive. The small squared difference δm^2 becomes manifest at very large distances, as shown in Figs. 2 and because of that, its sign can be determined through the Mikheyev-Smirnov-Wolfenstein effect in the interior of the Sun [59] (Section 2.2.2), thereby complementing Earth-based measurements of the sign of δm^2. On the other hand, the larger mass squared difference Δm^2 operates on smaller scales, as shown in Fig. 3 and its sign has not been determined yet by using the MSW effect. The sign of Δm^2 remains undetermined, and two possibilities arise: Normal Ordering (NO) and Inverted Ordering (IO). The NO corresponds to the scenario where $m_3 > m_2 > m_1$ and the IO to the scenario where $m_2 > m_1 > m_3$. At present, experiments favor the NO scenario [60], and there are available constraints for both scenarios from cosmology with a slight preference for the NO [61]. However, there is no conclusive evidence of this preference [62] and only future neutrino experiments can solve this issue in the upcoming years [63].

2.2.1.2 *Two-flavor framework*

There is only one mixing angle, and one mass squared difference for two active neutrino flavors. Under this assumption Eq. 2.11 allows to write down the transition probability $(\alpha \neq \beta)$ in the following way

$$P_{\alpha\beta}(L) = \sin^2(2\theta)\sin^2\left(1.27\frac{\Delta m^2 L}{E}\frac{[\mathrm{eV}^2][\mathrm{km}]}{[\mathrm{GeV}]}\right), \tag{2.13}$$

where a factor of $c^3/\hbar$ has to be restored in the oscillation argument of Eq. 2.11 to account for SI units. The mixing angle θ controls the amplitude of oscillations, while the mass squared difference Δm^2 sets the oscillation period. This oscillatory behavior is shown in Fig. 2 where $P_{e\mu}(L)$, $P_{ee}(L)$ are plotted using a 1 MeV neutrino traveling a distance of 100 km. Additionally, in Fig. 3 we show

Table 1: Table of the neutrino mixing parameters as measured experimentally. The best fit values are reported with their corresponding uncertainties. Values taken from from Table III of Ref. [60] and the PDG [64].

Parameter	Best fit value (NO)	3σ range (NO)	Best fit value (IO)	3σ range (IO)
$\theta_{12}[^\circ]$	34.3	$31.4 - 37.4$	34.3	$31.4 - 37.4$
$\theta_{13}[^\circ]$	8.53	$8.13 - 8.92$	8.58	$8.17 - 8.96$
$\theta_{23}[^\circ]$	49.26	$41.20 - 51.33$	49.46	$41.16 - 51.25$
$\delta m^2[\mathrm{eV}^2]$	7.5×10^{-5}	$(6.94 - 8.14) \times 10^{-5}$	7.5×10^{-5}	$(6.94 - 8.14) \times 10^{-5}$
$\Delta m^2[\mathrm{eV}^2]$	2.55×10^{-3}	$(2.47 - 2.63) \times 10^{-3}$	$\|2.55 \times 10^{-3}\|$	$(\|2.37\| - \|2.53\|) \times 10^{-3}$
$\delta_{\mathrm{CP}}[\mathrm{rad}]$	1.08π	$0.71\pi - 1.99\pi$	1.58π	$1.11\pi - 1.96\pi$

neutrino oscillations in vacuum of three neutrino flavors using the same neutrino energy. One direct consequence of neutrino oscillations in vacuum is that the probability of observing ν_e, $(\bar{\nu}_e)$ varies as a function of the distance between neutrino production and detection.

2.2.2 *Neutrino conversions in matter*

In astrophysical environments, a significant matter background modifies the way neutrino oscillates inside the source. The first to realize that was Wolfenstein [65], who showed that neutrinos traveling in matter experience a potential due to coherent forward scattering with particles in the medium. Later on, Mikheyev and Smirnov [59] showed that resonant flavor transitions are possible for neutrinos traveling through a medium if certain resonance conditions are met. Fulfilling the resonance condition leads to enhanced conversions in matter, often referred to as the MSW resonance effect. In this Section, the MSW resonance effect is revisited, pointing out critical phenomenological implications for neutrinos.

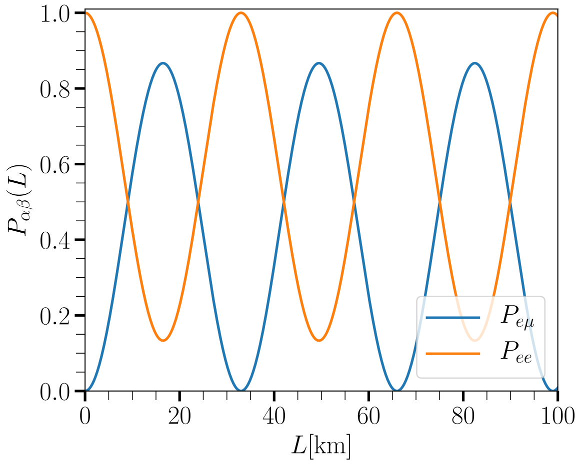

Figure 2: Neutrino vacuum oscillations in the two-flavor framework. The neutrino beam has an energy of $E = 1$ MeV and we assume the solar oscillation parameters δm^2 and θ_{12} as reported in Table 1. The amplitude of oscillations is controlled by $\sin^2 2\theta_{12}$ while the period of oscillation is fixed by $\delta m^2/E$. Equal oscillation probabilities result for antineutrinos.

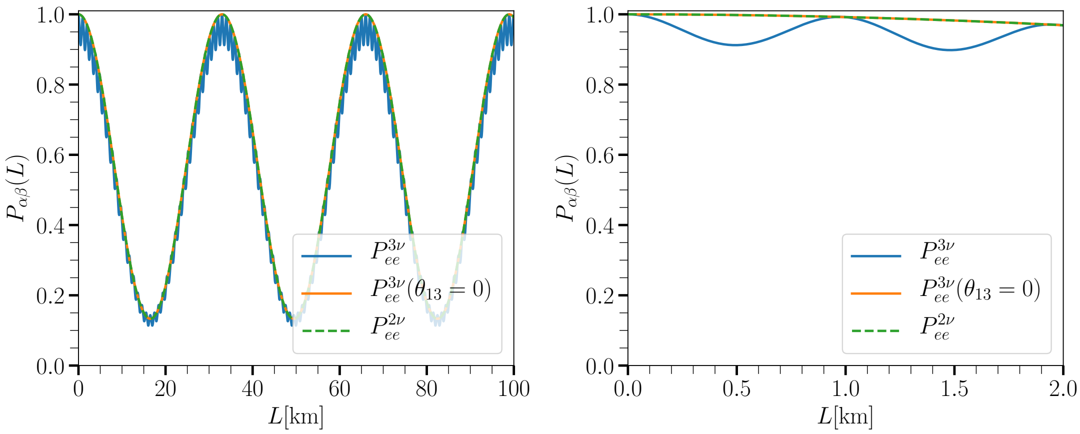

Figure 3: Neutrino vacuum oscillations in the three-flavor framework. The neutrino beam has an energy of $E = 1$ MeV. The survival probability $P_{ee}^{3\nu}$ is a function of the parameters $\theta_{12}, \theta_{13}, \delta m^2, \Delta m^2$. As in the two flavor case, the amplitude of oscillations is controlled by $\sin^2 2\theta_{12}$ while its period is fixed by $\delta m^2/E$. However, small-scale oscillations are happening as well. The amplitude of the small wiggles is controlled by θ_{13} (see that for $\theta_{13} = 0$ we recover $P_{ee}^{3\nu} = P_{ee}^{2\nu}$), while the period is set by Δm^2.

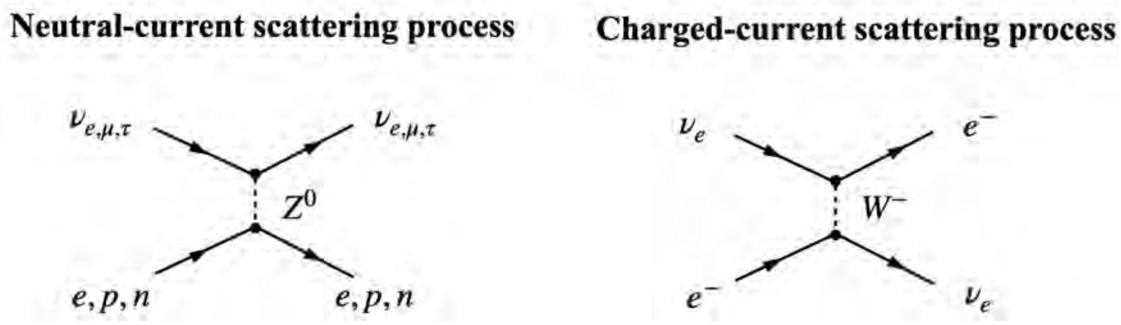

Figure 4: As neutrinos travel through matter, they can interact with background particles through neutral-current scattering and charged-current scattering processes. Neutral-current scatterings involve neutrinos of all flavors, while the charged-current interaction requires a charged-lepton to be present. In core-collapse supernovae and compact binary merger remnants, there is an overwhelming number of e in comparison to the abundance of heavy-leptons μ and τ .

As neutrinos propagate in a dense medium, they interact with background particles. The probability of incoherent scatterings occurring is quite small. For instance, the characteristic cross-section for a neutrino-proton scattering is roughly [64]

$$\sigma \sim \frac{G_F^2 s}{\pi} \sim 10^{-43}\,\mathrm{cm}^2 \left(\frac{E}{\mathrm{MeV}}\right)^2 , \tag{2.14}$$

where the Fermi constant $G_\mathrm{F} \equiv \sqrt{2} g^2 / 8 M_W^2 \simeq 1.166 \times 10^{-5}\,\mathrm{Gev}^{-2}$ and s is the square of the center of mass energy of the collision. In dense matter, however, neutrinos can also interact coherently with the background particles. During coherent interactions, the medium remains unchanged, and it is possible to have interference between the forward scattered and the unscattered neutrino waves, which results in the MSW effect. The effect of the medium is on the development of a phase difference of the neutrino waves and not on the intensity of the neutrino beam, which remains unchanged. For this reason, coherent forward scattering is proportional to G_F and not G_F^2 as for incoherent scatterings. For illustration, let us consider the evolution of ν_e in a medium constituted by electrons, protons, and neutrons with their corresponding number densities n_e, n_p and n_n.

In light of the fermionic Lagrangian for weak interactions in Eq. 2.1, the corresponding Hamiltonian is given by its Legendre transformation

$$H_F \supset - \sum_{\alpha = e,\mu,\tau} \left[\frac{g}{\sqrt{2}} \left(\bar{\nu}_{\alpha,L} \gamma^\mu e_{\alpha,L} W_\mu^+ + h.c. \right) + \frac{g}{2\cos\theta_w} \bar{\nu}_{\alpha,L} \gamma^\mu \nu_{\alpha,L} Z_\mu \right] . \tag{2.15}$$

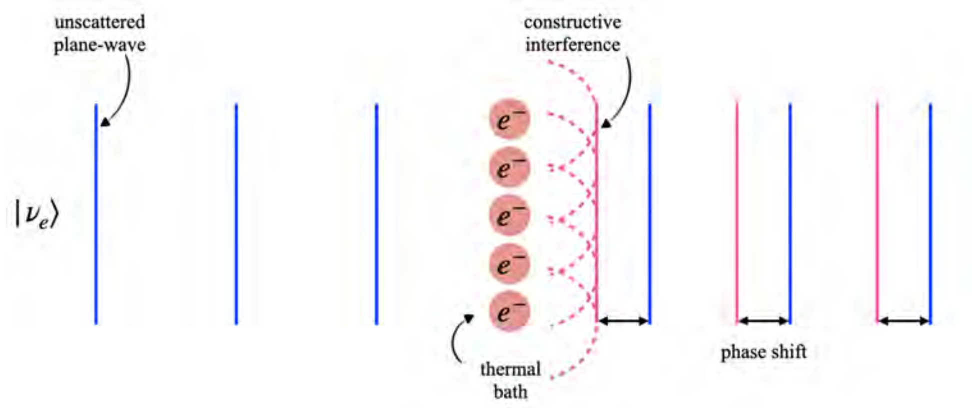

Figure 5: Schematic representation of coherent forward scattering of neutrinos. An unscattered ν_e plane-wave (blue) approaches a thermal bath of e^- and scatters. A wave-front emanates from each of the e^- in the bath, which adds coherently to form a plane-wave (magenta) constructively. This scattered plane wave, however, has developed a phase shift with respect to the unscattered one. The scattered plane wave interferes with the unscattered one because of the phase shift leading to the MSW effect.

In the low-energy limit, i.e., for neutrino energies much smaller than $M_W = 80.2$ GeV and $M_Z = 91.2$ GeV, the energy and momentum transferred by the weak bosons is much less than their masses. See Fig. 4 for the neutrino interaction diagrams mediated by the weak bosons. The low energies involved justify expanding the propagators and keeping only the first leading term. Thus, the propagator of the weak bosons can be approximated as

$$G^{(W,Z)}_{\mu\nu}(p) \quad = \quad i\frac{-g_{\mu\nu} + \frac{p_\mu p_\nu}{M^2_{W,Z}}}{p^2 - M^2_{W,Z} + i\epsilon} \longrightarrow i\frac{g_{\mu\nu}}{M^2_{W,Z}} \ . \tag{2.16}$$

This low-energy expansion allows to write down an effective Hamiltonian for the exchange of weak bosons known as Fermi's four fermion interaction [66, 67]. Let us first have a look at the effective Hamiltonian responsible for charged-current interactions of ν_e with background electrons

$$H_{\text{mat}} \quad \supset \quad \frac{g^2}{2M_W^2}\left[\bar{\nu}_{e,L}\gamma^\mu e_L\right]\left[\bar{e}_L\gamma^\mu \nu_{e,L}\right] \tag{2.17}$$

$$= \quad \frac{G_F}{\sqrt{2}}\left[\bar{\nu}_e\gamma^\mu(1-\gamma^5)e\right]\left[\bar{e}\gamma^\mu(1-\gamma^5)\nu_e\right] \ . \tag{2.18}$$

In order to isolate the electron components, one uses the Fierz identities [68, 69] which give

$$H_{\text{mat}} \supset \frac{G_F}{\sqrt{2}}\left[\bar{e}\gamma^\mu(1-\gamma^5)e\right]\left[\bar{\nu}_e\gamma^\mu(1-\gamma^5)\nu_e\right] \ . \tag{2.19}$$

The background electrons can be regarded as a static background. Their four-momenta (and helicities) are the same before and after the scattering. Only by leaving the background medium unchanged after the interaction can it coherently contribute to a shift in the neutrino energy. See Fig. 5 for a schematic representation of coherent forward scattering undergone by neutrinos via charge-current interactions. Therefore, it is reasonable to take the thermal average $\langle \cdot \rangle$ of the interaction Hamiltonian over the electron fields

$$H_{\text{mat}} \supset \frac{G_F}{\sqrt{2}} \langle \bar{e}\gamma^\mu(1-\gamma^5)e \rangle \left[\bar{\nu}_e \gamma^\mu (1-\gamma^5)\nu_e\right] . \tag{2.20}$$

Moreover, by assuming that the momentum distribution of electrons is isotropic, the contribution from $\mu = 1, 2, 3$ to the thermal average vanishes[1] and only $\mu = 0$ contributes

$$\langle \bar{e}\gamma^0(1-\gamma^5)e \rangle = n_e \quad , \quad \langle \bar{e}\gamma^i(1-\gamma^5)e \rangle = 0 \, , \tag{2.21}$$

where n_e is the electron number density. Therefore, the matter potential takes the following form

$$H_{\text{mat}} \supset \frac{G_F}{\sqrt{2}} n_e \left[\bar{\nu}_e \gamma^0 (1-\gamma^5)\nu_e\right] = V_{CC} \left[\bar{\nu}_{e,L} \gamma^0 \nu_{e,L}\right] , \tag{2.22}$$

where the charged-current potential due to electrons is

$$V_{CC} = \sqrt{2} G_F n_e \, . \tag{2.23}$$

This term can be interpreted as a contribution to the $\nu_{e,L}$ energy. In the case of antineutrinos, one ends up with the same expression up to a sign $V_{CC} = -\sqrt{2}G_F n_e$ [70, 71]. It is worth noting that H_{mat} has the same structure as that of an electron in the presence of an electrostatic potential, i.e., $\bar{e}\gamma^0 e\phi$, where ϕ is the usual electric potential field.

Following an equivalent derivation, one finds that the contribution of $\nu_{\mu,\tau}$ to the potential due to CC interactions is almost zero because of the very small abundance of μ and τ leptons, in contrast to the overwhelming abundance of e in the medium of core-collapse supernovae (Chapter 3) and the compact binary merger remnants (Chapter 4). For neutral-current interactions (NC), the effective potential is given by [64]

$$V_{NC} = \frac{\sqrt{2}}{2} G_F \Big[- n_e (1 - 4\sin^2\theta_w) + n_p (1 - 4\sin^2\theta_w) - n_n \Big] \, . \tag{2.24}$$

---

[1] This is not the case in the presence of a neutrino background where the momentum distribution cannot be assumed to be isotropic.

In neutral matter, one has the same amount of electrons and protons $n_e = n_p$, and their contributions to the potential cancel each other. This neutrality results in a simpler expression in terms of the neutron density only

$$V_{NC} = -\frac{G_F}{\sqrt{2}} n_n \,. \tag{2.25}$$

As a result of coherent forward scatterings with the medium, there is a shift in the ν_e energy. The modification to the conversion probability enters via the energy shift coming from the potential. Let us recall the expression for $P_{\alpha\beta}$ in Eq. 2.10 for neutrino conversions in vacuum

$$P_{\alpha\beta}(L) \;=\; \frac{1}{N}\sum_{j,k} U^*_{\alpha j} U_{\beta j} U_{\alpha k} U^*_{\beta k} \exp\left[i\left(\sqrt{E_j^2 - m_j^2} - \sqrt{E_k^2 - m_k^2}\right) L\right] \delta(E_j - E_k)\,. \tag{2.26}$$

Notice that the oscillation phase $\phi_j \equiv p_j L = \left(\sqrt{E^2 - m_j^2} - \sqrt{E^2 - m_k^2}\right) L$ will receive a contribution from CC and NC scatterings, which will result in new momentum (propagation) eigenstates, states with definite momentum. In the case of vacuum oscillations, the propagation eigenstates are just the mass eigenstates. This changes in the presence of a matter background.

In the flavor basis, the mass matrix and the matter potential matrix are given by

$$\hat{m} \;=\; \begin{pmatrix} \cos\theta & \sin\theta \\ -\sin\theta & \cos\theta \end{pmatrix} \begin{pmatrix} m_1 & \\ & m_2 \end{pmatrix} \begin{pmatrix} \cos\theta & -\sin\theta \\ \sin\theta & \cos\theta \end{pmatrix}, \tag{2.27}$$

$$H_{\text{mat}} \;=\; \begin{pmatrix} V_{CC} & 0 \\ 0 & 0 \end{pmatrix} + \underbrace{\begin{pmatrix} V_{NC} & 0 \\ 0 & V_{NC} \end{pmatrix}}_{\text{drop}}, \tag{2.28}$$

where we have assumed two flavors of neutrinos for simplicity. The contribution proportional to $1_{2\times 2}$ due to NC scatterings does not contribute to the conversion probability because only *phase differences* can be observed. The conversion probability $P_{\alpha\beta}(L)$ is unchanged if a term proportional to the identity matrix is introduced, so we can drop the NC term and keep only the CC contribution.

To find the propagation eigenstates in matter, we must diagonalize the matrix given by

$$\hat{p} = \sqrt{(E - H_{\text{mat}})^2 - \hat{m}^2} \simeq E - H_{\text{mat}} - \frac{\hat{m}^2}{2E}\,, \tag{2.29}$$

where we have assumed that the neutrino masses $\hat{m}$ and neutrino potentials H_{mat} are much smaller than the neutrino energy E. Therefore, H^2_{mat}/E^2 and other subleading terms can be neglected. The term introducing a phase difference in the conversion probability is $H_{\text{eff}} \equiv \hat{m}^2/2E + H_{\text{mat}}$, which is the effective Hamiltonian for the evolution of the wave functions. After inserting $\hat{m}$ and H_{mat} (Eqs. 2.27 and 2.28), the effective Hamiltonian in the flavor basis is

$$H_{\text{eff}} = \begin{pmatrix} -\frac{\omega}{2}\cos 2\theta + \frac{V_{\text{CC}}}{2} & \frac{\omega}{2}\sin 2\theta \\ \frac{\omega}{2}\sin 2\theta & \frac{\omega}{2}\cos 2\theta - \frac{V_{\text{CC}}}{2} \end{pmatrix} , \tag{2.30}$$

where we have defined the vacuum oscillation frequency $\omega \equiv \Delta m^2/2E$. The evolution equation is a Schrödinger equation with the effective Hamiltonian matrix in the flavor basis

$$i\frac{d}{dx}\begin{pmatrix} \psi_{ee}(x) \\ \psi_{e\mu}(x) \end{pmatrix} = H_{\text{eff}}\begin{pmatrix} \psi_{ee}(x) \\ \psi_{e\mu}(x) \end{pmatrix} , \tag{2.31}$$

where the initial states are, for an initial ν_e, given by

$$\Psi_e(0) = \begin{pmatrix} \psi_{ee}(0) \\ \psi_{e\mu}(0) \end{pmatrix} = \begin{pmatrix} 1 \\ 0 \end{pmatrix} . \tag{2.32}$$

In general cases, the flavor evolution of neutrinos must be solved numerically due to the absence of exact analytical solutions. However, in the cases of *constant* matter density (this Section) and *slowly-varying* matter density (Section 2.2.3), as is the case for the Sun's interior, the solutions can be found analytically, allowing us to learn a lot from the impact of the medium on neutrino conversions. After finding the solutions to the transition amplitudes, the transition and survival probabilities can be computed as

$$P_{e\mu}(x) = |\psi_{e\mu}(x)|^2 , \tag{2.33}$$

$$P_{ee}(x) = |\psi_{ee}(x)|^2 = 1 - P_{e\mu}(x) . \tag{2.34}$$

We must now diagonalize H_{eff} to find solutions to the Schrödinger equation (Eq. 2.31). The effective Hamiltonian can be diagonalized by a rotation introduced by U_m

$$U_m^T H_{\text{eff}} U_m = \begin{pmatrix} \lambda_1 & 0 \\ 0 & \lambda_2 \end{pmatrix} , \tag{2.35}$$

where the orthogonal matrix U_m is given by

$$U_m = \begin{pmatrix} \cos\theta_{\text{eff}} & \sin\theta_{\text{eff}} \\ -\sin\theta_{\text{eff}} & \cos\theta_{\text{eff}} \end{pmatrix} . \tag{2.36}$$

The quantities $\lambda_{1,2}$ are the eigenvalues of H_{eff}, which can be found straightforwardly

$$\lambda_{1,2} = \pm\frac{1}{2}\sqrt{(V_{\text{CC}} - \omega\cos 2\theta)^2 + \omega^2\sin^2 2\theta}. \tag{2.37}$$

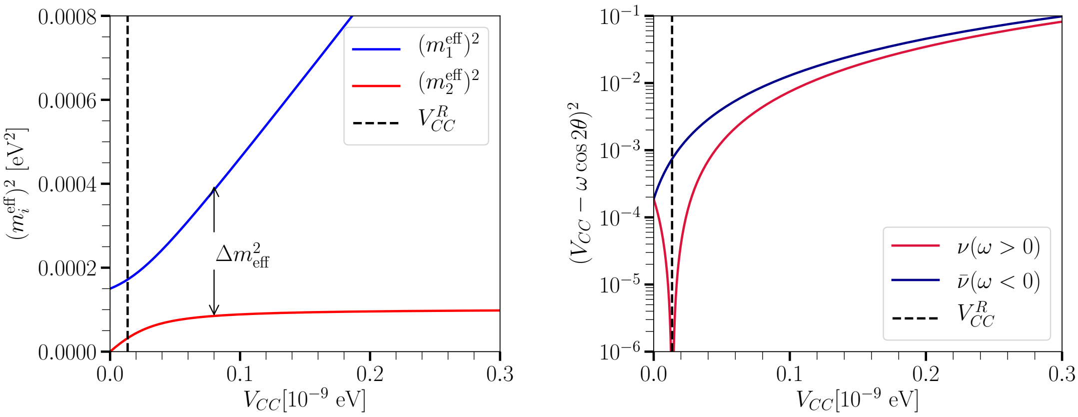

Figure 6: *Left:* The instantaneous mass eigenstates $(m_i^{\rm eff})^2 = (m_1^2 + m_2^2 + 2EV_{\rm CC} \pm \Delta m^2_{\rm eff})/2$ as a function of $V_{\rm CC}$. The resonance location is shown in black dashed line for a 1 MeV neutrino. At this location, the $\Delta m^2_{\rm eff}$ is minimal, and the masses of the effective mass eigenstates are the closest. *Right:* The resonance condition is fulfilled for neutrinos when $V_{\rm CC} = \omega\cos 2\theta$ (red line), as described by Eq. 2.39. Resonant conversion is only possible for neutrinos in the NO scenario. Notice that the change of sign $\omega \to -\omega$ in the antineutrino sector prevents neutrinos from meeting the resonance condition (blue line). The roles of neutrinos and antineutrinos are reversed in the IO scenario.

Furthermore, one defines an *effective mass squared difference* in the presence of a matter background so that the conversion probabilities in matter have the same structure as those in vacuum (Eq. 2.13). Thus, it is natural to define

$$\Delta m^2_{\rm eff} = 2E\sqrt{(V_{\rm CC} - \omega\cos 2\theta)^2 + \omega^2\sin^2 2\theta}\,. \tag{2.38}$$

Interestingly, for increasing $V_{\rm CC}$ (increasing matter density) the eigenvalues $\lambda_{1,2}$ approach each other at which point $\Delta m^2_{\rm eff}$ is minimal. This happens when $V_{\rm CC}$ takes the special value of

$$V^R_{\rm CC} = \omega\cos 2\theta, \tag{2.39}$$

where a resonance occurs, making the separation between the eigenvalues the smallest and $\Delta m^2_{\rm eff} = 2E\omega\sin\theta$. The behavior of $\Delta m^2_{\rm eff}$ and the resonance condition are shown in Fig. 6 for a 1 MeV neutrino, where the resonance location $V_{\rm CC} = V^R_{\rm CC}$ is marked with black dashed line. At this location, neutrinos are converted resonantly while antineutrinos are not. There can be no resonance for antineutrinos since $\omega \to -\omega$ and there is no cancellation of terms inside the square root in Eq. 2.38. In reality, for neutrinos we have $V_{\rm CC} > 0$ while for antineutrinos $V_{\rm CC} < 0$, however, we absorb the sign in the definition of the vacuum frequency i.e., $\omega > 0$ for neutrinos and $\omega < 0$ for

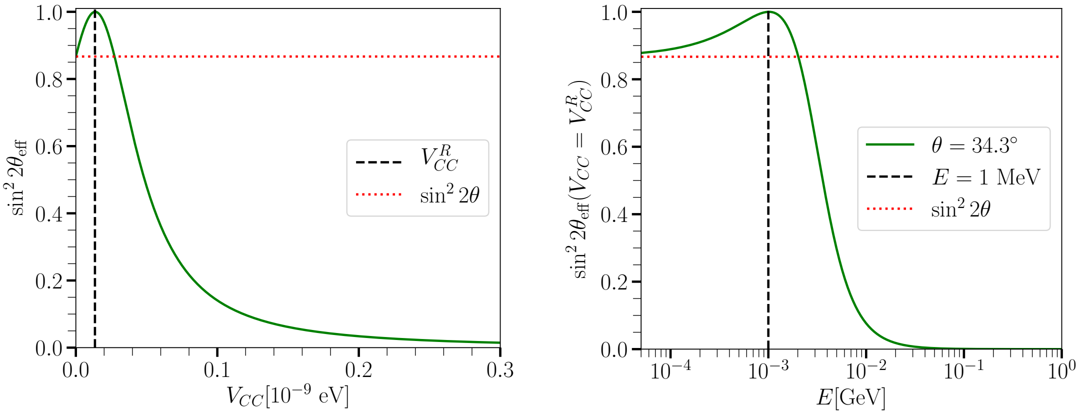

Figure 7: *Left:* Effective mixing angle as a function of V_{CC} for a 1 MeV neutrino. At the resonance location, the effective mixing angle is maximal, leading to an enhancement of conversions compared to the same neutrino traveling in vacuum. In red dotted line, we show the limiting case corresponding to the vacuum scenario ($V_{CC} = 0$). *Right:* Effective mixing angle at the resonance location $V_{CC} = V_{CC}^R \simeq 1.35 \times 10^{-11}$ eV as a function of neutrino energy.

antineutrinos. The roles of neutrinos and antineutrinos are reversed in the IO compared to the NO scenario.

Analogous to the definition of the effective mass squared difference (Eq. 2.38), one also defines an *effective mixing angle* $\theta_{\rm eff}$. The requirement of the rotation U_m was that it diagonalized $H_{\rm eff}$. The off-diagonal components of $U_m^T H_{\rm eff} U_m$ must therefore vanish according to Eq. 2.35. This allows solving for $\theta_{\rm eff}$

$$\sin 2\theta_{\rm eff} = \frac{\omega \sin 2\theta}{\sqrt{(V_{CC} - \omega \cos 2\theta)^2 + \omega^2 \sin^2 2\theta}} . \tag{2.40}$$

In Fig. 7 we show the behavior of the effective mixing angle as a function of the matter potential (left panel) and as a function of the neutrino energy at the resonance location (right panel). When the resonance conditions is met $\sin 2\theta_{\rm eff} = 1$ (or $\theta_{\rm eff} = \pi/4$) leading to an enhancement of conversions as compared to neutrinos traveling in vacuum.

By construction, the neutrino conversion probability can be expressed analogously to the one in vacuum (Eq. 2.11 in the two-flavor framework) with the help of the effective parameters in matter

$$P_{e\mu}(L) = \sin^2 2\theta_{\rm eff} \sin^2 \left(\frac{\Delta m^2_{\rm eff}}{4E} L \right) . \tag{2.41}$$

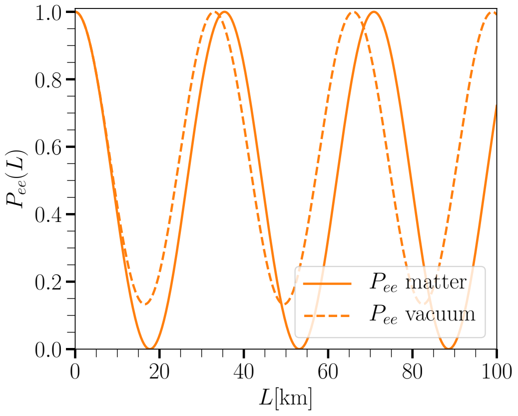

Figure 8: Neutrino survival probabilities P_{ee} in vacuum (dashed line) and matter (solid line) as a function of the separation between neutrino production and detection. In both cases, the neutrino beam has an energy of $E = 1$ MeV, and we assume the solar oscillation parameters δm^2 and θ_{12} as reported in Table 1. The survival probability in vacuum is the same as in Fig. 2. The survival probability in matter is for the case where the resonance condition is met for a 1 MeV, namely $V_{CC} = V_{CC}^R \simeq 1.35 \times 10^{-11}$ eV (black dashed lines in Figs. 7 and 6). The resonance condition leads to complete flavor conversion.

The effective mixing angle $\sin 2\theta_{\text{eff}}$ (Eq.2.40) has a quite remarkable consequence for the conversion probability. When the *Mikheyev-Smirnov-Wolfenstein (MSW) resonance* condition is fulfilled (Eq. 2.39) the mixing angle in matter reaches its maximum $\sin 2\theta_{\text{eff}} = 1$, as seen in Fig. 7, leading to an enhancement of conversions. In other words, for given mixing parameters and neutrino energy, a particular electron density exists, which leads to a maximal conversion probability. The latter effect is commonly referred to as the MSW effect. There are two interesting limits to consider. For $V_{CC} \to 0$ we recover oscillations in vacuum ($\sin^2 2\theta_{\text{eff}} \to \sin^2 2\theta$), while for the matter-dominated regime $V_{CC} \to \infty$ neutrino conversions are strongly suppressed (due to $\sin^2 2\theta_{\text{eff}} \to 0$) as can be seen in the left panel of Fig. 7.

The conversion probability in matter (Eq. 2.41) has important consequences for determining the absolute sign of the small mass squared difference δm^2. Using the MSW effect, it was possible to determine that $\delta m^2 > 0$ because the effective mixing angle $\sin^2 2\theta$ and the effective mass squared difference Δm^2_{eff} are sensitive to the sign δm^2 through the definition of ω. If $\delta m^2 > 0$ then the MSW effect occurs for neutrinos, while if $\delta m^2 < 0$ it instead occurs for antineutrinos.

2.2.3 *Adiabatic flavor conversions in slowly-varying matter density*

Let us consider a matter background that changes smoothly as a function of distance. Such smooth matter profiles could be found in the interiors of stars like our Sun.

The flavor evolution equation (Eq. 2.31) written in terms of the effective parameters Δm^2_{eff} and θ_{eff} is [72]

$$i\frac{d}{dx}\begin{pmatrix}\psi_{ee}(x)\\ \psi_{e\mu}(x)\end{pmatrix}=\frac{1}{4E}\begin{pmatrix}-\Delta m^2_{\text{eff}}\cos 2\theta_{\text{eff}} & \Delta m^2_{\text{eff}}\sin 2\theta_{\text{eff}}\\ \Delta m^2_{\text{eff}}\sin 2\theta_{\text{eff}} & \Delta m^2_{\text{eff}}\cos 2\theta_{\text{eff}}\end{pmatrix}\begin{pmatrix}\psi_{ee}(x)\\ \psi_{e\mu}(x)\end{pmatrix}. \tag{2.42}$$

By performing a rotation U_m (Eq. 2.36), which diagonalizes the Hamiltonian $U_m^T H_{\text{eff}} U_m = \text{diag}(\lambda_1, \lambda_2)$, we have that

$$\Psi_e = U_m\Phi_e \quad \text{where} \quad \Psi_e = \begin{pmatrix}\psi_{ee}\\ \psi_{e\mu}\end{pmatrix},\ \Phi_e = \begin{pmatrix}\phi_{e1}\\ \phi_{e2}\end{pmatrix}, \tag{2.43}$$

Thus, the evolution equation becomes

$$i\frac{d}{dx}\begin{pmatrix}\phi_{e1}(x)\\ \phi_{e2}(x)\end{pmatrix}=\frac{1}{4E}\begin{pmatrix}-\Delta m^2_{\text{eff}} & -4Ei\frac{d}{dx}\theta_{\text{eff}}\\ 4Ei\frac{d}{dx}\theta_{\text{eff}} & \Delta m^2_{\text{eff}}\end{pmatrix}\begin{pmatrix}\phi_{e1}(x)\\ \phi_{e2}(x)\end{pmatrix}. \tag{2.44}$$

The matrix would have been perfectly diagonal if it were not for the additional terms from computing the derivative of Ψ_e:

$$\frac{d\Psi_e}{dx}=\frac{d(U_m\Phi_e)}{dx}=\frac{dU_m}{dx}\Phi_e+U_m\frac{d\Phi_e}{dx}. \tag{2.45}$$

In the case of constant U_m, implying $\frac{d}{dx}\theta_{\text{eff}} = 0$, the amplitudes of the effective massive neutrinos decouple from each other, in which case one recovers the usual conversion probability as in Eq. 2.41. However, if U_m is not constant, the derivative does not vanish, and off-diagonal terms appear as in Eq. 2.44, making them couple to each other. With initial conditions as in Eq. 2.32 (i.e. $\psi_{ee}(0) = 1$ and $\psi_{e\mu}(0) = 0$), the initial conditions for the rotated evolution equation (Eq. 2.44) are given by

$$\begin{pmatrix}\phi_{e1}(0)\\ \phi_{e2}(0)\end{pmatrix}=\begin{pmatrix}\cos\theta^{(\text{i})}_{\text{eff}} & -\sin\theta^{(\text{i})}_{\text{eff}}\\ \sin\theta^{(\text{i})}_{\text{eff}} & \cos\theta^{(\text{i})}_{\text{eff}}\end{pmatrix}\begin{pmatrix}1\\ 0\end{pmatrix}=\begin{pmatrix}\cos\theta^{(\text{i})}_{\text{eff}}\\ \sin\theta^{(\text{i})}_{\text{eff}}\end{pmatrix}, \tag{2.46}$$

where $\theta^{(\text{i})}_{\text{eff}}$ corresponds to the effective mixing angle at the location where neutrinos were produced. The rate of change of θ_{eff} is

$$\frac{d\theta_{\text{eff}}}{dx}=\frac{1}{2}\frac{\sin 2\theta_{\text{eff}}}{\Delta m^2_{\text{eff}}}\frac{dA_{CC}}{dx}, \tag{2.47}$$

where $A_{CC} \equiv 2EV_{CC} = 2\sqrt{2}G_F n_e$. The off-diagonal terms in the flavor evolution equation (Eq. 2.44) allow for transitions between the two effective neutrino mass eigenstates $\nu_{1,\mathrm{eff}}$ and $\nu_{2,\mathrm{eff}}$. If the change of the matter potential is slow enough, the off-diagonal terms are extremely small ($d\theta_{\mathrm{eff}}/dx \simeq 0$) resulting in transitions between $\nu_{1,\mathrm{eff}}$ and $\nu_{2,\mathrm{eff}}$.

For instance, for neutrinos produced at the center of the Sun, n_e is so large that V_{CC} dominates resulting in $\sin 2\theta_{\mathrm{eff}} \to 0$ (or $\theta_{\mathrm{eff}} \to \pi/2$); see Fig. 7 at very large values of the matter potential. As a result, at the center of the Sun the electron neutrino is mostly $\nu_e \simeq \nu_2$ (see Eq. 2.46). Later, the neutrino traverses the medium inside the Sun, which changes slowly with distance, and it escapes the Sun as a $\nu_e \simeq \nu_2$. At that point, in vacuum, the ν_e has been *adiabatically* transformed into a mixture of ν_e and ν_μ because in vacuum $\nu_2 = \nu_e \sin\theta + \nu_\mu \cos\theta$. Adiabatic transitions mean that a neutrino starts on the blue curve in the left panel of Fig. 6 and remains there until it reaches the surface of the Sun. In the non-adiabatic case, there is a non-zero probability that a "jump" occurs between the red and blue curves in Fig. 6. The transition between $\nu_{1,\mathrm{eff}}$ and $\nu_{2,\mathrm{eff}}$ is negligible if the off-diagonal terms are much smaller than the terms on the diagonal. To quantify their level of adiabaticity, it is useful to introduce the *adiabaticity parameter* [72]

$$\gamma = \frac{\Delta m^2_{\mathrm{eff}}}{4E|d\theta_{\mathrm{eff}}/dx|} = \frac{(\Delta m^2_{\mathrm{eff}})^2}{2E\sin\theta_{\mathrm{eff}}|dA_{CC}/dx|}\,. \tag{2.48}$$

If along the trajectory of the neutrino crossing the medium is true that $\gamma \gg 1$, then the evolution is adiabatic and $\nu_{1,\mathrm{eff}}, \nu_{2,\mathrm{eff}}$ decouple from each other: there are no jumps or transitions between them. The solutions for the amplitudes evolve independently and can be found easily

$$\phi_{e1}(x) \;=\; e^{+i\Omega}\phi_{e1}(0) = e^{+i\Omega}\cos\theta^{(\mathrm{i})}_{\mathrm{eff}}, \tag{2.49}$$

$$\phi_{e2}(x) \;=\; e^{-i\Omega}\phi_{e2}(0) = e^{-i\Omega}\sin\theta^{(\mathrm{i})}_{\mathrm{eff}}, \tag{2.50}$$

where we have plugged in the initial conditions at the neutrino production site (Eq. 2.46) and have defined the phase in the exponential as

$$\Omega \equiv \int_0^x \frac{\Delta m^2_{\mathrm{eff}}(x')}{4E}dx'\,. \tag{2.51}$$

The survival probability $P_{ee} = |\psi_{ee}|^2$ can be computed once we transform back to the flavor basis to find an expression for ψ_{ee}. From Eq. 2.43 is clear that

$$\begin{pmatrix} \psi_{ee}(x) \\ \psi_{e\mu}(x) \end{pmatrix} = \begin{pmatrix} \cos\theta^{(\mathrm{f})}_{\mathrm{eff}} & \sin\theta^{(\mathrm{f})}_{\mathrm{eff}} \\ -\sin\theta^{(\mathrm{f})}_{\mathrm{eff}} & \cos\theta^{(\mathrm{f})}_{\mathrm{eff}} \end{pmatrix} \begin{pmatrix} e^{+i\Omega}\cos\theta^{(\mathrm{i})}_{\mathrm{eff}} \\ e^{-i\Omega}\sin\theta^{(\mathrm{i})}_{\mathrm{eff}} \end{pmatrix}, \tag{2.52}$$

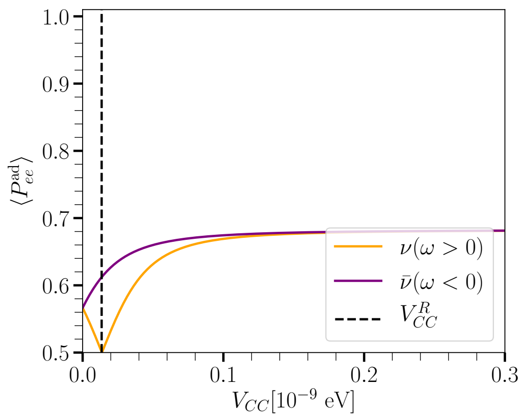

Figure 9: Averaged adiabatic survival probability as a function of the matter potential $V_{\rm CC}$ (Eq. 2.55). The resonance location $V_{\rm CC}^R$ is shown in black dashed line. At the resonance location, $P_{ee}^{\rm ad}(x)\rangle = 0.5$ is minimal, leading to enhanced conversions with respect to the vacuum ($V_{\rm CC} = 0$) and the matter-dominated scenario ($V_{\rm CC} \to \infty$). The resonance condition is only met by neutrinos (orange) and not by antineutrinos (purple) in the NO scenario. Their roles are reversed in the IO scenario.

where $\theta_{\rm eff}^{\rm (f)}$ is the mixing angle at the point of detection, i.e., it equals the vacuum mixing angle if the neutrino is detected outside the Sun. Thus, the survival probability is given by the square of the amplitude

$$\begin{aligned} P_{ee}^{\rm ad}(x) = |\psi_{ee}(x)|^2 &= \left| \cos\theta_{\rm eff}^{\rm (f)} \cos\theta_{\rm eff}^{\rm (i)} e^{+i\Omega} + \sin\theta_{\rm eff}^{\rm (f)} \sin\theta_{\rm eff}^{\rm (i)} e^{-i\Omega} \right|^2 &\quad (2.53)\\ &= \frac{1}{2}\left(1 + \cos 2\theta_{\rm eff}^{\rm (f)} \cos 2\theta_{\rm eff}^{\rm (i)} + \sin 2\theta_{\rm eff}^{\rm (f)} \sin 2\theta_{\rm eff}^{\rm (i)} \cos\Omega\right) . &\quad (2.54)\end{aligned}$$

Adiabaticity is a good approximation for neutrinos streaming out of stars like the Sun, which have a smooth density profile. Also, the detection point is typically very far away from the production site such that the effective mixing angle at detection is simply the mixing angle at vacuum $\theta_{\rm eff}^{\rm (f)} = \theta$. Moreover, since the traveled distance between the production and the detection site is quite large, there is a very rapid variation of the $\cos\Omega$ term, which then averages to zero at the detection point. Thus, what is seen in the detector is an average (adiabatic) survival probability given by

$$\langle P_{ee}^{\rm ad}(x)\rangle = \frac{1}{2}\left(1 + \cos 2\theta \cos 2\theta_{\rm eff}^{\rm (i)}\right) , \qquad (2.55)$$

which does not depend on the distance L between the neutrino production site and the detector but only on effective mixing angles at production and detection. In Fig. 9, we show the averaged adiabatic survival probability $\langle P_{ee}^{\rm ad}(x)\rangle$ as a function of the matter potential at which neutrinos were initially produced. A minimum in the survival probability is found at the resonance condition, where the effective mixing angle is maximal. At the resonance condition we have $P_{ee}^{\rm ad}(x)\rangle = 0.5$, which is smaller than the values in vacuum $V_{CC} = 0$ and in the matter-dominated scenario $V_{CC} \to \infty$, with averaged survival probabilities of $\langle P_{ee}^{\rm ad}(x)\rangle = 0.55$ and $\langle P_{ee}^{\rm ad}(x)\rangle = 0.65$, respectively.

2.2.4 *Density matrix formalism*

The flavor evolution of neutrinos can be described with $n \times n$ density matrices in flavor space for a given momentum mode [73]. The diagonal elements of the density matrices are the occupation numbers of the n-th flavor, while the off-diagonal terms encode the coherence between different flavors. The density matrix formalism is a handy tool to describe flavor evolution in vacuum, matter, and in the case where neutrinos constitute a significant background to themselves. This formalism becomes quite convenient when dealing with an ensemble of neutrinos interacting with neutrinos in the medium. Neutrino refraction describes the energy shift due to this neutrino background. The refractive index could be considered an $n \times n$ matrix [74–76] implying that there are also refractive indices off-diagonal in flavor space. A natural way to describe this refractive index matrix is via implementing density matrices in flavor space [73].

Let us begin with the momentum expansion of the left-handed neutrino field, which in this section we call $\hat{\psi}(x)$ to match the notation in Ref [73]

$$\hat{\psi}(x) = \int \frac{d^3\vec{p}}{(2\pi)^3} \left(a_{\vec{p}}(t) u_{\vec{p}} + b^\dagger_{-\vec{p}}(t) v_{-\vec{p}}\right) e^{i\vec{p}\cdot\vec{x}} \,, \tag{2.56}$$

where $a_{\vec{p}}$ is the annihilation operator for negative-helicity neutrinos with given momentum $\vec{p}$ and $b^\dagger_{-\vec{p}}$ is the creation operator for positive-helicity antineutrinos. The quantities $u_{\vec{p}}$ and $v_{-\vec{p}}$ are the Dirac spinors of the massless negative- and positive-helicity particles, respectively. In the two-flavor framework for instance, each $a_{\vec{p}}$ and $b^\dagger_{-\vec{p}}$ are column vectors of two entries, each of them corresponding to the particle annihilators $a_\alpha(\vec{p})$ and antiparticle creators $b^\dagger_\alpha(\vec{p})$ of the flavors $\alpha = e, x$ (with the admixture $x = \mu, \tau$). They obey the anti-commutation relations

$$\{a_\alpha(\vec{p}), a^\dagger_\beta(\vec{p}')\} = \{b_\alpha(\vec{p}), b^\dagger_\beta(\vec{p}')\} = \delta_{\alpha\beta}(2\pi)^3\delta^{(3)}(\vec{p} - \vec{p}'). \tag{2.57}$$

A neutrino ensemble is described by the m-particle Green functions [73] because the neutrino ensemble is a many-body system. The *mean-field approximation* averages over the many degrees of freedom in the underlying many-body system and treats the effect of all the other background particles as one single averaged effect. This allows reducing a many-body system to a one-particle system. In the case of one-body systems, only the expectation values of the products of *two* operators $a, a^\dagger, b, b^\dagger$ need to be considered. The bilinears aa, $a^\dagger a^\dagger$, $b^\dagger a$, $a^\dagger b$ violate lepton number and thus their expectation values are exactly zero. Moreover, the expectation values of the bilinears $a^\dagger b^\dagger$ and ab also vanish because they oscillate "fast" around zero [73] i.e. $\langle a_{\vec{p}}(t) a_{\vec{p}'}(t)\rangle \propto e^{-i(|\vec{p}|+|\vec{p}'|)t}$. Thus, the only remaining bilinears left that contribute are the "slow" density operators $a^\dagger_{\vec{p}} a_{\vec{p}'}$ and $b^\dagger_{\vec{p}} b_{\vec{p}'}$. The neutrino ensemble is completely described by the $n \times n$ density matrices $\rho(\vec{p}, t)$ and $\bar{\rho}(\vec{p}, t)$ given by

$$\langle a^\dagger_\beta(\vec{p}) a_\alpha(\vec{p}')\rangle = (2\pi)^3 \delta^{(3)}(\vec{p} - \vec{p}')(\rho(\vec{p}))_{\alpha\beta} \, , \tag{2.58}$$

$$\langle b^\dagger_\beta(\vec{p}) b_\alpha(\vec{p}')\rangle = (2\pi)^3 \delta^{(3)}(\vec{p} - \vec{p}')(\bar{\rho}(\vec{p}))_{\alpha\beta} \, . \tag{2.59}$$

Consequently, the density matrices above contain the usual neutrino and antineutrino occupation numbers in their diagonal entries, while the coherence between flavors is contained in the off-diagonal terms. In the interaction basis, at a given location $\vec{x}$ and time t, the flavor density matrices for (anti)neutrinos with momentum $\vec{p}'$ can be written as

$$(\rho(\vec{x}, \vec{p}', t))_{\alpha\beta} = \sum_{\nu'} n_{\nu', \vec{p}'}(\vec{x}, t) \, \langle \nu_\alpha | \psi_{\nu'}(\vec{x}, \vec{p}', t)\rangle \, \langle \psi_{\nu'}(\vec{x}, \vec{p}', t) | \nu_\beta \rangle \ , \tag{2.60}$$

$$(\bar{\rho}(\vec{x}, \vec{p}', t))_{\beta\alpha} = \sum_{\bar{\nu}'} n_{\bar{\nu}', \vec{p}'}(\vec{x}, t) \, \langle \bar{\nu}_\alpha | \psi_{\bar{\nu}'}(\vec{x}, \vec{p}', t)\rangle \, \langle \psi_{\bar{\nu}'}(\vec{x}, \vec{p}', t) | \bar{\nu}_\beta \rangle \ , \tag{2.61}$$

where $|\psi_{\nu'(\bar{\nu}')}(\vec{p}')\rangle$ is the state of a neutrino (antineutrino) $\nu'(\bar{\nu}')$ with momentum $\vec{p}'$, and $n_{\nu', \vec{p}'}(n_{\bar{\nu}', \vec{p}'})$ is its corresponding number density.

2.2.5 *Neutrino-neutrino interaction*

Neutrinos also constitute a significant background to other neutrinos and should be considered. The general expression for the neutrino self-interaction potential in the formalism of density matrices is given by [71]

$$\begin{aligned} H_{\nu\nu}(\vec{p}) &= \sqrt{2}G_F \int d\vec{q}\{G_S(\rho(\vec{q}) - \bar{\rho}(\vec{q}))G_S + G_S \mathrm{Tr}[(\rho(\vec{q}) - \bar{\rho}(\vec{q}))G_S]\}\Big(1 - \frac{\vec{p}\cdot\vec{q}}{|\vec{p}||\vec{q}|}\Big) \\ &- \sqrt{2}G_F \frac{8|\vec{p}|}{4M_W^2} \int d\vec{q}|\vec{q}|G_S(\rho(\vec{q}) + \bar{\rho}(\vec{q}))G_S\Big(1 - \frac{\vec{p}\cdot\vec{q}}{|\vec{p}||\vec{q}|}\Big)^2 . \end{aligned} \tag{2.62}$$

The quantity G_S is a matrix of coupling constants, and since we only deal with SM physics, G_S is simply the identity matrix. The term $\frac{\vec{p}\cdot\vec{q}}{|\vec{p}||\vec{q}|}$ is simply equal to the dot product of the velocities of specific momentum $\vec{v}_p \cdot \vec{v}_q$. Notice that the factor $(1 - \frac{\vec{p}\cdot\vec{q}}{|\vec{p}||\vec{q}|})$ is relevant for scenarios where the neutrino ensemble is not isotropic, and the dot product is essentially the angle between the test neutrino and a background neutrino. If the neutrino ensemble is isotropic, the term $\vec{v}_p \cdot \vec{v}_q$ integrates out to zero, giving no contribution to the background potential. However, in the context of core-collapse supernovae (Chapter 3) and the mergers of compact binary objects (Chapter 4), the degree of isotropy is high, and this contribution is important.

The last term in Eq. 2.62 is relevant for the early universe where the lepton-number asymmetry is possibly large [73]. This term is proportional to the sum of the number densities of neutrinos and antineutrinos, rather than the difference, as for the first-order refractive terms in Eq. 2.62.

For the work relevant to this thesis (where physics beyond the SM are not included) the neutrino self-interaction Hamiltonian induces pairwise conversions of the following kind $\nu_e(p) + \nu_x(q) \leftrightarrow \nu_e(q) + \nu_x(p)$ and $\nu_e(p) + \bar{\nu}_e(q) \leftrightarrow \nu_x(q) + \bar{\nu}_x(p)$; see Fig 10 for the relevant interaction diagrams. The corresponding neutrino self-interaction Hamiltonian is given by

$$H_{\nu\nu}(\vec{p}) = \mu \int d\vec{q}\Big[\rho(\vec{q}) - \bar{\rho}(\vec{q})\Big]\Big(1 - \frac{\vec{p}\cdot\vec{q}}{|\vec{p}||\vec{q}|}\Big) , \tag{2.63}$$

where the neutrino self-interaction strength $\mu = \sqrt{2}G_F(n_\nu + n_{\bar{\nu}})$ is determined by the neutrino and antineutrino number densities for all neutrino flavors. The velocity vectors $\vec{v}_p \cdot \vec{v}_q = \vec{p}\cdot\vec{q}/|\vec{p}||\vec{q}|$ in $H_{\nu\nu}(\vec{p})$ can be expressed in spherical coordinates as functions of the polar θ and azimuthal ϕ angles where $\vec{v}_p = (\sin\theta\cos\phi, \sin\theta\sin\phi, \cos\theta)$ and $\vec{v}_q = (\sin\theta'\cos\phi', \sin\theta'\sin\phi', \cos\theta')$ because

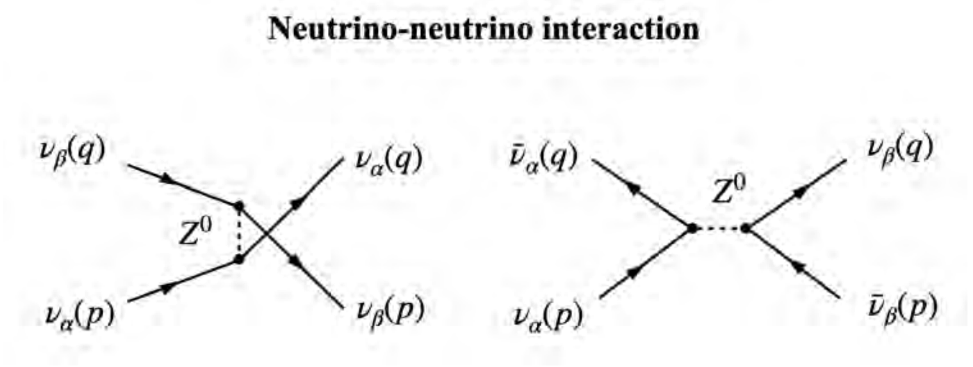

Figure 10: Interaction diagrams corresponding to neutrino-neutrino coherent forward scattering (similar to the sketch in Fig. 5 but with a ν-background). Flavor off-diagonal entries of the self-interaction Hamiltonian (Eq. 2.63) correspond to the Feynman diagrams shown above. In the diagram on the left, a pair of neutrinos exchange their momenta. In the diagram on the right, a neutrino-antineutrino pair changes its flavor and momenta.

neutrinos travel nearly at the speed of light and $|\vec{v}_p| = |\vec{v}_q| = 1$. Assuming that the integrand of Eq. 2.63 $F(\vec{q}) = [\rho(\vec{q}) - \bar{\rho}(\vec{q})]$ is azimuthally symmetric i.e. it does not depend on ϕ', we have that $F = F(\theta')$. Therefore the integration of the dot product over azimuthal angle ϕ' simplifies to

$$\int_0^{2\pi} d\phi' (1 - \vec{v}_p \cdot \vec{v}_q) = 2\pi(1 - \cos\theta \cos\theta'), \tag{2.64}$$

since two terms are proportional to the integrals of even functions i.e. $\int_0^{2\pi} d\phi' \sin\phi' = 0$ and $\int_0^{2\pi} d\phi' \cos\phi' = 0$. Therefore, under the assumption of azimuthal symmetry, the neutrino-neutrino Hamiltonian in Eq. 2.63 reduces to

$$H_{\nu\nu}(\cos\theta) = 2\pi\mu \int_{-1}^{1} d\cos\theta' \Big[\rho(\cos\theta') - \bar{\rho}(\cos\theta')\Big](1 - \cos\theta\cos\theta'). \tag{2.65}$$

Since we have assumed SM physics, i.e., $G_S = 1_{n\times n}$, the term with the trace is proportional to the identity matrix and does not contribute to the flavor evolution. However, when beyond the SM physics are included, G_S is not diagonal, and the trace term cannot be dropped; see Refs. [77, 78] for non-standard scenarios beyond the scope of this thesis. Moreover, we also neglect the term $\propto G_F/M_W^2(\rho + \bar{\rho})$ in the Hamiltonian where number-lepton asymmetry is important as in the case of the early universe [79–81] but nevertheless subleading for astrophysical sources.

2.2.6 *Flavor polarization vectors*

It is more challenging to describe neutrino conversion using the wave-function formalism when $H_{\nu\nu}$ is important. The reason is that $H_{\nu\nu}$ is a sum of the density matrices which contain bilinears of the wave-functions. The density matrices contain all the information to describe neutrino conversion.

To illustrate the polarization vector formalism, let us take a working example. Consider a homogeneous and isotropic neutrino gas whose flavor evolves with time. Isotropy implies that the factor $(1 - \frac{\vec{p}\cdot\vec{q}}{|\vec{p}||\vec{q}|})$ in $H_{\nu\nu}(\vec{p})$ (Eq. 2.63) averages to 1. Thus, neutrino propagation direction does not matter and homogeneity further allows to make the replacements $\rho(\vec{x}, \vec{p}, t) \to \rho_E(t)$ and $\bar{\rho}(\vec{x}, \vec{p}, t) \to \bar{\rho}_E(t)$. Therefore, the neutrino equations of motion are

$$\begin{aligned} i\dot{\rho}_E &= \Big[+ \omega \mathsf{B} + \lambda \mathsf{L} + \sqrt{2} G_F \int_0^\infty dE' (\rho_{E'} - \bar{\rho}_{E'}), \rho_E \Big] \,, \\ i\dot{\bar{\rho}}_E &= \Big[- \omega \mathsf{B} + \lambda \mathsf{L} + \sqrt{2} G_F \int_0^\infty dE' (\rho_{E'} - \bar{\rho}_{E'}), \bar{\rho}_E \Big], \end{aligned} \tag{2.66}$$

where $\omega = \Delta m^2/2E$ is the vacuum oscillation frequency, B is the vacuum mixing matrix, $\lambda = \sqrt{2} G_F n_e$ is the interaction strength of electrons and neutrinos, and $\mathsf{L} = \mathrm{diag}(1, 0)$. In the two-flavor framework, $\rho_E, \bar{\rho}_E$ are 2×2 Hermitian matrices, and they can be mapped into vectors that live in a three-dimensional space, which we will call *flavor space*. The components of the polarization vector $\vec{P}_\omega$ are given by

$$P_{\omega,a} = \left(\frac{1}{n_\nu}\right)\left(\frac{|\Delta m^2|}{2\omega^2}\right) \times \begin{cases} \mathrm{Tr}(\rho_E \sigma_a) & \text{neutrinos} \\ -\mathrm{Tr}(\rho_E \sigma_a) & \text{antineutrinos} \end{cases} \tag{2.67}$$

where the vacuum oscillation frequency is $\omega > 0$ for neutrinos and $\omega < 0$ for antineutrinos. We note that $\vec{P}_\omega$ can be normalized arbitrarily. For instance, if $\vec{P}_\omega$ is normalized to unity, then $\rho_E \propto (1 + \frac{1}{2}\vec{P}_\omega \cdot \vec{\sigma})$ for neutrinos and $\bar{\rho}_E \propto (1 - \frac{1}{2}\vec{P}_\omega \cdot \vec{\sigma})$ for antineutrinos. Because σ_a are traceless, the trace of the density matrices is not contained in the polarization vector. However, according to the equations of motion (Eqs. 2.66) the traces are constant in time, which means that neutrinos

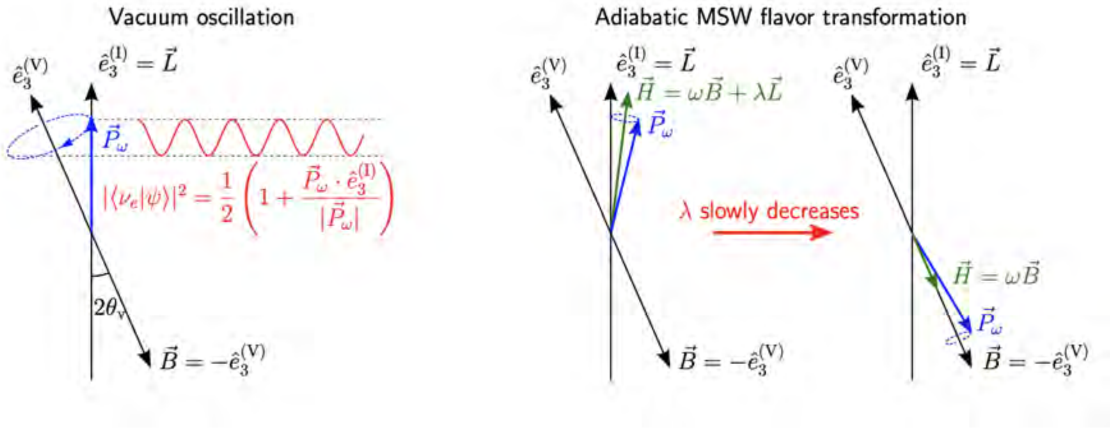

Figure 11: Geometric representations of vacuum oscillations and MSW resonant effect. *Left:* Polarization vector $\vec{P}_\omega$ initially as $|\nu_e\rangle$ starts to precess around $\vec{B}$. The projection of the precessing $\vec{P}_\omega$ onto the $\hat{e}_3^{(I)}$ represents flavor conversion. *Right:* Polarization vector $\vec{P}_\omega$ precession in the presence of matter. If the matter density decreases slowly, the angle between $\vec{P}_\omega$ and $\vec{H} = \omega\vec{B} + \lambda\vec{L}$ is constant. The latter is the adiabatic MSW resonance effect (Sec. 2.2.3). Image taken from Ref. [82].

are not created or annihilated. By using the definition of the Pauli matrices σ_a with $a = 1, 2, 3$, the traces can be computed explicitly

$$\mathrm{Tr}(\rho\sigma_1) = (\rho_{ex} + \rho_{ex}^*) = 2\mathrm{Re}[\rho_{ex}] \,, \tag{2.68}$$

$$\mathrm{Tr}(\rho\sigma_2) = i(\rho_{ex} - \rho_{ex}^*) = -2\mathrm{Im}[\rho_{ex}] \,, \tag{2.69}$$

$$\mathrm{Tr}(\rho\sigma_3) = \rho_{ee} - \rho_{xx} \,. \tag{2.70}$$

The polarization vectors for (anti)neutrinos have then the following structure

$$P_{\omega,a} \propto (2\mathrm{Re}[\rho_{ex}],\ -2\mathrm{Im}[\rho_{ex}],\ \rho_{ee} - \rho_{xx}) \,, \tag{2.71}$$

$$P_{-\omega,a} \propto (2\mathrm{Re}[\bar{\rho}_{ex}],\ -2\mathrm{Im}[\bar{\rho}_{ex}],\ \bar{\rho}_{ee} - \bar{\rho}_{xx}) \,. \tag{2.72}$$

In flavor space, the xy-components of the polarization vector contain the coherence information (see later Chapter 6), while the z-component is the amount of flavor converted. If the polarization vector points in the $+\hat{z}$ direction, there is pure ν_e flavor, and if it points in the $-\hat{z}$, there is pure ν_x flavor instead.

Using Eqs. 2.66 and 2.67 the equations of motion can be brought to vector form

$$\dot{\vec{P}}_\omega = (\omega\vec{B} + \lambda\vec{L} + \mu\vec{D}) \times \vec{P}_\omega \,, \tag{2.73}$$

where the components of the vectors $\vec{B}$ and $\vec{L}$ are given by $B_a = \mathrm{Tr}(\mathsf{B}\sigma_a)$ and $L_a = \mathrm{Tr}(\mathsf{L}\sigma_a)$. Moreover, the parameter μ is the strength of neutrino self-interaction, which is proportional to G_F and the number densities of (anti)neutrinos. The vector $\vec{D}$ is the total polarization vector $\vec{D} = \int_0^\infty d\omega(\vec{P}_\omega - \vec{P}_{-\omega}) = \int_{-\infty}^\infty d\omega \vec{P}_\omega$.

The vectors $\vec{B}$ and $\vec{L}$ are parallel to the vacuum basis vector $\hat{e}_3^{(V)}$ and interaction basis vector $\hat{e}_3^{(I)}$, respectively, as shown in Fig. 11. The Hilbert space spanned by the states $|\nu_\alpha\rangle$ $(\alpha = e, x)$ or $|\nu_i\rangle$ $(\alpha = 1, 2)$ can be mapped onto the 3D Euclidean flavor space spanned by basis vectors $\hat{e}_a^{(I)}$ or $\hat{e}_a^{(V)}$ $(a = 1, 2, 3)$. The interaction basis vectors $\hat{e}_{1,3}^{(I)}$ are obtained by rotating the vacuum basis vectors $\hat{e}_{1,3}^{(V)}$ by $2\theta_V$ around the common axis $\hat{e}_2^{(I)} = \hat{e}_2^{(V)}$.

In the absence of neutrino self-interactions the dynamics of $\vec{P}_\omega$ is equivalent to a "magnetic spin" coupled to the total "magnetic field" $\vec{H} = \omega\vec{B} + \lambda\vec{L}$ with "gyromagnetic ratio" equal -1. For comparison, see that the equation of motion of a real magnetic spin $\vec{s}$ with gyromagnetic ratio γ in the presence of a magnetic field $\vec{H}$ is given by $\dot{\vec{s}} = -\gamma\vec{H} \times \vec{s}$, and therefore the dynamics are equivalent [82].

With this geometric picture in mind, the adiabatic MSW flavor transformation presented in Sec. 2.2.2 becomes easier to visualize, as schematically shown in Fig. 11. For vacuum oscillations, $\vec{P}_\omega$ precesses around the vacuum direction $\hat{e}_3^{(V)}$. In the case where the matter density slowly decreases, the "total magnetic field" starts as $\vec{H} = \omega\vec{B} + \lambda\vec{L}$ and ends up as $\vec{H} = \omega\vec{B}$. The adiabaticity is important here because it allows the polarization vector $\vec{P}_\omega$ to respond to the changes of $\vec{H}$. If the change of $\vec{H}$ happens too fast, non-adiabatically, the $\vec{P}_\omega$ does not follow the evolution of $\vec{H}$.

The polarization vector notation introduced in this section is fully equivalent to the neutrino flavor isospin (NFIS) notation [83] where polarization vector is given by $\vec{s}_\omega = \frac{1}{2}\frac{\vec{P}_\omega}{|\vec{P}_\omega|}$. For more details on the geometric interpretation of the polarization vectors, we refer the reader to Ref. [84].

2.2.7 *Collective neutrino conversion*

The coherent forward scattering of neutrinos among themselves (Sec. 2.2.5) vastly differs from the coherent forward scattering of neutrinos with matter (Sec. 2.2.2). The crucial difference is that neutrino-neutrino interactions lead to a non-linear behavior of the neutrino flavor evolution [74, 85]. As a result, neutrinos with different momenta evolve in a *collective* fashion because the self-interaction Hamiltonian (Eq. 2.63) couples different neutrino modes to one another.

In general, the equations of motion that describe neutrino flavor conversion can be written as follows [73, 86, 87]

$$\begin{aligned}\left(\frac{\partial}{\partial t}+\vec{v}\cdot\vec{\nabla}_x\right)\rho(\vec{x},\vec{p},t) &= -i\Big[H(\vec{x},\vec{p},t),\rho(\vec{x},\vec{p},t)\Big]+\mathcal{C}\left(\rho(\vec{x},\vec{p},t),\bar{\rho}(\vec{x},\vec{p},t)\right),\\ \left(\frac{\partial}{\partial t}+\underbrace{\vec{v}\cdot\vec{\nabla}_x}_{\text{advection}}\right)\bar{\rho}(\vec{x},\vec{p},t) &= -i\underbrace{\Big[\bar{H}(\vec{x},\vec{p},t),\bar{\rho}(\vec{x},\vec{p},t)\Big]}_{\text{refraction}}+\underbrace{\bar{\mathcal{C}}\left(\rho(\vec{x},\vec{p},t),\bar{\rho}(\vec{x},\vec{p},t)\right)}_{\text{collisions}}.\end{aligned} \tag{2.74}$$

The advective term $\vec{v}\cdot\vec{\nabla}_x$ is determined by the velocity of the (anti)neutrino field $\vec{v}$ and it only contributes if the neutrino ensemble is non-homogeneous, i.e., the gradient of the density matrix does not vanish. The commutator on the right-hand side considers neutrino refraction effects (Sec. 2.2.5). The last term is the collision term which includes non-forward scatterings of neutrinos with background particles, including neutrinos.

In the field of neutrino collective conversion, there are two important regimes according to the relevant time scales involved in the EOMs (Eqs. 2.74) describing neutrino flavor transition: *slow flavor conversion* and *fast flavor conversion*. In the next Sections 2.2.7.1 and 2.2.7.2, we describe in detail the most important features of both slow and fast regimes and provide a glimpse into their main phenomenological signatures.

2.2.7.1 *Slow flavor conversion*

Neutrino self-interactions can lead to the so-called "slow" neutrino conversions [82, 88] which occur on a timescale determined by the vacuum oscillation frequency $\omega=\frac{\Delta m^2}{2E}\simeq\mathcal{O}(6)\ \mathrm{km}^{-1}$ for typical neutrino energies and for the largest squared mass difference. As the distance from the neutrinospheres increases, the magnitude of the neutrino self-interaction strength μ (Sec. 2.2.5) decreases accordingly. Very close to the neutrinospheres, however, the neutrino-neutrino interaction strength can be very large $\mu\simeq\mathcal{O}(10^5)\ \mathrm{km}^{-1}$. As such, slow collective conversions occur on a timescale determined by the inverse of $\sqrt{|\omega\mu|}$, which requires both the oscillation frequency and the neutrino interaction strength to be different from zero. Slow neutrino conversions are expected to be important far away from the neutrinospheres in regions where all neutrino species are decoupled from matter and in the free-streaming regime, as schematically shown in Fig. 12.

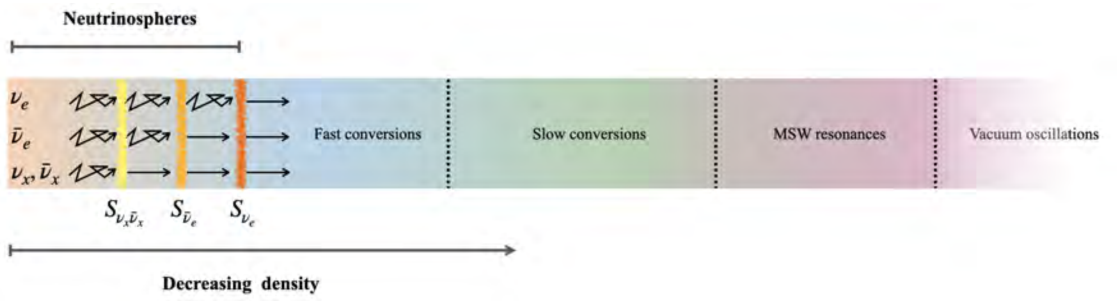

Figure 12: Schematic representation of the different regions of the astrophysical source where neutrino conversions could take place. Different regions are visible as a function of density. Different neutrinos $(\nu_e, \bar{\nu}_e, \nu_x, \bar{\nu}_x)$ with $x = \mu, \tau$) have different interaction rates and they kinematically decouple at $S_{\nu_x\bar{\nu}_x} < S_{\bar{\nu}_e} < S_{\nu_e}$, these spatially extended regions are the neutrinospheres (orange-shaded transition region). At the highest neutrino densities and near the neutrinospheres, fast flavor conversion is expected (blue-shaded region). As the neutrino density decreases, slow conversions (green-shaded region) and MSW resonances (pink-shaded region) are prone. Lastly, neutrinos undergo vacuum oscillations in the limit of vanishing density (light pink-shaded region).

Slow neutrino conversions have the distinct characteristic of producing so-called spectral swaps (or spectral splits), by which different energy modes (or bins) swap their flavor content as a function of the mass ordering [89, 90]. Such spectral swaps, which were long thought to be smoking guns for differentiating the mass ordering of neutrinos, assumed a very restrictive model, the so-called *bulb model* [89]. In this model, neutrinos are emitted uniformly and half-isotropically from a spherical neutrinosphere. Also, the neutrino emission is assumed to be azimuthally symmetric, and the only variable determining the properties of the star is the radial distance. This model offered for the first time an opportunity to numerically solve the equations of motion of neutrinos [83, 89–93] in what otherwise would have been an arduous task had the many symmetries not been assumed. Even more, analytical descriptions were developed showing that the flavor dynamics of slow conversions was formally that of a gyroscopic pendulum[2] in flavor space [90, 92, 93]. The main crucial observation was that flavor conversions occurred only in the inverted mass ordering scenario leading to maximal flavor conversions $\nu_e\bar{\nu}_e \rightarrow \nu_x\bar{\nu}_x$. Moreover, all energy modes of $\bar{\nu}_e$ were fully converted to $\bar{\nu}_x$ while for ν_e this only happened for $E > E_{\text{crit}}$. The spectral splits happened in this manner due to total lepton number conservation. It is now understood that the flavor outcome

---

[2] One of the main works within thesis shows that the gyroscopic pendulum analogy can be formally implemented for the case of fast pairwise neutrino conversions.

strongly depends on the symmetry simplifications assumed by the early calculations on spectral splits. The following works explored the deviations from the bulb model and included multi-angle effects [94–97], a three-flavor framework [98–103], the spontaneous breaking of azimuthal [104–108], spatial inhomogeneity [109–115] and stationarity [116, 117], and showed that spectral splits can develop in both mass orderings and are sometimes suppressed by the matter potential during the supernova accretion phase [118–123].

In the following sections, we revisit some of the main results pertaining slow collective conversion. For more details on the phenomenology of slow conversions, we refer the reader to Refs. [82, 124].

SYNCHRONIZED NEUTRINO CONVERSIONS The neutrino self-interaction is represented as the coupling between polarization vectors in Eq. 2.73. To illustrate the contribution of this coupling to the flavor dynamics, let us consider a homogeneous and isotropic neutrino ensemble with $\lambda = 0$ and $\mu = \text{const}$. It can be shown that one of the conserved quantities is the "total energy of the magnetic spins" [83]

$$\mathcal{E} = \int_{-\infty}^{\infty} d\omega\omega(\vec{P}_\omega \cdot \vec{B}) + \frac{\mu}{2}|\vec{D}|^2 , \tag{2.75}$$

where the first term corresponds to the "total energy" of the coupling between the "magnetic field" and the "spins," while the second term is the "total spin-spin coupling energy." This conservation law implies that a dense neutrino ensemble can support self-maintained coherent conversions [125]. For instance, if initially, the ensemble consists of neutrinos of the same flavor so that all $\vec{P}_\omega$ point in the same direction, then the flavor evolution of these vectors is coherent, and they remain aligned even when they do not have the same energy. These are the so-called *synchronized neutrino conversions* because all (anti)neutrinos oscillate collectively with the same frequency Ω_{synch}. This synchronized conversion frequency is given by

$$\Omega_{\text{synch}} = \frac{1}{|\vec{D}|^2} \int_{-\infty}^{\infty} d\omega\omega(\vec{D} \cdot \vec{P}_\omega) . \tag{2.76}$$

This frequency is the frequency at which the self-interactions couple a system of "magnetic dipoles" in Eq. 2.66 to form one larger magnetic dipole, which then oscillates coherently in an external magnetic field.

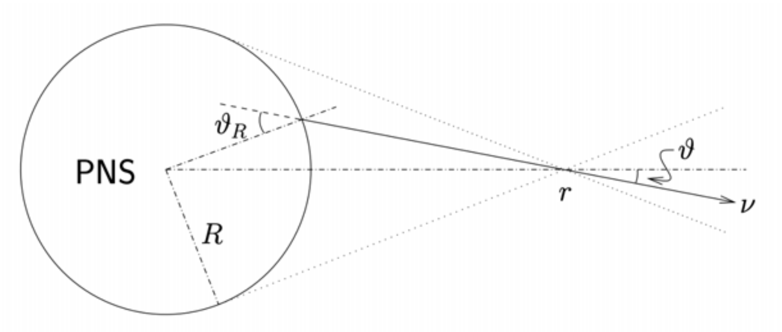

Figure 13: Schematic representation of the neutrino bulb model. According to this model, all neutrinos are emitted half-isotropically from the surface of the PNS, which has a radius of R. All neutrinos with the same initial flavor, energy, and emission angle ϑ_R follow the same flavor evolution because of spherical symmetry and isotropic emission from the PNS. The polarization vector $\vec{P}_{\omega,\vartheta}$ is determined by ω, ϑ (or ϑ_R) and r. In the sketch, ϑ is the angle at radius r between the radial and neutrino trajectory directions. Image taken from Ref. [82].

NEUTRINO BULB MODEL The neutrino bulb model was one of the first models proposed to study collective neutrino conversions. Here, we briefly discuss two of the schemes prevalent in the literature in the context of the supernova environment. Both bulb model schemes assume a spherically symmetric around the proto-neutron star; see Fig. 13 for a schematic representation of the system in question.

The following equation of motion determines the dynamics of the polarization vectors in the bulb model

$$\cos\vartheta \frac{d}{dr}\vec{P}_{\omega,\vartheta}(r) = \left[\omega\vec{B} + \lambda(r)\vec{L} + \vec{H}_{\nu\nu,\vartheta}(r)\right] \times \vec{P}_{\omega,\vartheta}(r)\,, \tag{2.77}$$

with the neutrino-neutrino interaction Hamiltonian as follows

$$\vec{H}_{\nu\nu,\vartheta}(r) = \sqrt{2}G_F n_{\bar{\nu}_e}(R)\int_{-\infty}^{\infty} d\omega' \int_{\cos\vartheta_{\max}}^{1} d\cos\vartheta' \vec{P}_{\omega',\vartheta'}(r)(1-\cos\vartheta\cos\vartheta')\,. \tag{2.78}$$

Note that due to spherical symmetry, the $(1-\vec{v}\cdot\vec{v}')$ is simply $(1-\cos\vartheta\cos\vartheta')$ after integrating over the azimuthal angle. Since neutrinos are emitted from a sphere of finite size, there is a maximum angle $\vartheta_{\max} = \arcsin(R/r)$ after which one sees no neutrinos coming from the source, see Fig. 13. The equation of motion in Eq. 2.77 can be solved numerically without further simplification. This corresponds to the *multi-angle* scheme. On the other hand, one also has the *single-angle* scheme, where it is assumed that $\vec{P}_{\omega,\vartheta}(r) = \vec{P}_{\omega}(r)$ identical for different neutrino trajectories. One version of the single-angle approximation is such that $\vec{P}_\omega(r)$ is computed pointing along the radial direction ($\vartheta_R = 0$) and this vector alone represents the evolution of all other directions through the single-angle equation of motion

$$\frac{d}{dr}\vec{P}_\omega(r) = \left[\omega\vec{B} + \lambda(r)\vec{L} + \mu(r)\vec{D}\right] \times \vec{P}_\omega(r)\,. \tag{2.79}$$

Moreover, a similar equation for antineutrinos follows with $\omega \to -\omega$. Here, $\mu(r) = \sqrt{2}G_F n_{\bar{\nu}_e}\mathcal{D}(r/R)$ with the geometric factor $\mathcal{D}(r/R)$ that, to some extent, takes into account the angle effect and the dilution of the neutrino fluxes. The geometric factor is given by $\mathcal{D}(r/R) = [1 - \sqrt{1-(R/r)^2}]^2/2$. In the single-angle approximation, flavor evolution is equivalent to the dynamics of a homogeneous and isotropic neutrino ensemble that expands with "time" r. In the limit $r \gg R$ when the bulb is a point-like source the geometric factor $\mathcal{D}(r/R) \propto (R/r)^4$. Although the single-angle was widely implemented in the literature because of its simplicity, it led to incorrect results because of the anisotropic component of the equations of motion that cannot be neglected in collective conversions.

BIPOLAR NEUTRINO CONVERSIONS Another important example of collective neutrino conversions is the so-called *bipolar conversions*. For illustration, let us consider a homogeneous and isotropic ensemble of mono-energetic (anti)neutrinos. Therefore, the system is fully described by the evolution of two polarization vectors, $\vec{P}_\omega$ (neutrino) and $\vec{P}_{-\omega}$ (antineutrino). For clarity, one can assume that there is no matter $\lambda = 0$ and that $\mu = \text{const}$. The excess of neutrinos over antineutrinos is parameterized through the lengths of the polarization vectors $|\vec{P}_\omega| = (1+\varepsilon)|\vec{P}_{-\omega}|$ with $\varepsilon \in [0,1]$. Initially, at $t = 0$, the vector $\vec{P}_\omega$ points in the direction of $\hat{e}^{(I)}$ and $\vec{P}_{-\omega}$ points in the opposite $-\vec{P}_\omega$ direction, therefore the name "bipolar" because such systems are represented by two vectors which point in opposite directions.

An interesting case to look at is the case where $\varepsilon = 0$, and $\theta_V = 0$ which means that $\vec{P}_\omega$ initially points in the $\hat{e}^{(I)} = \hat{e}^{(V)} = -\vec{B}$ direction. Energy conservation (Eq. 2.75) implies [83] that if $\omega > 0$, the system is stable meaning that both $\vec{P}_\omega$ and $\vec{P}_{-\omega}$ are stuck and cannot move. On the contrary, if $\omega < 0$ and $\mu \gg |\omega|$ the system is unstable, allowing $\vec{P}_\omega$ and $\vec{P}_{-\omega}$ to almost swap their orientations. Therefore, the system is expected to lead to almost no flavor conversion when $\Delta m^2 > 0$, $\theta_V \ll 1$

and to a significant amount of conversion for the case when $\Delta m^2 < 0,\ \theta_V \ll 1$. The former is the most representative example of bipolar conversions.

The equations of motion of the simplified bipolar system are given by

$$\begin{aligned}\dot{\vec{P}}_\omega &= (+\omega\vec{B} + \mu\vec{D}) \times \vec{P}_\omega\,,\\ \dot{\vec{P}}_{-\omega} &= (-\omega\vec{B} + \mu\vec{D}) \times \vec{P}_{-\omega}\,,\end{aligned} \tag{2.80}$$

which have been solved analytically using the gyroscopic pendulum or "flavor pendulum" analogy [92, 125, 126]. The bipolar equations of motion (Eq. 2.80) can be re-written in the following form

$$\begin{aligned}\dot{\vec{D}} &= \frac{\vec{q}\times\vec{g}}{\mu}\,,\\ \vec{D} &= \frac{\vec{q}\times\dot{\vec{q}}}{\mu} + \sigma_s\vec{q},\end{aligned} \tag{2.81}$$

where the definitions below have been introduced

$$\begin{aligned}\vec{q} &= \frac{\vec{Q}}{|\vec{Q}|} = \frac{\vec{P}_\omega - \vec{P}_{-\omega} - \frac{\omega}{\mu}\vec{B}}{|\vec{Q}|},\\ \vec{g} &= -\mu\omega|\vec{Q}|\vec{B},\\ \sigma_s &= \vec{q}\cdot\vec{D} = \text{const.}\end{aligned} \tag{2.82}$$

The pair of Eqs. 2.81 describe the dynamics of a gyroscopic pendulum in flavor space with a total angular momentum given by $\vec{D}$ in the presence of a gravitational field, where the gravitational acceleration is $\vec{g}$. In this analogy, the pendulum consists of a massless rod with a point-like particle of mass μ^{-1} attached to one of the extremes at position $\vec{q}$ and with the other extreme fixed. The flavor pendulum of a symmetric bipolar system ($\varepsilon = 0$) has a vanishing internal spin $\sigma_s = 0$, and the motion takes place on a plane. For an asymmetric system, $\varepsilon \neq 0$, the pendulum has an internal spin, and the motion takes place outside the plane in three dimensions instead of two. The stable $\omega > 0$ and unstable $\omega < 0$ configurations discussed above correspond to the two possible orientations of the gravitational field $\vec{g}$ with respect to $\vec{q}$. If $\omega > 0$, then $\vec{g} \propto -\vec{B}$ and the gravitational field pulls in the same direction at the orientation of $\vec{q}$. In the other case $\omega < 0$, we have $\vec{g} \propto \vec{B}$ and the gravitational field pulls in the opposite direction of the orientation of $\vec{q}$ making the pendulum swing under the influence of gravity.

The flavor pendulum can perform two kinds of motion: a precession around $\vec{B}$ and a nutation around the average precession trajectory. Bipolar conversions correspond to the nutation motion.

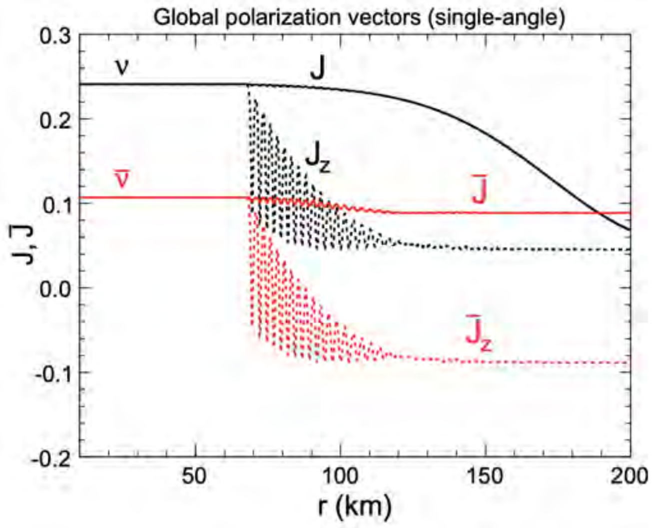

Figure 14: Single-angle simulation in the IH scenario. The norm and the z-component of the global (energy-integrated) polarization vector for neutrinos $\vec{J}$ and antineutrinos $\vec{\bar{J}}$ are shown as a function of distance r. The total lepton number $J_z - \bar{J}_z$ is a conserved quantity. Image taken from Ref. [90]

For certain configurations, the flavor pendulum is locked in the highest position because it spins so fast that energy and angular momentum conservation prevent it from moving: a so-called "sleeping top" configuration that does not fall in the presence of gravity [92, 93, 127]. This sleeping-top scenario is realized when μ is sufficiently large such that

$$\mu > \mu_{\text{crit}} \equiv \frac{2|\omega|}{(\sqrt{1+\varepsilon}-1)^2} \,. \tag{2.83}$$

The precession behavior in the large μ limit corresponds to synchronized conversions of the bipolar system with synchronized conversion frequency (Eq. 2.76) given by $\Omega_{\text{sync}} = (1+2\varepsilon^{-1})\omega$.

THE SPECTRAL SPLIT/SWAP The polarization vector equations in the single-angle approximation (Eqs. 2.79) can be solved assuming a SN bulb model. The phenomenon of the spectral split, or swap, is present in the single-angle and multi-angle framework. We will briefly comment on the multi-angle extension of the spectral splits. As described before, for bipolar neutrino conversions, the non-trivial, unstable case is the IH scenario $\omega < 0$ (see Eq. 2.81), and thus we focus on this case to illustrate the spectral splits phenomenon. It is convenient to define energy-integrated polarization vectors $\vec{J} \propto \int_0^\infty d\omega \vec{P}_\omega$ and $\vec{\bar{J}} \propto \int_0^\infty d\omega \vec{P}_{-\omega}$ to capture global effects of the evolution of flavor. The radial evolution of the norms of $\vec{J}$ and $\vec{\bar{J}}$ and their corresponding z-components J_z and $\bar{J}_z$, respectively, are shown in Fig. 14. The flavor evolution presented in Fig. 14 can be understood as follows. From small distances up to ~ 68 km, all polarization vectors are "glued" together (synchronized) along the vertical axis, i.e., $J = J_z$ and $\bar{J} = \bar{J}_z$ in this spatial range, and the gyroscopic pendulum finds itself in the "sleeping top" configuration because $\mu > \mu_{\text{crit}}$ (Eq. 2.83), therefore pointing upwards and not falling. Around $r \sim 68$ km, the pendulum starts to fall, and nutations start to occur, signalizing the transition from synchronized conversions to bipolar conversions. The amplitude of the nutations decreases with distance until bipolar conversions finally vanish around $r \gtrsim 10$ km.

In parallel, the spectral split phenomenon is at play. Antineutrinos reverse their polarization vector $\vec{\bar{J}} \to -\vec{\bar{J}}$ so that, asymptotically, their $z-$component component equals the norm of the energy-integrated polarization vector $\bar{\bar{J}}_z \simeq -\bar{J}$, as seen in the red dashed curve in Fig. 14 when $\bar{J}_z$ goes from ~ 0.1 to ~ -0.1. Neutrinos also try to display a similar behavior by inverting their energy-integrated polarization vector $\vec{J}$ as much as lepton-number conservation allows. At some point, $J_z \simeq J$ is reached as seen in black dashed line in Fig. 14 a bit further out than 200 km, at which point the spectral split is "frozen" corresponding to a final steady state where $\vec{J}$ points in the $+\hat{z}$ direction and $\vec{\bar{J}}$ in the $-\hat{z}$ direction. At all times of the evolution, the total lepton number $J_z - \bar{J}_z$ is conserved at any r.

The behavior of the z-components of the individual polarization vectors P_z for different energies is shown in Fig. 15 as a function of distance r. Five representative energies are shown: $E_1 = 5.2$ MeV, $E_2 = 12.4$ MeV, $E_3 = 19.1$ MeV, $E_4 = 23.8$ MeV and $E_5 = 31.3$ MeV. In Fig. 15, one can see that the onset of bipolar conversions and the nutation periods are the same for neutrinos and antineutrinos, making explicit the collective behavior of oscillations. Interestingly, the flavor evolution of each P_z and $\bar{P}_z$ indeed depends on energy. For neutrinos (see upper panel of Fig. 15), the spectral split occurs at $E_c \simeq 7$ MeV. The split means that there are two regions of energy doing different things: the mode with $E_1 < E_c$ does not change and ends up in the same initial value, while the other modes with $E_2, E_4, E_5 > E_c$ display the aforementioned inversion $P_z \to -P_z$. The mode E_3 does not change much because it is close to the equilibrium energy value at which the fluxes of ν_e and ν_x are almost identical, and conversions cannot do much. For antineutrinos (see lower panel of Fig. 15), all energy modes reverse their polarization vector orientation $P_z \to -P_z$. These results support the end of bipolar conversions, and the emergence of the energy split effect around $r \sim 100$ km [90].

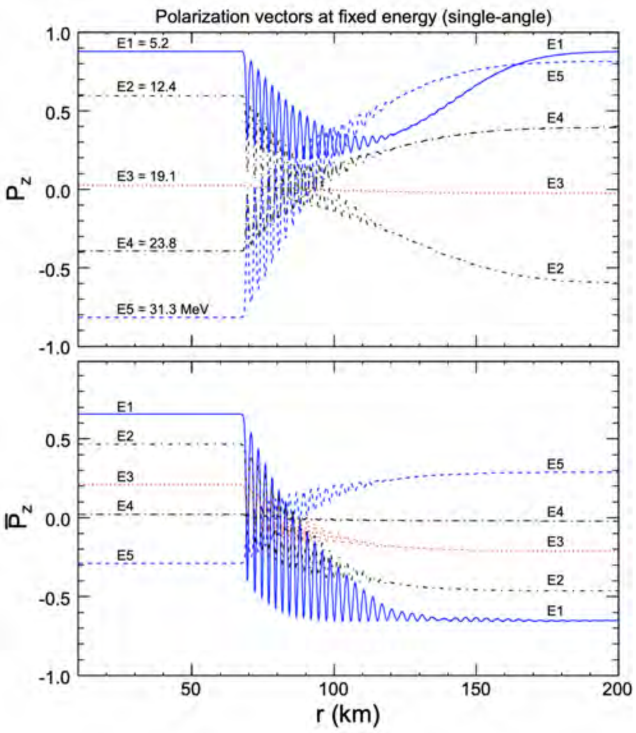

Figure 15: Single-angle simulation in the IH scenario. The z-component of the polarization vector of neutrinos P_z (upper panel) and antineutrinos $\bar{P}_z$ (lower panel) are shown as a function of distance r for five benchmark energy modes. Image taken from Ref. [90].

It is worth noting that the specific location of the transition from synchronized to nutation and the split energy depend on the initial conditions of the system assumed in Ref. [90]. However, qualitatively similar results were also reported in Ref. [82].

The spectra of neutrinos and antineutrinos are shown in the upper panels of Fig. 16. Neutrinos shown in the upper left panel of Fig. 16, clearly display the spectral split phenomenon and the associated swap of ν_e and ν_x fluxes for energies $E > E_c \simeq 7$ MeV. In the upper right panel of Fig. 16, the spectra of antineutrinos are shown, where there is an almost complete swap w.r.t. to the initial fluxes, except for a small region at low energies.

When including angle-dependence (multi-angle approach) in the equations of motion (Eqs. 2.79), kinematic decoherence between different modes is introduced, thereby smearing out some of the features of the single-angle approach. In the multi-angle approach, the nutation observed in Fig. 14 (single-angle) is largely suppressed, and the system is kept in the synchronized regime for a bit longer. In the lower panels of Fig. 16, we show the multi-angle version of the spectral split. The neutrino spectral split at $E > E_c \simeq 7$ MeV is clearly visible in the lower left panel of Fig. 16,

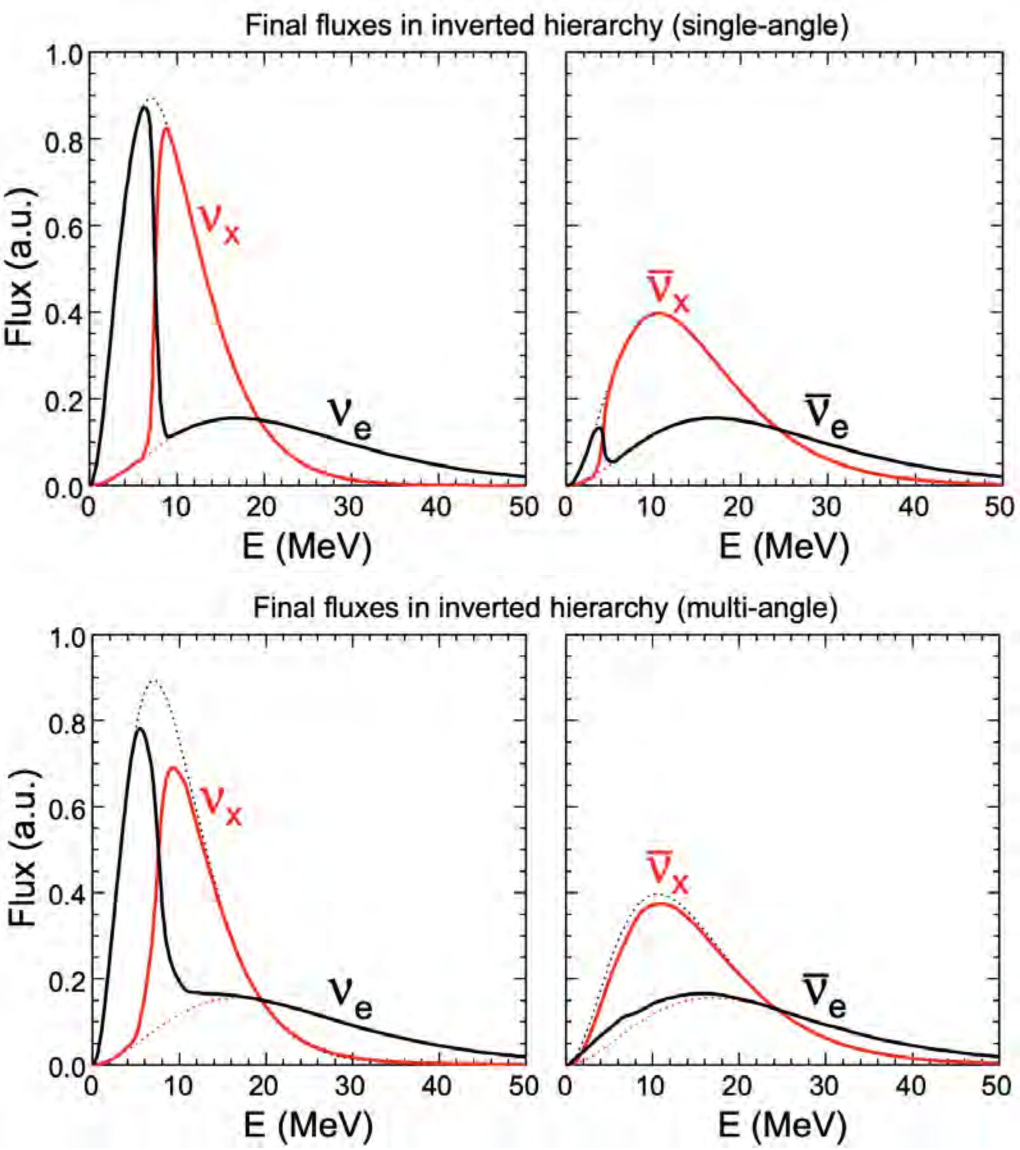

Figure 16: Single-angle (upper panels) and multi-angle simulations (lower panels) in the IH scenario. Final fluxes for neutrinos (left panels) and antineutrinos (right panels) as a function of energy. The initial fluxes are shown in dotted lines to make evident the spectral swap around $E = E_c \simeq 7$ MeV. Both the single-angle and the multi-angle simulations display spectral splits, although the multi-angle one is less sharp. Image taken from Ref. [90].

however less pronounced than in the single-angle case (upper panels of Fig. 16). In the lower right panel of Fig 16, the small region displaying an antineutrino spectral swap is strongly smeared. Therefore, spectral splits are present in both the single-angle and multi-angle frameworks.

2.2.7.2 *Fast flavor conversion*

Neutrino fast flavor conversions (also called fast pairwise conversions) are expected to take place in the vicinity of the neutrinospheres [128–130], in contrast to slow flavor conversions (Sec. 2.2.7.1) which are relevant far away from the neutrino decoupling regions; see Fig. 12 for a schematic representation of the relevant regions for conversions. One of the most attractive features of fast flavor conversion is that it is possible to convert neutrino flavor even in the case of vanishing mixing angle $\omega = 0$, which corresponds to the astrophysical scenario where the neutrino interaction strength dominates, i.e., $\mu \gg \omega$. This remarkable feature strongly differs from slow conversions where ω must not vanish for neutrinos to convert flavor (Eq. 2.81). Here, we refer to fast flavor conversions in the strict sense where $\omega = 0$ and vacuum oscillations play no role in the flavor evolution. Thus, in the absence of vacuum oscillations, fast pairwise conversions conserve the total lepton number and conversions are strictly pairwise $\nu_e \bar{\nu}_e \leftrightarrow \nu_x \bar{\nu}_x$.

The Hamiltonian that governs the evolution of the density matrices is usually broken down into three pieces, the vacuum-, matter-, and neutrino-neutrino terms. If the matter background is assumed to be static, the matter term is $H_{\text{mat}} = \sqrt{2} G_F n_e \text{diag}(1, 0)$ (see Section 2.2.2). If included, such matter term can be effectively ignored by assuming a tiny vacuum mixing angle $\theta_V \ll 1$, which accounts for the suppression of mixing in the presence of a very dominant matter term [131]. Since we are in the regime where $\mu \gg \omega$, the contribution from $H_{\nu\nu}$ strongly dominates over those of H_{mat} and H_{vac}. In this limit, we have that the Hamiltonian for neutrinos and antineutrinos are identical $H = \bar{H} = H_{\nu\nu}$, with only a contribution from neutrino refraction as in Eq. 2.63.

One necessary but not sufficient condition for the development of fast flavor conversions is the existence of an angular crossing between the angular distributions of electron-neutrinos and electron-antineutrinos. Such an angular crossing, the *Electron-Lepton-Number* (ELN) *crossings*, are illustrated schematically in Fig. 17. The neutrino-neutrino interaction Hamiltonian $H_{\nu\nu}$ can develop off-diagonal entries which grow exponentially, leading to unstable solutions which collectively

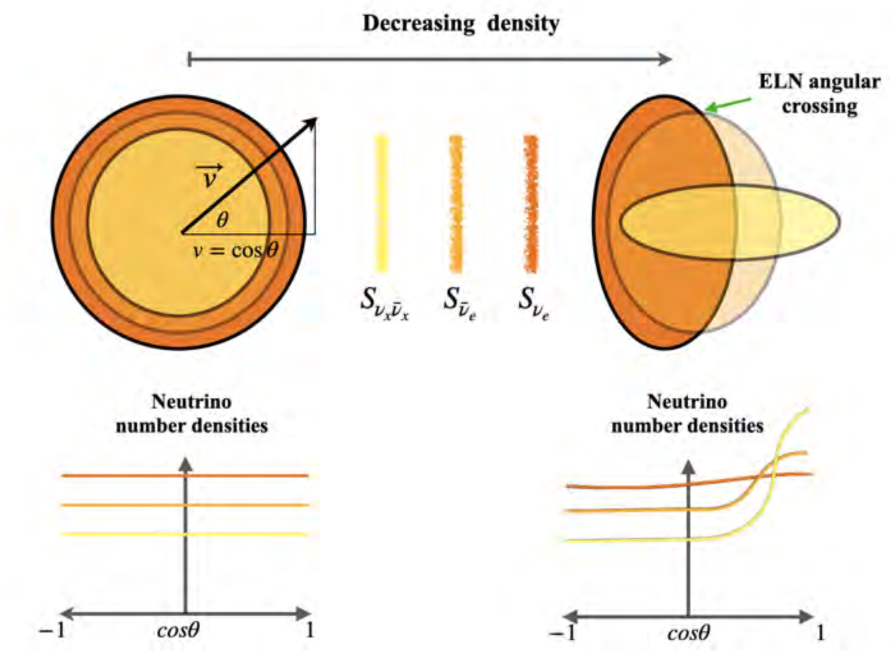

Figure 17: Schematic representation of the formation of ELN angular crossings. All neutrinos are trapped inside the neutrino decoupling regions, and their distribution as a function of the polar angle θ is nearly isotropic. In the free-streaming regime, the angular distributions are flavor dependent and $\nu_x, \bar{\nu}_x$ are the most forward-peaked distributions, followed by the $\bar{\nu}_e$ and the ν_e. Here, the forward direction is at $\cos\theta = 1$ and the backward direction at $\cos\theta = -1$. Due to the decoupling regions being spatially well separated, ELN angular crossings in the distributions of neutrinos form.

convert flavor. The slope of the exponential growth of the off-diagonal entries is what we call *the growth rate of flavor instability*, which is described in detail in Section 2.2.7.3.

Crossings in the angular distributions of neutrinos are the starting point for studying fast conversions. ELN crossings give rise to *temporal* flavor instabilities. Moreover, if the astrophysical conditions are such that there is a significant backward flux of neutrinos (i.e., due to collisions), a *spatial* flavor instability develops instead [132, 133]. Both temporal and spatial instabilities arise because of an effective ELN angular crossing [134]. Most of the works concerning fast flavor conversion attempt to find favorable conditions for the development of fast flavor conversions, and for that purpose, a standard procedure is the linear stability analysis (Sec. 2.2.7.3). The linear stability analysis mainly provides the growth rate of flavor conversions i.e., *when* fast instabilities occur, if any, and lacks information about the non-linear regime and, therefore the final flavor outcome. However, in one of the main works of this thesis (Chapter 5), we present the first example where the linear stability analysis offers a way of predicting the maximum amount of flavor conversion, which was previously only accessible through the numerical simulation of the non-linear regime.

In the next Section, we present the standard procedure behind the linear stability analysis, focusing on the equation of motion responsible for fast flavor conversion.

2.2.7.3 *Linear stability analysis*

The linear stability analysis (LSA) was first introduced in Ref. [135] to understand under what circumstances a system has unstable solutions to the neutrino equations of motion. The non-linear behavior of the neutrino flavor evolution displays counter-intuitive results on many occasions; in that sense, the *linear regime* is much simpler to understand and is accessible from the computational point of view. Typically, the primary outcome from the LSA is the growth rate of flavor instabilities.

For clarity, let us consider a non-homogeneous and azimuthally symmetric neutrino gas, whose dynamics is determined completely by the non-homogeneous version of $H = \bar{H} = H_{\nu\nu}$ in Eq. 2.65

$$\begin{aligned} i\frac{\partial}{\partial t}\rho(\vec{x},\theta,t) &= [H(\vec{x},\theta,t),\rho(\vec{x},\theta,t)], \\ i\frac{\partial}{\partial t}\bar{\rho}(\vec{x},\theta,t) &= [H(\vec{x},\theta,t),\bar{\rho}(\vec{x},\theta,t)]. \end{aligned} \tag{2.84}$$

Extending to more complicated systems can be lengthy, although straightforward and analogous to the derivation provided here. It is easy to check that the commutator in the equations of motion (Eqs. 2.84) contains products of the entries $\rho_{\alpha,\beta}$ and $\bar{\rho}_{\alpha,\beta}$ with $\alpha, \beta = e, x$. By definition, the linear regime is characterized by the smallness of the off-diagonal components of the density matrices ($\alpha \neq \beta$) in comparison with the diagonal ones ($\alpha = \beta$). Therefore, one can collect the terms that are proportional to the products of the off-diagonal terms (which are even smaller).

After grouping the terms, the density matrices can be written as

$$\begin{aligned}\rho(\vec{x},\theta,t) &= \begin{pmatrix} \rho_{ee}(\vec{x},\theta,0) - \mathcal{O}(\varepsilon^2) & \varepsilon(\vec{x},\theta,t) \\ \varepsilon^*(\vec{x},\theta,t) & \rho_{xx}(\vec{x},\theta,0) + \mathcal{O}(\varepsilon^2) \end{pmatrix}, \\ \bar{\rho}(\vec{x},\theta,t) &= \begin{pmatrix} \bar{\rho}_{ee}(\vec{x},\theta,0) - \mathcal{O}(\bar{\varepsilon}^2) & \bar{\varepsilon}(\vec{x},\theta,t) \\ \bar{\varepsilon}^*(\vec{x},\theta,t) & \bar{\rho}_{xx}(\vec{x},\theta,0) + \mathcal{O}(\bar{\varepsilon}^2) \end{pmatrix}. \end{aligned} \tag{2.85}$$

Since the off-diagonal terms $\varepsilon(\bar{\varepsilon}) = \rho_{ex}(\bar{\rho_{ex}})$ are much smaller than the diagonal terms during the linear regime, we have that $|\varepsilon(\vec{x},\theta,t)| \ll |\rho_{ee}(\vec{x},\theta,t) - \rho_{xx}(\vec{x},\theta,t)|$ and similarly for antineutrinos $|\bar{\varepsilon}(\theta,t)| \ll |\bar{\rho}_{ee}(\vec{x},\theta,t) - \bar{\rho}_{xx}(\vec{x},\theta,t)|$.

The LSA consists of keeping leading terms in the equations of motion and neglecting subleading terms of $\mathcal{O}(\varepsilon^2)$. After dropping terms of $\mathcal{O}(\varepsilon^2)$ in Eqs. 2.85, it is easy to see that the only dynamical variables left are $\varepsilon(\vec{x},\theta,t)$ and $\bar{\varepsilon}(\vec{x},\theta,t)$, while $\rho_{ee}(\vec{x},\theta,0)$ and $\bar{\rho}_{ee}(\vec{x},\theta,0)$ are simply constant inputs at a given angular mode and location in space.

After neglecting higher order terms, the equation of motion for $\varepsilon(\theta,t)$ is given by

$$\left(\frac{\partial}{\partial t} + \vec{v}\cdot\vec{\nabla}\right)\varepsilon(\vec{x},\theta,t) = -i\int_{-1}^{1} d\cos\theta' F(\vec{x},\theta,\theta',t)\varepsilon(\vec{x},\theta',t)\,, \tag{2.86}$$

and a similar equation follows for $\bar{\varepsilon}(\vec{x},\theta,t)$. The main goal of the LSA is to find the eigenvalues of the matrix F. If any of the eigenvalues of F is a complex number, then ε grows (shrinks) exponentially. On the other hand, if the eigenvalues are only real, then the solution is stable instead. The interesting cases correspond to eigenvalues which lead to exponentially growing solutions. If a solution is unstable (complex eigenvalue), the solution eventually reaches the regime where $\varepsilon \sim \rho_{ee}, \rho_{xx}$; this is the *non-linear regime* which is much more difficult to model.

Substitution of the density matrices (Eq. 2.85) in the equations of motion (Eq. 2.84) leads to the linearized equations of motion

$$\begin{aligned}
i\left(\frac{\partial}{\partial t}+\vec{v}\cdot\vec{\nabla}\right)\varepsilon(\vec{x},\theta,t) &= (H_{ee}-H_{xx})\varepsilon(\vec{x},\theta,t)\\
&+ (\rho_{xx}-\rho_{ee})\mu\int_{-1}^{1} d\cos\theta'\Big(\varepsilon(\vec{x},\theta',t)-\bar{\varepsilon}(\vec{x},\theta',t)\Big)(1-\cos\theta\cos\theta'),\\
i\left(\frac{\partial}{\partial t}+\vec{v}\cdot\vec{\nabla}\right)\bar{\varepsilon}(\vec{x},\theta,t) &= (H_{ee}-H_{xx})\bar{\varepsilon}(\vec{x},\theta,t)\\
&+ (\bar{\rho}_{xx}-\bar{\rho}_{ee})\mu\int_{-1}^{1} d\cos\theta'\Big(\varepsilon(\vec{x},\theta',t)-\bar{\varepsilon}(\vec{x},\theta',t)\Big)(1-\cos\theta\cos\theta').
\end{aligned} \tag{2.87}$$

The evolution of neutrinos and antineutrinos is collective when driven by $H_{\nu\nu}$ (Sec. 2.2.7). Therefore, ε and $\bar{\varepsilon}$ share a common growth rate [135]. An adequate ansatz for ε and $\bar{\varepsilon}$ is given by

$$\begin{aligned}
\varepsilon(\vec{x},\theta,t) &= Q_\theta e^{-i(\Omega t-\vec{k}\cdot\vec{x})},\\
\bar{\varepsilon}(\vec{x},\theta,t) &= \bar{Q}_\theta e^{-i(\Omega t-\vec{k}\cdot\vec{x})}.
\end{aligned} \tag{2.88}$$

In the situation where either the *eigenfrequency* Ω or the *wave-vector* $\vec{k}$ have non-vanishing imaginary solutions to the eigenvalue equation (Eq. 2.86), a flavor instability is identified. If spatial homogeneity is assumed ($\vec{k}=0$), *temporal instabilities* arise for values of $\mathrm{Im}(\Omega)\neq 0$. Similarly, for stationary systems ($\Omega=0$), *spatial instabilities* arise for $\mathrm{Im}(\vec{k})\neq 0$.

For simplicity, it is instructive to look at the homogeneous case first ($\vec{k}=0$). Direct substitution of the ansatz (Eq. 2.88) in the linearized equations of motion (Eq. 2.87) give

$$\begin{aligned}
\Big(\Omega-(H_{ee}-H_{xx})\Big)Q_\theta &= (\rho_{xx}-\rho_{ee})\mu\int_{-1}^{1} d\cos\theta'(Q_{\theta'}-\bar{Q}_{\theta'})(1-\cos\theta\cos\theta'),\\
\Big(\Omega-(H_{ee}-H_{xx})\Big)\bar{Q}_\theta &= (\bar{\rho}_{xx}-\bar{\rho}_{ee})\mu\int_{-1}^{1} d\cos\theta'(Q_{\theta'}-\bar{Q}_{\theta'})(1-\cos\theta\cos\theta'),
\end{aligned} \tag{2.89}$$

where the exponential $e^{-i\Omega t}$ has dropped out of the equation. The equations above allow to isolate Q_θ and $\bar{Q}_\theta$ on the left-hand-sides of Eq. 2.89, respectively. After inspection, it is clear that Q_θ, $\bar{Q}_\theta$ must have the following structure

$$\begin{aligned}
Q_\theta &= \frac{(\rho_{xx}-\rho_{ee})}{\Omega-(H_{ee}-H_{xx})}(a-b\cos\theta),\\
\bar{Q}_\theta &= \frac{(\bar{\rho}_{xx}-\bar{\rho}_{ee})}{\Omega-(H_{ee}-H_{xx})}(a-b\cos\theta),
\end{aligned} \tag{2.90}$$

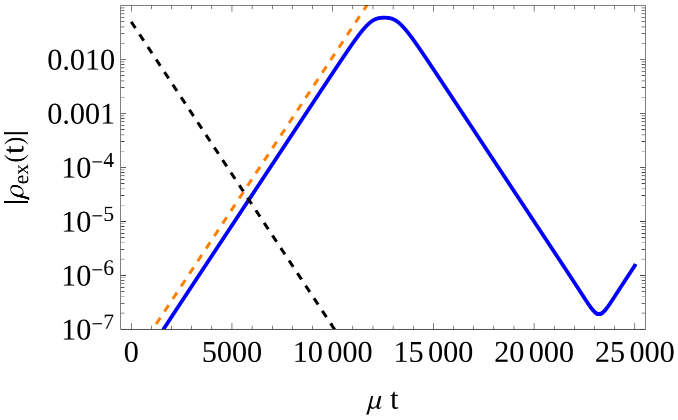

Figure 18: Illustrative example of the exponential growth of the off-diagonal term $|\rho_{ex}(t)| = \int_{-1}^{1} d\cos\theta |\rho_{ex}(\theta,t)|$ shown in blue. Time is expressed in terms of the only dimensionful quantity of the problem $\mu = 10^5\ \mathrm{km}^{-1} = 3\times 10^{10}\ \mathrm{s}^{-1}$, which sets the timescale for flavor conversion. The eigenfrequencies $\Omega^{\pm}$ are shown in dashed black and dashed orange; the agreement between the LSA and the numerical solution is excellent since the orange curve perfectly overlaps with the slope of the numerical solution.

where the a and b are real constant numbers unknown at this point since we do not know the explicit form of $Q_\theta, \bar{Q}_\theta$

$$\begin{aligned} a &= \int_{-1}^{1} d\cos\theta' (Q_{\theta'} - \bar{Q}_{\theta'}), \\ b &= \int_{-1}^{1} d\cos\theta' (Q_{\theta'} - \bar{Q}_{\theta'}) \cos\theta'. \end{aligned} \tag{2.91}$$

However, one can recursively substitute the parametric form of Q_θ and $\bar{Q}_\theta$ (Eqs. 2.90) back in Eq. 2.89. Thus, we obtain a system of equations for a and b such that

$$\begin{pmatrix} \mathcal{I}[1] & -\mathcal{I}[\cos\theta] \\ \mathcal{I}[\cos\theta] & -\mathcal{I}[\cos^2\theta] \end{pmatrix} \begin{pmatrix} a \\ b \end{pmatrix} = \begin{pmatrix} a \\ b \end{pmatrix}. \tag{2.92}$$

The system has a non-trivial solution $(a \neq 0 \neq b)$ if and only if the following determinant condition is fulfilled

$$\det \begin{pmatrix} \mathcal{I}[1] - 1 & -\mathcal{I}[\cos\theta] \\ \mathcal{I}[\cos\theta] & -\mathcal{I}[\cos^2\theta] - 1 \end{pmatrix} = 0\,, \tag{2.93}$$

where the definition of the functional $\mathcal{I}[\cdot]$ is given by

$$\mathcal{I}[f(\theta)] = \int_{-1}^{1} d\cos\theta f(\theta) \left(\frac{(\rho_{ee} - \rho_{xx}) - (\bar{\rho}_{ee} - \bar{\rho}_{xx})}{\Omega - (H_{ee} - H_{xx})} \right). \tag{2.94}$$

The determinant equation (Eq. 2.93) is a polynomial in the eigenfrequency Ω, the *characteristic equation*. Analytical solutions can be found to the characteristic equation for some simple cases; however, more general solutions are typically found numerically. In the case presented here, the characteristic equation is of order Ω^3. One of the roots Ω_1 is always found to be real (stable), while the other two are imaginary and come from solving a quadratic equation; they come therefore in complex conjugates $\Omega_\pm$. See, for instance, Fig. 18 for an illustrative example of the LSA in practice.

The procedure is completely analogous for the more general non-homogeneous case $(\mathrm{Im}(\vec{k}) \neq 0)$ where one looks for imaginary solutions $(\Omega, \vec{k})$ to the determinant equation (Eq. 2.93). Despite its limitations, the LSA presented in this Section can offer valuable insights into the nature of neutrino fast flavor conversion. The works presented in parts ii and iii heavily rely on a version of the LSA presented in this Section.

In the next Chapters 3 and 4, we cover the basics of CCSNe and the mergers of binary compact objects, respectively, and offer a glimpse into the recent developments in neutrino flavor conversion in dense astrophysical environments.

3

NEUTRINOS IN CORE-COLLAPSE SUPERNOVAE

Supernovae are among the densest astrophysical events in the Universe. In such astrophysical environments, tremendous amounts of neutrinos and antineutrinos of all flavors are produced ($\sim 10^{58}$). The binding energy resealed during a supernova explosion is estimated to be $\mathcal{O}(10^{53}\text{ erg})$, from which roughly 99% is radiated away in the form of neutrinos and antineutrinos, while the remaining 1% is sufficient to power the stellar explosion. Since neutrinos carry away 100 times more energy than the kinetic energy of a typical core-collapse supernova, neutrinos are expected to play an important role. For instance, since neutrinos interact with the matter and also other neutrinos in the medium, the modeling of the evolution of neutrino flavor in CCSNe is conceptually complex and represents an open issue in astrophysics. In this Section, we cover the basic concepts concerning CCSNe theory, the role of neutrinos in the explosion mechanism, and recent developments on the front of neutrino flavor conversion in core-collapse supernovae.

3.1 SUPERNOVA THEORY IN A NUTSHELL

Close to the end of their evolution, massive stars develop a so-called onion-shell structure: heavier elements sit at the center of the onion-shell structure while successively lighter elements surround them. Each shell is the result of the sequence of nuclear burning stages. Before collapse, the mass of the core is about $1.3 - 2\ M_\odot$ with densities between $10^9 - 10^{10}$ g cm^{-3} and temperatures of approximately 1 MeV. The cycle commences with hydrogen burning into helium to produce energy, while the produced helium sinks into the core of the star. The gravitational pull raises the core's density and temperature, igniting the burning of helium into carbon. Once again, the heavier carbon element settles in the core, which will subsequently contract and increase the temperature

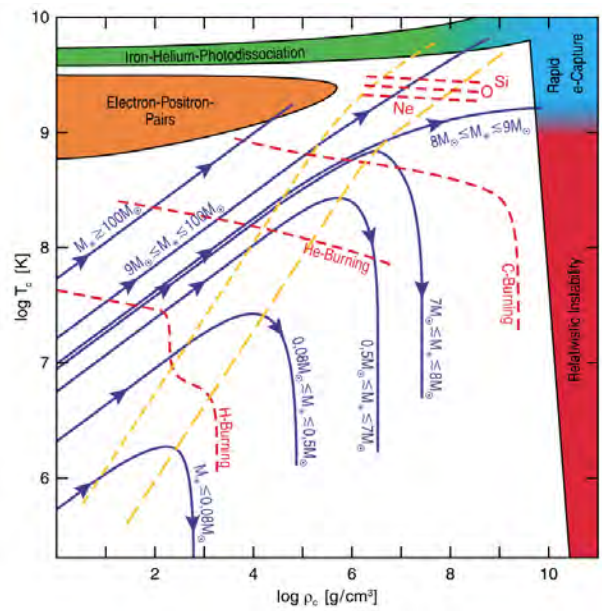

Figure 19: Stellar death regions with schematic stellar evolution paths as a function of the central density ρ_c and the central temperature T_c. The colored regions show the type of instability that leads to the collapse of the stellar core, and the blue lines correspond to different birth-mass ranges. Different nuclear burning stages are reached depending on the star's mass, shown in red dashed lines. Image taken from Ref. [136]

at the center to ignite the burning into neon. This cycle persists, allowing neon to burn into oxygen and oxygen into silicon, producing more stable and heavier elements with each burning stage.

Depending on the star's mass, the burning stages could reach the point where silicon burns into iron. Different mass ranges lead to different burning stages, leading to different categories of stellar deaths; see Fig 19 for a schematic representation of the different stellar evolution paths as a function of the stellar mass, central temperature, and central density.

Stars with masses $\gtrsim 8M_\odot$ can form an iron core. Iron is the element with the highest binding energy per nucleon and, therefore, the most favorable configuration. Up to that point, other burning stages require energy instead of providing it. Therefore, nuclear burning comes to a halt, energy production ceases, and the gravitational pressure forces the core to contract further and heat up.

COLLAPSE OF THE CORE The iron core becomes gravitationally unstable when thermal photons with sufficient energy are produced to dissociate the iron in the core to α-particles[1] and nucleons

$$\gamma +^{56}\mathrm{Fe} \rightarrow 13\,^{4}\mathrm{He} + 4n \quad \text{and then} \quad \gamma +^{4}\mathrm{He} \rightarrow 2p^{+} + 2n \tag{3.1}$$

while also electron captures on heavy nuclei[2] and free protons[3]

$$e^{-} + p \longrightarrow \nu_e + n\,, \tag{3.2}$$

$$e^{-} + (A, Z) \longrightarrow (A, Z-1) + \nu_e\,, \tag{3.3}$$

accelerate the implosion of the core. Notice that the positron capture on free neutrons $e^{+} + n \longrightarrow \bar{\nu}_e + p$ is strongly suppressed because the e^{+} density is very low due to high electron chemical potential. Also, the production of $\nu_{\mu,\tau}$ via charged-current interactions is strongly suppressed because the temperature is too low to produce heavy leptons, although some μ's could be present [137]. Pair production $e^{-} + e^{+} \longrightarrow \nu + \bar{\nu}$ and nucleon-nucleon bremsstrahlung $N + N \longrightarrow N + N + \nu + \bar{\nu}$ are the production paths of heavy-lepton neutrinos in the neutrinospheres [136, 138].

The electron captures (Eq. 3.2) reduce the number of electrons (deleptonization of the core), and the electron degeneracy pressure reduces as well, further contracting the core. At first, electron-neutrinos from the electron captures could escape freely until the density at the core is 10^{11}g cm^{-3} and the mean free path for coherent neutrino scattering off heavy nuclei becomes short enough that neutrinos diffuse instead. At last, when densities at the core are about 10^{12}g cm^{-3}, neutrinos cannot longer escape and become trapped while the stellar material from outer layers falls inwards.

SHOCK FORMATION The gravitationally unstable core implodes until the point where it reaches nuclear densities ($\sim 10^{14}$g cm^{-3}), and it is abruptly stopped. A new stable state is reached where matter can support its own gravitational pull due to the internal pressure of nucleons: they are so closely packed together that nucleon-nucleon interaction is highly repulsive, supporting the new stable state of the core. The collapsing inner core bounces back, and a shock front is formed.

---

[1] Helium-4 nucleus. Two protons and two neutrons.

[2] Heavy nuclei abundance is very high but the energy cost of converting a proton to neutron in a nucleus is high.

[3] Cross section high but the number of free protons is low.

SHOCK STAGNATION AND NEUTRINO BURST The shock propagates outwards, sweeping up the in-falling matter on its way, thereby dissipating kinetic energy. The temperature of the shock increases, which allows the creation of high-energy photons which dissociate iron nuclei to free nucleons. The conversion of kinetic energy to rest-mass energy drains energy from the shock (~ 9 MeV per nucleon or $\sim 10^{51}$ erg per $0.1\mathrm{M}_\odot$) reducing the post-shock pressure. After a ~ 1 ms, the shock still stagnates inside the collapsing iron core. Due to the density drop in the post-shock region, the abundant electron neutrinos from the electron captures start to free stream: a luminous flash of ν_e appears, the so-called *shock break-out neutrino burst*.

NEUTRINO HEATING AND REVIVAL OF THE SHOCK Three regions can be identified as far as neutrinos are concerned. Starting at the center of the star and moving outwards, the three regions of relevance are the following. The *neutrinospheres* $\mathcal{O}(50)$ km, then the *cooling region* $\mathcal{O}(100)$ km, followed by the *gain layer* $\mathcal{O}(200)$ km:

- The neutrinospheres (for each neutrino flavor) are the extended transition regions after which neutrinos are no longer trapped and start to free stream after the matter densities decrease sufficiently for neutrinos to escape.
- The cooling region is the zone where the emission rate of neutrinos is larger than their absorption rate, forcing the medium to lose energy via neutrino emission.
- The gain layer extends from the cooling region up to the stagnated shock position, and it is defined as the region where the absorption rates instead overcome the emission rates so that the reaction goes predominantly one way, favoring the re-absorption of neutrinos

$$\nu_e + n \longrightarrow p + e^- \ , \tag{3.4}$$

$$\bar{\nu}_e + p \longrightarrow n + e^+ \ . \tag{3.5}$$

Energy deposition is very effective in the gain layer, which can become convectively unstable [139, 140]. Also, the standing-accretion-shock instability (SASI) [141] can develop between the shock and the proto-NS giving rise to sloshing and spiral motion of the shock front, which can assist the neutrino heating. Another type of instability characterized by the dipole pattern of (anti)neutrino fluxes, the so-called Lepton-number Emission Self-sustained Asymmetry (LESA) phenomenon [142], which is ubiquitous in CCSNe simulations.

If neutrino heating is sufficient, the shock is pushed outwards, and the SN explosion is successful, escaping the iron core up to the outer layers of the star. This is the delayed neutrino heating mechanism capable of triggering supernova explosions even after shock stagnation. It is worth noting that besides the popular neutrino heating mechanism, other mechanisms could be invoked for the supernova explosion [136]. For instance, the thermonuclear mechanism, the bounce-shock mechanism, magnetohydrodynamic mechanism, acoustic mechanism, and phase-transition mechanism.

NUCLEOSYNTHESIS When the phase of simultaneous mass accretion and outflow near the NS ends, neutrinos-energy deposition launches a spherical outflow of matter from the NS surface, the so-called *neutrino-driven wind*. This wind is composed of free neutrons and protons, recombining into α particles and heavy nuclei. Depending on whether there is an excess of neutrons or protons, different nucleosynthetic yields are produced in the SN environment [143].

STATUS OF SUPERNOVA SIMULATIONS State-of-the-art hydrodynamical simulations of CCSNe have reached the milestone of successful explosions in three dimensions [144]. However, due to the difficulties in modeling such complex environments, the treatment of neutrino transport in CCSNe is approximate, and neutrino flavor conversion is usually performed in the post-processing stage. As far as the MSW resonances and slow collective conversions are concerned, such an approach is adequate because these phenomena occur beyond the shock. However, fast flavor conversion could occur in the vicinity of the neutrinospheres [130], with possible essential consequences for the explosion dynamics and the neutrino burst.

3.2 FAST PAIRWISE CONVERSION IN CORE-COLLAPSE SUPERNOVAE

The presence of angular crossings in the ELN distribution of neutrinos is critical for the development of fast flavor conversions [128–130], as described in Sec. 2.2.7.2. Such ELN crossings can

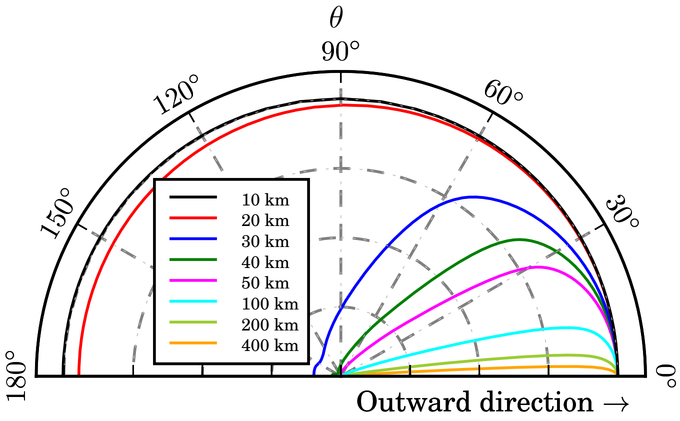

Figure 20: Radial variation of the spectral intensity of $\bar{\nu}_e$. This corresponds to a snapshot at 280 ms after bounce of a $15M\odot$ model as a function of the polar angle θ. Here, $\theta = 0$ corresponds to the local radial direction. The distribution of $\bar{\nu}_e$ is nearly isotropic at a few kilometers from the SN core, and it narrows in the forward direction as the radial distance increases. Image taken from Ref. [146].

lead to the development of flavor instabilities with fast growth rates proportional to the neutrino self-interaction strength μ. Furthermore, fast pairwise conversion of neutrinos can affect the physics of CCSNe given the fast timescale on which they operate. Due to the many possible implications, recent works have focused on understanding whether favorable conditions for fast flavor conversions exist in the SN environment [87, 124, 145].

3.2.1 *Angular moments approach*

One possible approach is to study the neutrino flavor evolution in terms of its momentum-space angular moments. Such an approach is tempting for two reasons. First, the angular distributions transition gradually from nearly isotropic to narrowly forward-peaked, see, for instance, Fig, 20 for the antineutrino emission as a function of radial distance. The second reason concerns computational implementations of state-of-the-art CCSNe simulations, which only track the lowest-order angular moments, and it is desirable to make neutrino conversion computations compatible with hydrodynamic simulations. As such, angular moments are an interesting tool for examining neutrino flavor conversions.

A homogeneous and mono-energetic (anti)neutrino gas can be represented through the density matrix formalism, i.e., $\rho_{\theta,\phi,t}$ ($\bar{\rho}_{\theta,\phi,t}$) where the subscripts indicate that the density matrix is a function of the polar angle θ, azimuthal angle ϕ, time t. Moreover, we have omitted the energy dependence since we intend to focus on fast pairwise conversion ($\mu \gg \omega$). In the two-flavor approximation, the (anti)neutrino density matrices are 2×2 Hermitian matrices (Sec. 2.2.4).

Under the assumption that neutrino interactions with the (isotropic) matter background and vacuum mixing have a negligible role in triggering fast pairwise conversion (see Refs. [147, 148] for detailed discussions on the topic), the EOMs for neutrinos and antineutrinos are entirely described by $H_{\nu\nu}$ (Eq. 2.63). We also neglect neutrino advection and collisions for simplicity, but we refer the reader to Refs. [149–153] for dedicated work on the implications of the physics of fast pairwise conversion.

The self-interaction Hamiltonian, which couples the evolution of neutrinos emitted along different directions (Eq. 2.63) can be written explicitly in spherical coordinates

$$H_{\nu\nu} = \mu \int d\Omega' g_{\theta'\phi'}(1 - c_\theta c_{\theta'} - s_\theta s_{\theta'} c_\phi c_{\phi'} - s_\theta s_{\theta'} s_\phi s_{\phi'}), \tag{3.6}$$

where μ is the self-interaction strength. The symbols c_θ and c_ϕ (s_θ and s_ϕ) stand for $\cos\theta$ and $\cos\phi$ ($\sin\theta$ and $\sin\phi$). Moreover, we have defined $g_{\theta\phi} = (\rho_{\theta\phi} - \bar{\rho}_{\theta\phi})$, which represents the neutrino lepton number density at (θ, ϕ), and the solid angle $d\Omega = d\phi dc_\theta$.

The angular dependence of (anti)neutrinos can be expressed in a basis of our convenience. The density matrix can be expanded, for instance, in spherical harmonics

$$\rho_{\theta\phi} = \sum_{l,m} \rho_l^m Y_l^m(\theta, \phi) \ , \tag{3.7}$$

ρ_l^m being suitable coefficients with $l = 0, 1, .., \infty$ and $m = -l, ..., l$. Reciprocally, one finds the coefficients ρ_l^m by computing

$$\rho_l^m = \int d\Omega Y_l^{*m}(\theta, \phi) \rho_{\theta\phi} \ , \tag{3.8}$$

where $Y_l^{*m}(\theta, \phi)$ is the complex conjugate of the spherical harmonics which, in turn, is a function of the associate Legendre polynomials $P_l^m(\cos\theta)$.

It is useful to introduce the matrices of particle densities (sum S) and the ones of lepton number densities (difference D) [154],

$$S_{\theta\phi} = \rho_{\theta\phi} + \bar{\rho}_{\theta\phi} \text{ and } D_{\theta\phi} = \rho_{\theta\phi} - \bar{\rho}_{\theta\phi} \ . \tag{3.9}$$

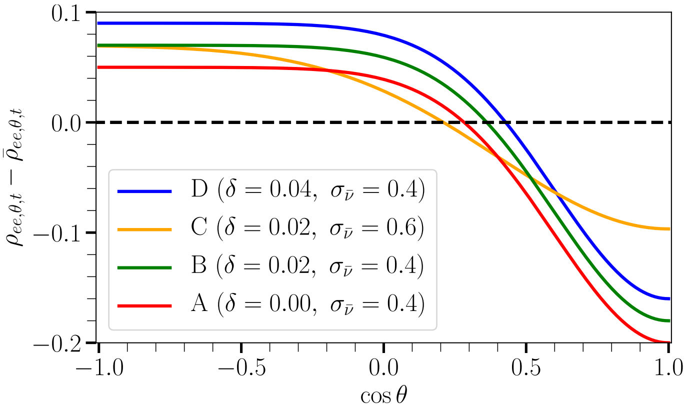

Figure 21: Representative initial distributions $g_\theta = (\rho_{ee,\theta,t} - \bar{\rho}_{ee,\theta,t})$ as functions of $\cos\theta$. For illustration, the angular distributions are parametrized as follows: $\rho_{ee,\theta,t=0} = 0.5$ and $\bar{\rho}_{ee,\theta,t=0} = 0.45 - \delta + 0.1/\sigma_{\bar{\nu}} \exp\left[-(\cos\theta - 1)^2/2\sigma_{\bar{\nu}}^2\right]$. The parameters δ and $\sigma_{\bar{\nu}}$ control the shape of the angular distributions. This choice of parametrization is motivated to mimic the angular distributions expected in SN environments as in Fig. 20. The dashed black line indicates $g_\theta = 0$ to guide the eye and show where ELN angular crossings occur.

By employing the formalism of the polarization vectors (Sec. 2.2.6) and expanding the equations of motion in multipoles as in Eq. 3.7, one obtains the equations that describe the evolution of the multipole vectors $\boldsymbol{S}_l^m$ and $\boldsymbol{D}_l^m$:

$$\begin{aligned}
\dot{\boldsymbol{S}}_l^m &= 2\sqrt{\pi}\mu\boldsymbol{D}_0^0 \times \boldsymbol{S}_l^m - 2\sqrt{\frac{\pi}{3}}\mu\boldsymbol{D}_1^0 \times \left(a_{l,l+1}^{m,m}\boldsymbol{S}_{l+1}^m + b_{l,l-1}^{m,m}\boldsymbol{S}_{l-1}^m\right) \\
&- 2\sqrt{\frac{2\pi}{3}}\mu\boldsymbol{D}_1^1 \times \left(c_{l,l+1}^{m,m+1}\boldsymbol{S}_{l+1}^{m+1} + d_{l,l-1}^{m,m+1}\boldsymbol{S}_{l-1}^{m+1}\right) \\
&- 2\sqrt{\frac{2\pi}{3}}\mu\boldsymbol{D}_1^{-1} \times \left(c_{l,l+1}^{m,m-1}\boldsymbol{S}_{l+1}^{m-1} + d_{l,l-1}^{m,m-1}\boldsymbol{S}_{l-1}^{m-1}\right), \qquad (3.10) \\
\dot{\boldsymbol{D}}_l^m &= 2\sqrt{\pi}\mu\boldsymbol{D}_0^0 \times \boldsymbol{D}_l^m - 2\sqrt{\frac{\pi}{3}}\mu\boldsymbol{D}_1^0 \times \left(a_{l,l+1}^{m,m}\boldsymbol{D}_{l+1}^m + b_{l,l-1}^{m,m}\boldsymbol{D}_{l-1}^m\right) \\
&- 2\sqrt{\frac{2\pi}{3}}\mu\boldsymbol{D}_1^1 \times \left(c_{l,l+1}^{m,m+1}\boldsymbol{D}_{l+1}^{m+1} + d_{l,l-1}^{m,m+1}\boldsymbol{D}_{l-1}^{m+1}\right) \\
&- 2\sqrt{\frac{2\pi}{3}}\mu\boldsymbol{D}_1^{-1} \times \left(c_{l,l+1}^{m,m-1}\boldsymbol{D}_{l+1}^{m-1} + d_{l,l-1}^{m,m-1}\boldsymbol{D}_{l-1}^{m-1}\right). \qquad (3.11)
\end{aligned}$$

For clarity, we do not show the explicit dependence of the coefficients a, b, c and d on the indices l and m. Interestingly, the evolution of $\boldsymbol{D}_l^m$ does not only depend on $l \pm 1$ but also $m \pm 1$, but it is completely independent of $\boldsymbol{S}_l^m$ (unless the vacuum term is included in the Hamiltonian).

From Eq. 3.11, we also derive that the monopole ($l = 0, m = 0$) is a conserved quantity:

$$\dot{\boldsymbol{D}}_0^0 = \boldsymbol{0}\,. \qquad (3.12)$$

This reflects that fast pairwise conversion conserves the neutrino lepton number even in the case of non-azimuthally symmetric equations of motion. However, the norm of the dipole vector ($l = 1, m = 0$) is not an invariant of motion:

$$\frac{\partial}{\partial t}|\boldsymbol{D}_1^0|^2 = 4\sqrt{\frac{\pi}{15}}\mu(\boldsymbol{D}_1^1 \times \boldsymbol{D}_2^2) \cdot \boldsymbol{D}_1^0 - 4\sqrt{\frac{\pi}{15}}\mu(\boldsymbol{D}_1^{-1} \times \boldsymbol{D}_2^0) \cdot \boldsymbol{D}_1^0 \,. \tag{3.13}$$

From the above, it is straightforward to observe that an azimuthally symmetric system ($m = 0$) is more constrained than a non-azimuthally symmetric one ($m \neq 0$), allowing for additional conservation laws [154, 155]; in the following, we focus on the simpler scenario with $m = 0$ for the sake of simplicity.

Under the assumption of azimuthal symmetry, Eqs. 3.10 and 3.11 become functions of the Legendre polynomials:

$$\dot{\boldsymbol{S}}_l = \mu\boldsymbol{D}_0 \times \boldsymbol{S}_l - \frac{\mu}{2}\boldsymbol{D}_1 \times (a_l\boldsymbol{S}_{l-1} + b_l\boldsymbol{S}_{l+1}) \,, \tag{3.14}$$

$$\dot{\boldsymbol{D}}_l = \mu\boldsymbol{D}_0 \times \boldsymbol{D}_l - \frac{\mu}{2}\boldsymbol{D}_1 \times (a_l\boldsymbol{D}_{l-1} + b_l\boldsymbol{D}_{l+1}) \,, \tag{3.15}$$

where $a_l = 2l/(2l+1)$ and $b_l = 2(l+1)/(2l+1)$. As in the $m \neq 0$ case, the monopole vector is an invariant of motion ($\dot{\boldsymbol{D}}_0 = \boldsymbol{0}$) in addition, the norm of the dipole $|\boldsymbol{D}_1|$ is also a conserved quantity:

$$\frac{\partial}{\partial t}|\boldsymbol{D}_1|^2 = \boldsymbol{0} \,. \tag{3.16}$$

Although the final flavor outcome requires fine-grained information about the emission properties of neutrinos [156], coarse-grained information (i.e., a few multipoles) maybe can shed light on the existence of flavor instabilities. In the following, we explore the latter option and comment on the implications of such an approach.

To better grasp the neutrino flavor dynamics, working in a co-moving frame rotating around the monopole at frequency μD_0 is useful. Equations 3.14 and 3.15 in the co-rotating frame become

$$\dot{\boldsymbol{S}}'_l = -\frac{\mu}{2}\boldsymbol{D}'_1 \times (a_l\boldsymbol{S}'_{l-1} + b_l\boldsymbol{S}'_{l+1}) \,, \tag{3.17}$$

$$\dot{\boldsymbol{D}}'_l = -\frac{\mu}{2}\boldsymbol{D}'_1 \times (a_l\boldsymbol{D}'_{l-1} + b_l\boldsymbol{D}'_{l+1}) \,, \tag{3.18}$$

where primed quantities are defined in the co-rotating frame. Since the z-component of $\boldsymbol{D}_{0,t=0}$ in Cartesian coordinates is the only one different from zero and $\dot{\boldsymbol{D}}_0 = 0$, the transformation to the comoving frame leaves the z-components unchanged.

For a given set of initial conditions for our (anti)neutrino ensemble, we can extract the multipoles of $\boldsymbol{D}'$:

$$\boldsymbol{D}'_{l,t=0} = \left(0, 0, \int_{-1}^{1} d\cos\theta P_l(\cos\theta) g_\theta\right), \tag{3.19}$$

where $g_\theta = (\rho_{ee,\theta,t=0} - \bar{\rho}_{ee,\theta,t=0})$ and $P_l(\cos\theta)$ are the Legendre polynomials. For simplicity, we assume that at $t = 0$ only the electron flavors populate the (anti)neutrino ensemble, i.e. $\rho_{xx,\theta,t=0} = \bar{\rho}_{xx,\theta,t=0} = 0$. In this notation, the initial ELN and ELN flux are $D_{l,z,t=0}$ for $l = 0$ and $l = 1$ respectively, where z indicates the third vector component in the Cartesian coordinate system (x, y, z).

The multipole expansion prescription presented in this Section accounts for the flavor dynamics when low-order multipoles are included but remains agnostic of the influence of higher-order ℓ terms. Possibly, the stability criteria that include higher-l moments can be taken into account with some clever manipulation of the multipole equations; however, it has not been shown in the literature, and a stability criterion for high-order terms remains to be found. Such an approach suggests that the multipole expansion of the equations of motion and the truncation involved in the procedure are not very convenient when describing neutrino fast flavor conversion in dense astrophysical environments like CCSNe.

3.2.2 *Overview: recent developments*

The linear stability analysis provides a first diagnosis of the role of fast flavor conversions (Sec. 2.2.7.3). In particular, a dispersion-relation version of the linear stability analysis [133] has presented a novel method to identify unstable solutions. Further works have implemented this dispersion-relation approach and classified the different kinds of instabilities [157–159], showing that two types of instabilities can arise: convective and absolute instabilities [160, 161]. The former is an instability that moves away faster than it spreads, while the latter is an instability that grows locally. Core-collapse supernovae are believed to host absolute instabilities. This has been demonstrated for a simplified neutrino gas model [160], and more recent works have diagnosed and classified ELN crossings in more than a dozen CCSNe models [162].

New insights have also been put forward using analytical approaches under spatial homogeneity and azimuthal symmetry [155, 163, 164]. Under these assumptions, one deals with the most straightforward system that exhibits fast flavor conversion and is analytically tractable to some extent.

For instance, using a four-beam (four angular modes) toy model, the conversion dynamics can be understood as a particle rolling down a quartic potential in the presence of an "external magnetic field" if initially there is a neutrino-antineutrino asymmetry [163]. Although simplified, this work provides insights into the dependence of the fast flavor dynamics on the angular distribution of the beams in the limit $\mu \gg \omega$. Another analytical interpretation of the EOMs (although misleading) is the "pendulum" in flavor space constructed from the lowest-order moments of the neutrino distributions [155], which has little predictive power due to their high-order multipole truncation scheme (Sec. 3.2.1), leading to spurious artifacts when small angular scale errors propagate back to larger scales [156]. More formally, it has been shown that the correct interpretation of the flavor pendulum is the one presented in Ref. [164] which assumes no truncation and is thoroughly discussed in Chapter 5.

In more complicated scenarios, the linear stability analysis has been implemented on data from hydrodynamic CCSNe simulations to predict whether favorable conditions for fast flavor instabilities exist, see, for instance, some of the first works that pursued that goal [146, 165]. One of the present challenges, however, is that hydrodynamic simulations do not provide the angular distributions of neutrinos as such but only their lowest-order angular moments, which means that our knowledge of the neutrino angular distribution is minimal. A wide variety of methods [162, 166–169] have been suggested to assess the existence of flavor instabilities using the lowest-order moments provided by simulations. Such works provide methods to reconstruct the angular distributions of neutrinos and propose simple searches of ELN angular crossings. However, leaving aside the uncertainties intrinsic to the particular methods, even if an angular ELN crossing is identified, this does not mean flavor conversion occurs.

The search for ELN crossings has been prevalent in the literature, and works have reported their existence in different regions of the supernova. For instance, flavor unstable conditions have been found in the proto-neutron star due to the strong convective activity in three dimensions [170–172], however, the possible consequences for the SN dynamics and neutrino observations are unsettled. In the neutrino decoupling regions, ELN crossings are expected due to the later decoupling of ν_e to that of $\bar{\nu}_e$ [173, 174]. Thus, the angular distributions of $\bar{\nu}_e$ would be more forward-peak than that of ν_e. After decoupling, in the free-streaming regime (scattering-induced) ELN crossings can form by neutrino backward scatterings off heavy nuclei [175–177], hinting towards the existence of ELN crossings in both the pre-shock and post-shock regions. The impact of ELN crossings in the pre-shock and post-shock regions is still unclear, although there are claims on the minimal impact of ELN crossings in the pre-shock region based on slow growth rates [178, 179].

Another popular approach is the direct numerical simulation of the flavor evolution of neutrinos within simplified frameworks. A direct numerical solution models the flavor evolution described by the neutrino EOMs (Eq. 2.74). In this case, the final flavor outcome can be directly obtained by the evolution of the equations as a function of different initial ELN configurations. However, whether fast flavor conversion leads to flavor equilibration (as allowed by total lepton number conservation) remains unsettled.

Ultimately, the various terms in the equations of motion of neutrinos need to be implemented under different conditions to quantify their impact on the flavor dynamics. For instance, the evolution of the neutrino field evolves simultaneously in time and space, and even if a system has an ELN crossing at the beginning and develops flavor instabilities, the spatial propagation can smear out or cancel the crossing [149]; the interplay between advection and fast flavor conversion will be covered in detail as part of this thesis in Chapter 7. Related work has investigated the role of the advective term, mimicking a 1D system with periodic boundary conditions, and reported the development of small scale structure leading to flavor decoherence [180]. In connection with these works, also the development of fast flavor conversion has been investigated in 3D (however, using a particle-in-cell framework [181]) to cross-check the validity of lower-dimensional computations and the assumptions of symmetries in the EOMs [182].

As in the case of slow collective conversions, the non-linear flavor dynamics spontaneously breaks the symmetries imposed by the initial conditions [183], with the possibility of flavor mixing not occurring in the vicinity of the ELN angular crossing as it spreads through all angular modes. This puts in question the assumption of axial symmetry, for instance. Another common simplification is to assume that the energy dependence of the flavor dynamics plays a negligible role, motivated by the substantial neutrino densities. However, the non-linear regime can be affected by the vacuum oscillation frequency and, therefore, the neutrino energy [147].

Another active research topic is the interplay between fast flavor conversions and inelastic collisions with the matter background. Such numerical simulations are motivated by the fact that favorable conditions for fast flavor conversions could take place in regions where neutrinos are partially or entirely trapped in the decoupling regions. On the one hand, collisions could enhance flavor conversions as the system is evolved in time [150, 184], while on the other hand, if the system is evolved in both space and time, collisions might suppress (or at least delay) fast flavor conversions [152, 185]. Another common assumption when exploring the phenomenology of fast flavor conversions is to implement initial single-crossed ELN distributions, as motivated by supernova simulations [146]. Although this is a good approximation, scenarios with multiple crossings in the ELN distributions have been proposed [186]; however, it is not clear under which conditions multiple crossings could emerge.

In the context of the number of neutrino families, it is typically assumed that there are only two flavors of (anti)neutrinos (ν_e, ν_x) motivated by the fact that heavy-lepton neutrinos decouple at the same time and have the roughly the same energies. However, fast flavor instabilities can arise in one or more of the three channels $e\mu, e\tau, \mu\tau$ [187]. Even more, in the three-flavor framework, when ELN angular distributions in the μ and τ sector are equal, the flavor outcome departs from what was observed in the two-flavor framework [148], putting in question the validity of assuming the two-flavor scheme.

4

NEUTRINOS IN COMPACT BINARY MERGER REMNANTS

Neutron stars (NS) are among the densest form of matter in the Universe. The mergers of two neutron stars are thus one of the most mesmerizing events in the cosmos, with significant scientific potential spanning many domains across physics. For instance, by understanding the inner workings of NS mergers, one could uncover the physics behind interactions at supra-nuclear densities and the equation of state in dense environments, new insights into the strong-gravity regime only feasible in the vicinity of compact objects, high-energy astrophysical sources like gamma-ray bursts (GRB), the origin and synthesis of elements heavier than iron [188–190].

In the following years, multimessenger astrophysics will most likely result in multiple detections from different classes of sources [191]. Binary Neutron Star (BNS) and Neutron Star Black Hole (NSBH) mergers, or simply NS mergers to refer to both classes here, will play a crucial role in understanding the fundamental properties of our Universe and its constituents [188].

The disk that forms around the hyper-massive NS (or BH) after the merger of two compact objects is incredibly neutrino-dense. Many neutrinos are produced in this extreme environment during the post-merging phase. Order of magnitude, the total neutrino energy luminosity ascends to a maximum value of $\sim 10^{53} - 10^{54}$ erg/s for ~ 100 ms of which $90 - 95\%$ stem from the toroidal gas cloud around the central compact object [46, 47, 50]. The neutrino emission features are qualitatively very similar to those from CCSNe, except for the $\bar{\nu}_e$ luminosity from neutron star mergers which is a factor $3 - 6$ higher than the luminosities of ν_e and ν_x due to the neutron-rich environment; see for instance Figs. 3 and 4 of Ref. [46]. One can compare this with the neutrino burst in CCSNe (Sec. 3.1), where the largest neutrino luminosity is the one for ν_e and orders of magnitude larger than the other neutrino species; see, for instance, Figs. 5 and 37 in Ref. [88].

Compact binary mergers are ideal sites for neutrino self-interactions (Sec. 2.2.5) given the extreme densities. A key aspect that makes mergers interesting for neutrino conversions is the excess of $\bar{\nu}_e$ over ν_e due to the protonization of the neutron-rich matter. Due to this natural $\bar{\nu}_e$ excess, there are various phenomenological implications. One consequence of this $\bar{\nu}_e$ excess, are the matter-neutrino resonances (Sec. 4.2), which are expected to occur above the disk of the merger [192–195] and can lead to enhanced flavor transformations in a similar fashion as the MSW effect (Sec. 2.2.2).

Another interesting consequence is the ubiquity of ELN angular crossings in the accretion disk and, therefore, the possibility of flavor instabilities in such region [196]. As in the case of CCSNe, ν_e decouple later than $\bar{\nu}_e$, which means that the decoupling region for ν_e is larger to that of $\bar{\nu}_e$. On the other hand, there is the overall excess of $\bar{\nu}_e$. These two components allow for ELN crossings in the region above the disk of the merger where the local neutrino emission favors either ν_e or $\bar{\nu}_e$ depending on the specific location above the disk.

This section introduces the essential tools to comprehend neutron star mergers, their dynamics, expected observable signatures, and how neutrinos affect these. We then present recent works on neutrino flavor conversion in compact binary merger remnants.

4.1 COMPACT BINARY MERGERS IN A NUTSHELL

Binary neutron stars can radiate gravitational waves fast enough to make the objects inspiral and merge within the age of the universe ($\sim 13.8 \times 10^9$ yr). The merger of NS is followed by a strong emission of GW, a broad range of electromagnetic (EM) signals over the whole spectrum (from gamma-rays to radio signals), and neutrino signatures. In particular, high-energy neutrinos are produced in the short GRB associated with the merger [42], while thermal neutrinos of $\mathcal{O}(10)$ MeV are produced during the merger phase [46, 197–199]. For the work relevant to this thesis, we are interested in the latter type of neutrino emission.

In what follows, we briefly describe the stages of the evolution of NS mergers, which are illustrated in Fig. 22 in chronological order starting from the inspiral phase up to the kilonova emission.

SYSTEM FORMATION The interesting events are the BNS and NSBH systems that originate and merge within the age of the universe [201]. The relevant time scale is the merging time scale

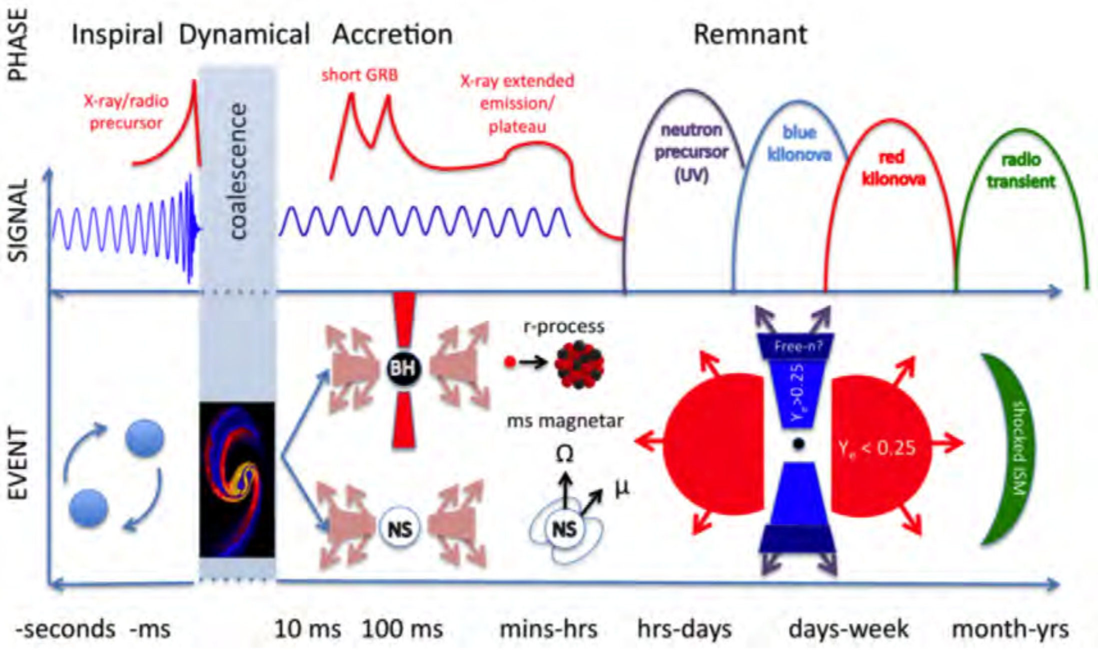

Figure 22: Phases of a neutron star merger as a function of time, displaying the related observational signatures and physical phenomena. Image taken from Ref. [200].

t_{merger}, which is given in terms of the orbital separation radius R for two objects inspiraling via GW emission is [188]

$$\begin{aligned} t_{\text{merge}}(r) &= \frac{5}{256}\frac{c^5}{G^3}\frac{R^4}{M_1 M_2 (M_1 + M_2)} \\ &\approx 54\,\text{Myr}\left(\frac{1}{q(1+q)}\right)\left(\frac{R}{R_\odot}\right)^4\left(\frac{1.4M_\odot}{M_1}\right)^3, \end{aligned} \tag{4.1}$$

where M_1, M_2 are the masses of the objects and the mass ratio $q = M_2/M_1$, and where Eq. 4.1 adopts circular orbits as compact binary systems circularize fast in comparison with their total inspiral time [189]. It is clear that depending on the masses and the separation of the individual objects, the merger may or may not merge within the age of the universe.

A star with a mass $\sim 8 - 10 M_\odot$ will end as a CCSNe (Chapter 3). Stars close to the lower end of the range will form a NS, and the ones in the high end will form a BH [202]. These heavy stars become supergiants near the end of their stellar evolution with radii $R \gtrsim 30 R_\odot$. If two of such stars form and are already in a binary system, they can result in compact binaries once both go supernova. Nevertheless, for BNS with separations larger than the progenitor supergiant, GW alone cannot make the objects merge since t_{merger} is a thousand times larger than the age of the universe. For BNS to merge within this time via GW emission exclusively, they must have an initial separation of $\lesssim 5M_\odot$ which requires a *common envelope stage*. The common envelope stage accelerates the inspiral and provides a smaller separation between compact objects.

INSPIRAL After the formation of the BNS or NSBH system, the two objects will lose energy via the emission of GWs, resulting in the inspiral of both objects towards one another. Two important regimes can be observed individually. The first regime is long before the merger when GW emission is weak, and the orbital evolution is slow. The second regime is close to the merger time when the GW emission is powerful and the orbital evolution accelerates. The inspiral long before the merger is better studied using EM observations of galactic BNS systems [203]. The inspiral times of BNS range from ~ 85 Myr to values larger than a Hubble time.

The first time that the orbital decay of a compact binary system was studied and measured was when the Hulse-Taylor binary system was discovered [204], allowing for the first confirmation of the existence of GW radiation [205]. These systems spend a tiny fraction of their lives in the late inspiral phase, which ranges from hours to minutes before the merger, as seen in Fig. 22. We are unlikely to observe NS binaries because the estimated merger rate in current and forthcoming neutrino detectors is low [201, 206]. BNS and NSBH systems far away are nearly undetectable using photons during the early inspiral stage. In the last seconds before the merger, there is a possibility of detecting EM emissions from nearby sources. The most robust evidence is the claim of precursor activity prior to short GRB emission [207], but this remains unsettled.

GW observations of compact object inspiral offer a new window to study these systems in the late inspiral stage. As the objects approach the merger time, where the orbital radius is comparable to NSs radii, the GW signal enters the ground-based interferometers range.

MERGER The energy loss via GWs decreases the orbital separation, increasing the orbital frequency and enhancing the GW emission. The frequency evolution is known as the *compact binary coalescence* chirp signal. Close the merger time, the peak GW luminosity is 10^{56} erg/s [208, 209]. During the merger, the NS is disrupted, launching material to the surroundings, which can power ultra-relativistic jets and mildly relativistic quasi-isotropic outflows that generate the known EM and expected neutrino components.

The remnant can launch matter through tidal tails that become spiral arms, which eject matter along the equatorial direction. This *dynamical ejecta* is launched within milliseconds of the merger. After the merger, more matter is ejected after the dynamical phase and continues for ~ 10 s. This is referred to as *wind ejecta* or *post-merger ejecta*. The physical mechanisms for the origin of disk winds could be many, for instance, due to magnetic fields [210], viscous heating and nuclear combination dominating over neutrino cooling [211], and NS remnants which can host neutrino winds [212].

The ejecta (unbound material) is characterized by its mass, average velocity, and electron fraction $Y_e = n_p/(n_n + n_p)$ where n_n, n_p are the number densities of neutrons and protons, respectively. The wind, however, can modify these quantities by heating the outflows, changing the total mass of the ejecta, or altering Y_e through neutrino charged-current interactions

$$p + e^- \quad \longleftrightarrow \quad \nu_e + n \, , \tag{4.2}$$

$$n + e^+ \quad \longleftrightarrow \quad \bar{\nu}_e + p \, . \tag{4.3}$$

Since the initial number density of neutrons is much larger than that of protons (small Y_e), neutrino charge-current interactions will drive Y_e to higher values until equilibration is reached. The thermal neutrinos come from the accretion disk or in pair interactions in the vicinity of the remnant NS (if one is present)

$$e^+ + e^- \longleftrightarrow \nu + \bar{\nu} \, . \tag{4.4}$$

It is worth noting that due to the larger neutron number density, the neutrino emission from the remnant is characterized by an excess of $\bar{\nu}_e$ over ν_e due to the charged-current interactions (Eq. 4.2) taking place in the wind. In CCSNe one find the opposite scenario where instead excess of ν_e over $\bar{\nu}_e$ is present.

JETS The bound material accretes onto the remnant compact object. In some cases, this accretion results in a highly collimated, ultra-relativistic jet that gives rise to a short GRB, as observed with GW170817 and GRB170817A. However, the mechanism powering short GRBs is still poorly understood, and only phenomenological arguments are available at this point [200].

The jets that form in BNS mergers have huge kinetic energies, and some of the most luminous EM events with approximately 10^{50} erg [213]. They are powered by the accretion disks [214] which have a mass between $10^{-4} - 0.3 M_\odot$ as guided by numerical simulations. The ideal effective conversion of $0.1 M_\odot$ of matter into energy gives $0.1 M_\odot c^2 \approx 10^{53}$ erg which is enough to power short GRB. How exactly this energy budget is transformed into the jet is unsettled. However, it is consensus that this enormous amount of energy from accreting matter is deposited in the polar regions near the compact object, which launches an ultra-relativistic fireball along the polar axis in the outward direction. The outflow is collimated into a jet by the accretion disk and magnetic fields. The jet opening angle is $1/\Gamma$ due to Doppler beaming, where Γ is the bulk Lorentz factor ($\Gamma \sim 100$).

QUASI-ISOTROPIC OUTFLOWS The ejecta evolves very differently than the bound material which powers the jet [200]. The ejecta is neutron-rich with a mass of $\sim 10^{-3} - 0.1 M_\odot$ with velocities $\sim 0.1 - 0.3c$ in the outward direction. As the ejecta expands and releases energy through thermal neutrinos, it rapidly cools and starts a slow homologous expansion in $\sim 10 - 100$ ms.

At $T \lesssim 10^{10}$ K free nuclei combines into α particles. The ejecta keeps cooling and at $T \lesssim 5 \times 10^9$ K the α-process forms seed nuclei with $A \sim 90 - 120$ and $Z \sim 35$ [215]. The neutron-to-seed ratio allows rapid neutron captures at a much faster rate than the β decay of the seeds synthesizing heavy elements: this is the so-called *r-process* that provides half of the elements heavier than iron. Rapid neutron captures continue to build heavier nuclei until $A \gtrsim 250$ is achieved. At this point, fission splits the atoms and then pushes them to higher atomic masses through *fission recycling*. This process results in peaks near the closed shell numbers $A = 82, 130, 196$ as observed in the solar abundances.

After a few seconds, the heavy nuclei radioactively decay, copiously producing neutrinos ($\sim 0.1 - 10$ MeV), nuclear gamma-rays (keV $-$ MeV), and elements that eventually end up falling in the line of stability [216]. At early times, the ejecta is opaque to photons, and as a result, most of the energy is released in the form of neutrinos. In kilonova models, the first photons to escape are the nuclear gamma-rays. At this point, neutrinos escape with $\sim 30 - 40\%$ of the energy, while gamma-rays take $20 - 50\%$ of it, significantly decreasing the remaining energy of the system before reaching peak luminosity [217]

As time passes, the ejecta loses energy through neutrinos and gamma rays, cools, and expands until photons in the UVOIR[1] (Ultraviolet, Optical, and Infrared) range can escape, which results in a transient called *kilonova*. Ejecta with somewhat high initial electron fraction $Y_e \gtrsim 0.3$ produces lanthanide-free material which gives rise to a *blue kilonova* (peak luminosity ~ 1 day) [49]. On the other hand, ejecta with low electron fraction $Y_e \lesssim 0.3$ makes lanthanide-rich material (and maybe actinides) that produces a *red kilonova* (peak luminosity ~ 1 week) [218]. The blue and red components of the kilonova are schematically represented in Fig. 22.

AFTERMATH In a matter of years, the event transitions to the nebular phase. Over thousands of years, a kilonova remnant (KNR) is formed. These have a shock wave and surrounding material, similar to supernova remnants but with lower total kinetic energies. Even long after the merger event, they remain radioactive with decaying isotopes that have half-lives of a similar order of magnitude to the age of the remnant [219, 220]. Eventually, the kinetic energy will be spent, and the shock will dissipate. The ejecta will become part of the diffuse galactic material, which is later circulated throughout the galaxy [219].

4.2 MATTER-NEUTRINO RESONANCE IN NEUTRON STAR MERGER REMNANTS

Neutron star merger remnants can experience *matter-neutrino resonance* (MNR) transitions, first found in Ref. [221], which occurs when the matter and neutrino-neutrino potentials cross each other. The latter is only possible in merger remnants because of the overabundance of $\bar{\nu}_e$. The MNR transition effect is different from the bipolar (nutation) conversion (Sec. 2.2.7.1) and can occur nearer to the neutrino decoupling regions for both mass neutrino hierarchies [222]. While the MNR is at play, neutrinos stay "on-resonance," i.e., neutrino flavor evolves in such a way that all entries of the Hamiltonian are almost vanishing [192]. The MNR transformation effect requires a matter potential $H_{\rm mat}$ (Sec. 2.2.2) and a neutrino-neutrino potential $H_{\nu\nu}$ (Sec. 2.2.5) of *opposite* sign and more or less the same magnitude. Neutron star merger remnants are excellent sites for MNR because they either 1) supply a natural excess of $\bar{\nu}_e$ over ν_e (neutron-rich medium) or 2)

---

[1] The UVOIR is the main frequency range for the observation of kilonovae.

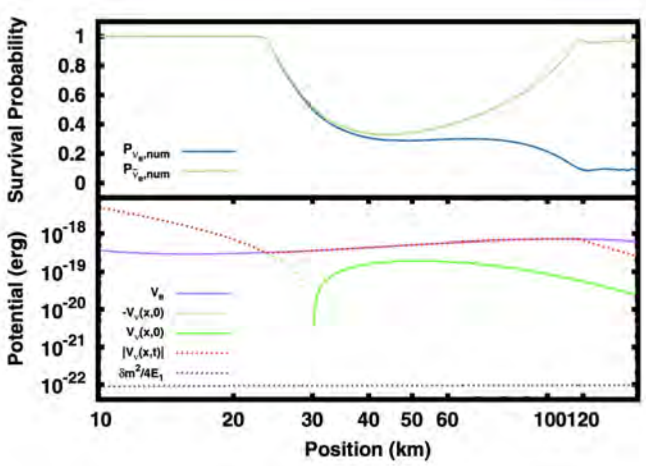

Figure 23: Results for the neutrino trajectory 1: Numerical solution of the survival probability (solid) as a function of position. Moreover, one can use unoscillated quantities to calculate the predicted survival probability [192, 224] due to MNR transitions, as shown in the dashed line. The beginning of the MNR transitions can be seen around 24 km at which point the survival probability declines significantly until the MNR transition ends. Image adapted from Ref. [222].

their geometry changes the contributions from neutrinos and antineutrinos to the self-interaction potential as they travel. It is worth noting that one would not anticipate MNR to emerge in CCSNe (Sec. 3.1) because both $H_{\nu\nu}$ and H_{mat} have the same sign; however for a counterexample see Ref. [78].

One can identify two types of MNR transitions in merger remnants. One of them, the "standard" MNR transition, can be recognized by a complete conversion of ν_e's to other neutrino species, while $\bar{\nu}_e$ partially convert but then go back to their original flavor content [192]. The standard MNR transition takes place in locations where the neutrino-neutrino potential $H_{\nu\nu}$ starts as the dominant potential in the system but drops in magnitude, ultimately having a comparable magnitude as the matter potential H_{mat}. The other type of MNR transition completely transforms both ν_e and $\bar{\nu}_e$ "symmetrically" and is called the symmetric MNR transition [223]. The latter differs from the standard MNR in that it occurs when the geometry causes the system to transition from a location where $\bar{\nu}$'s dominate the $H_{\nu\nu}$ to a location where ν's dominate it instead [223, 224]. Both classes of MNR transitions could potentially impact nucleosynthesis due to the closeness to the (anti)neutrino decoupling regions [221, 223].

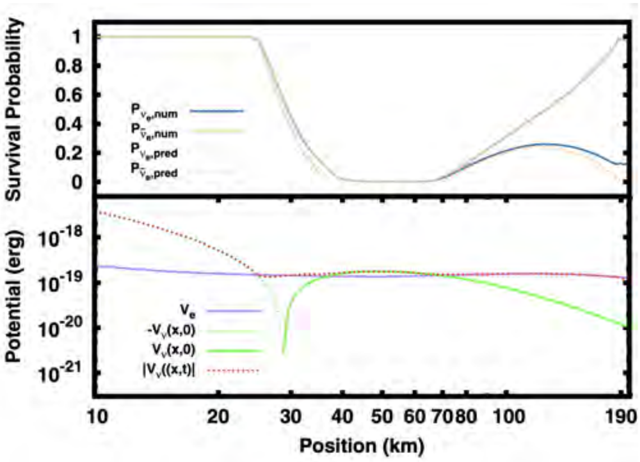

Figure 24: Results for the neutrino trajectory 2: Matter potential V_e (purple), magnitude of oscillated neutrino-neutrino interaction potential $|V_\nu(\vec{x})|$ (dashed red), positive (dashed green) and negative (solid green) unoscillated neutrino-neutrino potential $V_\nu^{\mathrm{un}}(\vec{x})$, and the vacuum oscillation frequency (dashed purple). The beginning of the MNR transitions can be seen around 24 km similar to Fig. 23. Image adapted from Ref. [222].

The work in Ref. [222] concentrates on neutrinos emitted from the massive neutron star. As an illustrative example, one can take the neutrinos emitted from the ~ 10 MeV electron-neutrino decoupling surface (cyan line in Fig. 2 of Ref. [222]) and consider two different neutrino trajectories which are marked by the arrows in the same figure. As neutrinos move along their trajectory, the magnitude of $H_{\nu\nu}$ and H_{mat} will change with distance allowing for MNR transitions. Initially, neutrinos encounter a large negative $H_{\nu\nu}$ due to the surplus of $\bar{\nu}_e$ over ν_e along the funnel (see Fig. 3 of Ref. [222]); these potentials are shown in red dash lines in the lower panels of Figs. 23 and 24. The condition for MNR transitions is at the locations where the diagonal components of $H_{\nu\nu}$ cancel with the diagonal entry of H_{mat}, i.e.

$$V_e(\vec{x}) + V_\nu(\vec{x}) \approx 0, \tag{4.5}$$

where $V_e(\vec{x}) = \sqrt{2} G_F n_e(\vec{x})$, being $n_e(\vec{x})$ the neutrino number density (Eq. 2.23). The quantity $V_\nu(\vec{x})$ is the contribution from the diagonal components of the neutrino-neutrino Hamiltonian

$$V_\nu(\vec{x}) \equiv H_{\nu\nu}^{ee}(\vec{x}) - H_{\nu\nu}^{xx}(\vec{x}) = V_{\nu_e} - V_{\nu_x} - (V_{\bar{\nu}_e} - V_{\bar{\nu}_x}), \tag{4.6}$$

where $H_{\nu\nu}^{\alpha\alpha}$ are the diagonal components of the neutrino-neutrino Hamiltonian with $\alpha = e, x$. Note that Eq. 4.5 does not depend on time, as it uses the unoscillated quantities at the start of the evolution. The location where the MNR condition is fulfilled (Eq. 4.5) is shown in Figs. 23 and 24 and can be identified as the location where the red dashed line, and the purple line in the bottom panels meet around ~ 24 km. This prediction is verified numerically in Fig. 24 since the predicted survival probabilities (orange dashed line in the upper panel of Fig. 24) closely follow the numerical results (solid lines). It is worth noting that during MNR transitions, ν_e and $\bar{\nu}_e$ convert in such a way that they stay "on-resonance," which means that the MNR condition (Eq. 4.5) is fulfilled along a portion of the trajectory. The end of the MNR is marked when Eq. 4.5 is no longer fulfilled, which is visible in the lower panel of Fig. 23 when the red dashed line and the purple line drift apart from each other.

4.3 FAST PAIRWISE CONVERSION IN COMPACT BINARY MERGER REMNANTS

Even though the detection of thermal neutrinos from compact binary merger remnants is unlikely due to a low local merger rate [43], neutrinos can still indirectly influence future merger observations. The evolution of the disk and the formation of the neutrino-driven wind depend on the competition between neutrino absorption and emission. Thus, neutrinos play an essential role in the cooling of the disk and in the production of elements heavier than iron [46–50]. Given the significant role of neutrinos, it is crucial to address neutrino flavor conversions in such dense environments.

4.3.1 *Flavor instabilities: ubiquitous in compact binary merger remnants*

Fast flavor conversion of neutrinos could result in equilibration among neutrino flavors and are driven by the ELN angular distributions. In Chapter 8 we argue that flavor equilibration might be unrealistic in some cases, as the final flavor outcome crucially depends on the particular ELN crossings of the system. Despite the relevance of the angular distributions of neutrinos, they have been typically ignored in most previous studies on neutrino conversions in merger remnants.

As in the case of core-collapse supernovae, the decoupling region of $\bar{\nu}_e$ is located inside the ν_e one in compact binary merger remnants. However, two critical differences concerning the SNe

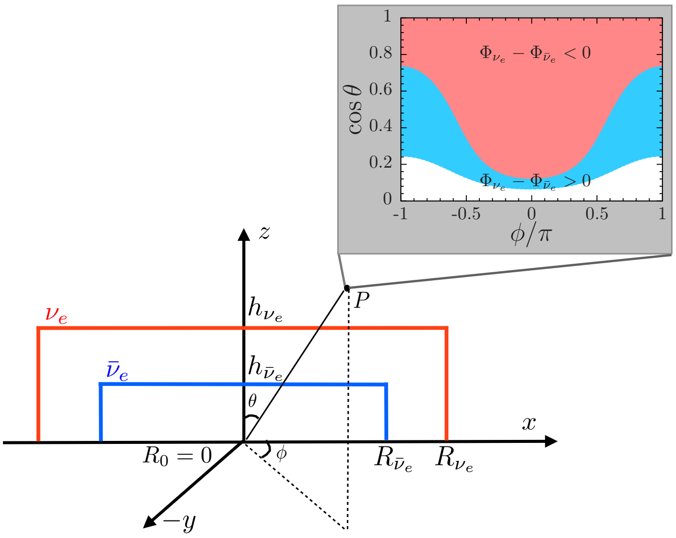

Figure 25: Layout of the two-neutrino disk model implemented in Ref. [196]. The neutrino (red) and antineutrino (blue) emitting surfaces with radii given by R_{ν_e} and $R_{\bar{\nu}_e}$, and heights h_{ν_e} and $h_{\bar{\nu}_e}$, respectively. The radius R_0 is the innermost stable circular orbit for a BH-disk system; therefore, it is $R_0 = 0$ for the NS-disk remnant. The inset shows what an observer at a given (x, z) would see as a function of the polar θ and the azimuthal angle ϕ. The region in red signalizes that $\Phi_{\bar{\nu}_e} - \Phi_{\nu_e} > 0$ while the region in blue that $\Phi_{\bar{\nu}_e} - \Phi_{\nu_e} < 0$. For any value of $\phi =$ const there is a particular θ for which $\Phi_{\bar{\nu}_e} - \Phi_{\nu_e} = 0$ and therefore a crossing exists. Image taken from Ref. [196].

scenario are important. First, the $\bar{\nu}_e$ flux is larger than the one of ν_e due to the protonization of the merger. And second, the decoupling regions of ν_e and $\bar{\nu}_e$ are spatially well separated, and the ratio of their sizes can be as much as 3/4 [47]. This results from the neutron-rich remnant and the extension of the accretion disk, which allows for a smaller density gradient than the supernova proto-neutron star.

The disparity in the (anti)neutrino fluxes and the spatial separation between the decoupling regions lead to angular crossings between the distributions of neutrinos $\Phi_{\nu_e} = dn_{\nu_e}/d\Omega$ and antineutrinos $\Phi_{\bar{\nu}_e} = dn_{\bar{\nu}_e}/d\Omega$, where $d\Omega = d\cos\theta d\phi$ is the differential solid angle. If an angular crossing is present at a given location of the merger, the ELN distribution $\Phi_{\bar{\nu}_e} - \Phi_{\nu_e}$ reverses its sign as a function of the polar θ and the azimuthal angle ϕ i.e. either $\Phi_{\bar{\nu}_e} - \Phi_{\nu_e} > 0$ or $\Phi_{\bar{\nu}_e} - \Phi_{\nu_e} < 0$ for some choice of parameters. Notably, an ELN angular crossing is present at any location above the disk of the remnant, as shown in Fig. 25. This finding hints that ELN crossings are ubiquitous in such environments [196] and deserve to be investigated in dedicated works. The

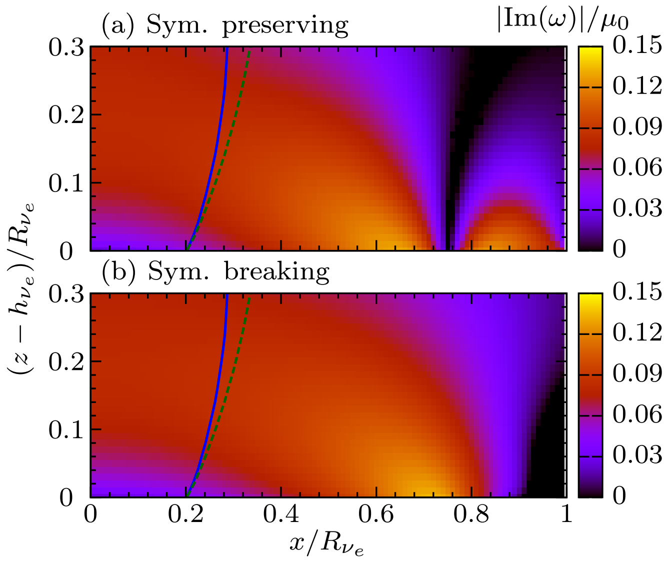

Figure 26: Contour plot of the instability growth rate $|\mathrm{Im}(\omega)|/\mu_0$ as a function of the location (x,z) above the ν_e decoupling region. Solutions that preserve and break the y-axis mirror-symmetry are presented in the upper and lower panels, respectively. The locations where the MNR resonances are expected are shown in solid blue and dashed green, where neutrinos were emitted at $(x,z)=(0,h_{\nu_e})$ and $(x,z)=(-R_{\nu_e},h_{\nu_e})$, respectively, using the number density profiles n_e from Ref. [50] to model the matter potential. Image taken from Ref. [196].

model implemented in Ref. [196] relies on a simple two-neutrino-emitting disk model as shown in Fig. 25, whose specific choice of parameters is motivated by more realistic hydrodynamical simulations of the NS-disk evolution [50].

Finding an ELN crossing is a necessary but not sufficient condition for flavor instabilities, and their existence still needs to be determined. The linear stability analysis (Sec. 2.2.7.3) offers the analytical tools to determine the growth rate of the temporal instabilities above the NS-disk system. As a benchmark value for the neutrino interaction strength, Ref. [196] implements $\mu_0=\mathcal{O}(10^5)\ \mathrm{km}^{-1}$ which is a typical order of magnitude value near the decoupling regions. The results in Fig. 26 show contour plots of the growth rate of instability $|\mathrm{Im}(\omega_0)|$ in units of μ_0 in the (x,z) plane. Since the azimuthal symmetry is broken by including the ϕ-dependence, there are flavor instabilities that preserve the mirror-symmetry with respect to the y-axis (upper panel) and those that do not preserve it (lower panel). However, the symmetry-preserving and symmetry-breaking results are qualitatively very similar: flavor instabilities exist in most regions over the ν_e decoupling surface. Yellow-orange regions are regions that display a large value growth rate, and therefore flavor conversions are expected to occur on a time scale of $0.1\mu_0$ which roughly corresponds to a few nanoseconds; equivalently, since neutrinos travel at the speed of light a few nanoseconds time interval corresponds to conversions occurring on a length scale of a few centimeters. These results motivated the works contained in Part iii where the flavor of neutrinos is evolved in a multi-dimensional fashion in the region above the disk of the remnant.

Moreover, the findings of Ref. [196] suggest a change of paradigm to what concerns MNR transitions (Sec. 4.2) in the remnant environment. Notably, neutrinos emitted from the neutrino decoupling regions will traverse locations prone to develop flavor instabilities before reaching the regions where MNR (see blue and green lines in Fig. 26) are expected. Therefore, the fast flavor instabilities might change the location where the MNR transition occurs.

4.3.2 *Overview: recent developments*

The lessons learned from Ref. [196] (Sec. 4.3.1) motivated dedicated works on the role of neutrino fast flavor conversion in merger remnants, which moved beyond the simplified two-neutrino emitting surfaces model. A conclusive description of the implications of flavor instabilities in merger remnants remains unsettled; however, dedicated works have begun to parametrically study fast flavor instabilities and their impact on the electron-fraction of the disk outflow. Particularly, the works in Refs. [225–232] took a step forward in the modeling of neutrinos in compact binary merger remnants and in assessing the role of neutrino flavor transformations. One of the main findings of some of these works is that the region that could host fast flavor instabilities can shrink within ~ 10 ms as the BH-disk remnants evolves [225], but it is also possible that the flavor unstable region remains constant within the same ~ 10 ms of post-merger evolution [226]. These findings highlight the dynamical nature involved in determining instability regions in merger remnants, which is challenging.

One common simplification is to assume flavor equilibration. A dedicated work presented in this thesis (Sec. 8) models the non-linear regime using a simplified setup of the merger system, showing that flavor equilibration might be too extreme and, in some cases, unrealistic (see also

Ref. [233]). Even more, there is no formal connection between large growth rates and a significant amount of flavor conversion, which is formally demonstrated in another dedicated work of this thesis (Sec. 5). Therefore, it is crucial to cross-check whether flavor equilibration is a reasonable assumption even if large growth rates are present and move beyond the linear stability analysis and the existence of crossings to gauge the final flavor outcome.

Despite the crude simplifications, assuming flavor equilibration can shed light on the maximum possible effect that fast flavor conversion can have on the merger observables. For instance, flavor equilibration can mainly affect the nucleosynthesis in the polar ejecta within $\lesssim 30^\circ$, thereby affecting the abundances in the iron-peak and the first-peak nuclei, but instead leaving the lanthanide mass fraction unaffected [226]. Along the same vein and assuming flavor equilibration, a significant enhancement of nuclei with mass numbers $A > 130$ is possible, together with a change of the lanthanide mass fraction by a factor of 10^3 [225]. A similar approach is followed in Ref. [231], which follows the evolution of a magneto-hydrodynamical simulation of an accretion disk.

Part II

NEW CONCEPTUAL DEVELOPMENTS ON THE PHYSICS OF NEUTRINO FAST FLAVOR CONVERSION

5

THE GYROSCOPIC PENDULUM OF FAST FLAVOR CONVERSION

Based on: **Ian Padilla-Gay**, Irene Tamborra, Georg G. Raffelt, *Neutrino flavor pendulum reloaded: The case of fast pairwise conversion*, Phys. Rev. Lett. 128 (2022) 12, 12, arXiv:2109.14627

ABSTRACT In core-collapse supernovae or compact binary merger remnants, neutrino-neutrino refraction can spawn fast pair conversion of the type $\nu_e\bar{\nu}_e \leftrightarrow \nu_x\bar{\nu}_x$ (with $x = \mu, \tau$), governed by the angle-dependent density matrices of flavor lepton number. In a homogeneous and axially symmetric two-flavor system, all angle modes evolve coherently, and we show that the nonlinear equations of motion are formally equivalent to those of a gyroscopic pendulum. Within this analogy, our main innovation is to identify the elusive characteristic of the lepton-number angle distribution that determines the depth of conversion with the "pendulum spin." The latter is given by the real part of the eigenfrequency resulting from the linear normal-mode analysis of the neutrino system. This simple analogy allows one to predict the depth of flavor conversion without solving the nonlinear evolution equations. Our approach provides a novel diagnostic tool to explore the physics of nonlinear systems.

5.1 INTRODUCTION

In neutrino-dense astrophysical environments, such as core-collapse supernovae and the remnants of neutron star mergers, neutrinos experience a significant potential due to the presence of other neutrinos. This refractive effect strongly impacts the flavor evolution of the neutrino radiation field and can lead to collective flavor conversion. While the underlying equations are simple, their nonlinear nature provides for a rich and sometimes confusing plethora of solutions [82, 87, 88, 132].

One case in point is fast pairwise flavor conversion of the type $\nu_e\bar{\nu}_e \to \nu_x\bar{\nu}_x$ (where x indicates a generic heavy-lepton flavor, μ or τ), conserving the net flavor content and often called "fast flavor conversion (FFC)." Neutrino-neutrino refraction is dimensionally quantified by a typical interaction energy $\mathcal{O}(\sqrt{2}G_\mathrm{F}n_\nu)$. Specifically, we will use $\mu = \sqrt{2}G_\mathrm{F}n_{\nu_e}$ as an overall scale.

Another manifestation of neutrino-neutrino refraction concerns "slow flavor conversion," driven by the energy spectrum and involving flavor exchange between different energy modes. A typical flavor conversion speed is $\sqrt{\omega\mu}$, where $\omega = \Delta m^2/2E$ is the vacuum oscillation frequency depending on the mass-squared difference Δm^2 and energy E. This is defined as "slow" because $\mu \gg \omega$. The interpretation of the nonlinear evolution [89] as a gyroscopic flavor pendulum has been long since established [90, 92, 93, 234, 235] and is the archetype for our study.

Fast flavor conversion is a multi-angle effect of the flavor lepton-number densities. While the nonlinear evolution is a three-flavor problem [98, 100, 102, 103, 148, 187], the initial instability is between one pair of flavors [133, 135, 157, 158], in practice ν_e and ν_x. For identical ν_x and $\bar{\nu}_x$ distributions, FFC is driven by neutrino electron lepton number (ELN) [133, 155, 160, 161, 236], but it is straightforward to include nontrivial ν_x and $\bar{\nu}_x$ distributions [148, 159, 187]. An instability of the flavor field requires the ELN angular distribution to change sign at least once—it needs one or more "crossings." In the slow case, spectral crossings are required instead [237].

Various methods have been proposed to identify ELN crossings in hydrodynamical simulations [166, 167, 169, 238] and significant efforts have been devoted to understand when and where favorable conditions exist for FFC instabilities in astrophysical environments and related implications [146, 156, 162, 168, 170, 171, 173–177, 196, 225, 226, 239–241]. However, despite ELN crossings, only minimal flavor conversion may occur depending on the initial configuration [242], because it is the exact ν_e and $\bar{\nu}_e$ angular distribution that determines the ELN crossings and the final flavor outcome [149, 155, 161, 183, 186, 239, 242].

This *Letter* aims to elucidate under which conditions one should expect large flavor conversion due to FFC in a homogeneous and azimuthally symmetric neutrino gas. For the first time, we provide a simple diagnostic criterion to predict whether FFC should occur and how much conversion should be expected, without solving the neutrino equations of motion (EOMs). In doing so, we rely on a formal analogy of the EOMs with the ones of a gyroscopic pendulum [155].

The linear normal-mode analysis [133, 135, 157, 158, 243, 244] has been widely employed to obtain the growth rate of the flavor instability. Our main new insight consists of taking full advantage of this approach and to recognize, for the first time, the fundamental information provided by the initial rate of precession as well as by the universal form of the linear eigenfunction for the angle-dependent flavor conversion. Such findings provide crucial new insights into the physics of nonlinear systems.

5.2 MEAN FIELD EQUATIONS

We describe [anti]neutrinos through the usual density matrices $\varrho(\vec{p},\vec{r},t)$ $[\bar{\varrho}(\vec{p},\vec{r},t)]$. The diagonal elements are occupation numbers, whereas the off-diagonal ones encode flavor coherence. Ignoring collisions, the commutator EOM for neutrinos is [154]

$$i\,(\partial_t + \vec{v}\cdot\vec{\nabla})\varrho_{\vec{p}} = \left[\Omega_E, \varrho_{\vec{p}}\right] + \sqrt{2}\,G_{\mathrm{F}}\left[\mathsf{H}_{\vec{v}}, \varrho_{\vec{p}}\right] \ , \tag{5.1}$$

where vacuum oscillations are spawned by $\Omega_E = \mathsf{M}^2/2E$ with M being the neutrino mass matrix. Antineutrinos require $\Omega_E \to -\Omega_E$, but as we study FFC we set $\Omega_E = 0$ henceforth, also implying that $\vec{v} = \vec{p}/E$ is a unit vector. The Hamiltonian matrix

$$\mathsf{H}_{\vec{v}} = \int \frac{d^3\vec{q}}{(2\pi)^3}(\varrho_{\vec{q}} - \bar{\varrho}_{\vec{q}})\,(1 - \vec{v}_{\vec{q}}\cdot\vec{v}) \tag{5.2}$$

represents neutrino-neutrino refraction. The EOMs are understood in a co-moving frame in flavor space such that refraction on ordinary matter disappears.

One central feature of FFC is that all $\varrho(\vec{p},\vec{r},t)$ and $\bar{\varrho}(\vec{p},\vec{r},t)$, and any linear combination, follow the same EOM that depends on $\vec{v}$ but not on E. We thus consider the density matrices for lepton number $\mathsf{D}_{\vec{p}} = \varrho_{\vec{p}} - \bar{\varrho}_{\vec{p}}$, which we also integrate over energy and normalize to the ν_e density. The matrices $\mathsf{D}_{\vec{v}} \equiv n_{\nu_e}^{-1}\int_0^\infty E^2 dE/(2\pi^2)\,\mathsf{D}_{E,\vec{v}}$ thus defined obey the closed system of equations

$$i\,(\partial_t + \vec{v}\cdot\vec{\nabla})\mathsf{D}_{\vec{v}} = \mu\,[\mathsf{H}_{\vec{v}}, \mathsf{D}_{\vec{v}}] \ . \tag{5.3}$$

Here, $\mu \equiv \sqrt{2}G_{\mathrm{F}}n_{\nu_e}$ is a typical neutrino-neutrino interaction energy, whereas $\mathsf{H}_{\vec{v}} = \int (d^2\vec{u}/4\pi)\,D_{\vec{u}}(1 - \vec{u}\cdot\vec{v})$.

It is perhaps somewhat under-appreciated that it is the energy-integrated lepton-number matrices that drive the entire FFC dynamics. Solving the EOMs amounts to the task of finding $\mathsf{H}_{\vec{v}}(t)$.

Once it has been found, the solutions for $\varrho_{\vec{p}}$ and $\bar{\varrho}_{\vec{p}}$ or the particle-number densities $\mathsf{S}_{\vec{p}} = \varrho_{\vec{p}} + \bar{\varrho}_{\vec{p}}$ can be determined.

In our case study, we impose several symmetries, the most restrictive one being that of homogeneity of the initial setup *and* the solutions. Dropping the gradient and integrating both sides over $\int d^2\vec{v}/4\pi$ reveals that the total lepton-number matrix $\mathsf{D}_0 = \int (d^2\vec{v}/4\pi)\mathsf{D}_{\vec{v}}$ is conserved, meaning that $n_{\nu_\ell} - n_{\bar{\nu}_\ell}$ is separately conserved for every flavor $\ell = e$, μ, and τ. Indeed, FFC does not convert any net flavor. The corresponding number-density matrix S_0 is not conserved. While the total particle number (trace of S_0) is conserved, the individual $n_{\nu_\ell} + n_{\bar{\nu}_\ell}$ are not, commensurate with a pair-conversion effect.

As D_0 is conserved, it causes a global precession on the r.h.s. of Eq. (5.3) that can be "rotated away" by the unitary transformation $\mathsf{U}(t) = \exp[-i\mathsf{D}_0 t]$ as for the ordinary matter effect. The Hamiltonian matrix becomes $\mathsf{H}_{\vec{v}} = -\vec{v} \cdot \int (d^2\vec{u}/4\pi)\, \vec{u}\, D_{\vec{u}}$. Note that we have *not* assumed $\mathsf{D}_0 = 0$, we have only absorbed its effect by going to a co-moving frame. So we recognize that, in the homogeneous case, the evolution is entirely driven by $\vec{\mathsf{D}}(t) = \int (d^2\vec{u}/4\pi)\, \vec{u}\, \mathsf{D}_{\vec{u}}(t)$. While the latter is not conserved, $\operatorname{Tr}\vec{\mathsf{D}}^2$ is conserved, meaning that the lepton-number flux, summed over all flavors, is conserved.

As a further simplification, we impose axial symmetry on the initial setup *and* the solutions. Measuring $\vec{v}$ against the symmetry axis (zenith angle θ), we integrate out the azimuth angle ϕ and define $\mathsf{D}_v = \int_0^{2\pi}(d\phi/4\pi)\mathsf{D}_{\vec{v}}$ where $v = \cos\theta$ is the velocity along the symmetry axis (v is not $|\vec{v}| = 1$) with $-1 \leq v \leq +1$. The flux matrix now has only one nonvanishing component: $\mathsf{D}_1 = \int_{-1}^{+1} dv\, v\mathsf{D}_v$. A possible factor 1/2 in front of $\int_{-1}^{+1} d\cos\theta$ has been absorbed in the definition of D_v.

Last, we consider only two flavors, although three-flavor solutions can be much richer in the nonlinear regime [148, 157, 159, 187]. The corotating EOM thus becomes

$$i\dot{\mathsf{D}}_v = \mu v[\mathsf{D}_v, \mathsf{D}_1] \quad \text{or} \quad \dot{\boldsymbol{D}}_v = \mu\, v\boldsymbol{D}_v \times \boldsymbol{D}_1\,. \tag{5.4}$$

We here express the 2×2 Hermitian D_v matrices through the usual Bloch vectors (polarization vectors) such that $\mathsf{D}_v = (\operatorname{Tr}\mathsf{D}_v + \boldsymbol{D}_v \cdot \boldsymbol{\sigma})/2$ with $\boldsymbol{\sigma}$ a vector of Pauli matrices.

The cross product on the r.h.s. reveals that the length of each $\boldsymbol{D}_v$ is conserved. Moreover, $\boldsymbol{D}_0$ and $|\boldsymbol{D}_1|$ are conserved. It is $\boldsymbol{D}_1(t)$ that drives the motion of the system and moves like a gyroscopic pendulum [155].

5.3 SINGLE-CROSSED ELN SPECTRA

Except for small seeds, our system begins diagonal in the flavor basis where every $\boldsymbol{D}_v$ has only a z-component. (We use x, y and z for directions in flavor space.) So the initial condition is represented by what we call the ELN spectrum,

$$g_v = D_v^z\big|_{t=0} \propto (n_{\nu_e} - n_{\bar{\nu}_e} - n_{\nu_x} + n_{\bar{\nu}_x})_v \ . \tag{5.5}$$

One or more "crossings" (g_v changes sign) are necessary for run-away solutions to exist. This condition is also sufficient for solutions that may break homogeneity and axial symmetry [236].

Motivated by the qualitative shape of the ELN angular distributions near the neutrino decoupling regions, we use a family of single-crossed distributions defined by

$$\varrho_{ee}(\cos\theta) \quad = \quad 0.50\,, \tag{5.6a}$$

$$\bar{\varrho}_{ee}(\cos\theta) \quad = \quad 0.45 - a + \frac{0.1}{b}\exp\left[\frac{-(1-\cos\theta)^2}{2b^2}\right]. \tag{5.6b}$$

Here $\int_{-1}^{+1}\varrho_{ee}d\cos\theta = 1$, whereas the two free parameters $a \in [-0.04, 0.12]$ and $b \in [0.1, 1]$ determine the shape and normalization of $g_v = \varrho_{ee} - \bar{\varrho}_{ee}$ with $v = \cos\theta$. Figure 27 shows four representative examples and illustrates the effect of the a and b parameters.

We have solved the EOMs for the cases A–D specified in Fig. 27 and show the evolution $D_1^z(t)/D_1$ in Fig. 28. Recall that $D_1 = |\boldsymbol{D}_1|$ is conserved, so we really show $\cos\vartheta$ with $\vartheta(t)$ the zenith angle of $\boldsymbol{D}_1(t)$ in flavor space. Case A has no instability, in agreement with the results of the linear stability analysis, whereas B–D show the characteristic behavior of an inverted pendulum. The waiting time between dips depends logarithmically on the smallness of the chosen seeds. The component $\sqrt{(D_1^x)^2 + (D_1^y)^2}$ grows exponentially during that period. (For an example, see the Supplemental Material.)

In Fig. 29 we show snapshots of the evolution of the entire spectrum for Case B at four times indicated in Fig. 28. So we can see how the lepton-number flux evolves in time as a function of

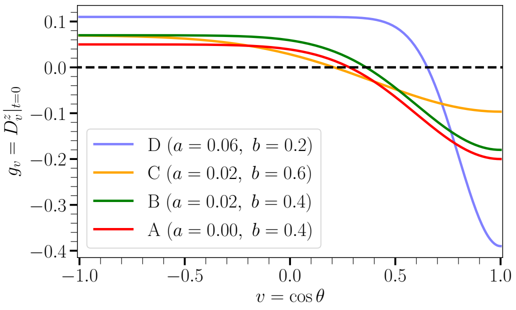

Figure 27: Representative ELN distributions g_v defined in Eqs. (5.6a) and (5.6b) for the shown values of a and b.

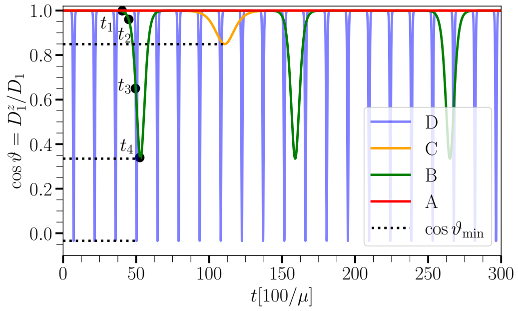

Figure 28: Solutions for the z-component (flavor direction) of the lepton-number flux $D^z_1(t)$ for the cases A–D specified in Fig. 27, where Case A has no instability. We show the normalized quantity $\cos\vartheta = D^z_1/D_1$. Its lowest point for each of Cases B–D perfectly agrees with $\cos\vartheta_{\rm min}$ predicted in Eq. (5.13).

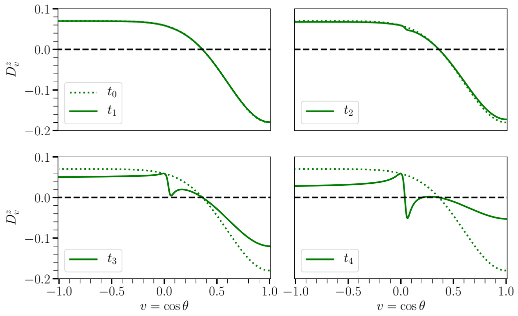

Figure 29: Snapshots for $D^z_v(t)$ for case B. The time shots are chosen at t_1–t_4 indicated in Fig. 28 between the beginning of the pendular dip and the maximum excursion.

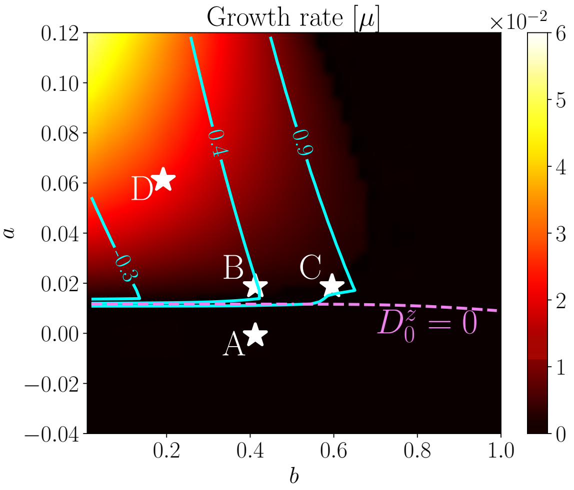

Figure 30: Contour plot of the growth rate in the plane spanned by the parameters a and b (see Eqs. 5.6a and 5.6b). The white contours represent $D_1^z(t)/D_1|_{\rm min}$. The locus of vanishing lepton number ($D_0^z = 0$) is marked with a dashed line. We also mark our configurations A–D. We see that large growth rates do not always correspond to large flavor conversion.

$v = \cos\theta$. All modes evolve coherently and return to their initial position—the overall evolution remains periodic within the limits of numerical precision. The same applies to the analogous evolution of the lepton-number modes $\boldsymbol{S}_v(t)$.

Finally, in Fig. 30 we show contours of $D_1^z(t)/D_1|_{\rm min} = \cos\vartheta_{\rm min}$ in the plane spanned by a and b overlaid with contours of the growth rate obtained by the linear normal-mode analysis [133, 135]. Evidently large flavor conversion does not always correlate with a large growth rate. Moreover, seemingly similar ELN configurations can cause very different flavor outcomes.

The coherence of all modes suggests a small number of underlying degrees of freedom. In fact, by applying the Gram matrix method [234], we find that our system with single-crossed ELN spectra is equivalent to three discrete angle modes, which form a gyroscopic flavor pendulum in the unstable case (see Supplemental Material for more details).

5.4 PENDULUM IN FLAVOR SPACE

The first of the linearly independent functions suggested by the Gram matrix is the conserved vector $\boldsymbol{G} = \boldsymbol{D}_0 = \int dv\, \boldsymbol{D}_v(t)$ of lepton number. The second is the lepton-number flux $\boldsymbol{R}(t) = \boldsymbol{D}_1(t) = \int dv\, v\boldsymbol{D}_v(t)$ with conserved length. The third is what we call $\boldsymbol{J}(t) = \int dv\, w_v \boldsymbol{D}_v(t)$ with unknown weight function w_v. They represent a gyroscopic pendulum, if they obey the EOMs [234]

$$\dot{\boldsymbol{G}} = 0\,, \ \dot{\boldsymbol{R}} = \mu \boldsymbol{J} \times \boldsymbol{R} \ \text{ and } \ \dot{\boldsymbol{J}} = \gamma \boldsymbol{G} \times \boldsymbol{R}\,. \tag{5.7}$$

In a mechanical analogy, $\boldsymbol{G}$ represents gravity, $\boldsymbol{R}$ the center-of-mass position relative to the point of support, $\boldsymbol{J}$ the total angular momentum, and μ^{-1} the moment of inertia. Besides the conserved $\boldsymbol{G}$, the EOMs imply four conserved quantities: length R of the radius vector, angular momentum $J_z = \boldsymbol{J}\cdot\boldsymbol{G}/G$ along "gravity," spin $S = \boldsymbol{J}\cdot\boldsymbol{R}/R$, and energy $E = V + T = \gamma\boldsymbol{G}\cdot\boldsymbol{R} + (\mu/2)\boldsymbol{J}^2$. Moreover, the natural pendulum frequency $\lambda\mu$ is given by $\lambda^2 = \gamma G R/\mu$. We here assume that $\gamma > 0$, a possible negative sign is absorbed by redefining $\boldsymbol{G} = -\boldsymbol{D}_0$.

We use coordinates where $\boldsymbol{G}$ defines the z-direction so that $\boldsymbol{G} = (0, 0, G)$, whereas the pendulum is described in polar coordinates (ϑ, φ) by $\boldsymbol{R} = R(s_\vartheta c_\varphi, s_\vartheta s_\varphi, c_\vartheta)$ with $s_\vartheta = \sin\vartheta$ and so forth.

Solving the EOMs for $\vartheta(t)$ and $\varphi(t)$ in terms of the conserved quantities is shown in any mechanics textbook or Appendix B of Ref. [234]. One important simplification is that we always begin with $\boldsymbol{R}$ parallel or antiparallel to $\boldsymbol{G}$ without an initial velocity, implying that $\boldsymbol{J}|_{t=0} = \boldsymbol{S}|_{t=0}$, and because J_z and S are conserved, we may use $J_z = S$. Moreover, we assume that $\boldsymbol{S}$ is parallel to $\boldsymbol{R}$ and not antiparallel. One thus finds

$$\dot{\varphi} = \mu \frac{2\lambda\sigma}{1+\cos\vartheta}\,, \tag{5.8a}$$

$$\dot{\vartheta}^2 = \mu^2\lambda^2\left[2\,(1-\cos\vartheta) - \sigma^2 \frac{4\,(1-\cos\vartheta)^2}{\sin^2\vartheta}\right], \tag{5.8b}$$

where we have expressed the spin, $S = 2\lambda\sigma$, in terms of a parameter σ and the dimensionless natural pendulum frequency $\lambda = \sqrt{\gamma G R/\mu}$. Besides the overall scale μ, the pendulum is fully described by the parameters λ and σ.

The zenith-angle EOM of Eq. (5.8b) becomes yet more informative with $c_\vartheta = \cos\vartheta$ as independent variable, so that $\dot{c}_\vartheta^2 = \mu^2\lambda^2\, 2(1-c_\vartheta)^2(1+c_\vartheta-2\sigma^2)$. For the r.h.s. to be positive in the neighborhood of $c_\vartheta = 1$, we obtain $\sigma < 1$ as a condition for instability. For larger σ, the pendulum is stuck in the "sleeping top position." In the unstable case, it nutates between the upright position and a minimal latitude $\vartheta_{\min}$ given by $\cos\vartheta_{\min} = -1 + 2\sigma^2$. For $\sigma = 0$, it reaches the vertical downward position.

In the linear regime ($\vartheta \ll 1$), the solutions (5.8a) and (5.8b) are

$$\dot{\varphi} = \mu\lambda\sigma \quad \text{and} \quad \dot{\vartheta} = \pm\mu\lambda\sqrt{1-\sigma^2}\,\vartheta\,. \tag{5.9}$$

The pendulum performs a uniform precession, whereas ϑ grows or shrinks exponentially, according to whether the pendulum moves away from the stable position or, after a full swing, comes back to it.

5.5 NORMAL MODE ANALYSIS

To match these parameters with our full system, we consider the latter in the linear regime. Initially $D_v^{xy} = D_v^x + iD_v^y$ is small, whereas D_v^z is at its initial value g_v. Thus the linearized version of Eq. (5.4) is $(i\partial_t + vD_1)D_v^{xy} = vg_z \int du\, uD_u^{xy}$. A collective normal mode would be of the form $g_v Q_v e^{-i\omega t}$ with $\omega = \omega_\mathrm{P} \pm i\Gamma$ being the complex eigenfrequency, where the subscript P stands for "precession." The solution is

$$D_v^{xy}(t) = f\,\frac{v\,g_v}{\omega + vD_1}\,e^{-i\omega t}\,, \tag{5.10}$$

where f depends on the initial conditions. Inserting this back into the linear EOM reveals that ω is fixed by

$$\int_{-1}^{+1} dv\,\frac{v^2 g_v}{\omega + vD_1} = \int_{-1}^{+1} dv\, g_v v^2\,\frac{\omega_\mathrm{P} + vD_1 - i\Gamma}{(\omega_\mathrm{P} + vD_1)^2 + \Gamma^2} = 1\,. \tag{5.11}$$

For convenience, we also provide a step-by-step derivation in the Supplemental Material.

The crucial final step is to match the real and imaginary parts of ω with the corresponding pendulum parameters of Eq. (5.9): $\dot{\varphi} = \mu\lambda\sigma = \omega_\mathrm{P}$ and $\dot{\vartheta} = \pm\mu\lambda\sqrt{1-\sigma^2}\,\vartheta = \pm\Gamma\vartheta$. Inverting these relations and selecting the positive solution for the second equation only reveals

$$\sigma = \sqrt{\frac{\omega_\mathrm{P}^2}{\omega_\mathrm{P}^2 + \Gamma^2}} \quad \text{and} \quad \lambda = \frac{1}{\mu}\sqrt{\omega_\mathrm{P}^2 + \Gamma^2}\,. \tag{5.12}$$

Hence, the lowest pendulum position is

$$\cos\vartheta_\mathrm{min} = -1 + 2\,\frac{\omega_\mathrm{P}^2}{\omega_\mathrm{P}^2 + \Gamma^2}\,. \tag{5.13}$$

The equation above crucially links the maximal latitude reached by the gyroscopic pendulum to the real and imaginary parts of the complex eigenfrequency ω, providing a way to predict the depth of flavor mixing without solving the equations of motion. This prediction is in excellent agreement for all our ELN configurations, see our examples shown in Fig. 28 for a comparison. We also see that $\omega_{\mathrm{P}} = 0$ implies $\sigma = 0$, leading to complete conversion, whereas $\Gamma = 0$ implies $\sigma = 1$ and the pendulum is stable.

5.6 CONCLUSIONS

For a homogeneous and azimuthally symmetric two-flavor neutrino gas, we have explicitly shown that flavor conversion physics strongly depends on details of the ELN distribution. Similar looking angular distributions can lead to completely different outcomes. Notably, the amount of flavor conversion does not directly correlate with the growth rate obtained from the linear normal-mode analysis.

Obvious characteristics are the conserved Bloch vector of the lepton number that we call $\boldsymbol{D}_0$ and the one of lepton-number flux $\boldsymbol{D}_1$ with conserved length, and it is also evident that $\boldsymbol{D}_1(t)$ is what drives the evolution of all Bloch vectors (or density matrices) for individual modes of lepton or particle number.

The evolution of $\boldsymbol{D}_1(t)$ appears to be equivalent to a gyroscopic pendulum, with $\boldsymbol{D}_0$ playing the role of gravity, suggesting that the third characteristic is what plays the role of spin or equivalently the total angular momentum $\boldsymbol{J}$. However, identifying $\boldsymbol{J}$ as a simple combination of $\boldsymbol{D}_n = \int dv\, v^n \boldsymbol{D}_v$ is not generally successful [155].

Our main innovation was to match the pendulum parameters (natural frequency and spin) with the precession frequency ω_{P} and growth rate Γ obtained from the usual normal-mode analysis of the neutrino system. It is important to stress that, while attention was usually focused on Γ, the previously ignored ω_{P} provides the spin and thus allows one to gain insight on the amount of flavor mixing.

Our work provides new insights and a simple tool to unveil the rich phenomenology of FFC, shedding light on the complicated physics of neutrino-dense media and, in general, nonlinear systems of this type. While our findings are based on a single-crossed, homogeneous and azimuthally symmetric neutrino gas, they could provide a first step to analytically forecast the amount of flavor conversion in neutrino-dense astrophysical environments. As such, this work could have fundamental implications on our understanding of neutrino flavor evolution in core-collapse supernovae and the synthesis of heavy elements in compact binary merger remnants, where progress is currently halted by its intrinsic numerical challenges.

5.7 CRITICAL OUTLOOK

5.7.1 *Overview and main findings*

The formal equivalence between the equations that describe the fast flavor dynamics and those of a classical gyroscopic pendulum has remained unknown until now. However, it is not the first time that the equations of a gyroscopic pendulum have been formally implemented to describe a possible manifestation of collective neutrino conversion. For slow flavor conversion (Sec. 2.2.7.1), the interpretation of the non-linear evolution as a gyroscopic pendulum is well-known and has been subject of study for quite some time [90, 92, 93, 234]. More in detail, Eqs. 2.81 describe the dynamics of the "slow" gyroscopic pendulum $\vec{q} \propto \vec{P}_\omega - \vec{P}_{-\omega} - \frac{\omega}{\mu}\vec{B}$ with a total angular momentum given by $\vec{D} = \int_{-\infty}^{\infty} d\omega \vec{P}_\omega$ in the presence of a (constant) gravitational field where the gravitational acceleration is $\vec{g} = -\mu\omega\vec{B}$. The slow gyroscopic pendulum conserves its spin $\sigma_s = \text{const}$ and it is non-zero for asymmetric systems $|\vec{P}_\omega| = (1+\varepsilon)|\vec{P}_{-\omega}|$ with $\varepsilon \neq 0$. The slow pendulum does not swing if $\omega = 0$ since there is no gravitational pull exerting a torque on the pendulum $\vec{q}$.

The classical dynamics are identical in the case of the "fast" gyroscopic pendulum. However, the *identification* of the physical quantities such as gravity, angular momentum, and even the pendulum itself is completely different. In the fast case, the gravitational acceleration is given by the conserved quantity $\vec{G} = \vec{D}_0 = \int_{-1}^{1} dv \vec{D}_v(t)$, the pendulum is $\vec{R} = \vec{D}_1 = \int_{-1}^{1} dv v \vec{D}_v(t)$, where $\vec{D}_v = \vec{P}_v - \vec{\bar{P}}_v$; notice that now the polarization vectors are a function of the angular variable $v = \cos\theta$ rather than energy as for the slow case. Interestingly, the angular momentum $\vec{J}$ is a non-trivial combination of the polarization vectors $\vec{P}_v, \vec{\bar{P}}_v$, which remains unknown. In Section 3.2.1 we examined the angular moments approach where a prediction on the final flavor outcome is unsuccessful even in the simplest of cases.

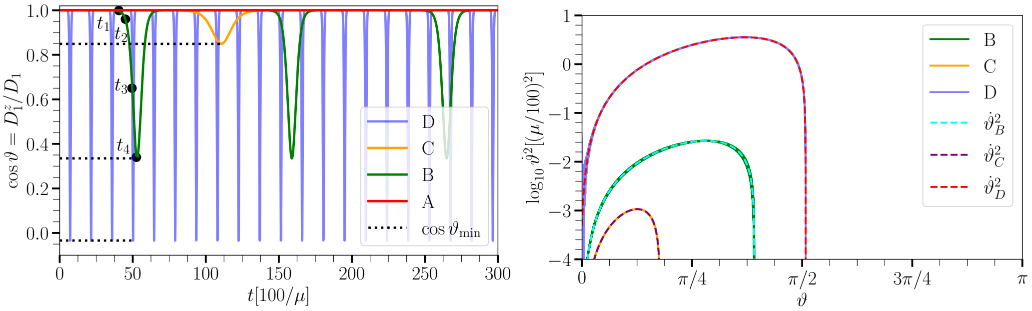

Figure 31: *Left:* Solutions for the z-component of the lepton-number flux $D_1^z(t)$ for the some representative initial ELN distributions (cases A–D). We show the maximum excursion of the pendulum given by $\cos\vartheta = D_1^z/D_1$ both from the numerical solution and our prediction. *Right:* Parametric plots of $\dot\vartheta^2$ as functions of ϑ for the unstable configurations. This plot includes the numerical results for our three unstable examples B–D (solid lines) and the analytical ones (dashed lines). The agreement between the two is excellent, even in the non-linear regime.

However, we stress that, due to conservation of energy and angular momentum, only knowledge of the initial ELN angular distribution is needed to make accurate estimates of the maximum excursion of the pendulum, as thoroughly described in this Chapter.

One of the most important results of this work is the formal identification of the pendulum parameters based entirely on the initial ELN distribution. We found that the linear stability analysis (Sec. 2.2.7.3) can serve as a bridge between the properties of the initial ELN distribution and the flavor dynamics that the gyroscopic pendulum can display. This "matching" through the linear stability analysis is possible because of the small number of degrees of freedom of the system and might not be valid in less symmetric scenarios [183], although this has not been explicitly proven. The few degrees of freedom in the equations of motion allow to find a simple formula that predicts the lowest point of the gyroscopic pendulum:

$$\cos\vartheta_{\rm min} = -1 + 2\,\underbrace{\frac{\omega_P^2}{\omega_P^2+\Gamma^2}}_{\sigma^2}\,, \tag{5.14}$$

where σ is the spin of the gyroscopic pendulum. Here, the angle ϑ describes the angle between the pendulum and the $\hat{z}$ direction in flavor space, i.e., $\cos\vartheta = 1$ means no conversion, and $\cos\vartheta = -1$ means maximal conversion, as allowed by total lepton number conservation. The quantities ω_P and Γ are real and imaginary parts of the eigenfrequency, respectively, obtained through the linear stability analysis $\Omega = \omega_P + i\Gamma$. The formula for $\cos\vartheta_{\rm min}$ can be easily implemented for given initial ELN distributions. For instance, for some representative initial ELN angular distributions, the values of the quantity $\cos\vartheta_{\mathrm{min}}$ can be computed and compared directly with full numerical solutions. The agreement between the analytical prediction and the numerical solution is excellent, as shown in Fig. 31. This estimation offers a new diagnostic to evaluate whether flavor conversion is significant and bypasses cumbersome numerical calculations often involved in collective neutrino conversion.

5.7.2 *Limitations and future perspectives*

The field of fast flavor conversion heavily relies on numerical simulations to tackle the non-linear behavior of evolution. Less demanding tools like the linear stability analysis (Sec. 2.2.7.3) have been beneficial in assessing the presence of instabilities; however, we need to go beyond the linear regime. In the same way, the gyroscopic pendulum presented in this Chapter constitutes a step forward in connecting the linear and the non-linear regimes and answering elusive questions about the final flavor outcome of evolution. Despite all the progress, much work is ahead before the astrophysical implications are conclusively sorted out.

5.7.2.1 *Mean-field Approximation*

The validity of the mean field approximation should be studied in detail because of the new conceptual developments on neutrino fast flavor conversion. For instance, our prediction for the maximum amount of conversions in Eq. 5.13 (mean-field) could be directly compared with calculations in the many-body framework [245–248] without explicitly solving the mean-field equations. The latter suggestion could be a quick way of assessing the validity of mean-field approximation within our symmetric framework.

5.7.2.2 *Relaxing symmetry assumptions*

The gyroscopic pendulum might be extended by relaxing some symmetry assumptions implemented in its "standard" version (this Chapter). Due to the spontaneous breaking of axial symmetry [104], the ϕ-dependence in the neutrino EOMs (Eq. 2.74) needs to be included and translated into the language of the standard gyroscopic pendulum. One immediate issue is that by including ϕ-modes, the non-conservation of the length of standard pendulum D_1 follows as a result of the coupling of different angular modes (Eqs. 3.10 and 3.11). This implies that new conservation laws need to be found which have not been explored analytically but only numerically [183]. Similarly, there is also the breaking of the spatial symmetry [110], which forces us to deal with inhomogeneities and include the advective term (Chapter 7). One major complication is that the advective term would lead to the non-conservation of not only D_1 but also of D_0 since (anti)neutrinos stream in and out at a given $\vec{x}$; this scenario is better understood from the numerical point of view [149, 180, 182, 249], rather than from the analytical perspective.

5.7.2.3 *Multiple ELN crossings*

Single-crossed ELN spectra are motivated by the conditions expected in the proximity of the decoupling regions [239]. However, from the theoretical point of view, multiple ELN crossings are also possible, and their effect has been acknowledged to be progressively less relevant for flavor conversion as the number of ELN crossings increases [186]. Whether angular distributions with multiple crossings are possible in astrophysical environments remains unsettled.

5.7.2.4 *More realistic scenarios*

Another growing line of research is assessing fast flavor instabilities in more realistic CCSNe and compact binary mergers simulations. Recent works [146, 162, 165–169] have focused on using the little ELN angular distribution information that is provided from simulations to determine whether flavor instabilities arise. One possibility is that within some regions of the astrophysical source, homogeneity and axial symmetry are approximately valid such that the predictions from the gyroscopic pendulum are not too far from reality. For instance, the works in Refs. [196, 226, 231] have determined likely regions in the merger remnants where instabilities arise. In principle, one could also determine the regions where maximum flavor mixing occurs based on our prescription (Eq. 5.13) and cross-check the assumption of flavor equilibration in fast flavor computations.

6

THE GYROSCOPIC PENDULUM WITH COLLISIONAL DAMPING

Based on: **Ian Padilla-Gay**, Irene Tamborra, Georg G. Raffelt, *Upshot of Collisional Damping on Neutrino Fast Flavor Conversion*, **to appear soon**.

ABSTRACT In compact astrophysical sources, the neutrino density is so high that neutrino refraction leads to fast flavor conversion of the kind $\nu_e\bar{\nu}_e \leftrightarrow \nu_x\bar{\nu}_x$ with $x = \mu, \tau$. Under the assumption of homogeneity and axial symmetry, we explore the impact on flavor conversion physics of random collisions of neutrinos with the background medium. Albeit the formal analogy of the neutrino equations of motion with the ones of a gyroscopic pendulum does not hold in the presence of damping, it is possible to predict the final flavor outcome analytically by relying on the fact that our neutrino ensemble behaves as a gyroscopic pendulum at each given time. We provide a simple analytical expression as a function of the lowest point reached by the gyroscopic pendulum to compute the final flavor configuration. Interestingly, the final steady state is independent of the specific value of the damping rate as long as the latter is different from zero; however, the time needed to reach the steady state configuration depends on the amount of damping. The eventual presence of a small asymmetry between the neutrino and antineutrino damping rates allows for the development of flavor instabilities in systems otherwise stable. Furthermore, we establish a formal connection with a stationary and non-homogeneous neutrino ensemble, showing that our findings also apply to this system.

6.1 INTRODUCTION

The flavor evolution of neutrinos and antineutrinos in dense sources is nonlinear because of the coherent forward scattering of neutrinos among each other [250]. This phenomenon is commonly referred to as collective neutrino oscillation and can span over different time and length scales [82, 87, 88, 124, 145].

The physics of neutrino self-interaction is driven by the shape of the flavor-dependent momentum distributions [239]. In particular, if a crossing occurs between the angular distributions of electron neutrinos and antineutrinos (ELN crossing), "fast" flavor conversion develops on timescales regulated by the neutrino number density [128–130, 132, 133, 236]. On the other hand, if collective neutrino transformation is characterized by a scale defined by the combination of the neutrino-neutrino self-interaction strength and the vacuum oscillation frequency, then it is considered to be "slow" [82, 88].

The physics of fast pairwise conversion remains full of unknowns. However, recent work has shown that non-forward collisions of neutrinos with the matter background could affect fast flavor conversion [150–153, 184, 185, 233, 251–253]. In addition, the ELN angular distribution can be modified by neutrino advection dynamically [149, 182, 233, 251, 254].

In Ref. [164], we focused on an axially symmetric and homogeneous system and showed that the neutrino equations of motion (EOMs) are formally equivalent to those of a gyroscopic pendulum. Relying on this simple formal analogy, we provided a simple tool to predict the depth of flavor conversion without solving the EOM but exploiting the real part of the eigenfrequency resultant from the linear normal-mode analysis. In this paper, we intend to build on the findings of Ref. [164] and include a damping term in the EOMs mimicking neutrinos being scattered randomly [75]. We aim to provide an analytical method that allows computing the final flavor state without solving the EOMs numerically. At the same time, we intend to gain insight into the yet elusive physics of fast flavor conversion.

This work is organized as follows. In Sec. 6.2, we present the EOMs of (anti)neutrinos and their multipole decomposition and introduce the ELN angular distributions considered in this work. Section 6.3 focuses on the role of damping under the assumption of equal damping rates for neutrinos and antineutrinos. We consider the linear and non-linear regime of flavor evolution and offer analytical estimates on how to compute the final flavor outcome based on initial ELN distributions without solving the EOMs numerically. In Sec. 6.4, we assume different damping rates for neutrinos and antineutrinos and quantify the departure from the case of equal damping rates for particles and antiparticles. In Sec. 6.5 we generalize our findings for a wide range of ELN distributions. We connect to a stationary and non-homogeneous system in Sec. 6.6 and show that our results are also valid for such a setup. Finally, closing remarks are reported in Sec. 6.7. Appendix B.1 outlines the normal mode analysis in the presence of collisional damping.

6.2 SETTING THE STAGE

In this section, we introduce the EOMs and their decomposition in multipoles. We then illustrate the initial angular configurations adopted for neutrinos and antineutrinos.

6.2.1 *Neutrino mean field equations*

For simplicity, we consider two flavors of neutrinos and refer the reader to Refs. [148, 159, 187, 249] for investigations dedicated to three flavor effects. The evolution of the neutrino flavor field can be modeled in terms of Wigner transformed 2 × 2 density matrices, $\varrho(\vec{p}, t)$ for neutrinos and $\bar{\varrho}(\vec{p}, t)$ for antineutrinos. Since we are interested in exploring fast flavor conversion, for simplicity, we ignore the energy dependence of the density matrices, and hence $\vec{v} = \vec{p}/E$ is a unit vector. Moreover, we impose axial symmetry on the initial configurations and the solutions—see Ref. [183] for details on symmetry breaking effects in non-axially symmetric systems.

The vector $\vec{v}$ is defined with respect to the symmetry axis (zenith angle θ), while the azimuthal angle ϕ has been integrated out. The velocity component along the symmetry axis is $v = |\vec{v}| \cos\theta = \cos\theta$, since $|\vec{v}| = 1$ for (anti)neutrinos traveling at the speed of light. The velocity component takes values between $v = 1$ (forward direction) and $v = -1$ (backward direction).

After these simplifications, the neutrino density matrix is

$$\varrho(v, t) = \begin{pmatrix} \varrho_{ee}(v, t) & \varrho_{ex}(v, t) \\ \varrho^{*}_{ex}(v, t) & \varrho_{xx}(v, t) \end{pmatrix}, \tag{6.1}$$

whose diagonal elements represent the occupation numbers of neutrinos of different species, while the off-diagonal terms contain information about the coherence between flavors. An analogous expression holds for the density matrix associated to antineutrinos, $\bar{\varrho}(v, t)$.

The EOMs for neutrinos and antineutrinos are respectively

$$i(\partial_t + \vec{v} \cdot \vec{\nabla})\varrho(v,t) = [H_{\nu\nu}(v,t), \varrho(v,t)] + i\mathcal{C}(\varrho(v,t)) \,, \tag{6.2}$$

$$i(\partial_t + \vec{v} \cdot \vec{\nabla})\bar{\varrho}(v,t) = [H_{\nu\nu}(v,t), \bar{\varrho}(v,t)] + i\bar{\mathcal{C}}(\bar{\varrho}(v,t)) \,. \tag{6.3}$$

The term on the left-hand side of the EOMs is the advective operator, $\vec{v} \cdot \vec{\nabla}$, which affects flavor evolution if the medium is non-homogeneous [149, 180]. In this work, we neglect the advective term and focus on homogeneous cases while still connecting with stationary non-homogeneous systems in Sec. 6.6. On the right-hand-side of the EOMs, the neutrino self-interaction Hamiltonian is responsible for the development of flavor transformation:

$$H_{\nu\nu}(v,t) = \mu \int dv' [\varrho(v',t) - \bar{\varrho}(v',t)][1 - vv'] \,; \tag{6.4}$$

it couples neutrinos of different momenta and renders the flavor evolution non-linear. Since we focus on fast flavor conversion, we neglect the vacuum and matter terms in the Hamiltonian. However, we refer the reader to Refs. [147, 255] for work dedicated to exploring the impact of these terms on the fast flavor conversion phenomenology.

The second term on the right-hand side of the EOMs is the collision term $\mathcal{C}$, which takes neutrino scattering with the background medium into account. We assume neutrinos being scattered randomly by the background medium [75] and that our collisional term conserves flavor (more complex implementations of the collision term and its impact on the flavor conversion phenomenology is explored in Refs. [150–153, 184, 185, 233, 251–253]):

$$i\mathcal{C}(\varrho(v,t)) = -\Gamma \begin{pmatrix} 0 & \varrho_{ex}(v,t) \\ \varrho^*_{ex}(v,t) & 0 \end{pmatrix} . \tag{6.5}$$

An analogous expression holds for $\bar{\mathcal{C}} = \alpha\mathcal{C}$ where the parameter α accounts for the possibility that quantum damping effects act differently on neutrinos and antineutrinos. The damping term contributes to a loss of coherence of the evolution [75].

Because of the definition of our collision term (Eq. 6.5), all v-modes are equally damped, thus we expect solutions of the kind $\varrho_{ex}(v,t) \propto \exp(-\Gamma t)$ in the absence of flavor conversion. In the following, we assume equal damping rates between neutrinos and antineutrinos ($\alpha = 1$). In the second part of this paper (Sec. 6.4), we also explore the scenario of different damping rates for neutrinos and antineutrinos (i.e. $\alpha \neq 1$).

6.2.2 *Multipole decomposition*

Since fast flavor conversion is driven by the ELN distribution [133, 236] and is a collective phenomenon, we introduce $g_v(t) = \varrho_{ee}(v,t) - \bar{\varrho}_{ee}(v,t)$ as well as the density matrices for the particle number S_v and lepton number D_v:

$$\mathsf{S}_v(t) = \varrho(v,t) + \bar{\varrho}(v,t) \,, \tag{6.6}$$

$$\mathsf{D}_v(t) = \varrho(v,t) - \bar{\varrho}(v,t) \,. \tag{6.7}$$

The latter can be represented as Bloch vectors in flavor space, $\boldsymbol{D}_v(t)$ and $\boldsymbol{S}_v(t)$, respectively, and $g_v(t)$ corresponds to the z-component of $\boldsymbol{D}_v(t)$. It is also useful to introduce the moments of $\boldsymbol{S}_v(t)$ and $\boldsymbol{D}_v(t)$:

$$\boldsymbol{S}_n(t) = \int_{-1}^{+1} dv v^n \boldsymbol{S}_v(t) \,, \tag{6.8}$$

$$\boldsymbol{D}_n(t) = \int_{-1}^{+1} dv v^n \boldsymbol{D}_v(t) \,. \tag{6.9}$$

Initially, $\boldsymbol{D}_0$ is parallel to the flavor axis and its z-component equals its norm:

$$D_0(t_0) = D_0^z(t_0) \,. \tag{6.10}$$

Moreover, the z-component of the ELN flux vector,

$$D_1^z(t) = \int dv v[\varrho_{ee}(v,t) - \varrho_{xx}(v,t) - \bar{\varrho}_{ee}(v,t) + \bar{\varrho}_{xx}(v,t)] \,, \tag{6.11}$$

is such that $D_1(t_0) = D_1^z(t_0)$. Note that in the following, we omit the explicit time dependence for simplicity unless otherwise specified.

By relying on the moment decomposition (Eqs. 6.8 and 6.9), the EOMs can be written as

$$\dot{\boldsymbol{D}}(v) = -\mu\, \boldsymbol{D}(v) \times \boldsymbol{D}_0 + \mu\, v \boldsymbol{D}(v) \times \boldsymbol{D}_1 - \Gamma \boldsymbol{D}^{xy}(v) \,, \tag{6.12}$$

$$\dot{\boldsymbol{S}}(v) = -\mu\, \boldsymbol{S}(v) \times \boldsymbol{D}_0 + \mu\, v \boldsymbol{S}(v) \times \boldsymbol{D}_1 - \Gamma \boldsymbol{S}^{xy}(v) \,. \tag{6.13}$$

where $\boldsymbol{D}^{xy}(v) = (D^x(v), D^y(v), 0)$ and $\boldsymbol{S}^{xy}(v) = (S^x(v), S^y(v), 0)$ are the transverse vectors of the lepton number and particle number vectors, respectively.

By assuming the absence of collisions (i.e., $\Gamma = \bar{\Gamma} = 0$), Refs. [92, 164] pointed out a formal analogy of the EOMs with the ones of a gyroscopic pendulum. In this scenario, $\boldsymbol{D}_0$ corresponds to the (constant) gravitational field, which exerts a torque on the pendulum $\boldsymbol{D}_1$, making it swing away from the flavor axis and convert flavor. In the presence of damping, $\boldsymbol{D}_0$ is still a constant of motion ($\dot{\boldsymbol{D}}_0 = 0$, resulting in the net ELN conservation, regardless of the initial configuration), similar to the case with $\Gamma = \bar{\Gamma} = 0$. On the contrary, $\boldsymbol{D}_1$ changes with time and resembles the dynamics of a pendulum in flavor space. However, because of $\Gamma \neq 0$, the norm of D_1 is no longer conserved as opposed to the more straightforward pendulum-like solutions obtained for $\Gamma = 0$ (see for instance Fig. 2 of Ref. [164]).

6.2.3 *System setup*

For fast flavor instabilities to occur, a necessary and sufficient condition is the presence of a crossing in the ELN angular distribution [236]. However, the presence of flavor instability does not necessarily imply large flavor conversion [164, 242]. Therefore, for the sake of simplicity, we restrict ourselves to the case of single-crossed families of ELN distributions of the form:

$$\varrho_{ee}(v, t_0) = 0.50\,, \tag{6.14}$$

$$\bar{\varrho}_{ee}(v, t_0) = 0.45 - a + \frac{0.1}{b} \exp\left[\frac{-(1-v)^2}{2b^2}\right], \tag{6.15}$$

such that the shape of the distributions is set by the free parameters: $a \in [-0.04, 0.12]$ and $b \in [0.1, 1]$, and the normalization is $\int_{-1}^{+1} dv \varrho_{ee}(v, t_0) = 1$. In order to show how the ELN angular distribution changes for different values of a and b, we show $g_v(t_0)$ as a function of v in Fig. 32 for four selected examples Cases A–D; note that Cases A–D are identical to the benchmark configurations adopted in Ref. [164]. Moreover, we assume that our system is initially composed of electron flavors only [$\varrho_{xx}(v, t_0) = \bar{\varrho}_{xx}(v, t_0) = 0$].

We consider a constant neutrino self-interaction strength: $\mu = 10^5\ \mathrm{km}^{-1} = 3 \times 10^{10}\ \mathrm{s}^{-1}$. Unless otherwise specified, we use $\Gamma = 2.5 \times 10^6\ \mathrm{s}^{-1}$, which is $\simeq 8.3 \times 10^{-5} \mu = 8.3\ \mathrm{km}^{-1}$, and therefore much smaller than μ. Note that if the damping rate is sufficiently large, it can freeze the evolution of our neutrino ensemble similarly to the Zeno effect [76].

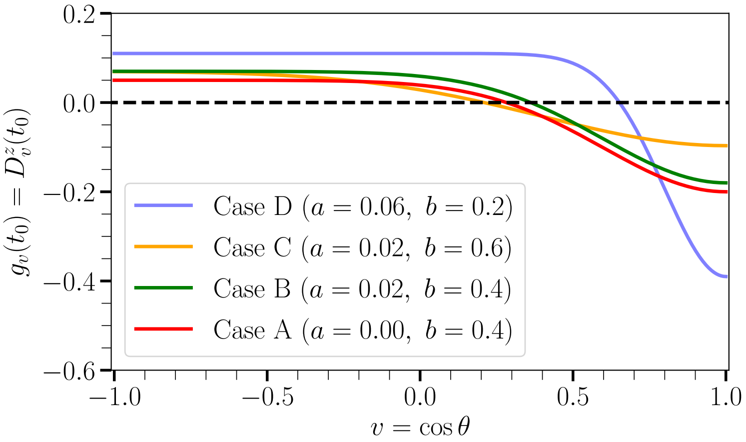

Figure 32: Representative ELN angular distributions $g_v(t_0)$ (see Eqs. 6.14 and 6.15).

6.3 IMPACT OF COLLISIONAL DAMPING ON FLAVOR CONVERSION

In this section, we investigate the consequences of damping on the flavor conversion physics. For simplicity, we rely on a discrete (three mode) decomposition of the ELN angular distribution. We then explore the steady state reached by the system as a function of the damping rate and compare the flavor phenomenology to the one obtained for cases without damping.

6.3.1 *Decomposition in three angular modes*

The coherent evolution of all angular modes implies that our continuous system (Eqs. 6.14 and 6.15) can be reduced to a three-mode equivalent one [164, 234]. Since $\boldsymbol{D}_0 = \sum_{i=1}^{3} \Delta v_i \boldsymbol{D}(v_i)$ is a constant of motion, it amounts to a global precession and can be "rotated away" from Eqs. 6.12 and 6.13 by going to a co-moving frame that rotates at a frequency μD_0. The linearized EOMs in the co-moving frame are:

$$\dot{\boldsymbol{D}}(v_i) = \mu\, v_i \boldsymbol{D}(v_i) \times \boldsymbol{D}_1 - \Gamma \boldsymbol{D}^{xy}(v_i)\,, \tag{6.16}$$

$$\dot{\boldsymbol{S}}(v_i) = \mu\, v_i \boldsymbol{S}(v_i) \times \boldsymbol{D}_1 - \Gamma \boldsymbol{S}^{xy}(v_i)\,, \tag{6.17}$$

for $i = 1, 2$ and 3. The related equations for the transverse components are

$$\begin{aligned} \dot{D}^x(v_i) &= +\mu v_i \Big[D^y(v_i) D_1^z - D_1^y D^z(v_i) \Big] - \Gamma D^x(v_i)\,, \qquad (6.18) \\ \dot{D}^y(v_i) &= -\mu v_i \Big[D^x(v_i) D_1^z - D_1^x D^z(v_i) \Big] - \Gamma D^y(v_i)\,. \qquad (6.19) \end{aligned}$$

where $D_1^{x,y,z}$ are the x, y and z components of $\boldsymbol{D}_1 = \sum_{i=1}^{3} v_i \Delta v_i \boldsymbol{D}(v_i)$, respectively, and Δv_i is the spacing between modes. Equations 6.18 and 6.19 hold when $\mathcal{C} = \bar{\mathcal{C}}$, otherwise $\boldsymbol{S}(v_i)$ and $\boldsymbol{D}(v_i)$ couple to each other, as discussed in Sec. 6.4.

Let us define the following linear combinations

$$\begin{aligned} \epsilon_{S,i} &= S^x(v_i) - i S^y(v_i)\,, \qquad (6.20) \\ \epsilon_{D,i} &= D^x(v_i) - i D^y(v_i)\,, \qquad (6.21) \end{aligned}$$

and take advantage of the linearized version of the EOMs. The linearization consists of assuming that the transverse components $\epsilon_{(S,D),i}$ are much smaller than $S^z(v_i)$ and $D^z(v_i)$ so that quadratic terms $\epsilon^2_{(S,D),i}$ (and higher) can be safely neglected; we refer the reader to Appendix B.1 for step-by-step calculations of the normal mode analysis in the presence of damping. Since the evolution of $\epsilon_{S,i}$ is determined by that of $\epsilon_{D,i}$, we can focus on the equations for $\epsilon_{D,i}$ [164]. Thus, using the definitions of $\epsilon_{(S,D),i}$ (Eqs. 6.20 and 6.21), the EOMs (Eqs. 6.18 and 6.19) turn into a set of equations which only involve terms linear in $\epsilon_{D,i}$:

$$\dot{\epsilon}_{D,i} = (-i)\mu v_i \Big[-\epsilon_{D,i} D_1^z + D^z(v_i) \sum_{j=1}^{3} v_j \Delta v_j \epsilon_{D,j} \Big] - \Gamma \epsilon_{D,i}\,. \qquad (6.22)$$

This set of equations can be further expressed in matrix form as follows

$$\begin{bmatrix} \dot{\epsilon}_{D,1} \\ \dot{\epsilon}_{D,2} \\ \dot{\epsilon}_{D,3} \end{bmatrix} = (-i) M'_D \begin{bmatrix} \epsilon_{D,1} \\ \epsilon_{D,2} \\ \epsilon_{D,3} \end{bmatrix}. \qquad (6.23)$$

As a result, the matrix M'_D is completely determined by velocity modes v_i, $D^z(v_i)$, μ, and Γ:

$$M'_D = \begin{bmatrix} -\mu v_1 D_1^z - i\Gamma + \mu D^z(v_1) v_1^2 \Delta v_1 & \mu v_1 D^z(v_1) v_2 \Delta v_2 & \mu v_1 D^z(v_1) v_3 \Delta v_3 \\ \mu v_2 D^z(v_2) v_1 \Delta v_1 & -\mu v_2 D_1^z - i\Gamma + \mu D^z(v_2) v_2^2 \Delta v_2 & \mu v_2 D^z(v_2) v_3 \Delta v_3 \\ \mu v_3 D^z(v_3) v_1 \Delta v_1 & \mu v_3 D^z(v_3) v_2 \Delta v_2 & -\mu v_3 D_1^z - i\Gamma + \mu D^z(v_3) v_3^2 \Delta v_3 \end{bmatrix} \qquad (6.24)$$

The determinant equation $\det(M'_D - \Omega 1_{3\times3}) = 0$ ensures that there are non-trivial solutions to the linear equations (Eq. 6.23). Although the final expression for the determinant is significantly more complicated than in the collisionless case, it is still tractable. Solving the determinant equation reveals a common eigenfrequency of $\epsilon_{D,i}(t)$ [and $\epsilon_{S,i}(t)$] since we have assumed that all velocity modes evolve collectively i.e. $\epsilon_{D,i}(t) = \epsilon_{D,i}(t_0)e^{-i\Omega t}$.

The determinant equation is a polynomial in the eigenfrequency Ω. Once the determinant equation is solved for Ω, we can test the possible existence of flavor instabilities. For the sake of simplicity, we neglect terms proportional to Γ^2/μ^2 and Γ^3/μ^3, which is justified because $\mu \gg \Gamma$:

$$\Omega^3 + \Omega^2\mu\left[3i\frac{\Gamma}{\mu} + \left(D_1^z(v_1+v_2+v_3) - D_2^z\right)\right] + \Omega\mu^2\left[2i\frac{\Gamma}{\mu}D_{123}^z + v_1v_2v_3D_0^zD_1^z\right] + i\mu^3\frac{\Gamma}{\mu}v_1v_2v_3D_0^zD_1^z = 0\,, \tag{6.25}$$

where $D_{123}^z \equiv v_1(v_2+v_3)\Delta v_1 D^z(v_1) + v_2(v_1+v_3)\Delta v_2 D^z(v_2) + v_3(v_1+v_2)\Delta v_3 D^z(v_3)$. The solution to this equation cannot be found analytically; we instead rely on numerical solutions. Contrary to the $\Gamma = 0$ case [164], the roots $\Omega_{1,2,3}$ of Eq. 6.25 do not come in complex conjugates ($\Omega_2^* \neq \Omega_1$), and one of the solutions corresponds to $\mathrm{Im}[\Omega_3/\mu] = \Gamma$.

The top panel of Fig. 33 displays the transverse components $|D_1^{xy}|$ (solid lines) and the growth rates (dashed lines) for the ELN configuration corresponding to Case B, see Fig. 32, for $\Gamma = 0$ (green lines) and $\Gamma \neq 0$ (purple lines). The linear regime occurs within the first 2×10^{-7} s, as visible from the exponential growth of $|D_1^{xy}|$. Once the linear regime is over, the solutions with and without damping depart from each other, and damping significantly impacts the final flavor outcome after 1×10^{-6} s, as shown in the middle panel of Fig. 33.

Our benchmark damping rate is small enough that the linear regime is almost unaffected; see the top panel of Fig. 33. The latter can also be appreciated by noticing that the first dip in D_1^z/D_1 is almost identical in both cases. After a few iterations (middle panel of Fig. 33), the solution with damping saturates and reaches a steady state solution while the case without damping continues to oscillate regularly and indefinitely [164].

In flavor space, one can introduce the angle ϑ defined as the angle between the flavor axis (also that of $\boldsymbol{D}_0$) and the vector $\boldsymbol{D}_1$ (see Eq. 8 of Ref. [164] for more details); thus, $\cos\vartheta = 1$ corresponds to pure electron-flavor content (and therefore no conversion) while $\cos\vartheta = -1$ corresponds to maximal flavor conversion, as allowed by the total lepton number conservation. An alternative approach to visualize the flavor evolution for the cases with and without damping is reported in the bottom panel of Fig. 33, where a parametric plot of the angular velocity $\dot{\vartheta}$ is shown as a function

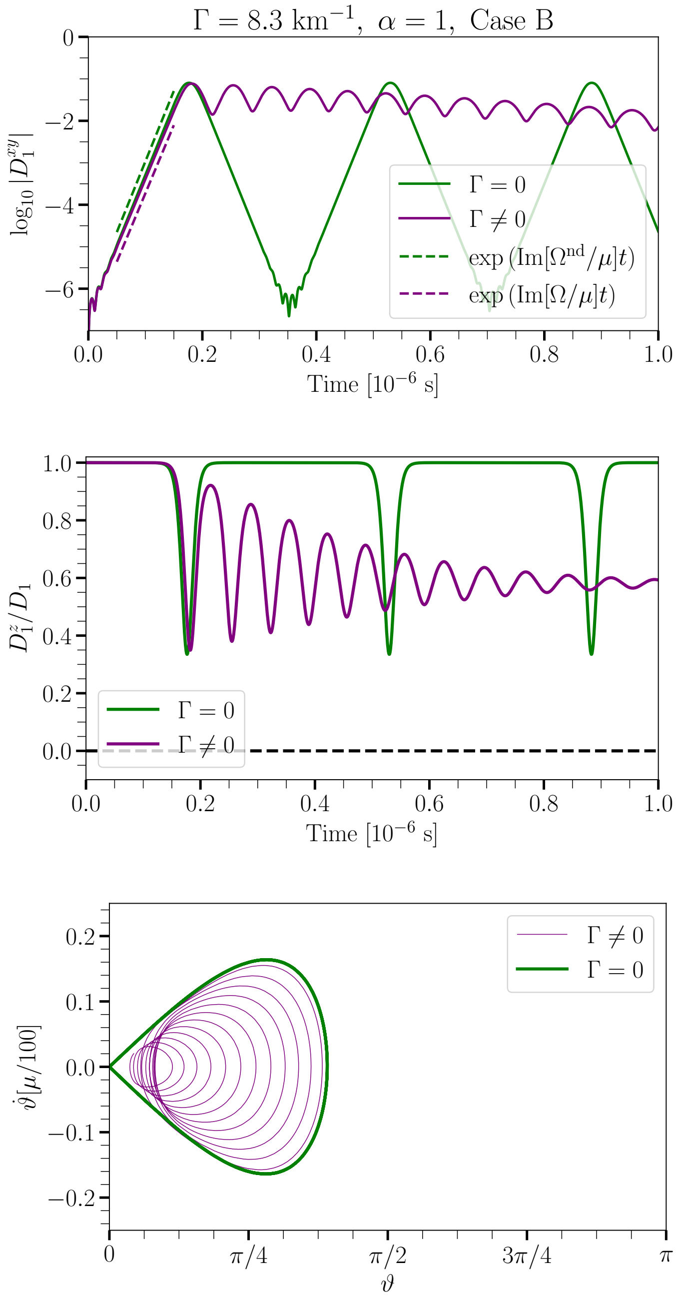

Figure 33: Flavor evolution for Case B without (green lines) and with (purple lines) damping, under the assumption of equal damping rates for ν and $\bar{\nu}$. *Top panel:* Evolution of the transverse components $|D_1^{xy}|$ (solid lines) and their corresponding growth rates $\mathrm{Im}[\Omega/\mu]$ (dashed lines). With no damping, we find a growth rate of $\mathrm{Im}[\Omega^{\mathrm{nd}}/\mu] = 2.58 \times 10^{-3}$, while with damping it is modestly modified to $\mathrm{Im}[\Omega/\mu] = 2.49 \times 10^{-3}$; this correspond to a 4% variation. *Middle panel:* Evolution of the z component of the lepton-number flux, D_1^z, where the effect of damping is visible in the non-linear regime. While the solution without damping periodically oscillates, the damped solution tends to reach an average steady state. *Bottom panel:* Parametric plot of $\dot{\vartheta}$ as a function of ϑ. The case without damping encloses the damped solution.

of the angular position ϑ. The solution with $\Gamma = \bar{\Gamma} = 0$ (bottom green line in Fig. 33) encloses the damped solution (purple line) as it reaches the steady state $\dot{\vartheta} \to 0$, $\vartheta \to 0$. The maximum excursion of the pendulum $\boldsymbol{D}_1$ from its initial orientation along the flavor axis is given by [164]:

$$\cos \vartheta_{\text{min}} = -1 + 2\sigma^2. \tag{6.26}$$

Here, σ is the spin parameter that is connected to the spin of the pendulum (no damping) through $S = 2\sigma\lambda$, where λ is the natural frequency of the pendulum. For a solution to be unstable, the spin parameter σ must be such that $\sigma < 1$ [164]. In the example presented in Fig. 33 (see lower panel), the ELN angular distribution is such that $\sigma = 0.817$ therefore $\cos \vartheta_{\text{min}} = 0.335$ (or $\vartheta_{\text{min}} \approx \pi/3$). When the damped solution reaches the steady state, the pendulum $\boldsymbol{D}_1$ is oriented along the flavor axis and conversions cease.

While in the $\Gamma = 0$ case, we have discussed the existence of a formal similarity of our system with a gyroscopic pendulum [164], for $\Gamma \neq 0$, there is no simple mechanical analogy, although some similarities are preserved. In fact, the damping term affects the pendulum-like behavior in the following way: it takes one pendulum configuration with a particular spin S to a configuration with a different spin S' until the transverse components of the polarization vectors are effectively damped. Thus, damping forces the polarization vectors to point along the z-direction as the steady state is reached and the spin S is restored to its initial value. However, to predict the final flavor configuration in the presence of damping, we need to move beyond the linear stability analysis.

6.3.2 *Average steady state*

The top left panel of Fig. 34 shows the final configuration reached by the system for a particular ELN crossing (Case B) and four different values of the damping rate, while the top right panel of Fig. 34 shows the evolution of the off-diagonal terms. One can see that the time taken from the system to achieve the steady state configuration is fixed by Γ. However, this does not affect the final flavor outcome.

The steady-state configuration depends on the initial ELN, as displayed in the bottom panels of Fig. 34. Since the off-diagonal terms can only exponentially shrink, as described by Eq. 6.16, our collision term cannot lead to a dynamical enhancement of the transverse components $|D_1^{xy}|$.

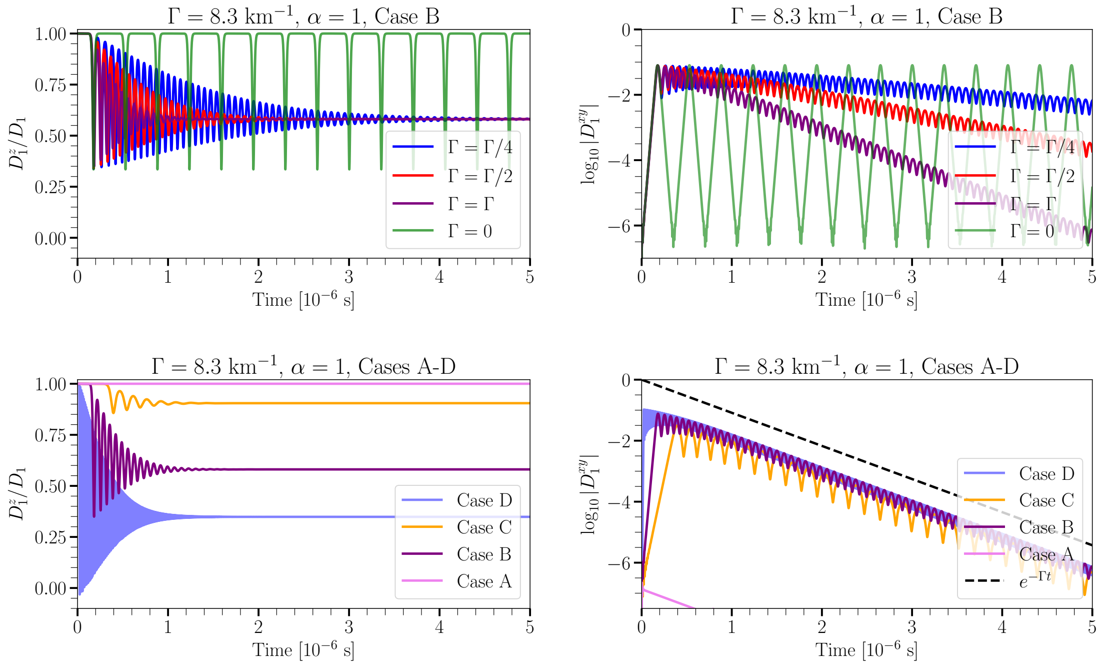

Figure 34: *Top panels:* Evolution of D_1^z/D_1 (left panel) and D_1^{xy} (right panel) for Case B, same damping rates for neutrinos and antineutrinos, for different values of Γ. The final flavor outcome at $t = 5 \times 10^{-6}$ s is the same for all configurations independent of the value of Γ. However, the time taken to achieve such a configuration depends on Γ. *Bottom panels:* Evolution of D_1^z/D_1 (left panel) and D_1^{xy} (right panel) for Cases A–D. The dashed line scaling as $\exp(-\Gamma t)$ mimics the descent of the transverse component $|D_1^{xy}|$; they all have the same slope, even the stable configuration such as Case A.

In practice, this means that if a configuration is stable in the absence of damping, such as Case A (pink curve in lower panels of Fig. 34), damping ($\mathcal{C} = \bar{\mathcal{C}}$) will not affect the stability of the solution, as seen by the exponential decrease of the transverse component (pink curve) in the bottom right panel of Fig. 34. However, this is not necessarily the case for scenarios with different collision terms for neutrinos and antineutrinos i.e. $\mathcal{C} = \alpha\bar{\mathcal{C}}$, where the stability of the solution is sensitive to the value of α (see Sec. 6.4).

In order to gain insight into the final flavor outcome with damping, one can compute an expression for the final length of the shrinking pendulum. We can multiply both sides of Eq. 6.16 by v_i, sum over the velocity variable to obtain an equation for $\dot{\boldsymbol{D}}_1$

$$\dot{\boldsymbol{D}}_1 = \mu \boldsymbol{D}_2 \times \boldsymbol{D}_1 - \Gamma \boldsymbol{D}_1^{xy} \,. \tag{6.27}$$

Computing the dot product $\dot{\boldsymbol{D}}_1 \cdot \boldsymbol{D}_1$ reveals that

$$\frac{1}{2}\frac{d}{dt}|\boldsymbol{D}_1|^2 = -\Gamma|\boldsymbol{D}_1^{xy}|^2 , \tag{6.28}$$

where the cross-product has vanished. By integrating both sides over t, we obtain

$$\frac{|\boldsymbol{D}_1|_{t_1}}{|\boldsymbol{D}_1|_{t_0}} = \sqrt{1 - \frac{2\Gamma}{|\boldsymbol{D}_1|^2_{t_0}} \int_{t_0}^{t_1} dt |\boldsymbol{D}_1^{xy}|^2} . \tag{6.29}$$

The equation above implies that, in order to extract $|\boldsymbol{D}_1|_{t_1}$, one needs to know the solution with damping for $\boldsymbol{D}_1^{xy}$. Alternatively, instead of solving the EOM for $\boldsymbol{D}_1^{xy}$, an empirical expression for the final steady state that matches the numerical solutions regardless of the chosen configuration is the following:

$$\cos\vartheta_{\rm ave} = A + (1-A)\cos\vartheta_{\rm min} , \tag{6.30}$$

where $\cos\vartheta_{\rm min}$ is defined as in Eq. 6.26 and A is a constant. In the presence of collisional damping, $A = 0.37$. The horizontal solid line in Fig. 34 corresponds to the average (steady state) value we predict empirically. In order to highlight the predictive power of Eq. 6.30, Table 2 shows the values of $\cos\vartheta_{\rm min}$ and $\cos\vartheta_{\rm ave}$ for Cases A–D, which are in perfect agreement with the numerical solutions.

Table 2: Values for the spin parameter σ, the lowest point of the pendulum $\cos\theta_{\rm min}$ and the final (average) steady state value $\cos\theta_{\rm ave}$. Cases B–D are unstable, while Case A is stable.

Case	σ	$\cos\vartheta_{\rm min}$	$\cos\vartheta_{\rm ave}$
A	—	—	—
B	0.817	$+0.335$	0.581
C	0.962	$+0.849$	0.904
D	0.694	-0.034	0.348

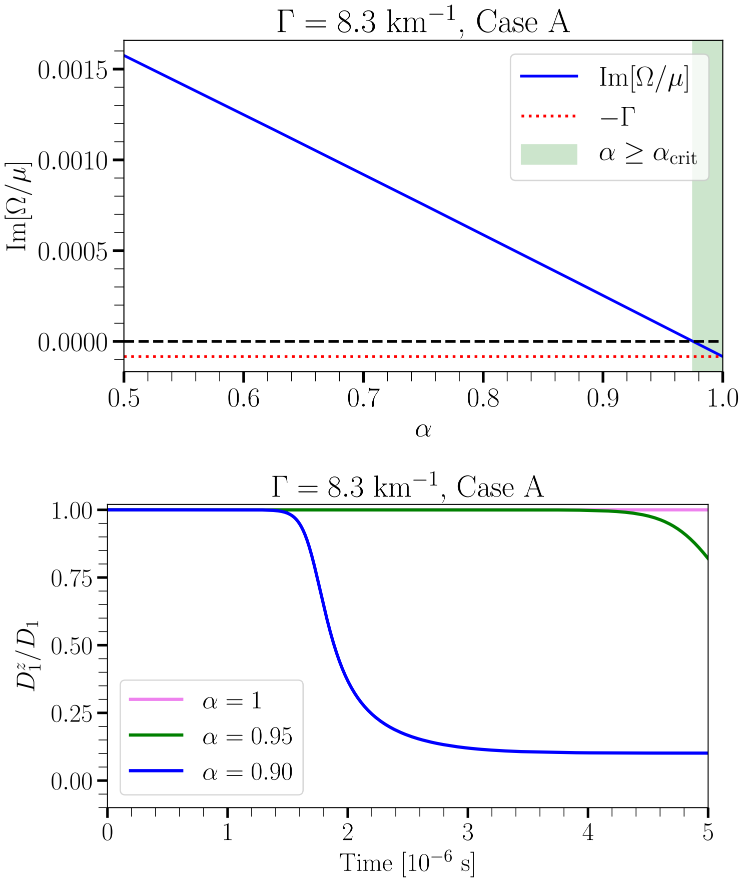

Figure 35: Flavor evolution for Case A under the assumption of different damping rates for neutrinos and antineutrinos. *Top panel:* Growth rate as a function of α. Case A is stable in the absence of damping and with damping for $\alpha = 1$. For $\alpha = 1$, one finds $\mathrm{Im}[\Omega] = -\Gamma$ and the solutions grow exponentially (unstable solutions) for $\alpha < \alpha_{\mathrm{crit}}$ which we found to be $\alpha_{\mathrm{crit}} \simeq 0.975$. The stable region is marked by the green shaded area where $\alpha \geq \alpha_{\mathrm{crit}}$. *Bottom panel:* Temporal evolution of D_1^z/D_1 for three selected values of α. Allowing $\alpha \neq 1$, the flavor solutions become unstable in agreement with Fig. 35.

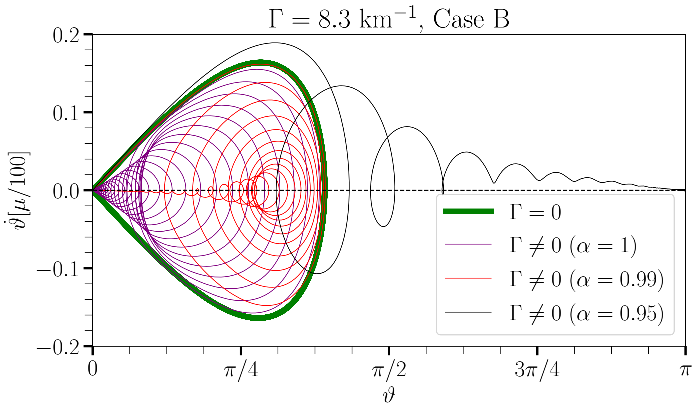

Figure 36: Parametric plot of $\dot{\vartheta}$ as a function of ϑ for Case B for different damping rates for neutrinos and antineutrinos. For $\alpha \neq 1$, the trajectory escapes the "envelope" defined by the pendulum solution (green line), flipping the orientation of the polarization vector while shrinking.

6.4 DIFFERENT DAMPING RATES FOR NEUTRINOS AND ANTINEUTRINOS

Equations 6.16 and 6.17 can be combined to obtain a set of equations for the vectors $\boldsymbol{S}(v_i)$ and $\boldsymbol{D}(v_i)$ for the case of unequal damping rates $\mathcal{C} = \alpha\mathcal{C}$:

$$\begin{aligned} \dot{\boldsymbol{D}}(v_i) &= \mu v_i \boldsymbol{D}(v_i) \times \boldsymbol{D}_1 - \frac{\Gamma}{2}\left[(\boldsymbol{S}^{xy}(v_i) + \boldsymbol{D}^{xy}(v_i)) - \alpha(\boldsymbol{S}^{xy}(v_i) - \boldsymbol{D}^{xy}(v_i))\right] , && (6.31) \\ \dot{\boldsymbol{S}}(v_i) &= \mu v_i \boldsymbol{S}(v_i) \times \boldsymbol{D}_1 - \frac{\Gamma}{2}\left[(\boldsymbol{S}^{xy}(v_i) + \boldsymbol{D}^{xy}(v_i)) + \alpha(\boldsymbol{S}^{xy}(v_i) - \boldsymbol{D}^{xy}(v_i))\right] , && (6.32) \end{aligned}$$

For $\alpha = 1$, the equations for $\boldsymbol{D}(v_i)$ are a closed set of equations [155, 164] as opposed to the case with $\alpha \neq 1$. The fact that $\boldsymbol{D}(v_i)$ and $\boldsymbol{S}(v_i)$ couple to each other for $\alpha \neq 1$ gives rise to flavor instabilities where there were none for $\alpha = 1$.

Figure 35 demonstrates the effect of the coupling between $\boldsymbol{D}(v_i)$ and $\boldsymbol{S}(v_i)$ as in Eqs. 6.31 and 6.50. We focus on Case A, which is stable for $\mathcal{C} = 0$ and $\mathcal{C} = \bar{\mathcal{C}}$ ($\alpha = 1$) and explore its flavor evolution for $\mathcal{C} = \alpha\bar{\mathcal{C}}$ ($\alpha \neq 1$). In the top panel of Fig. 35, we show the dependence of the growth rate $\mathrm{Im}[\Omega/\mu]$ on the magnitude of α. For $\alpha = 1$, the growth rate equals $-\Gamma$ (red dotted line) and the solution is stable, in agreement with Fig. 34. Eventually, α reaches the critical value $\alpha_{\mathrm{crit}} \simeq 0.975$ for which the growth rate transitions from $\mathrm{Im}[\Omega/\mu] < 0$ to $\mathrm{Im}[\Omega/\mu] > 0$, making the solution unstable. The growth rates of Case A are larger for smaller values of α; hence systems with asymmetric damping rates between neutrinos and antineutrinos lead to solutions that grow faster.

In the bottom panel of Fig. 35, we show the evolution of the normalized z-component of the ELN flux vector D_1^z/D_1 for three different values of α such that the new unstable region $\alpha < \alpha_{\mathrm{crit}}$ is illustrated. Even for a modest asymmetry between the neutrino and antineutrino damping rate ($\alpha = 0.95$, green line), a significant amount of flavor is converted in the first 5×10^{-6} s. A more extreme asymmetry ($\alpha = 0.90$, blue line) leads to almost flavor equipartition within the same time interval.

In Fig. 36, we show the phase space dynamics for different values of α for Case B. For $\alpha \neq 0$, the phase space trajectories escape the "envelope" subtended by the undamped solution (green line). For instance, for $\alpha = 0.95$, the phase space trajectory escapes the envelope during the first iterations of the evolution, reaching its steady state $(\dot{\vartheta} = 0)$. At that point, the polarization vector $\boldsymbol{D}_1$ points downwards ($\vartheta = \pi$) in contrast to the $\alpha = 1$ case where $\boldsymbol{D}_1$ points upwards ($\vartheta = 0$).

6.5 DEPENDENCE OF THE FINAL FLAVOR CONFIGURATION FROM THE ELN CROSSING

In this section, we generalize our findings to a family of ELN distributions, modeled as described in Eqs. 6.14 and 6.15. The ensemble of ELN angular configurations determined by the parameters a and b can be represented with a two-dimensional grid as shown in Fig. 37. The parameter a controls the relative normalization between neutrinos and antineutrinos, while b parametrizes how forward-peaked the angular distributions are. Running over a range of values of a and b allows us to explore a family of single-crossed ELN spectra systematically. Each point in the plane represents an ELN configuration for which we compute $\cos\vartheta_{\mathrm{ave}}$ through Eq. 6.30. We find that the analytical results match very well the final flavor outcome obtained numerically.

Figure 37 shows contour plots of $D_1^z/D_1|_{\mathrm{ave}}$, where $D_1|_{\mathrm{ave}}$ is computed in the plane spanned by the parameters a and b. The average is calculated within a time interval $\Delta t = 2.5 \times 10^{-6}$ s to ensure that most configurations have reached a steady state as confirmed by Fig. 34. We consider the following three scenarios: no damping ($\Gamma = 0$, top panel), equal damping rates for neutrinos and antineutrinos (middle panel), and unequal damping rates for neutrinos and antineutrinos ($\alpha = 0.9$, bottom panel). For $\Gamma = 0$ (top panel of Fig. 37), a large portion of the parameter space has an average value of $D_1^z/D_1|_{\mathrm{ave}} \simeq 0.95$, since conversions are periodic. For the case with

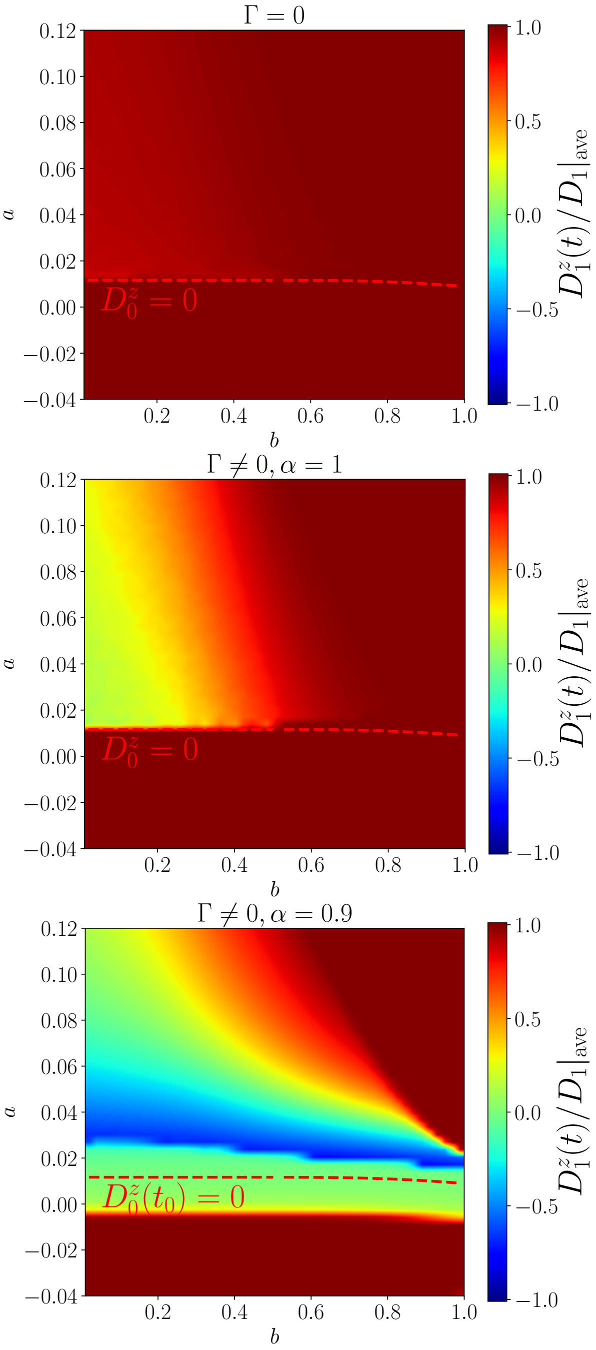

Figure 37: Flavor evolution for a wide range of single-crossed ELN spectra characterized by the parameters a and b (see Eqs. 6.14 and 6.15). From top to bottom respectively, we present the case of no damping ($\Gamma = 0$), same damping rates for neutrinos and antineutrinos ($\Gamma \neq 0, \alpha = 1$), and unequal damping rates for neutrinos and antineutrinos ($\Gamma \neq 0, \alpha = 0.9$). The locus of vanishing lepton number $D_0^z = 0$ (Eq. 6.10) is marked with a red dashed line. The contours represent the time averaged D_1^z/D_1 after 2.5×10^{-6} s. The red regions show little to no conversions, while blue shows significant flavor transitions. In agreement with Fig. 35, the ($\Gamma \neq 0, \alpha \neq 1$) case displays the largest regions of the parameter space where flavor conversion occurs, including cases otherwise stable when $\Gamma = 0$ or $\alpha = 1$.

equal damping rates for neutrinos and antineutrinos (middle panel of Fig. 37), flavor decoherence forces the pendulum to settle around the value fixed by $\cos\vartheta_{\text{ave}}$ (Eq. 6.30), without returning to the $\cos\vartheta = 1$ (stable) configuration, in agreement with the results reported in Figs. 33 and 34. Therefore, $D_1^z/D_1|_{\text{ave}}$ is smaller, reaching $D_1^z/D_1|_{\text{ave}} \simeq 0$ for a large region of the parameter space, especially for forward-peaked ELN configurations (small values of b). The most extreme scenario is the one obtained for unequal damping rates for neutrinos and antineutrinos (bottom panel of Fig. 37), where the average value of $D_1^z/D_1|_{\text{ave}}$ can even reach negative values (blue region) $D_1^z/D_1|_{\text{ave}} \simeq -0.9$, in agreement with our findings in Fig. 35 where the vector $\boldsymbol{D}_1$ can change its orientation for smaller values of α. For the case with unequal damping rates for neutrinos and antineutrinos, the lepton number is not a constant of motion; see Eq. 6.31. For these systems, we show the locus of initially-vanishing lepton number $D_0^z(t_0) = 0$, which helps visualize the deviation from the pendulum-like solution and well as where new instabilities arise as a result of $\alpha \neq 1$. In the other cases with no damping and equal damping rates (upper and middle panels), the lepton number D_0^z is strictly conserved, and the locus of $D_0^z = 0$ remains constant. No conversions are allowed in this region, in agreement with the stability criteria for the gyroscopic pendulum [164].

6.6 STATIONARY NON-HOMOGENEOUS SYSTEM

In this section, we extend our findings to stationary and non-homogeneous systems, while we focused on non-stationary and homogeneous configurations in the previous sections. Our results also apply to stationary non-homogeneous systems, as pointed out in Ref. [155]. However, we do not approximate the equations to their first multipoles as in Ref. [155]; instead rely on the formal pendulum analogy developed in Ref. [164], which alleviates the challenges reported in Ref. [155].

In the case of a stationary non-homogeneous system, the roles of $\boldsymbol{D}_0$ and $\boldsymbol{D}_1$ are swapped; the EOMs for a stationary system are analogous to those of a non-stationary homogeneous system (Eq. 6.16), with some differences, however:

$$\boldsymbol{D}'_v = -\frac{\mu}{v}\boldsymbol{D}_v \times \boldsymbol{D}_0 - \Gamma \boldsymbol{D}_v^{xy} \, , \tag{6.33}$$

where the primed notation indicates the spatial derivative d/dz, in contrast to previous sections, now the spatial derivative appears in the EOMs instead of the time derivative (dotted notation). The co-rotation is about $\boldsymbol{D}_1$ with frequency μD_1, contrary to the homogeneous case where the precession is around $\boldsymbol{D}_0$. The global precession around $\boldsymbol{D}_1$ has been rotated away in Eq. 6.33. From Eq. 6.33, we see that $\boldsymbol{D}_1' = 0$ and $D_0' = 0$ because of the extra factor of v^{-1}. Now the pendulum is defined by $\boldsymbol{D}_0$ with conserved length D_0, and gravity is represented by $\boldsymbol{D}_1$. The dynamics is completely analogous to what is discussed in Sec. 6.2.2, but the roles of $\boldsymbol{D}_0$ and $\boldsymbol{D}_1$ are swapped.

Focusing on the case without damping ($\Gamma = 0$), one can solve the EOMs numerically and contrast the numerical solution to the analytical prediction for $\cos\vartheta_{\text{min}}$. For this purpose, we rely on the linear stability analysis for a stationary and non-homogeneous system which we can adapt from Appendix D of Ref. [164]. We use plane-wave solutions of the form $S_v(t,z) = Q_v\, e^{-i(\Omega t - Kz)}$, where Q_v depends on the wave vector (Ω, K) and K is the wavevector in the z direction. The EOM in the Fourier space is then

$$[\underbrace{(\Omega - \Lambda_0)}_{\omega} - v\underbrace{(K - \Lambda_1)}_{k}]\,Q_v = -\mu \int du\, g_u \left(Q_u - vuQ_u\right) . \tag{6.34}$$

For a physically homogeneous system ($K = 0$) we have $k = -\Lambda_1$. However, we are interested in a stationary system ($\Omega = 0$) which implies $\omega = -\Lambda_0$. The r.h.s. of Eq. A.26 has the structure $\beta_1 - \beta_2 v$, where β_1 and β_2 are numbers that depend on the initial ELN spectrum, but not on v. Therefore, the eigenfunction must have the following form

$$Q_v = \frac{\beta_1 - \beta_2 v}{\omega - vk} , \tag{6.35}$$

implying

$$\beta_1 - \beta_2 v = -\int du\, G_u \frac{\beta_1 - \beta_2 u - vu(\beta_1 - \beta_2 u)}{\omega - uk} , \tag{6.36}$$

where we have now absorbed μ in $G_v = \mu\, g_v$. This equation must be true regardless of the value of v therefore, one has two equations in terms of the moments I_n

$$\underbrace{\begin{pmatrix} I_0 + 1 & -I_1 \\ -I_1 & I_2 - 1 \end{pmatrix}}_{\Pi} \begin{pmatrix} \beta_1 \\ \beta_2 \end{pmatrix} = 0 , \tag{6.37}$$

where the quantities I_n are defined as

$$I_n(\omega, k) = \int du\, G_u \frac{u^n}{\omega - uk} , \tag{6.38}$$

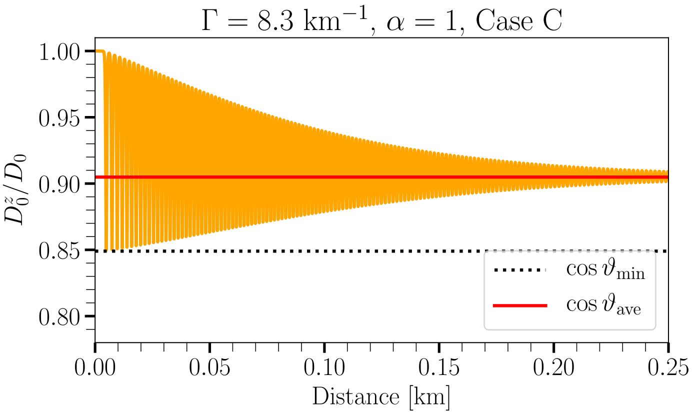

Figure 38: Evolution of D_0^z/D_0 (solid orange line) as a function of the distance for a stationary non-homogeneous system. We assume the same ELN angular distribution as for case C (see orange curve in bottom panels of Fig. 34), $\mu = 10^5$ km^{-1} and $\Gamma = 8.3$ km^{-1}. After roughly 0.25 km, the system reaches its steady state. The dotted line marks the value of $\cos\vartheta_{\rm min}$ (Eq. 6.46), while the red solid line indicates $\cos\vartheta_{\rm ave}$ (Eq. 6.47). Note that the values of $\cos\vartheta_{\rm min}$ and $\cos\vartheta_{\rm ave}$ (see Table 2) are the same for both homogeneous and non-homogeneous cases, reflecting the roles of $\boldsymbol{D}_0$ and $\boldsymbol{D}_1$ are swapped while keeping the flavor evolution identical.

which we can evaluate for the stationary case i.e.

$$I_n(\omega = -\Lambda_0, k) = \int du\, G_u \, \frac{u^n}{-\Lambda_0 - uk} \,. \tag{6.39}$$

The dispersion relation results from requiring not trivial solutions i.e. that the matrix is not invertible

$$\det \Pi = (I_0 + 1)(I_2 - 1) - I_1^2 = 0 \,. \tag{6.40}$$

We solve the equation above to look for solutions such that $k = k_p + i\kappa$ has a non-vanishing imaginary component κ.

Similarly, there are simplified conditions from the dispersion relation as for the homogeneous case. Let us evaluate the moments for the stationary case, i.e. $\omega = -\Lambda_0$

$$I_0(-\Lambda_0, k) = \frac{\Lambda_0(-\Lambda_0 + \Lambda_0) + k(k + \Lambda_1)}{-\Lambda_0(-\Lambda_0 + \Lambda_0) - k(k + \Lambda_1)} = -1 \,. \tag{6.41}$$

Using the dispersion relation, this implies that

$$I_1(-\Lambda_0, k) = 0 \,, \tag{6.42}$$

and additionally substituting $I_1 = 0$ in $\Lambda_1 = \omega I_1 - k I_2$ we get

$$I_2(-\Lambda_0, k) = \frac{\Lambda_1}{k} \,. \tag{6.43}$$

Moreover, for $I_0 = -1$, $I_1 = 0$ and $I_2 = \Lambda_1/k$, one can show that $\beta_1 = 0$ and $\beta_2 \neq 0$ in Eq. A.29. The latter means that the eigenfunction must take the following form

$$Q_v(\omega = -\Lambda_0, k) = \frac{\beta_2 v}{\Lambda_0 + vk} \,, \tag{6.44}$$

which implies that the solution for the transverse components is the following

$$D_v^{xy}(z) = f \, \frac{v \, g_v}{D_0 + vk} \, e^{ikz} \,. \tag{6.45}$$

By solving the equations numerically and comparing them with the prediction of the lowest point, we find that the definition of $\cos\vartheta_{\min}$ still offers an excellent estimation of the lowest point of the stationary non-homogeneous pendulum

$$\cos\vartheta_{\min} = -1 + 2\sigma^2 = -1 + 2\frac{k_p^2}{k_p^2 + \kappa^2} \,, \tag{6.46}$$

where k_p and κ are the real and imaginary components of the eigenfrequency k, respectively.

We can extend our results for the average value of flavor conversions in the presence of damping to the case of stationary systems. Thus, the equivalent of Eq. 6.30 for stationary systems is given by

$$\cos\vartheta_{\text{ave}} \quad = \quad A + (1 - A)\cos\vartheta_{\min} \,, \tag{6.47}$$

with $\cos\vartheta_{\min}$ as found in Eq. 6.46 and $A = 0.37$ as in Eq. 6.30.

In Fig. 38 we show the evolution of the normalized z-component D_0^z/D_0 as a function of distance, and show the prediction of the steady state value $\cos\vartheta_{\text{ave}}$ as in Eq. 6.47.

6.7 CONCLUSIONS

Our earlier work [164] shows that it is possible to exploit a formal analogy of the neutrino EOM with the ones of a gyroscopic pendulum, allowing us to predict the final flavor configuration analytically for a homogeneous and axially symmetric system. In this work, we follow up on our previous findings and investigate the role of damping due to random collisions in the final flavor configuration. We assume spatial homogeneity and axial symmetry and work in the two-flavor framework. In the presence of damping, the ELN lepton number vector, $\boldsymbol{D}_0$, is conserved and plays the role of "gravity," exerting a torque on the dynamical ELN flux vector, $\boldsymbol{D}_1$.

Although no simple gyroscopic pendulum analogy can be found in the presence of damping, most of the features of the gyroscopic pendulum outlined in Ref. [164] are preserved. We provide a simple analytical formula to estimate the final steady state achieved by the system and show that it is a simple linear combination of the one found to predict the lowest point of the pendulum in Ref. [164]. Our predictions are in excellent agreement with our numerical computations for a wide range of single-crossings ELN spectra.

For equal damping rates for neutrinos and antineutrinos, the final flavor outcome differs from the scenario without damping. In particular, we find that the same steady state flavor configuration is reached in the presence of damping and independently of the particular values of the damping rate Γ (as long as $\mu \gg \Gamma$). However, the time the system takes to reach such a configuration is a function of the damping rate. When the damping rates for neutrinos and antineutrinos are different, new regions of instability appear.

Our findings for homogeneous systems also apply to stationary but non-homogeneous systems. In particular, the evolution of the ELN number component D_0^z/D_0 as a function of the spatial coordinate for the non-homogeneous system is analogous to that of the ELN flux component D_1^z/D_1 in time for the homogeneous one, reflecting on the fact that the roles of $\boldsymbol{D}_0$ and $\boldsymbol{D}_1$ are swapped.

This work offers new insight into the flavor evolution of neutrinos in dense neutrino environments. Our analytical findings shed light on the rich phenomenology of fast flavor conversion in the presence of random collisions, offering simple predictions on the final flavor outcome.

6.8 CRITICAL OUTLOOK

6.8.1 *Overview and main findings*

Neutrino flavor conversion is well understood when dealing with the propagation of a beam of neutrinos in vacuum or matter (Sec. 2.2.1 and 2.2.2). However, there is another class of problems where we are interested in the evolution of a neutrino ensemble that simultaneously mixes and scatters in a medium, as it is the case in core-collapse supernovae (Chapter 3) or compact binary merger remnants (Chapter 4). In these scenarios, the problem is hard to formulate in terms of a beam since we do not expect coherent conversions of the wave function under stochastic interactions with the background. The central question here is the following: if one has the state $\alpha |\nu_e\rangle + \beta |\nu_x\rangle$ and a collision occurs, is there after the collision a linear superposition again or an incoherent mixture? This question was the central work of Ref. [75], where the treatment of neutrino flavor conversions in the presence of random scatterings was investigated for the first time [76]. When a matter background is included, two types of effects are at play:

- One effect would be an index of refraction which results in a medium-induced contribution to the evolution of the Hamiltonian, changing the precession speed and the axis of rotation (see Fig. 11). Under special conditions, the vacuum $\boldsymbol{B}$ and matter $\boldsymbol{L}$ vectors point in opposite directions and are about the same size, leading to MSW resonance transformation (Sec. 2.2.2).
- The second effect is the shrinkage of the polarization vector $\boldsymbol{P}$ due to collisions that destroy the coherence of evolution. The assumption of flavor conversion in the scattering on the medium implies that the shrinking of the polarization vector $\boldsymbol{P}$ must be perpendicular to the z-axis. Note that the field of neutrino flavor conversion in the presence of momentum-changing collisions is very active [150, 152, 184, 233, 251–253, 256–258]. However, we focus on the effect of collisions destroying the coherence in the evolution while conserving flavor to describe the dynamics with the gyroscopic pendulum of Chapter 5.

We are concerned with the second of these effects, which is induced by stochastic collisions on the medium. The evolution of $\boldsymbol{P}$ can then be formulated as follows [75]:

$$\dot{\boldsymbol{P}} = \boldsymbol{H} \times \boldsymbol{P} - \Gamma \boldsymbol{P}^{xy}, \tag{6.48}$$

where, in the simplest of cases, $\mu = 0$ and we have $\boldsymbol{H} = \omega \boldsymbol{B} + \lambda \boldsymbol{L}$. The quantity Γ is the damping parameter that measures the rate of loss of coherence in the system. The "transverse" vector $\boldsymbol{P}^{xy}$ is given by $\boldsymbol{P}^{xy} = (P^x, P^y, 0)$. In reality, the damping parameter Γ is a function of scattering amplitudes (see Eq. 5 and 6 of Ref. [76]); however, for this thesis, we regard Γ as a free parameter which we can vary. The damping parameter Γ can be understood as a rate parameter that gauges the effectiveness of collisions in interrupting the flavor conversion of the two states $|\nu_e\rangle$ and $|\nu_x\rangle$, i.e., the frequency at which random collisions hinder the coherent evolution of the wave function. If the damping parameter is smaller than the characteristic frequency of the system, then we are in the *weak damping* regime, and oscillations are damped. However, in the *strong damping* regime, Γ is much larger than the characteristic time scale of oscillations, and $\boldsymbol{P}$ becomes fixed to the z-axis because $\boldsymbol{P}^{xy}$ is quickly diminished: the system is measured so often than it "freezes" and the evolution of the polarization vector is blocked similarly as in the Zeno effect [76].

In the work presented in this Chapter, we focus on the interplay between neutrino fast flavor conversion (Sec. 2.2.7.2) and random collisions with the background medium under the approximation of *weak damping*. To some extent, such a system can be described using the tools developed for the fast gyroscopic pendulum in Chapter 5. We study the influence of weak damping on the neutrino equations of motion and look for analytical predictions on the final decohered state of the polarization vectors.

The equations of motion that describe neutrino fast flavor conversion in the presence of collisional damping can be expressed in terms of the difference $\boldsymbol{D}_v = \boldsymbol{P}_v - \bar{\boldsymbol{P}}_v$ and the sum $\boldsymbol{S}_v = \boldsymbol{P}_v + \bar{\boldsymbol{P}}_v$ of the polarization vectors,

$$\dot{\boldsymbol{D}}(v) = \mu v \boldsymbol{D}(v) \times \boldsymbol{D}_1 - \frac{\Gamma}{2}\left[(\boldsymbol{S}^{xy}(v) + \boldsymbol{D}^{xy}(v)) - \alpha(\boldsymbol{S}^{xy}(v) - \boldsymbol{D}^{xy}(v))\right] , \tag{6.49}$$

$$\dot{\boldsymbol{S}}(v) = \mu v \boldsymbol{S}(v) \times \boldsymbol{D}_1 - \frac{\Gamma}{2}\left[(\boldsymbol{S}^{xy}(v) + \boldsymbol{D}^{xy}(v)) + \alpha(\boldsymbol{S}^{xy}(v) - \boldsymbol{D}^{xy}(v))\right] , \tag{6.50}$$

where Γ is the rate of collisions, μ is the strength of neutrino-neutrino interactions and α is a parameter that allows to have different collision rates for ν and $\bar{\nu}$ i.e. $\alpha = 1$ implies that the collision terms in the equations of motion are the same for neutrinos and antineutrinos $\mathcal{C} = \bar{\mathcal{C}}$, while $\alpha \neq 1$ implies that they are different by a multiplicative constant factor $\mathcal{C} = \alpha\bar{\mathcal{C}}$. Notice that for the special case where $\alpha = 1$ (equal damping rates for ν and $\bar{\nu}$) the equations reduce to $\dot{\boldsymbol{D}}_v = \mu v \boldsymbol{D}_v \times \boldsymbol{D}_1 - \Gamma \boldsymbol{D}_v^{xy}$ and the equation for $\boldsymbol{D}_v$ is self-contained, decoupling from that of $\boldsymbol{S}_v$ as demonstrated in Chapter 5.

The impact of α on the dynamics phase space is visible in Fig. 39, where we show the angular velocity $\dot{\vartheta}$ as a function of its angular position ϑ as time progresses. In flavor space, the angle ϑ is the angle between the flavor axis and the vector $\boldsymbol{D}_1$. Therefore, $\cos\vartheta = 1$ corresponds to pure

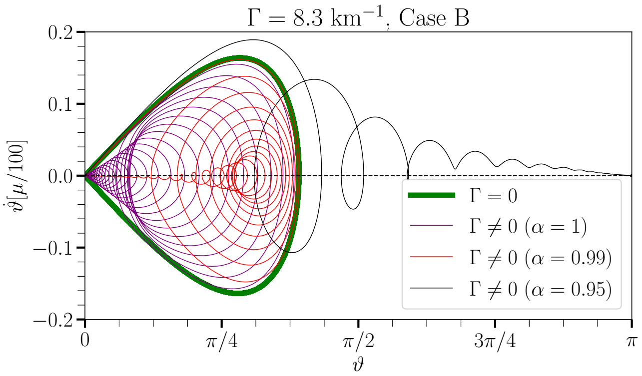

Figure 39: Phase-space dynamics for different damping terms using the same ELN spectra (case B). For values of $\alpha \neq 1$, the trajectory escapes the "envelope" defined by the pendulum solution (green line), flipping the orientation of the polarization vector while shrinking. For a comparison of the same quantities in the case of the gyroscopic pendulum, see Fig. 78 in Appendix A.

electron-flavor content while the opposite orientation $\cos\vartheta = -1$ corresponds to maximal flavor conversion.

In particular, for the case of equal damping rates $\alpha = 1$, we find an empirical expression for the final steady state that matches the numerical solutions regardless of the configuration chosen, namely

$$\cos\vartheta_{\text{ave}} = A + (1-A)\cos\vartheta_{\text{min}}\,, \tag{6.51}$$

where $\cos\vartheta_{\text{min}}$ is as defined in Eq. 5.13 in Chapter 5. In the presence of collisional damping, we report that a value of $A = 0.37$ can accurately predict the final flavor outcome of all the ELN angular distributions considered in this work. The horizontal solid line in Fig 40 corresponds to the average (steady state) value we predict empirically.

We report a perfect agreement between our prediction and our numerical simulations for a wide range of single-crossings ELN angular distributions. See for instance Fig. 40, where we compute the flavor evolution of D_1^z/D_1 for different ELN distributions labeled Cases A–D (same as Chapter 5). The final steady state is visible after $\sim 10^{-6}$ s, at which point the polarization vectors are parallel to the z-axis. Interestingly, Eq. 6.51 predicts the following values for the final steady states in Fig. 40: $\cos\vartheta_{\text{ave}} = 0.581$ (Case B), $\cos\vartheta_{\text{ave}} = 0.904$ (Case C), $\cos\vartheta_{\text{ave}} = 0.348$ (Case D), while Case A is stable, in good agreement with the results obtained from direct simulations.

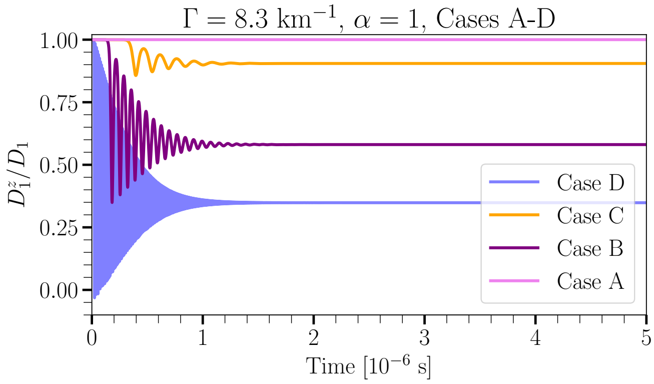

Figure 40: Time evolution of D_1^z/D_1 for a representative ELN angular distribution (Case B) with equal damping rates for neutrinos and antineutrinos ($\alpha = 1$). The benchmark parameter values are $\Gamma = 8.3\,\text{km}^{-1}$, $\mu = 10^5\,\text{km}^{-1}$ and $t_f = 5 \times 10^{-6}$ s.

The work presented in this chapter helps to build intuition on the rich phenomenology of fast flavor conversion in the presence of random collisions with a medium and provides analytical tools to predict the final steady state in terms of the undamped gyroscopic pendulum presented in Chapter 5.

6.8.2 *Limitations and future perspectives*

One clear limitation of this work is the simplicity of the collision terms in the EOMs, which affect only the coherence of the evolution while conserving neutrino flavor. Most of the current studies on the interplay between fast flavor conversion and collisions revolve around momentum-changing collision processes [150, 152, 184, 233, 251–253, 256–258], including the recent work in Ref. [259]. In order to establish a connection with those works a more complete modeling of the collision term is needed.

6.8.2.1 *Direction-changing collision term*

One could implement a collision term similar to that of Refs. [150, 252] where either an enhancement or damping of conversion was reported as a result of collisions:

$$\begin{aligned}\mathcal{C} &= \frac{\Gamma}{2}\left[\int_{-1}^{1} dv' \boldsymbol{P}(v') - 2\boldsymbol{P}(v)\right] \\ &= \frac{\Gamma}{2}\int_{-1}^{1} dv' \boldsymbol{P}(v') - \Gamma P^z(v)\hat{\boldsymbol{z}} - \underbrace{\Gamma \boldsymbol{P}^{xy}(v)}_{\text{this work}}. \end{aligned} \tag{6.52}$$

The first and second terms in the last line of Eq. 6.52 are the contributions that will change the neutrino flavor, while the third term is the transverse contribution to the evolution of the polarization vectors implemented in this Chapter. Note that the collision term in Eq. 6.52 is an approximation of the full collision term in Eq. 2.74, which is in practice computationally very expensive. The approximated collision term in Eq. 6.52, however, captures the change of direction in the velocity of (anti)neutrinos due to collisions [150], which is at the moment absent in the work of this Chapter. We foresee, however, that a simple analogy in terms of the gyroscopic pendulum might not be possible, or at least it is not obvious how to proceed at first glance. However, it is interesting to investigate limiting scenarios where the complicated dynamics introduced by Eq. 6.52 could be captured. More work along this line is still needed to find analytical estimations of the final flavor outcome of more detailed collision terms than the one presented in this Chapter.

Part III

NUMERICAL MODELING AND PHENOMENOLOGY OF NEUTRINO FAST FLAVOR CONVERSION

7

NON-HOMOGENEOUS NEUTRINO GASES IN THE NON-LINEAR REGIME

Based on: Shashank Shalgar, **Ian Padilla-Gay**, Irene Tamborra, *Neutrino propagation hinders fast pairwise flavor conversions*, JCAP06(2020)048, arXiv:1911.09110

ABSTRACT Neutrino flavor conversions may dramatically affect the inner working of compact astrophysical objects as well as the synthesis of the heavier elements. We present the first sophisticated numerical solution of the neutrino flavor conversion within a (2+1+1) dimensional setup: we include the advective term in the neutrino equations of motion and track the flavor evolution in two spatial dimensions, one angular variable, and time. Notably, the advective term hinders the development of neutrino pairwise conversions, if the conditions favoring such conversions (i.e., crossings between the angular distributions of ν_e and $\bar{\nu}_e$ or a non-negligible flux of neutrinos traveling backward with respect to the main propagation direction) exist for time scales shorter than the typical time scale of the advective term. As a consequence, fast pairwise conversions can only occur when the conditions favoring flavor conversions are self-sustained and global, such as the ones induced by the lepton emission self-sustained asymmetry (LESA) in core-collapse supernovae. Our work highlights the major impact of the dynamical evolution of the neutrino field on the growth of flavor instabilities and the strong interplay between classical and quantum effects. Critical limitations of the linear stability analysis, used to predict neutrino flavor instabilities, are also pointed out.

7.1 INTRODUCTION

In the interior of neutrino dense astrophysical environments, such as neutron star mergers and core-collapse supernovae (SNe), neutrinos experience a non-negligible potential due to the presence of other neutrinos. This potential is analogous to the one due to electrons in the well known Mikheyev-Smirnov-Wolfenstein (MSW) effect [59, 65]. The neutrino-neutrino scattering gives rise to an extremely fascinating phenomenology, inducing non-linear effects in the neutrino equations of motion [82, 88]. Notably, as a result of the non-linear nature of the evolution equations, the flavor evolution of neutrinos with different momenta is correlated.

The non-linearity of the neutrino equations of motion in compact astrophysical objects makes the solution of the neutrino flavor evolution extremely challenging, even when unrealistic simplifying assumptions are made. One of the first successful self-consistent calculations of neutrino flavor evolution including neutrino-neutrino interactions has been performed assuming spherical symmetry and instantaneous decoupling of all neutrino flavors at the same radius [83, 89–91, 260], the so-called "neutrino-bulb model." Despite being extremely simplified, the calculation of neutrino flavor evolution within the bulb model still proves to be challenging. In fact, it requires the numerical solution of several millions of differential equations that may take up to several hundred CPU-hours depending on the desired accuracy.

Any relaxation of the assumptions of the neutrino-bulb model makes the numerical solution of the flavor problem unfeasible. However, semi-analytical techniques proved that the non-linear nature of the problem implies that the bulb model provides different results than the ones obtained when some of the assumptions of this model are relaxed [104, 110, 135, 261].

In addition, since the decoupling of different flavors occurs at different radii and neutrinos undergo flavor-dependent interactions, the initial angular distributions are flavor dependent. In some circumstances, this can lead to coherent pairwise conversion of neutrinos [129, 130, 133]. Pairwise conversions are fast in the sense that their characteristic time scale is proportional to the neutrino number density, instead than the typical neutrino vacuum frequency [133]. Favorable conditions for fast flavor conversions may occur in the proximity of the neutrino decoupling region [130, 133, 153, 262]. Therefore, fast pairwise conversions may have important implications for the neutrino-driven explosion mechanism in SNe as well as the nucleosynthesis of heavy elements.

One of the conditions that has been identified as being relevant to the development of fast pairwise conversions is the existence of crossings in the electron neutrino lepton number (ELN) or a non-negligible flux of neutrinos propagating in the backward direction [133, 160, 161]. In a spherically symmetric SN, the occurrence of ELN crossings in the proximity of the decoupling region requires a sharp radial evolution of the baryon density, with electron neutrino and antineutrino number densities being comparable [175, 239]. Moreover, localized regions of ELN crossings may also occur in the early SN stages. It is not clear whether in this case the neutrino flavor evolution may affect the SN physics on a macroscopic scale, or whether there are fast neutrino conversions at all [155, 239]. In neutron star mergers, the occurrence of ELN crossings seems to be favored by the more complex geometry and the natural excess of $\bar{\nu}_e$'s over ν_e's [196, 225].

The major implications of the eventual occurrence of fast pairwise conversions in compact astrophysical objects has triggered a remarkable effort from the community to better grasp this phenomenon [134, 146, 170, 171, 173–175, 239, 240], but there is a long road ahead. In fact, one of the major complications is related to the numerical solution of this problem with high enough spatial and angular resolution, as dictated by the high frequency imposed by the neutrino fast conversions.

Given the complications induced by the non-linear nature of the system, and due to the spontaneous breaking of spatial and axial symmetries [104, 110], a minimum of two spatial dimensions is required to properly grasp the physics of the system. We here present the first sophisticated (2+1+1) dimensional modeling of the fast pairwise conversions in compact astrophysical objects; we solve the equations of motion in two spatial dimensions, one angular variable, and time and we include the advective term in the equations of motion. Within a simplified framework mimicking patches of the dense SN core, we explore the time evolution of the neutrino and antineutrino distributions in the presence of localized ELN crossings and of extended regions of ELN crossings similar to the ones induced by the lepton emission self-sustained asymmetry (LESA) [263].

The main goal of our work is to investigate under which conditions flavor instabilities may grow within a dynamical system. To do that, we explore two different scenarios reproducing global and localized regions of ELN crossings similar to the ones found in hydrodynamical simulations of SNe [170, 173–175, 263]. We also introduce the “instability parameter” and generalize the criteria under which fast pairwise conversions may occur.

This paper is organized as follows. In Sec. 7.2 we discuss the conditions favoring the occurrence of fast pairwise conversions proposed in the literature and adapt them to our (2+1+1) dimensional model. We also provide a generalization of the criteria leading to favorable conditions for fast conversions by introducing the “instability parameter.” In Sec. 7.3, we describe the setup of our (2+1+1) model and its numerical implementation. In Sec. 7.4, for the first time, we explore the impact of the advective term on the ELN evolution and on the growth of flavor instabilities. We then explore the flavor evolution when one localized ELN excess occurs and in the presence of an extended stripe of ELN crossings. Finally, an outlook of our work and conclusions are presented in Sec. 7.5.

7.2 FAST PAIRWISE NEUTRINO FLAVOR CONVERSION

The non-linearity induced by the neutrino-neutrino interactions makes the flavor evolution strongly dependent on the geometry and the number of dimensions of the system. Since at least two spatial dimensions are required for exploring any eventual effect of the advective term on the neutrino angular distributions, we explore the evolution of the (anti)neutrino angular distributions in time, within a two-dimensional (2D) box, and for one angular variable. In this Section, we introduce the neutrino equations of motion in the 2D box and generalize the criteria leading to fast pairwise conversions by introducing the “instability parameter.”

7.2.1 *Equations of motion*

Our system consists of a 2D box with width and height given by L_x and L_y and periodic boundary conditions. For each point (x, y) in the box, 2×2 density matrices describe the neutrino and antineutrino fields, respectively, at time t:

$$\rho(\vec{x}, \theta, t) = \begin{pmatrix} \rho_{ee} & \rho_{ex} \\ \rho_{ex}^* & \rho_{xx} \end{pmatrix} \quad \text{and} \quad \bar{\rho}(\vec{x}, \theta, t) = \begin{pmatrix} \bar{\rho}_{ee} & \bar{\rho}_{ex} \\ \bar{\rho}_{ex}^* & \bar{\rho}_{xx} \end{pmatrix} . \tag{7.1}$$

The density matrix of neutrinos is normalized such that $\mathrm{tr}(\rho) = 1$ and we fix the asymmetry between neutrinos and antineutrinos such that $\mathrm{tr}(\bar{\rho}) = a$. For each point (x, y) in the box, the (anti)neutrino field has a distribution in momentum. For the sake of simplicity and since we intend to focus on fast pairwise conversions, we assume all (anti)neutrinos have the same energy, and the momentum is only determined by the angle θ with respect to the $y-$axis.

The flavor evolution is determined by the following equations of motion for neutrinos and antineutrinos:

$$i\left(\frac{\partial}{\partial t} + \vec{v} \cdot \vec{\nabla}\right) \rho(\vec{x}, \theta, t) = [H(\theta), \rho(\vec{x}, \theta, t)] , \tag{7.2}$$

$$i\left(\frac{\partial}{\partial t} + \vec{v} \cdot \vec{\nabla}\right) \bar{\rho}(\vec{x}, \theta, t) = [\bar{H}(\theta), \bar{\rho}(\vec{x}, \theta, t)] . \tag{7.3}$$

The advective term, $\vec{v} \cdot \vec{\nabla}$, depends on the velocity of the (anti-)neutrino field $\vec{v}$. The latter has modulus equal to the speed of light c and is oriented along the direction of propagation. The Hamiltonian, H, consists of a vacuum term that depends on the neutrino mixing angle θ_V and the vacuum frequency ω (assumed to be identical for all neutrinos in our system for simplicity), a term describing the interactions of neutrinos with the matter background with λ being the interaction strength, and a self-interaction term, see e.g. [88]:

$$H(\theta) = \frac{\omega}{2} \begin{pmatrix} -\cos 2\theta_V & \sin 2\theta_V \\ \sin 2\theta_V & \cos 2\theta_V \end{pmatrix} + \begin{pmatrix} \lambda & 0 \\ 0 & 0 \end{pmatrix} + \mu \int d\theta' \left[\rho(\vec{x}, \theta', t) - \bar{\rho}(\vec{x}, \theta', t)\right] \left[1 - \cos(\theta - \theta')\right] . \tag{7.4}$$

The Hamiltonian of antineutrinos, $\bar{H}(\theta)$, is the same as $H(\theta)$ except for ω which is replaced by $-\omega$. In the latter term on the right hand side of Eq. 7.4, μ represents the strength of neutrino-neutrino interactions

$$\mu = 10^2 \text{ km}^{-1} . \tag{7.5}$$

In order to track the flavor evolution numerically in a reasonable number of CPU hours, our benchmark value for μ corresponds to the typical neutrino-neutrino interaction strength at $\mathcal{O}(100 \text{ km})$ from the SN core during the accretion phase (see, e.g., Fig. 22 of Ref. [88]). Larger values of μ, descriptive of the neutrino self-interaction strength in the proximity of the neutrino decoupling region, would lead to the development of flavor conversions on scales smaller than what we discuss here without changing the overall conclusions, also for what concerns the impact of neutrino advection on the flavor evolution.

Unless otherwise specified, in the following, we assume $\omega = 0.1 \text{ km}^{-1}$ as typical of neutrinos in compact astrophysical objects, and $\theta_V = 10^{-6}$ in order to effectively ignore the matter term [264]. The default value adopted for the advective velocity is $c = 1$ in natural units (corresponding to 3×10^5 km/sec). In addition, as we will discuss in Sec. 7.4, we neglect the collision term.

Significant evolution in the number of (anti-)neutrinos can occur only if the off-diagonal term of the Hamiltonian is not very small compared to the diagonal term. In the case of neutrino-neutrino interactions, the magnitude of the off-diagonal component of the Hamiltonian is a dynamical quantity, whose initial seed is set by the momentum distribution of the density matrices (i.e., our vacuum frequency ω). For a given initial angular and spatial distribution, whether there will be significant flavor evolution depends on the temporal evolution of the off-diagonal elements of the density matrices which are connected to the probability of flavor transition. If the off-diagonal components of the density matrices grow with time (i.e., a flavor instability occurs), they will eventually lead to a change in the diagonal components of the density matrices which are directly connected to the spatial and temporal evolution of the number density of the different flavors. For the sake of simplicity and without loss of generality, in what follows, we assume $\rho_{xx}(t = 0 \text{ s}) = \bar{\rho}_{xx}(t = 0 \text{ s}) = 0$, $a = 0.5$, and $L_x = L_y = 20$ km. If all off-diagonal terms of the density matrices are zero at $t = 0$ s, then they will remain zero in the absence of the linear terms of the Hamiltonian (vacuum or matter term).

7.2.2 *Instability parameter*

The rate of growth of the off-diagonal terms of the density matrices (and therefore of the flavor instability) can be estimated by using the linear stability analysis for given initial conditions [133, 135]. In particular, Ref. [133] found that fast pairwise conversions may be induced by ELN crossings or in the presence of a non-negligible backward flux. In the case of ELN crossings, the growth of flavor instabilities may be affected by the depth of ELN crossings [161, 265].

We here introduce the "instability parameter" that depends on the shape of the angular distributions of ν_e and $\bar{\nu}_e$ and it is approximately proportional to the growth rate of the off-diagonal components of the density matrices:

$$\zeta = \frac{I_1 I_2}{(I_1 + I_2)^2} \tag{7.6}$$

with

$$I_1 = \int_0^{2\pi} \Theta\left[\rho_{ee}(\theta) - \bar{\rho}_{ee}(\theta)\right] d\theta \tag{7.7}$$

$$I_2 = \int_0^{2\pi} \Theta\left[\bar{\rho}_{ee}(\theta) - \rho_{ee}(\theta)\right] d\theta \tag{7.8}$$

where Θ is the Heaviside function, which vanishes when the argument is negative and is equal to the identity operator otherwise. It should be noted that, since the definition of ζ contains two powers of $I_{1,2}$ in the numerator and in the denominator, ζ is independent of the overall normalization of the density matrices. The ζ parameter is zero when there is no ELN crossing or when there is no backward flux, therefore it generalizes the criteria outlined in Ref. [133].

7.3 NEUTRINO FLAVOR EVOLUTION IN A TWO-DIMENSIONAL BOX

We explore two configurations of our 2D box. The first scenario corresponds to the case where neutrinos and antineutrinos are initially localized in a small region in our 2D box which should mimic the evolution of random fluctuations occurring within the inner SN core. The second scenario consists of neutrinos and antineutrinos that are initially located along a stripe in the 2D box. This would mimic the evolution of flavor conversions in the case of an extended region of

ELN crossings such as in the presence of LESA. In the following, we will introduce the numerical framework adopted to explore the flavor evolution in all these configurations.

7.3.1 *Model setup*

We define a 2D spatial grid with length $L_x = L_y = 20$ km which is identical in all simulations. The "one dot configuration" is shown in the top panel on the left of Fig. 41. It has been obtained by assuming

$$\rho_{ee}, \bar{\rho}_{ee} \propto \exp\left[-\frac{(x-x_0)^2}{2\sigma^2}\right] \exp\left[-\frac{(y-y_0)^2}{2\sigma^2}\right] , \tag{7.9}$$

with each distribution centered on $x_0 = y_0 = 1/2L_x$ and $\sigma = 5\%L_x$. It corresponds to the initial box configuration consisting of neutrinos distributed according to two Gaussians, along the $x(y)$-axis, each as displayed in the 1D projection in the middle panel of Fig. 41.

At $t = 0$ s, for each (x, y) the angular distributions of neutrinos and antineutrinos are fixed to be two top hat angular distributions centered on $\pi/2$,

$$\rho_{ee}(\theta) = \begin{cases} g & |\theta - \frac{\pi}{2}| < b \\ 0 & |\theta - \frac{\pi}{2}| \geq b\,, \end{cases} \tag{7.10}$$

$$\bar{\rho}_{ee}(\theta) = \begin{cases} \bar{g} & |\theta - \frac{\pi}{2}| < \bar{b} \\ 0 & |\theta - \frac{\pi}{2}| \geq \bar{b}\,, \end{cases} \tag{7.11}$$

with b being the opening angle of the ν_e angular distribution (assumed to be $\pi/6$ unless otherwise specified) and $\bar{b} = \pi$ being the one of $\bar{\nu}_e$. This scenario aims to mimic the evolution of the ELN crossings generated by stochastic fluctuations in the proximity of the decoupling region. A sketch of the initial ν_e and $\bar{\nu}_e$ angular distributions for three selected points across x is shown in the bottom panel of Fig. 41.

The "one stripe configuration" is shown in the top panel on the right of Fig. 41. It corresponds to the initial box configuration consisting of neutrinos localized along a stripe, which is homogeneous along the y-axis and distributed according to a Gaussian along the x-axis as displayed in the 1D projection in the middle panel of Fig. 41. The non-zero diagonal terms of the density matrix are defined as follows

$$\rho_{ee}, \bar{\rho}_{ee} \propto \exp\left[-\frac{(x-x_0)^2}{2\sigma^2}\right] , \tag{7.12}$$

with $\sigma = 5\% L_x$ and the center of the distribution $x_0 = 1/2 L_x$. This configuration mimics what should happen in the presence of LESA, when the ELN changes its sign.

Note that we assume that the angular distribution of ν_e is forward peaked and the $\bar{\nu}_e$ one is isotropic. However, in a realistic framework, the angular distributions of neutrinos and antineutrinos are both forward peaked after decoupling. As we will see later, we focus on a more extreme scenario since any growth of a flavor instability would be further suppressed, if both distributions are assumed to be forward peaked at $t = 0$ s. Moreover, the occurrence of fast neutrino oscillations requires that the values of the heights $(g, \bar{g})$ and the widths $(b, \bar{b})$ of the angular distributions are different for neutrinos and antineutrinos.

7.3.2 *Numerical implementation*

We perform numerical simulations with different initial conditions, while keeping the overall architecture of the numerical simulations and the grid size unchanged. For each (x, y) point, we define the angular distributions of neutrinos and antineutrinos as described in Sec. 7.3.1 and evolve the (anti)neutrino equation of motions according to Eqs. 7.2, 7.3. In the numerical runs, we adopt the following number of spatial and angular bins: $N_x = N_y = 400$ and $N_\theta = 100$. We use an adaptive method for the temporal evolution of the system. Note, however, that for the cases without the advective term, the number of spatial bins is not relevant since the spatial gradient in the advective term is zero. Although, we impose periodic boundary conditions on our box, we let the stripe configuration evolve within a time interval such that (anti)neutrinos never cross the boundaries.

The spatial gradient on the left-hand-side of Eqs. 7.2 and 7.3 can be solved analytically in the absence of flavor evolution. This term is responsible for transporting the neutrino density matrices from one bin to another. To this purpose, we implement a transport algorithm to move the density

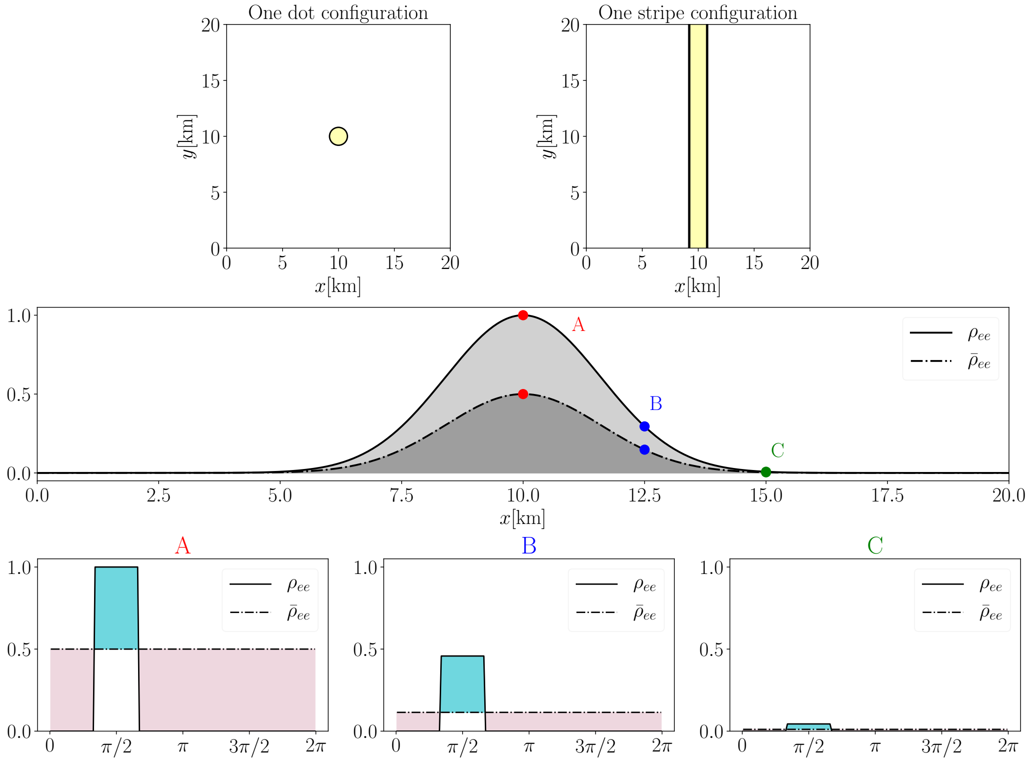

Figure 41: *Top*: Sketch of the 2D box at $t = 0$ s for the two configurations adopted in this paper: "one dot configuration" (on the left) and "one stripe configuration" (on the right), see main text for more details. *Middle*: 1D projection of the dot or stripe configuration to show ρ_{ee} (continuous line) and $\bar{\rho}_{ee}$ (dot-dashed line) as a function of x. *Bottom*: ν_e and $\bar{\nu}_e$ angular distributions for the three points A, B, and C highlighted in the middle panel, respectively from left to right.

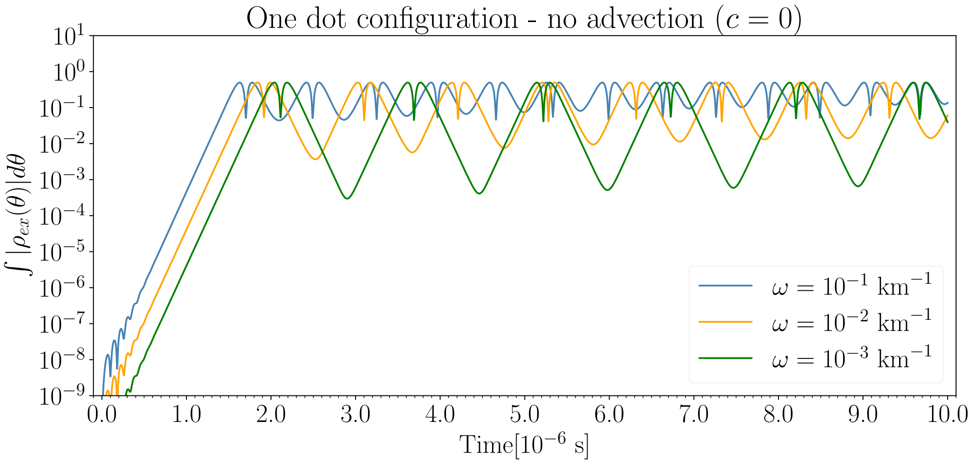

Figure 42: Temporal evolution of $\int d\theta |\rho_{ex}(\theta)|$ in the absence of advection for the (x_0, y_0) point in our 2D box and several values of vacuum frequency ω. Flavor transformation occurs when $\rho_{ex} \sim 1$ and gives rise to bipolar fast conversions. The oscillation period is inversely correlated to ω.

matrices to neighbouring spatial bins in regular time steps. For the temporal evolution we use the Runge-Kutta-Fehlberg(7,8) method from the odeint library of Boost [266].

In order to speed up the computational time, we parallelize our numerical code through the OpenMP interface [267]. We evolve the simulations for $\mathcal{O}(10^{-5}\ \text{s})$ which is enough to gauge the flavor conversion phenomenology in astrophysical environments. Within this simplified setup, each simulation run takes about 200 CPU-hours.

7.3.3 *Fast conversions in the absence of advection*

We now explore the general features of the linear and non-linear flavor evolution within our 2D box. Figure 42 shows an example of the outcome of our simulations for the "one dot configuration" (top left of Fig. 41). It shows the off-diagonal term of the density matrix $\int d\theta \rho_{ex}(\theta)$ as a function of time for the (x_0, y_0) point in our 2D box in the absence of advection for $\omega = 10^{-3}, 10^{-2}, 10^{-1}$ km^{-1} (see Eq. 7.4). As we will discuss in Sec. 7.3.4, $\int d\theta \rho_{ex}(\theta)$ grows exponentially until it transitions to the non-linear regime. When the magnitude of the off-diagonal elements of the density matrix reaches the same order as the diagonal elements ($\sim \rho_{ee}$), flavor transformations start.

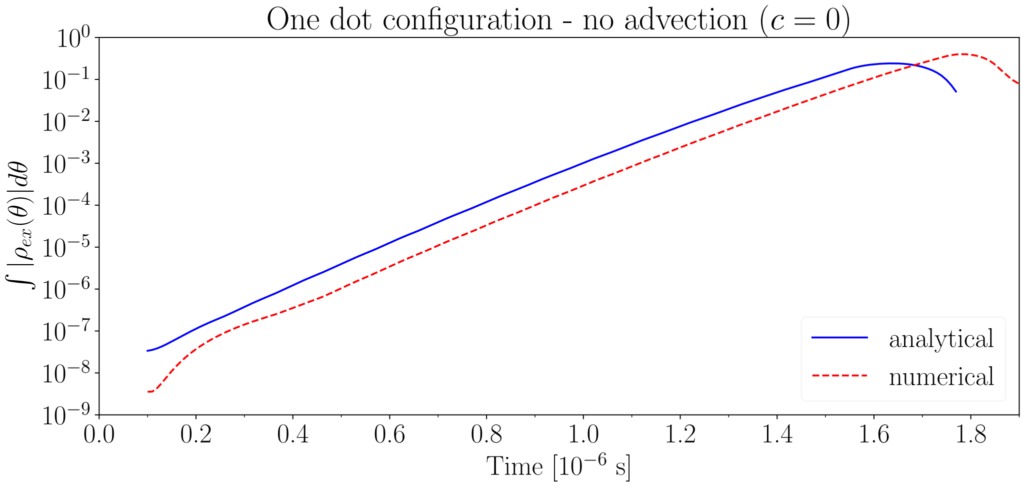

Figure 43: Temporal evolution of $\int d\theta \rho_{ex}(\theta)$ for the (x_0, y_0) point in the box ("one dot configuration") in the absence of advection from our numerical simulation (dashed line) compared with the analytical approximation of Eq. 7.13 (continuous line). The analytical expression of Eq. 7.13 perfectly matches the numerical growth rate of the instability.

Interestingly, in the non-linear regime, the neutrino flavor evolution closely resembles the bipolar oscillations commonly found for slow collective oscillations [83, 92]. Although the growth rate at smaller times is completely independent of the vacuum frequency, ω, the non-linear evolution of flavor is inversely correlated to ω; in addition, a second frequency seem to affect the evolution of ρ_{ex} independently of ω. However, the latter does not affect the overall flavor evolution. This is a new finding for what concerns the phenomenology of fast pair-wise conversions. In fact, the vacuum term has been neglected in the stability analysis under the assumption that fast-pairwise conversions are completely driven by μ, see e.g. [130, 133], if crossings in the angular distributions of ν_e and $\bar{\nu}_e$ exist. However, we find that the separation in time between two bipolar transformations is inversely correlated to ω. Although not shown here, we tested configurations with $\mu \in [10^2, 10^5]$ km^{-1} as well as cases with $\lambda \neq 0$ and observed a bipolar regime in all cases. As we will discuss in Sec. 7.4, this picture will be modified by advection.

7.3.4 *Growth of the flavor instability*

As shown in Fig. 41, when the advective term is neglected in Eqs. 7.2 and 7.3, the absolute value of the off-diagonal component of ρ grows exponentially in time, before reaching the non-linear regime. We find that the exponent, κ, satisfies the following relation

$$\kappa = \epsilon \mu_{\text{eff}} \zeta \tag{7.13}$$

with

$$\mu_{\text{eff}} = \mu \int_0^{2\pi} d\theta \left[(\rho_{ee}(\theta) - \rho_{xx}(\theta)) - (\bar{\rho}_{ee}(\theta) - \bar{\rho}_{xx}(\theta)) \right] \ , \tag{7.14}$$

where this definition of μ_{eff} depends on the ELN, while the one of μ in Eq. 7.5 is meant to be related to the total (anti)neutrino number density. The proportionality factor in Eq. 7.13 was found to be $\epsilon = 34.8$ for a wide range of initial configurations where $b(\bar{b})$ and $g(\bar{g})$ were varied according to Eqs. 7.10 and 7.11.

The growth of the flavor instability is shown in Fig. 43 as a dashed line as a function of time for the “one dot configuration” and for the (x_0, y_0) point in the box. The continuous line has been obtained by using Eq. 7.13. As one can see, Eq. 7.13 perfectly reproduces the growth rate of the off-diagonal terms of the density matrix. It should be noted that the definition of κ is heuristic in nature; although it is not clear whether a single parameter can encapsulate the growth rate of the instability for all angular distributions, the parametrization in Eq. 7.13 works for all cases that we have explored. When $\vec{v} \cdot \nabla = 0$, the exponential growth of the off-diagonal term of ρ does not depend on the neighboring regions, and it continues to grow until the non-linear regime is reached.

7.4 ROLE OF THE ADVECTIVE TERM IN THE NEUTRINO EVOLUTION EQUATION

In this Section, after general considerations on the impact of the advective term, we discuss the role that the latter plays on the growth of flavor instabilities in the “one dot configuration,” and in the “one stripe configuration.” We also discuss how advection affects the evolution of the ELN distribution as a function of time.

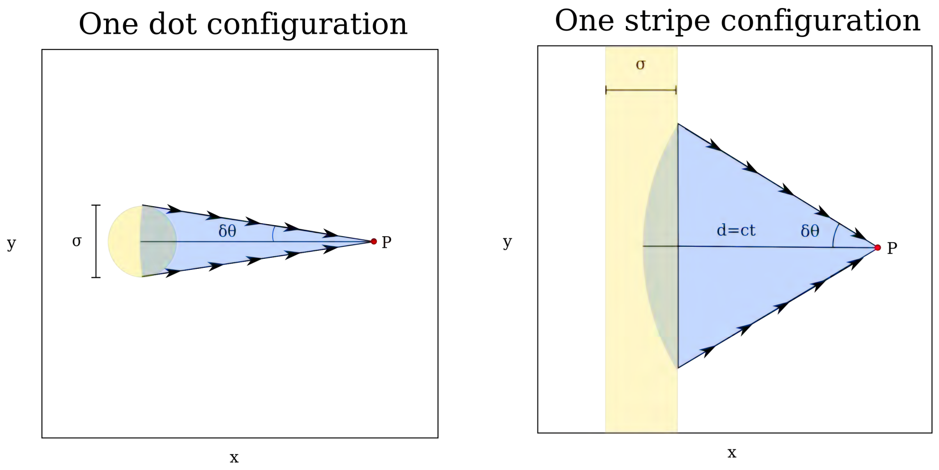

Figure 44: *Left:* Schematic diagram of the box in the “one dot configuration.” The maximum width of the angular distribution $\delta\theta$ is determined by the dot size in the dot configuration. *Right:* Schematic diagram of the box in the “one stripe configuration.” Within the yellow stripe, ELN crossings are distributed in the plane following a Gaussian distribution of width σ. After a time t, the neutrino angular distribution in P will have maximum opening angle $\delta\theta$ because of geometric effects.

7.4.1 *Impact of the advective term on the neutrino distributions*

Before exploring the growth of flavor instabilities in the different configurations assumed for our 2D box, we adopt geometrical arguments to forecast how the angular distributions should evolve in the presence of advection. The left panel of Fig. 44 shows a schematic diagram of the box in the “one dot configuration.” Let us consider a point $P = (x, y)$ outside the initial location of the dot ($|(x - x_0)| > \sigma$). At $t \sim (x - x_0)/c$, neutrinos from various points across the dot and emitted along different θ’s will reach P.

It is easy to estimate the width of the angular distribution at any given time, which is dependent on the width of the initial distribution $b(\bar{b})$, see Eqs. 7.12-7.11. If the width of the initial distribution is zero (i.e., we start with Dirac delta function), then at any given time t, only neutrinos traveling along a certain direction can reach the point P. In other words, for any point P that was not on the dot initially, the angular distribution will still be a Dirac delta distribution in θ. Understanding the limiting case with $b(\bar{b}) \to 0$ allows to draw insightful conclusions regarding the evolution of the ELN crossings in time.

Let us consider a point $P = (x, y)$ outside the "dot" in the 2D box, i.e. $d^2 = (x - x_0)^2 + (y - y_0)^2 > \sigma^2$. From simple geometric considerations, it can be seen that the advective term acts like a narrow pass filter. In fact, at t the (anti)neutrino angular distribution will have width

$$\delta\theta \approx \min\left[w, \arctan\left(\frac{\sigma}{d}\right)\right] , \tag{7.15}$$

where w is the width of the initial angular distribution of neutrinos or antineutrinos.

Similar considerations hold for the "one stripe configuration," see the right panel of Fig. 44, the effect of advection is less prominent than that in the "one dot configuration," but it exists nonetheless. If the distance between P and x_0 is d, then the width of the angular distribution at a certain time t will be

$$\delta\theta \approx \min\left[w, \arctan\left(\sqrt{\frac{\sigma}{d}}\right)\right] , \tag{7.16}$$

where w is the width of the initial angular distribution, which is b or $\bar{b}$ (Eqs. 7.10 and 7.11). Equation 7.16 is such that no matter how large σ is, the angular width cannot be greater than w. The second argument of the min function in Eq. 7.16 can be easily gleaned by noticing that the width of the angular distribution is given by the neutrino which is emitted at $x - x_0 = \sigma$. If $\arctan\left(\sqrt{\sigma/d}\right) < w$, then the angular distributions of ν_e and $\bar{\nu}_e$ have the same width, and fast conversions cannot occur.

To gain physical intuition as of the meaning of Eq. 7.16, we consider a limiting case where neutrinos have traveled a very large distance compared to the initial width of the ELN crossings i.e. when $\sigma/d \to 0$. In this limit, Eq. 7.16 gives $\delta\theta \approx 0$ which corresponds to Dirac-delta's for the final angular distributions of (anti)neutrinos. As one can see in Fig. 44, in this limit the neutrinos reaching a fixed point P after time t are from the same direction, which results in final angular distributions with an almost vanishing $\delta\theta$. In other words, the finite size of the source cannot be resolved by an observer at infinite distance.

We now explore the role of the advective term in the neutrino equations of motion. We expect that the advective term will have several effects on the neutrino flavor evolution. On the one hand, the advective term should diffuse any eventual ELN excess localized in a small spatial region, diluting it over a broader region. On the other hand, the parameter ζ should be modified as a result of advection. Moreover, as it will become clear in the following, by modifying the instability parameter, the advective term will also affect the occurrence of fast conversions. In the non-linear regime, the effect of advection can be grasped by similar arguments. At a given time, neutrinos in a different phase of bipolar oscillations arrive at the point $P = (x, y)$. This leads to erasing the bipolar nature of oscillations, since oscillations with different phases overlap with each other.

The time-scale required for the advective term to wipe out the instability parameter ($\zeta \to 0$) is given by the time at which the two arguments of the min function in Eq. 7.16 are comparable:

$$t_{\rm conv} \approx \frac{\sigma}{w^2} \, . \tag{7.17}$$

In this case, the width of the angular distribution of ν_e and $\bar{\nu}_e$ becomes independent of the initial angular distribution, and it is the same for ν_e and $\bar{\nu}_e$.

The characteristic time scale of neutrino advection, $t_{\rm conv}$, should be compared with the other characteristic time scale of the system $t_{\rm osc}$, which defines the time required for flavor transformations to occur. In fact, because of flavor instabilities, the off-diagonal term of the density matrix evolves like $\rho_{ex}(t = 0) \exp(\kappa t_{\rm osc}) = \mathcal{O}(\rho_{ee})$; $t_{\rm osc}$ obviously depends on the initial magnitude of the off-diagonal term, the effective neutrino number density, and ζ. In turn, the latter two evolve in time because of the advective term in the equations of motion.

7.4.2 *Flavor evolution in the one dot configuration*

We now consider the case of neutrinos and antineutrinos initially localized within a dot in the 2D box ("one dot configuration"), see Eq. 7.9 and the left top panel of Fig. 41. We assume the initial angular distributions as described in Sec. 7.3.1 and fix $b = \pi/6$ and $\bar{g} = 0.5$ (see Sec. 7.3.1 for more details). Animations of the temporal evolution of the ν_e and $\bar{\nu}_e$ angular distributions, as well as the diagonal and off-diagonal terms of the neutrino and antineutrino density matrices are provided as Supplemental Material.

The top panels of Fig. 45 show iso-contours of $\int \rho_{ee}(\theta) d\theta$ for four different time snapshots, from left to right respectively, in the absence of advection. Bipolar oscillations develop over time and give rise to concentric circles in the neutrino density iso-contours (see $t = 2.9, 4.4 \times 10^{-6}$ s). This behavior is identical to what is shown in Fig. 42 for a selected point in the (x, y) plane. The bottom panels of Fig. 45 show the correspondent evolution of $\bar{\nu}_e$ for the same time snapshots, highlighting the collective behavior of neutrinos and anti-neutrinos. It should be noted that the contours of $\bar{\nu}_e$ are less extreme than the ones of ν_e, since ν_e and $\bar{\nu}_e$ can transform as long as the lepton number is conserved.

The picture described above is drastically modified by advection, as shown in Fig. 46. By comparing this figure to Fig. 45 (i.e., to the case without advection), one notices that advection contributes to erase the small scale structures characterizing flavor conversions: the bipolar behavior of flavor conversions disappears and the flavor change is confined to a more localized region. The correspondent reduction in the value of the ELN parameter ζ can be clearly seen in the bottom panels where the ν_e and $\bar{\nu}_e$ angular distributions are shown. The reduction of the ELN parameter ζ, in turn, drives the system towards a more stable configuration disfavoring further flavor change.

As time progresses, the ζ parameter is reduced so much that diffusion becomes the only dominant phenomenon as shown in Fig. 47, where the iso-contours of $\int \rho_{ee}(\theta)d\theta$ and $\int \bar{\rho}_{ee}(\theta)d\theta$ are

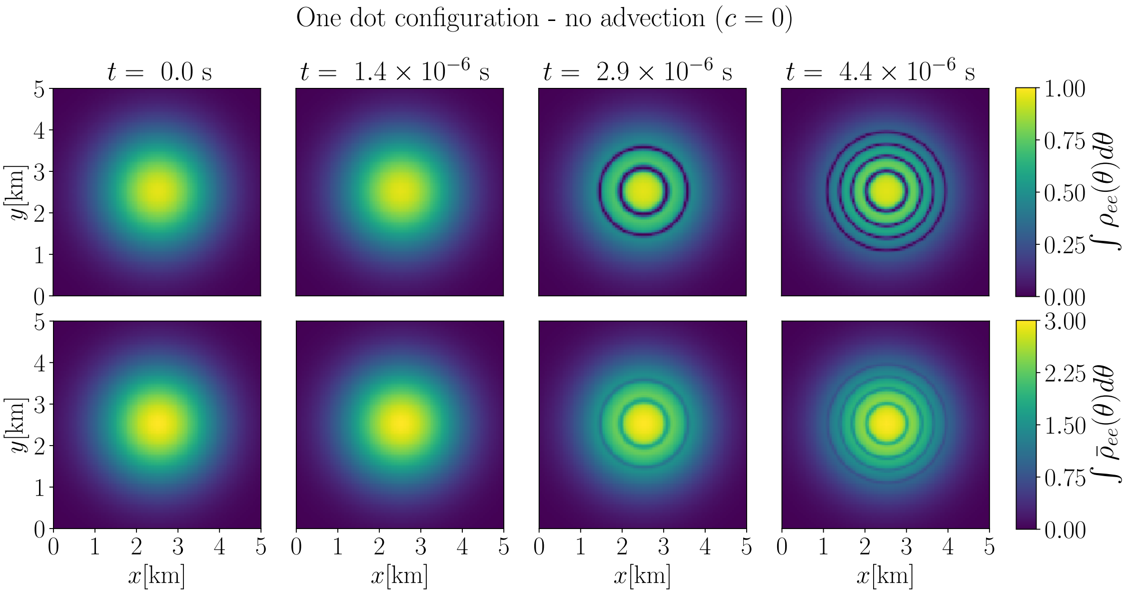

Figure 45: Evolution of $\int d\theta \rho_{ee} d\theta$ (top) and $\int d\theta \bar{\rho}_{ee} d\theta$ (bottom) in the 2D box for the "one dot configuration" (see Fig. 41) in the absence of advection. The four panels from left to right correspond to four different time snapshots ($t = 0.0, 1.4 \times 10^{-6}, 2.9 \times 10^{-6}$, and 4.4×10^{-6} s). The concentric circles in the neutrino density iso-contours highlight the regime of bipolar oscillations. The contours of $\bar{\nu}_e$ are less extreme than the ones of ν_e, since flavor conversions occur in such a way to guarantee the lepton number conservation.

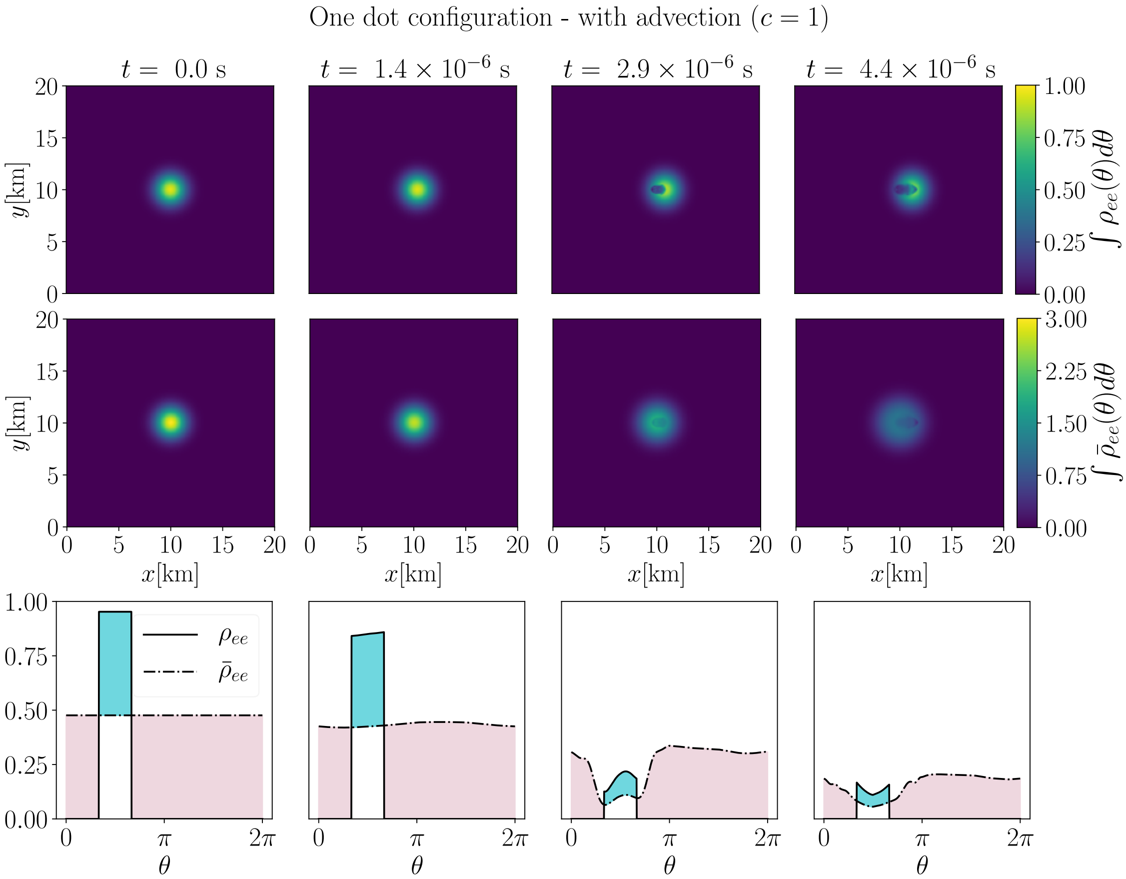

Figure 46: *Top and middle:* Same as Fig. 45, but in the presence of advection. Because of advection flavor transformations occur in a localized region and the bipolar structure is smoothed out. Since the angular distribution of $\int \bar{\rho}_{ee} d\theta$ is isotropic, advection favors a decrease of the local density of $\bar{\nu}_e$ very rapidly (see bottom panel of Fig. 45 for comparison). *Bottom:* Evolution of the angular distributions of ν_e and $\bar{\nu}_e$ as a function of θ for a comoving point in our 2D box. Due to advection, the ζ parameter decreases with time, hindering fast conversions.

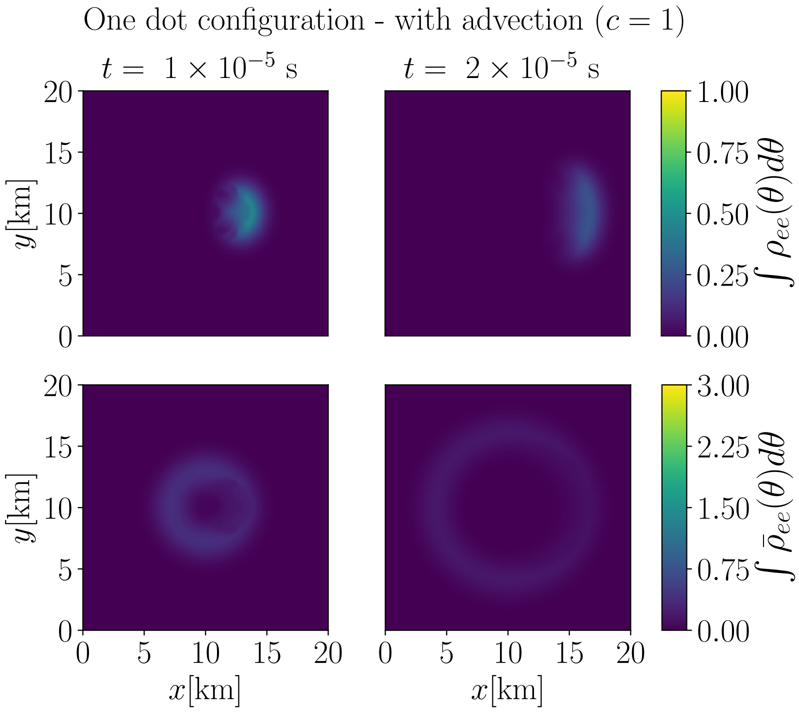

Figure 47: Same as in the top and middle panels of Fig. 46, but for $t = 10^{-5}$ and 2×10^{-5} s. The initial angular distributions of ν_e's are forward peaked, hence neutrinos tend to diffuse forward because of non-negligible advection. This effect becomes even more extreme for $\bar{\nu}_e$'s that have an initially homogeneous angular distribution. Advection also contributes to progressively reduce the local density in time, spreading all particles throughout the box.

displayed in our 2D box for later times ($t = 10^{-5}$ and 2×10^{-5} s). Since the initial ν_e angular distribution is forward peaked, ν_e's tend to diffuse forward more prominently; while, the effect of advection is stronger on $\bar{\nu}_e$'s that have an initially homogeneous angular distribution.

In order to highlight how the bipolar regime is modified by advection, the top panel of Fig. 48 shows the evolution of $\int |\rho_{ex}(\theta)| d\theta$ for a range of values of c different from our default value ($c = 1$) for a comoving point in the 2D box. Although this is an academic exercise, it shows that advection becomes more and more relevant as $c \to 1$. In addition, as c increases, the ζ parameter is also affected since the ELN crossings are smeared and the overall flavor conversion probability tends to reach a smaller asymptotic value.

The "one dot configuration" mimics what would happen in SNe or compact binary mergers in the presence of localized ELN excess, e.g. generated by stochastic hydrodynamical fluctuations.

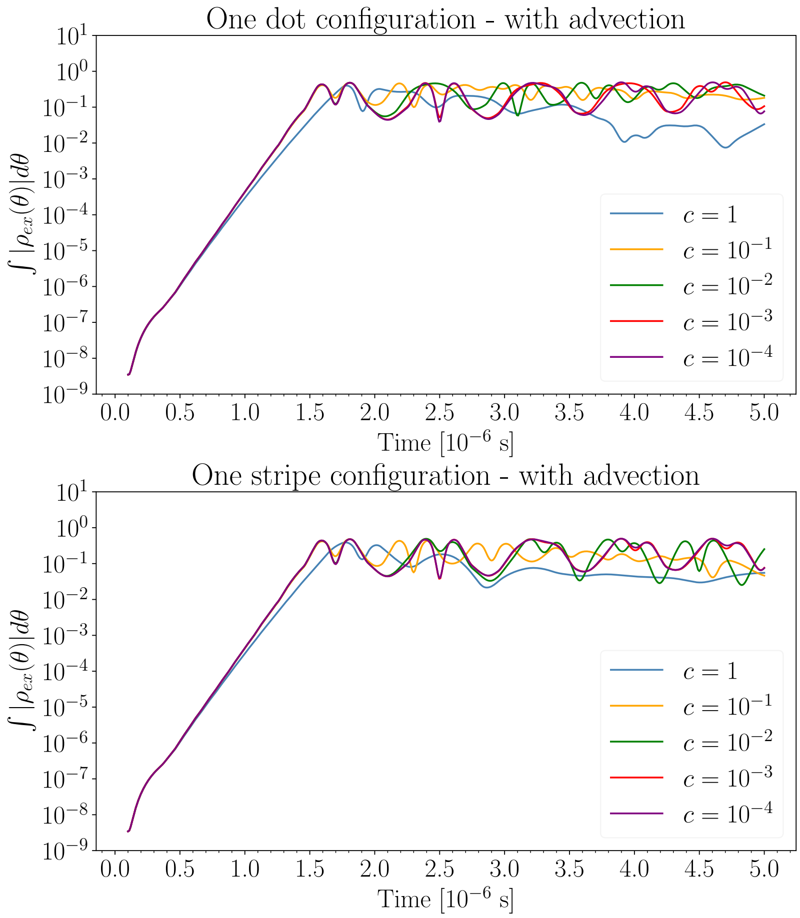

Figure 48: Temporal evolution of $\int |\rho_{ex}(\theta)| d\theta$ for different values of the advective velocity c for a comoving point in the 2D box for the "one dot configuration" (top) and for the "one stripe configuration" (bottom). For small values of c the deviation from the bipolar oscillations is minimal. As c increases the ζ parameter becomes smaller, and the overall flavor conversion probability tends to reach a smaller asymptotic value. Because of the different geometry, the impact of advection is slightly less pronounced in the "one stripe configuration."

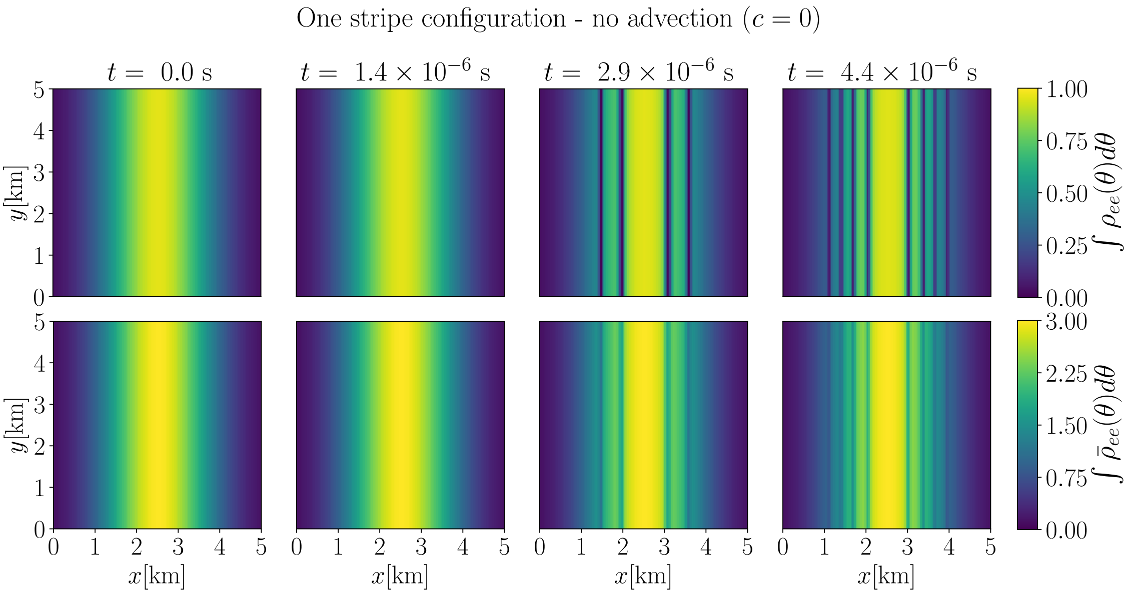

Figure 49: Same as Fig. 45, but for the "one stripe configuration." Neutrino-neutrino interactions lead to a bipolar structure in the flavor evolution in the non-linear regime.

We can conclude that advection smears the ELN crossings in this configuration most likely leading to minimal changes in the flavor configuration.

7.4.3 *Flavor evolution in the one stripe configuration*

We now focus on the "one stripe configuration" of our 2D box, see the top panel on the right of Fig. 41. Similarly to the "one dot configuration," we investigate the flavor evolution, first in the absence of advection and then by including the advective term in the neutrino equations of motion for $b = \pi/6$ and $\bar{g} = 0.5$ (see Sec. 7.3.1 for more details). We provide animations of ν_e and $\bar{\nu}_e$ angular distributions, the diagonal and off-diagonal terms of the neutrino and antineutrino density matrices as Supplemental Material.

In the absence of advection, the bipolar nature of flavor conversions is evident also for the "one stripe configuration" as shown in Fig. 49 where four snapshots of the iso-contours of $\int \rho_{ee} d\theta$ and $\int \bar{\rho}_{ee} d\theta$ are shown. For comparison, the effect of advection is visible in Fig. 50. As evident from the bottom panels, the ζ parameter becomes smaller as a function of time. However, in comparison to the "one dot configuration," the ELN parameter ζ decreases more slowly because of the differences in the initial geometry between the two configurations.

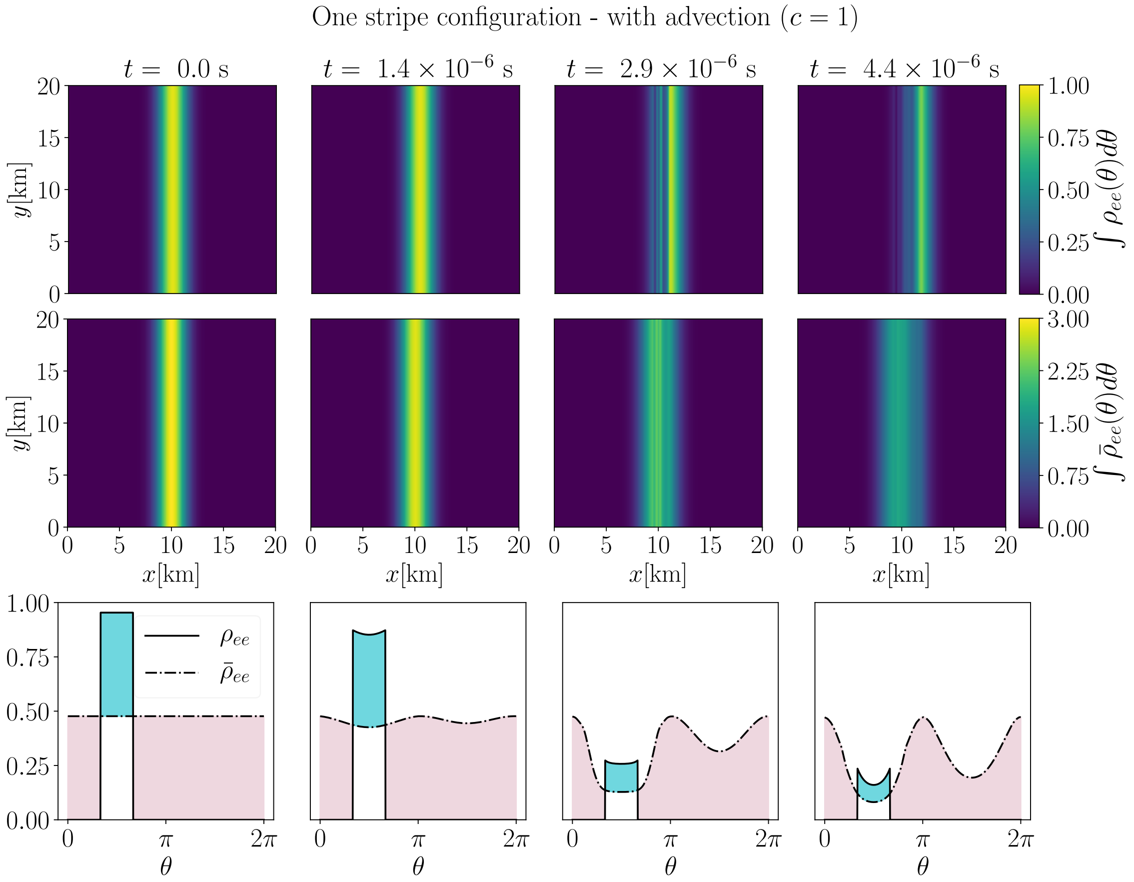

Figure 50: Same as Fig. 46, but for the “one stripe configuration.” The ELN parameter becomes smaller as a function of time. However, its decrease is slower than in the “one dot configuration” because of the differences in the initial geometry of the two configurations.

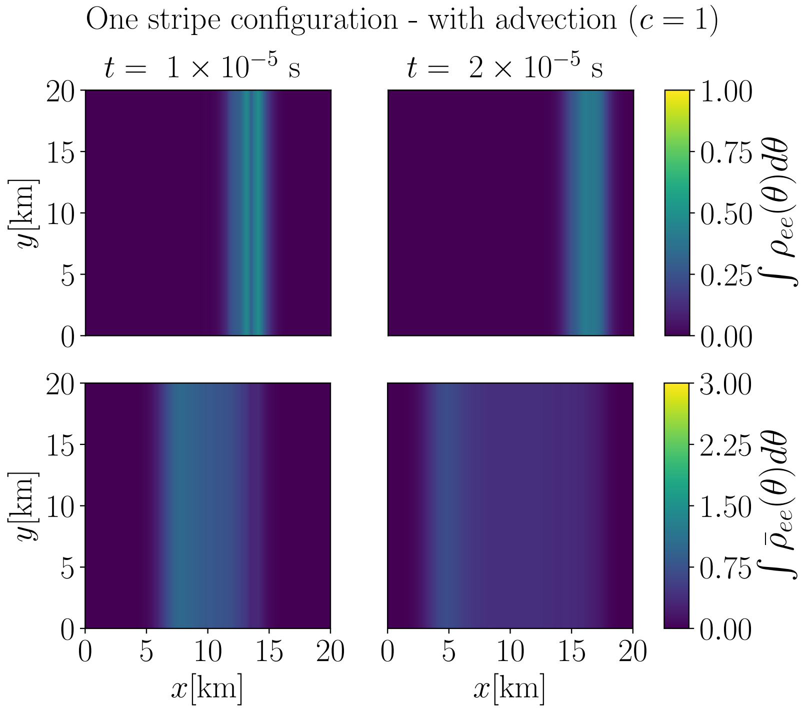

Figure 51: Same as Fig. 47, but for the “one stripe configuration.” Advection spreads the original stripe across our 2D box, disfavoring the occurrence of favorable conditions for fast conversions.

The effect of advection is less pronounced in the “one stripe configuration” because the neutrinos reaching any spatial point (x, y) in our 2D box are emitted from a region more extended in space than the “one dot configuration” and therefore have a larger spread in their angular distributions. As a consequence, longer time is needed to obtain completely forward peaked angular distributions. This can be also seen in Fig. 51 which focuses on the flavor evolution at later times ($t = 1 \times 10^{-5}$ and 2×10^{-5} s).

The effect of advection on $\int \rho_{ex} d\theta$ in the “one stripe configuration” is shown for a comoving point in the bottom panel of Fig. 48 for various values of c. For $c \to 1$, $\int \rho_{ex} d\theta$ is closer to unity than in the “one dot configuration” (see top panel of Fig. 48 for comparison).

This configuration of the 2D box tends to mimic what would happen in a SN patch in the presence of a front of ELN crossings. As one can see, unless the ELN crossings are self-sustained (as it could be in the case of LESA), they would be wiped out by the neutrino advective term. As a consequence, fast pairwise conversions would only lead to partial flavor conversion. Notably, our setup overestimates the effect of flavor conversions since we assume $\mu =$ const. in the box and maximize the initial ζ by assuming an isotropic distribution for $\bar{\nu}_e$. In a realistic case, μ would tend to decrease as the distance from the decoupling region increases and $\zeta(t = 0\ \mathrm{s})$ would be likely smaller than in our case given that the angular distribution of $\bar{\nu}_e$ is not isotropic outside the proto-neutron star radius.

7.5 OUTLOOK AND CONCLUSIONS

Compact astrophysical objects are so dense in neutrinos that quantum effects are expected to manifest at macroscopic scales. In this work, we explore an interesting and insightful interplay between the neutrino pairwise conversions (quantum effect) and the propagation of the neutrino field driven by the advective term in the equations of motion (classical effect). In order to do this, for the first time, we track the neutrino flavor evolution within a (2+1+1) framework, i.e. we solve the neutrino equations of motion in time, two spatial dimensions, and one angular variable.

We explore a simplified scenario with constant neutrino–neutrino potential for the sake of simplicity, however we mimic configurations similar to the ones that could occur in compact astrophysical objects where favorable conditions for fast pairwise conversions have been found through the stability analysis. In particular, we explore two different configurations: 1. one localized excess of particles with electron lepton number (ELN) crossings, mimicking ELN fluctuations that could occur because of stochastic hydrodynamical fluctuations; 2. neutrinos and antineutrinos initially localized along one stripe in our 2D box, mimicking a situation similar to LESA.

We generalize the conditions leading to the development of fast pairwise conversions introducing the instability parameter ζ that broadly captures the essence of the shape of the neutrino angular distributions leading to flavor instabilities. The instability parameter ζ along with the effective strength of neutrino-neutrino interactions determines the instantaneous growth rate of the off-diagonal components of the density matrices. However, the numerical solution of the neutrino equations of motion highlights a fascinating interplay between the growth of fast pairwise conversions and neutrino advection. Our sophisticated numerical simulations show that the advective term in the equations of motion hinders the growth of flavor instabilities, unless the front of ELN crossings (or of neutrinos moving in the opposite direction of $\vec{v}$) is self-sustained in time.

As a consequence, our simple model predicts that significant flavor evolution due to fast pairwise conversions can occur in the presence of the LESA instability (scenario 2), but would not be significant for a localized ELN excess (scenario 1). However, a more in-depth analysis including collisions is mandatory, since collisions may damp the growth of flavor instabilities even in the presence of self-sustained crossings.

This work demonstrates a critical limitation of the linear stability analysis widely used in the field of collective neutrino conversions, as the time scales that are relevant from the point of view of classical evolution (i.e., advection) may be comparable to the time scale of flavor conversions. In addition, the advective term in the equations of motion is such that the conditions leading to the growth of flavor instabilities are dynamically affected from the surroundings. This aspect is not captured by the stability analysis.

Ours is the first numerical solution of the neutrino flavor evolution within a sophisticated and dynamical multi-dimensional framework. Although our work is in no way the final setup resembling the evolution of the neutrino field in core-collapse supernovae or compact binary mergers, it highlights the dynamical nature of flavor evolution.

7.6 CRITICAL OUTLOOK

7.6.1 *Overview and main findings*

Our knowledge of the flavor evolution of neutrinos in non-homogeneous environments is very limited. The reason is that the neutrino equations of motion (Eqs. 2.74) involve not only neutrino refraction with the background medium (Sec. 2.2.5) but also a term proportional to the gradient of the density matrices: the advective term $\vec{v} \cdot \nabla \rho(\vec{x}, \vec{p}, t)$. Due to these complications, the flavor evolution of non-homogeneous media is mostly investigated in the linear regime [133, 258]. See for instance, Fig. 52 where inhomogeneities ($\vec{k} \neq 0$) are included in the linear stability analysis (Sec. 2.2.7.3). Computations in the linear regime are widely implemented in the literature to identify favorable conditions for fast flavor conversion in non-homogeneous environments. Nevertheless,

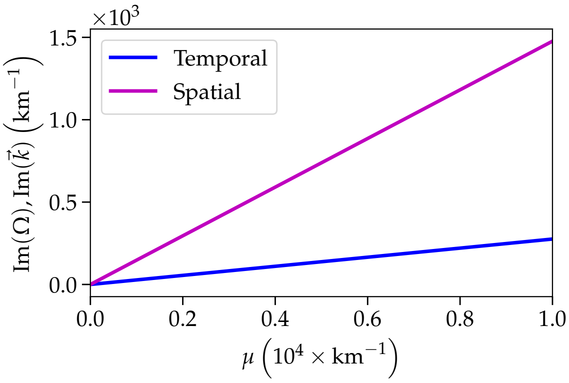

Figure 52: Flavor instabilities as predicted from the linear stability analysis. *Left:* Temporal ($\mathrm{Im}(\Omega) \neq 0$) and spatial ($\mathrm{Im}(\vec{k}) \neq 0$) growth rates as a function of the neutrino-neutrino interaction potential μ. The ELN distributions $g_\theta = \rho_{ee} - \bar{\rho}_{ee} =$ are single-crossed ELN spectra such that initially $g_\theta = -0.5$ for $\theta \in (0, \pi/3)$ and $g_\theta = 0.25$ for $\theta \in (\pi/3, \pi)$, while $\rho_{xx} = \bar{\rho}_{xx} = 0$. The growth rate depends linearly on μ. Image adapted from Ref. [87].

a direct computation of flavor evolution is still needed to understand the non-linear regime and the final flavor outcome.

The non-linear behavior of collective conversions can lead to the spontaneous breaking of spatial [110] and axial symmetries [104], and although these findings have been appreciated for quite some time, the non-linear regime remains poorly understood, and only a few works on the topic are available in the literature [149, 180, 181, 242, 249, 268]. The work presented in this Chapter deals with the development of fast flavor conversion of non-homogeneous systems in two spatial dimensions, one angular variable and time.

The advective term depends on the velocity of the (anti)neutrino field; for non-homogeneous (spatially-varying) configurations, it is non-zero. One crucial feature of the advective term is that it determines the angular distribution of neutrinos at any given location in space. For illustration, let us imagine that the density matrices of neutrinos evolve only classically, i.e., there is no neutrino mixing of any kind. Therefore, the EOMs are pretty simple and ν decouple from $\bar{\nu}$ in the classical limit:

$$\left(\frac{\partial}{\partial t} + \vec{v}\cdot\vec{\nabla}\right)\rho(\vec{x},\theta,t) = 0\,, \qquad \text{and} \qquad \left(\frac{\partial}{\partial t} + \vec{v}\cdot\vec{\nabla}\right)\bar{\rho}(\vec{x},\theta,t) = 0\,. \tag{7.18}$$

If we assume that there is a stationary source of (anti)neutrinos of a given size and located at position $\vec{x}$, Eqs. 7.18 can be solved geometrically to determine the angular distributions of the

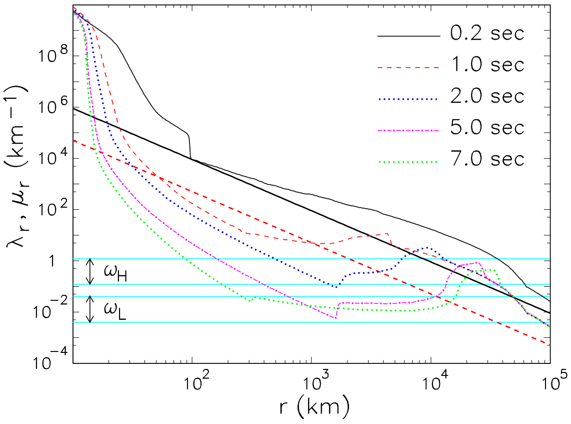

Figure 53: Snapshots of SN potentials at different post-bounce times for a $27M_\odot$ SN progenitor from the Garching group. The thin lines represent the matter potential λ_r, while the thicker lines the neutrino potential μ_r as a function of distance from the progenitor. At early times ~ 0.2 s, the potentials are representative of the conditions expected before the shock revival (Sec. 3.1). A few seconds later, in the accretion phase, the potentials have decreased such that $\mu_r \simeq 10^2 - 10^3$ km^{-1} (thick red dashed line). Image taken from Ref. [88].

density matrices. See, for instance, the formation of the ELN angular distributions in Fig. 17, where we show a schematic representation of what an observer might see as a function of $\cos\theta$. A similar procedure was followed for the neutrino bulb model (Sec. 2.2.7.1). However, in realistic astrophysical sources, the problem is much more complex since we do not know what the spatial distribution of (anti)neutrinos looks like at a given time and location. Moreover, the spatial distributions of neutrinos (and matter) can also vary in length scales varying from fractions of meters and up to the kilometer scale. On top of that, the angular distributions are not static but time-evolving with time scales comparable to that of neutrino fast flavor conversion in some regions of the astrophysical sources in question.

Let us take the core-collapse supernova environment (Chapter 3) as an illustrative example. Let us assume a modest value of $\mu = 10^2$ km^{-1}, which is representative of the neutrino-neutrino interaction strength at $\mathcal{O}(100\text{ km})$ from the SN core during the accretion phase as seen in Fig. 53. Larger values of μ correspond to conditions in the vicinity of the neutrino decoupling region, leading to flavor conversion on much smaller scales. A neutrino potential of $\mu = 10^2$ km^{-1} $= 3 \times 10^7$ s^{-1} implies that the time scale of fast flavor conversion is $\tau_{\text{FFC}} = \mu^{-1} \simeq 10^{-7}$ s. This means that flavor instabilities with growth rates (Sec. 2.2.7.3) comparable to $\sim \tau_{\text{FFC}}^{-1}$ are expected.

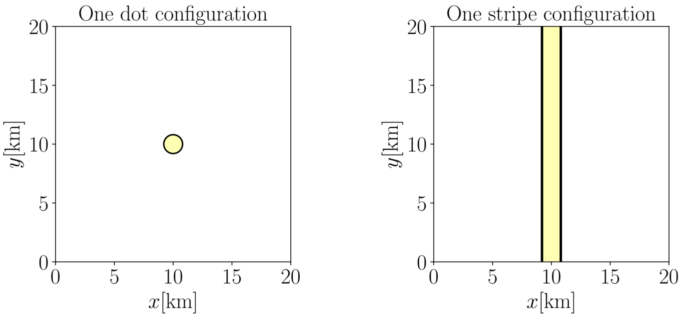

Figure 54: Sketch of the 2D box at $t = 0$ s for the two configurations adopted in this work: "one dot configuration" (on the left) and "one stripe configuration" (on the right).

Moreover, after a few characteristic time scales, say $T = 10\tau_{\rm FFC} = 10^{-6}$ s, fast flavor conversion is well in the non-linear regime and possibly converted neutrino flavor. On the other hand, after the time T (anti)neutrinos have travelled a distance of $L_{\rm travel} = c(10^{-6}\ {\rm s}) = 0.3$ km. Therefore, flavor conversion can develop in space and time over much shorter time and length scales than those that characterize the SN environment (few km).

The work presented in this Chapter investigates two kinds of spatial distributions of neutrinos and their evolution under the influence of FFC: *global* and *local* spatial distributions. The global spatial distributions are self-sustained spatial distributions (such as LESA [142]) while the local ones could be a result of small stochastic fluctuations of the density profiles and, therefore, are not self-sustained.

The global and local spatial configurations correspond to the "one stripe configuration" and the "one dot configurations" schematically shown in Fig. 54. Each spatial location in the 2D grid has an initial ELN angular distribution which evolves in space-time as described by the EOMs (Eqs. 2.74). For instance, apart from the θ-dependence, the "one stripe configuration" (right panel Fig. 54) has a xy-spatial dependence such that $\rho_{ee}, \bar{\rho}_{ee} \propto \exp\left[-(x-x_0)^2/2\sigma^2\right]$, while for the "one dot configuration" (left panel Fig. 54) $\rho_{ee}, \bar{\rho}_{ee} \propto \exp\left[-(y-y_0)^2/2\sigma^2\right] \exp\left[-(x-x_0)^2/2\sigma^2\right]$.

The main results of this work can be summarized in Fig. 55, where we show the evolution of angle-integrated off-diagonal term $\int |\rho_{ex}(\theta)| d\theta$ for a point that propagates together with the neutrino gas. The value of the speed of light c is kept as a free parameter to gauge the impact of the advective term $c\hat{v} \cdot \vec{\nabla}\rho(\vec{x}, \theta, t)$ in the EOMs. For small values of c, the deviation from the bipolar oscillations is minimal; the scenario $c = 0$ would correspond to no spatial gradient, and each point

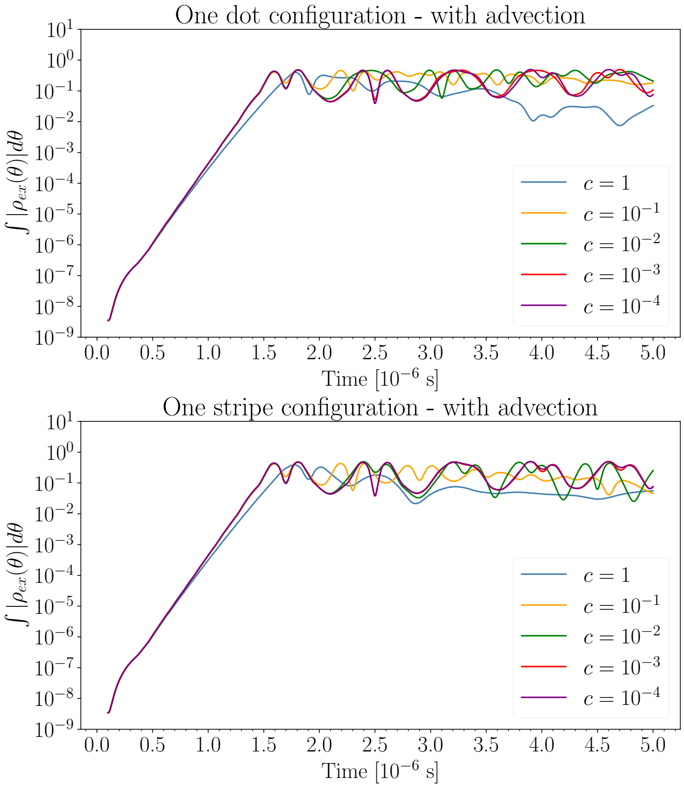

Figure 55: Temporal evolution of $\int |\rho_{ex}(\theta)|d\theta$ for different values of the advective velocity c for a comoving point in the 2D box for the “one dot configuration” (top) and for the “one stripe configuration” (bottom). The impact of advection is less pronounced in the "one stripe configuration" because the gradient vanishes along the $y-$direction. This leads to a weaker "dilution" of the (anti)neutrino excess as a function of the spatial coordinates.

in the 2D grid would oscillate strictly in a bipolar fashion. As the value of c increases (and with it the impact of the advective term), the flavor conversion probability reaches a steady state as a result of gradual flavor decoherence; see the blue line corresponding to $c = 1$, which goes down much faster than the one for $c \ll 1$, implying flavor decoherence due to the presence of neutrino advection. Contrary to what one would expect from the linear stability analysis (Fig. 52), neutrino flavor conversions are inhibited by the advective term, i.e., by the propagation of neutrinos across the 2D spatial domain.

Interestingly, the impact of advection is more pronounced in the "one dot configuration" because the neutrino gas has a non-vanishing gradient along the $x-$ and $y-$directions while for the "one stripe configuration," the gradient vanishes along the $y-$direction. This leads to a weaker "dilution" of the (anti)neutrino excess as a function of x, y. These results (Fig. 55) highlight two critical aspects of the flavor evolution of neutrinos. First, they stress the importance of implementing the neutrino advective term in the EOMs since it significantly affects the coherence of the evolution. And secondly, they highlight the non-trivial interplay between the spatial and temporal variations of the density matrices, which cannot be captured through the widely-implemented linear stability analysis (Fig. 52).

7.6.2 *Limitations and future perspectives*

More sophisticated numerical frameworks are required to tackle the flavor evolution of non-homogeneous systems. Better and faster numerical routines are needed to model fast flavor conversion in more than two spatial dimensions and to account for the breaking of symmetries in the system and its solutions. Even though a great deal of progress has been made, many open questions and technical difficulties need to be addressed before we fully understand the evolution of non-homogeneous systems.

7.6.2.1 *Higher-dimensional simulations*

The hindering of flavor conversion in the presence of neutrino advection was explored in the "one dot configuration" and "one stripe configuration" (Fig. 41) of this Chapter. These two systems helped assess the role of the advective term in two spatial dimensions. We observed that the "dilution" of the (anti)neutrino excess was more prominent in the one dot configuration (Fig. 46) than in the one stripe configuration (Fig. 50) because of the spatial dimensionality of the (anti)neutrino distribution; the dot is essentially a 2D distribution while the stripe can be seen as a 1D distribution. Therefore, one can extrapolate our results to 3D and speculate that the dilution of the neutrino gas would be even more prominent for a 3D dot than for a 2D dot (this Chapter). Nevertheless, when moving to 3D setups, the notion of ELN angular crossing changes: there can be not only a crossing as a function of the polar angle θ but also one along the ϕ direction. The latter forces us to think about ELN angular crossings as two-dimensional structures, i.e., something reminiscent of rings in the ELN angular distribution [182, 183] (see, for instance, Fig. 1 of Ref. [183]). On the other hand, the flavor evolution of the ELN rings in axially-breaking systems has only been explored in a few works (Refs. [181–183]), and only preliminary results are available on the flavor evolution of neutrinos in conjunction with the advective term in full 3D [181, 182]. According to these works, the flavor evolution in 1D and 2D are qualitatively very similar to those in 3D (see Fig. 2 of Ref. [182]), although small spatial structure can develop within the nanosecond time scale. Nevertheless, an extension of the work presented in this Chapter could verify these early findings and corroborate whether our results in Figs. 48 are still valid when including 3D neutrino advection and the ϕ-dependence in the EOMs.

7.6.2.2 *Boundary conditions*

One common issue when modeling flavor conversion together with neutrino advection is the choice of boundary conditions of the system, which is closely related to the choice of refinement in the spatial grid implemented in numerical simulations. For example, if the spatial domain is very small and finely resolved ($\sim$ cm scale), one models a tiny patch of the astrophysical environment, and periodic boundary conditions are naively assumed. However, the periodicity of the boundary conditions can lead to ELN angular intersections at the boundaries, which propagate across the box, possibly leading to flavor equilibration [180, 269]. On the other hand, one can assume a coarse-grained system ($\sim$ km scale) that contains the global features of the astrophysical system at the cost of not resolving small-scale structures. In this case, one has a well-defined neutrino source, and the boundary conditions cannot be periodic anymore. Therefore, future work should study coarse- and fine-grained astrophysical systems with different boundary conditions to understand what features of the flavor evolution correspond to each particular assumption.

8

FAST FLAVOR CONVERSION ABOVE THE DISK OF COMPACT BINARY MERGER REMNANTS

Based on: **Ian Padilla-Gay**, Shashank Shalgar, Irene Tamborra, *Multi-Dimensional Solution of Fast Neutrino Conversions in Binary Neutron Star Merger Remnants*, JCAP01(2021)017, arXiv:2009.01843

ABSTRACT Fast pairwise conversions of neutrinos are predicted to be ubiquitous in neutron star merger remnants with potentially major implications on the nucleosynthesis of the elements heavier than iron. We present the first sophisticated numerical solution of the neutrino flavor evolution above the remnant disk within a (2+1+1) dimensional setup: two spatial coordinates, one angular variable, and time. We look for a steady-state flavor configuration above the remnant disk. Albeit the linear stability analysis predicts flavor instabilities at any location above the remnant disk, our simulations in the non-linear regime show that fast pairwise conversions lead to minimal neutrino mixing ($< 1\%$); flavor equilibration is never achieved in our models. Importantly, fast neutrino conversions are more prominent within localized regions near the edges of the (anti)neutrino decoupling surfaces and almost negligible in the polar region of the remnant. Our findings on the role of fast pairwise conversions should be interpreted with caution because of the approximations intrinsic to our setup and advocate for further work within a more realistic framework.

8.1 INTRODUCTION

The coalescence of a neutron star (NS) with another NS or a black hole (BH) leads to the birth of a compact binary merger. Gravitational waves (GW) from a binary neutron star merger have been detected by the LIGO and Virgo Collaborations, the GW170817 event, together with the multiwavelength electromagnetic counterpart [270–272]. The multi-messenger detection of GW170817 has confirmed theoretical predictions according to which compact binary mergers are the precursors of short gamma-ray bursts (sGRBs), one of the main factories where the elements heavier than iron are synthesized—through the rapid neutron-capture process (*r*-process)—and power kilonovae (electromagnetic transients bright in the optical and infrared wavebands) [48, 273–277].

The GW170817 observation has shed light on the poorly explored physics of NS mergers. However, a robust theoretical understanding of the physics of these objects is still lacking and three-dimensional general-relativistic magnetohydrodynamical simulations with detailed neutrino transport are not yet available. In particular, the role of neutrinos is especially unclear despite the fact that a copious amount of neutrinos is produced in the coalescence. Neutrinos should affect the cooling of the merger remnant, as well as the overall ejecta composition, and contribute to power sGRBs [50, 200, 274, 278–286].

A crucial ingredient possibly affecting the neutrino reaction rates and energy deposition is the neutrino flavor conversion physics, currently neglected in most of the literature on the subject. Besides the ordinary interactions of neutrinos with matter [59, 65], in compact binary mergers, the neutrino density is so high that ν–ν interactions cannot be neglected, similarly to the case of core-collapse supernovae [82, 88, 132]. A characteristic feature of compact binary mergers is the excess of $\bar{\nu}_e$ over ν_e due to the overall protonization of the merger remnant [46, 47, 50]. As a consequence, a matter-neutrino resonance can occur as the matter potential cancels the ν–ν potential [192, 194, 195, 222, 287–289].

In addition to the matter-neutrino resonance, ν–ν interactions can be responsible for the development of fast pairwise conversions [129, 130, 133]. The latter can be triggered by the occurrence of electron lepton number (ELN) crossings in the neutrino angular distributions and could lead to flavor conversions on a time scale $G_\mathrm{F}|n_{\nu_e} - n_{\bar{\nu}_e}|^{-1}$, where G_F is the Fermi constant and n_{ν_e} ($n_{\bar{\nu}_e}$) is the local number density of ν_e ($\bar{\nu}_e$). Reference [196] pointed out that fast pairwise conversions could be ubiquitous above the remnant disk because of the accretion torus geometry and the natural protonization of the remnant leading to an excess of $\bar{\nu}_e$ over ν_e.

Whether flavor equipartition is achieved as a consequence of fast pairwise conversions is a subject of intense debate, also in the context of core-collapse supernovae [134, 147, 149, 153, 155, 187, 239, 290, 291]. If fast pairwise conversions lead to flavor equilibration in compact binary mergers, the nucleosynthesis of the heavy elements in the neutrino-driven wind can be drastically affected, and the fraction of lanthanides boosted with major implications for the kilonova observations [225]. The possible consequences of fast pairwise conversions on the physics of compact mergers justify a modeling of the flavor conversion physics that goes beyond the predictions of the linear stability analysis [104, 133, 135].

Building on Ref. [149], we present the first sophisticated modeling of fast pairwise conversions in the non-linear regime above the disk of merger remnants. We rely on a (2+1+1) dimensional setup: we track the neutrino flavor evolution in two spatial coordinates, one angular variable, and time. We solve the equations of motion of (anti)neutrinos in the absence of collisions and aim to investigate the flavor evolution of the neutrino-dense gas above the disk of the remnant, searching for a steady-state configuration of flavor. Our goal is to identify the location and extent of regions with significant flavor conversion.

This work is organized as follows. In Section 8.2, we introduce the 2D box configuration that we adopt to model the neutrino emission and propagation above the merger remnant disk. The neutrino equations of motion and the semi-analytical tools to explore the eventual occurrence of flavor instabilities in the context of fast pairwise conversions are introduced in Sec. 8.3. In Sec. 8.4, we present our findings on fast pairwise conversions above the massive NS remnant disk in the non-linear regime; we also explore how the steady-state flavor configuration is affected by variations of the input model parameters. In Sec. 8.5, we investigate the flavor oscillation physics above a BH remnant disk. Finally, our conclusions are presented in Sec. 8.6. The routine adopted to take into account the effects of neutrino advection in the presence of flavor conversions is outlined in Appendix C.1. Appendix C.2 instead provides details on the convergence of our results for the adopted spatial resolution.

8.2 MERGER REMNANT DISK SETUP

Given the numerical challenges involved in the modeling of the flavor conversion physics within a realistic astrophysical framework, we here focus on a simpler toy model inspired by the ones adopted in Refs. [149, 196]. We model the neutrino emission above the remnant disk in a 2D box with width L_x and height L_y, with $L_x = L_y \equiv L = 80$ km, as sketched in Fig. 56. Although this is a small patch of the overall region above the merger remnant, it is large enough to explore the development and evolution of fast pairwise conversions. First, we model a NS-disk remnant; our findings are extended to the case of a BH-disk remnant in Sec. 8.5. At the bottom edge of the grid ($y = 0$) in Fig. 56, we locate a thin neutrino source, $\mathcal{S}_\nu$, of length $R = L/4 = 20$ km, which represents the ν_e neutrinosphere. Similarly, we consider a source of $\bar{\nu}_e$, $\mathcal{S}_{\bar{\nu}}$, of length $\bar{R} = 75\%R$. The neutrino and antineutrino emission surfaces are centered on $(x = L/2, y = 0)$. The neutrino source $\mathcal{S}_\nu$ is such that $x \in [L/2 - R, L/2 + R]$ and similarly for $\mathcal{S}_{\bar{\nu}}$ with the replacement $R \to \bar{R}$.

Our choice of the $\mathcal{S}_\nu$ size with respect to the one of $\mathcal{S}_{\bar{\nu}}$ is guided by hydrodynamical simulations of a massive NS-disk [50]. Although it is well known that the decoupling surfaces of ν_e and $\bar{\nu}_e$ are spatially well separated, see e.g. [47, 225], we assume that the neutrinospheres of ν_e and $\bar{\nu}_e$ are coincident and the decoupling occurs suddenly for the sake of simplicity. As we will discuss later, this has an impact on the formation of ELN crossings, but it does not affect the overall flavor conversion picture above the remnant disk.

We also assume that non-electron flavors are generated through flavor conversions only. In the case of NS-disk remnants, a small amount of non-electron (anti)neutrinos is naturally produced in the NS-disk remnant (see, e.g., Refs. [50, 292]); in this case, our extreme assumption enhances the likelihood of having flavor conversions and, as we will discuss in Sec. 8.4, it does not affect our overall conclusions. Our ansatz closely mimics the BH-disk remnant case instead (see Sec. 8.5 and, e.g., Ref. [293]).

As for the boundary conditions in our 2D box, we assume that, except for the edge containing the (anti)neutrino sources, the other edges of the 2D box act as sinks for (anti)neutrinos. Since the (anti)neutrinos continuously flow from the sources into the sinks, the total number density of neutrinos and antineutrinos is conserved.

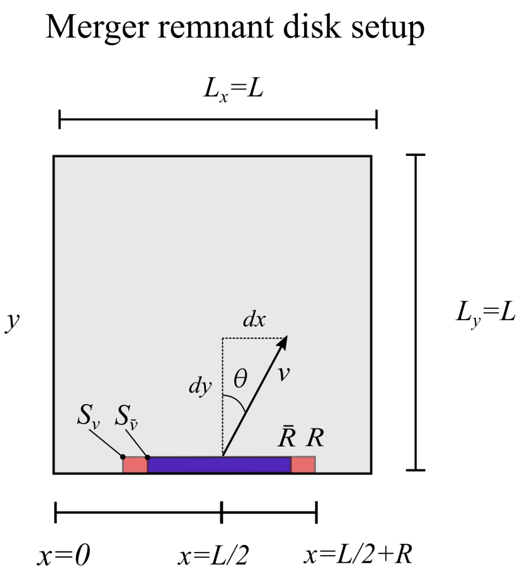

Figure 56: Schematic representation of our merger remnant setup in a 2D box of size $L_x = L_y = L$. The neutrino source ($\mathcal{S}_\nu$, in red) and the antineutrino one ($\mathcal{S}_{\bar\nu}$, in blue) have widths $2R$ and $2\bar{R}$ and are centered on $(x, y) = (L/2, 0)$, respectively. The (anti)neutrino sources emit ν_e and $\bar\nu_e$ in the forward direction only i.e. $\theta \in (-\pi/2, \pi/2)$.

We work in a two-flavor approximation, (ν_e, ν_x), and denote with ν_x a mixture of the non-electron flavors. In order to describe the neutrino and antineutrino fields, we rely on 2×2 density matrices defined for each (x, y) point in the 2D box:

$$\rho(\vec{x}, \theta, t) = \begin{pmatrix} \rho_{ee} & \rho_{ex} \\ \rho_{ex}^* & \rho_{xx} \end{pmatrix} \quad \text{and} \quad \bar\rho(\vec{x}, \theta, t) = \begin{pmatrix} \bar\rho_{ee} & \bar\rho_{ex} \\ \bar\rho_{ex}^* & \bar\rho_{xx} \end{pmatrix} . \tag{8.1}$$

The diagonal terms of the density matrix encode the flavor content information and are proportional to the (anti)neutrino number densities in (x, y); the off-diagonal terms are connected to the probability of flavor transitions, as we will discuss in the next section. As such, we normalize the density matrices in the following way: $\mathrm{tr}(\rho) = 1$ and $\mathrm{tr}(\bar\rho) = a$. The parameter a takes into account the asymmetry between neutrinos and antineutrinos, and we take $a = 2.4$ [225] in the numerical runs.

The flavor conversion physics is affected by the distributions in angle and in energy of neutrinos and antineutrinos. However, since we focus on fast pairwise conversions, in the following we assume a monoenergetic distribution of (anti)neutrinos, with average energy $\langle E_{\nu_e} \rangle = \langle E_{\bar\nu_e} \rangle \simeq 20$ MeV to mimic typical average energies in the proximity of the (anti)neutrino decoupling region; as shown in Ref. [147], the assumption of a monoenergetic distribution reproduces the flavor outcome that one would obtain when an energy distribution centered on $\langle E_{\nu_e,\bar{\nu}_e} \rangle$ is considered. As a consequence, the neutrino distribution, for each point in the (x, y) box and at the time t, is defined by the emission angle θ (see Fig. 56).

In order to model the physics of fast pairwise conversions, we need to take into account the (anti)neutrino angular distributions. We assume that the emission surfaces of neutrinos and antineutrinos are perfect black-bodies and (anti)neutrinos are uniformly emitted in the forward direction across the source, i.e., $\theta \in (-\pi/2, \pi/2)$ with θ measured with respect to the y direction (see Fig. 56). In order to guarantee that the emitting surfaces are Lambertian and the neutrino radiance is the same along any viewing angle, we assume the angular distributions to be proportional to $\cos\theta$:

$$\rho_{ee}(\theta) = \cos\theta \times \begin{cases} 1 & \text{if } x_{0,\nu} \in \mathcal{S}_\nu \\ \exp\left(\frac{(x-L/2\mp R)^2}{2\sigma^2}\right) & \text{otherwise}\,, \end{cases} \tag{8.2}$$

$$\bar{\rho}_{ee}(\theta) = a\cos\theta \times \begin{cases} 1 & \text{if } x_{0,\bar{\nu}} \in \mathcal{S}_{\bar{\nu}} \\ \exp\left(\frac{(x-L/2\mp \bar{R})^2}{2\bar{\sigma}^2}\right) & \text{otherwise}\,, \end{cases} \tag{8.3}$$

where σ, $\bar{\sigma}$ smooth the edges of $\mathcal{S}_\nu$ and $\mathcal{S}_{\bar{\nu}}$ and are set to $20\%R$ and $20\%\bar{R}$, respectively.

By projecting the neutrino and antineutrino angular distributions from the sources on any (x, y) point in the 2D box, we obtain the contour plots in Fig. 57 for the resultant angle-integrated density matrices of ν_e and $\bar{\nu}_e$, $\int d\theta \rho_{ee}(\vec{x}, \theta)$ and $\int d\theta \bar{\rho}_{ee}(\vec{x}, \theta)$, in the absence of flavor conversions (see also Sec. 8.3) for the NS-disk remnant configuration. One can see that the neutrino density gradually decreases as one moves from $\mathcal{S}_\nu$ and $\mathcal{S}_{\bar{\nu}}$ towards the edges of the box.

In order to explore the variation of the (anti)neutrino angular distributions across the 2D box, Fig. 58 displays the angular distributions of ν_e and $\bar{\nu}_e$ in the points A, B, and C highlighted in Fig. 57. The width of the ELN crossings varies as one moves away from $\mathcal{S}_\nu$ and $\mathcal{S}_{\bar{\nu}}$, with implications on the flavor conversion physics, as we discuss in Sec. 8.3.

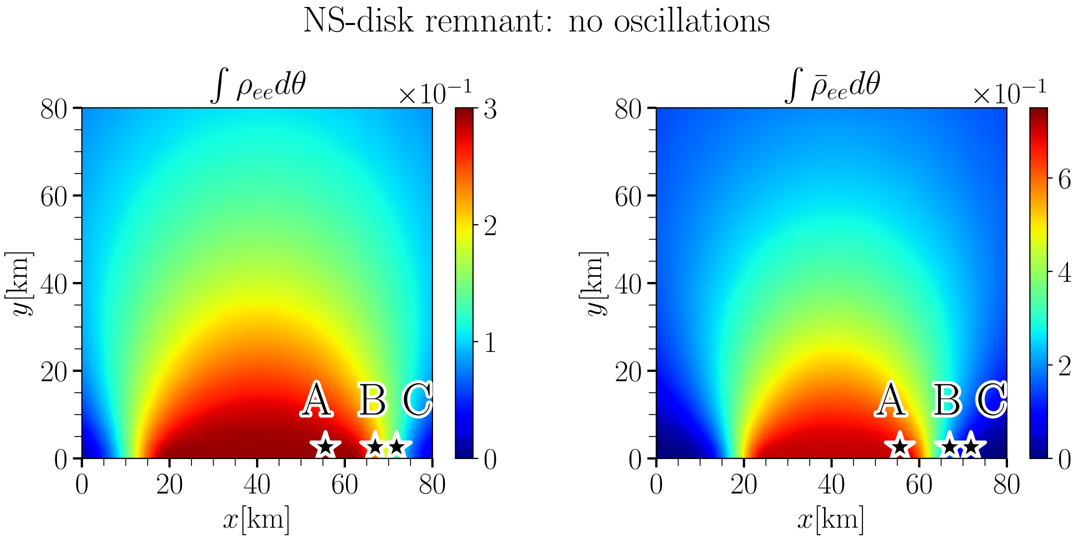

Figure 57: Contour plots of the angle-integrated density matrices, $\rho(\vec{x}, \theta, t)$ (on the left) and $\bar{\rho}(\vec{x}, \theta, t)$ (on the right), in the absence of flavor conversions for the NS-disk remnant configuration. This configuration can be obtained by solving Eqs. 8.4 and 8.5 for $H(\theta) = \bar{H}(\theta) = 0$, i.e. the time evolution of $\rho(\vec{x}, \theta, t)$ and $\bar{\rho}(\vec{x}, \theta, t)$ is completely determined by the advective operator $\vec{v} \cdot \vec{\nabla}$ (see Sec. 8.3 for more details). The quantities $\int \rho_{ee} d\theta$ and $\int \bar{\rho}_{ee} d\theta$ are normalized to the maximum total particle number in the box $[\int (\rho_{ee} + \bar{\rho}_{ee} + 2\rho_{xx}) d\theta]$. The coordinates of the points A, B, and C marked on the plane are: $(x, y) \simeq (56, 1)$ km, $(67, 1)$ km, and $(72, 1)$ km, respectively. The (anti)neutrino density gradually decreases as one moves away from $\mathcal{S}_\nu$ and $\mathcal{S}_{\bar{\nu}}$.

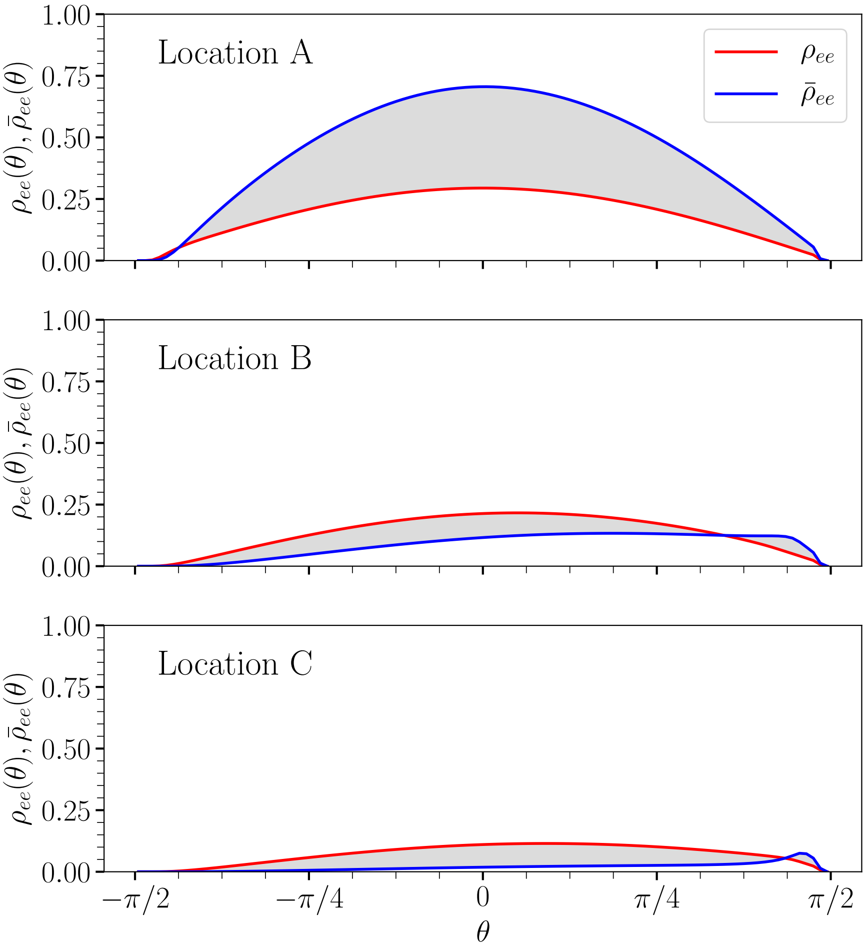

Figure 58: Angular distributions of ρ_{ee} (red) and $\bar{\rho}_{ee}$ (blue) in A, B and C (see Fig. 57). The presence of two disjoint grey areas imply the existence of ELN angular crossings. The angle-dependent density matrix elements are normalized to the maximum total particle number in $(x, y)_{\mathrm{A,B,C}}$: $(\rho_{ee} + \bar{\rho}_{ee} + 2\rho_{xx})$. As one moves away from $\mathcal{S}_\nu$ and $\mathcal{S}_{\bar{\nu}}$, the width of the ELN crossings varies with implications on the flavor conversion physics.

8.3 FAST PAIRWISE NEUTRINO FLAVOR CONVERSION

In this section, we introduce the equations of motion adopted to track the flavor evolution above the NS-disk remnant in our 2D setup. In order to gauge the role of neutrino flavor conversions above the NS-disk remnant, we discuss the variation of the ν–ν interaction strength across the 2D box and introduce the instability parameter to characterize the depth of the ELN crossings. We also adopt the linear stability analysis to compute the growth rate of the flavor instabilities in the regions with the largest instability parameter.

8.3.1 *Equations of motion*

The (anti)neutrino field is described through the density matrix approach introduced in Sec. 8.2. Neglecting collisions, the flavor evolution of neutrinos and antineutrinos is described by the following set of equations of motion (EoM):

$$i\left(\frac{\partial}{\partial t}+\vec{v}\cdot\vec{\nabla}\right)\rho(\vec{x},\theta,t) = [H(\theta),\rho(\vec{x},\theta,t)]\,, \tag{8.4}$$

$$i\left(\frac{\partial}{\partial t}+\vec{v}\cdot\vec{\nabla}\right)\bar{\rho}(\vec{x},\theta,t) = [\bar{H}(\theta),\bar{\rho}(\vec{x},\theta,t)]\,, \tag{8.5}$$

where the advective term, $\vec{v}\cdot\vec{\nabla}$, is proportional to the velocity of (anti)neutrinos, which we assume to be equal to the speed of light, and is tangential to the neutrino trajectory. The contour plots of the angle-integrated density matrices of ν_e and $\bar{\nu}_e$ in Fig. 57 can be obtained by solving Eqs. 8.4 and 8.5 when the right hand side of both EoMs is vanishing, i.e., (anti)neutrinos do not change their flavor.

The neutrino Hamiltonian is

$$H(\theta)=\frac{\omega}{2}\begin{pmatrix}-\cos 2\theta_V & \sin 2\theta_V \\ \sin 2\theta_V & \cos 2\theta_V\end{pmatrix}+H_{\nu\nu}(\vec{x},\theta)\,, \tag{8.6}$$

with the first term depending on the vacuum frequency $\omega = 0.3\ \mathrm{km}^{-1}$, where $\omega = \Delta m^2/2\langle E_{\nu_e,\bar{\nu}_e}\rangle$, Δm^2 is the atmospheric squared mass difference and $\langle E_{\nu_e,\bar{\nu}_e}\rangle$ the average mean energy of ν_e's and $\bar{\nu}_e$'s introduced in Sec. 8.2. The vacuum mixing angle is $\theta_V = 10^{-6}$; note that we assume a very small mixing to effectively ignore the matter potential [264]. The second term of the Hamiltonian is the ν–ν interaction term:

$$H_{\nu\nu}(\vec{x},\theta) = \mu(|\vec{x}|) \int d\theta' \left[\rho(\vec{x},\theta',t) - \bar{\rho}(\vec{x},\theta',t)\right] \left[1 - \cos(\theta - \theta')\right] \ . \tag{8.7}$$

The potential, $\mu(|\vec{x}|)$, parametrizes the strength of neutrino-neutrino interactions for each point (x, y) in the box and its functional form is defined in Sec 8.3.2. The Hamiltonian of antineutrinos, $\bar{H}(\theta)$, is identical to $H(\theta)$ except for the following replacement: $\omega \to -\omega$ [89]. The integration over $d\theta'$ is a consequence of our 2D setup. In a 3D box, the integration over $d\theta'$ would be replaced by an integration over the solid angle. We have checked, however, that the integration over $d\cos\theta$ that would arise in an azimuthally symmetric 3D system virtually gives the same results as our 2D setup (see also Sec. 8.3.2).

8.3.2 *Neutrino self-interaction potential*

The ν–ν interaction potential varies across our 2D box, by taking into account the dilution of the (anti)neutrino gas as we move away from the sources $\mathcal{S}_\nu$ and $\mathcal{S}_{\bar{\nu}}$. We parametrize it as

$$\mu(|\vec{x}|) = \mu_0 \eta(|\vec{x}|) \ , \tag{8.8}$$

where $\eta(|\vec{x}|)$ is a scaling function, and $\mu_0 = 10^5\ \mathrm{km}^{-1}$ is the ν–ν interaction strength at the neutrinosphere [196].

Since the modeling of flavor evolution in 3D is computationally challenging at present, we mimic the 3D setup by solving the EoM in 2D while taking into account the dilution of the neutrino gas in 3D. For an observer located at (x, y), the distance d above the source, $\mathcal{S}_{\nu,\bar{\nu}}$, can be computed as $d = dy/\cos\theta$, where dy is the vertical displacement from the source to (x, y), see Fig. 56. For observers that are not located above the source, the dilution of the flux is determined by the distance d. With this convention, the scaling function η is defined as

$$\eta = \left(1 - \frac{1}{\sqrt{(R/d)^2 + 1}}\right)^2 \left[\arccos\left(\frac{1}{\sqrt{(R/d)^2+1}}\right) - \sqrt{1 - \frac{1}{(R/d)^2+1}}\right]^{-1} \ . \tag{8.9}$$

To better understand the role of η, let us look at one limiting case for an observer along the axis of symmetry. When $dy \gg R$, $\eta \propto (R/dy)$, hence $H_{\nu\nu} \propto (R/dy)^4$ for a 3D bulb model, as expected [89].

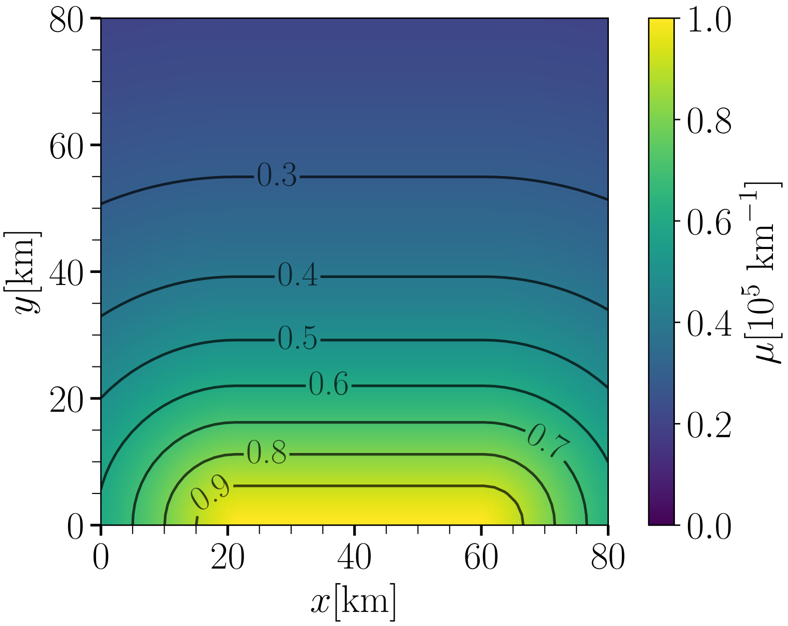

Figure 59: Contour plot of the neutrino self-interaction strength, $\mu(|\vec{x}|)$, in the 2D box. The neutrino-neutrino potential is maximum in the proximity of the (anti)neutrino source and it gradually decreases as the distance from the (anti)neutrino sources increases.

Figure 59 shows $\mu(|\vec{x}|)$ in our 2D box (see Eq. 8.8). At the (anti)neutrino emission surfaces, μ assumes the maximum value (μ_0) and drops as a function of the distance from the source.

8.3.3 *Instability parameter*

A favorable condition for the development of fast pairwise conversions is the presence of ELN crossings between the angular distributions of ν_e and $\bar{\nu}_e$ [133]. To this purpose, the "instability parameter" has been introduced in Ref. [149] to gauge the growth rate of flavor instabilities; the latter being dependent on the depth of the ELN crossings [161, 265]:

$$\zeta = \rho_{\mathrm{tot}} \frac{I_1 I_2}{(I_1 + I_2)^2} , \tag{8.10}$$

where ρ_{tot} is the total particle number defined as $\int [\rho_{ee} + \bar{\rho}_{ee} + 2\rho_{xx}] d\theta$ and the factors $I_{1,2}$ are defined as

$$I_1 = \int_{-\pi/2}^{\pi/2} \Theta\left[\rho_{ee}(\theta) - \bar{\rho}_{ee}(\theta)\right] d\theta \text{ and } I_2 = \int_{-\pi/2}^{\pi/2} \Theta\left[\bar{\rho}_{ee}(\theta) - \rho_{ee}(\theta)\right] d\theta \, ; \tag{8.11}$$

the Heaviside function, Θ, is vanishing for $\rho_{ee}(\theta) - \bar{\rho}_{ee}(\theta) < 0$ and otherwise equal to the identity operator. The instability parameter ζ vanishes when the ELN crossing is zero. The instability parameter is a useful predictor of the growth rate of the off-diagonal components of the density matrices and, therefore, of the flavor instabilities (see Sec. 3.4 of Ref. [149] for more details).

The left panel of Fig. 60 shows a contour plot of the instability parameter in the absence of flavor conversions across our 2D box. One can see that ζ is large in the proximity of the edges of the neutrino emitting surfaces ($x \simeq 15, 65$ km and $y \in [0, 15]$ km) and it gradually decreases as we move away from the sources, since the (anti)neutrino gas dilutes and the ELN crossings become less prominent. As a consequence, and by taking into account that $\mu(|\vec{x}|)$ decreases as we move away from $\mathcal{S}_{\nu}$ and $\mathcal{S}_{\bar{\nu}}$ (see Eq. 8.8), we should expect fast pairwise conversions to possibly occur where the ζ parameter is larger. Also, it is worth noticing that ζ is approximately zero in the central region of the emitting sources ($x \in [20, 60]$ km and $y \in [0, 15]$ km), this is mostly a consequence of the fact that we assume the neutrinospheres of ν_e and $\bar{\nu}_e$ to be coincident with each other, despite differing in width. Similarly to Ref. [196], we expect to find a suppression of the flavor instabilities in the proximity of the emitting surfaces around the polar region (ζ is very small in our case) and a growth of the instabilities at larger distances from the source (ζ becomes larger).

Note that flavor conversions affect the (anti)neutrino angular distributions. Hence, the instability parameter shown in Fig. 60 can be dynamically modified by fast pairwise conversions. However, the plot provides with insights on the regions where flavor conversions may have larger effects, as we will see in Sec. 8.4.

8.3.4 *Linear stability analysis*

In order to explore the growth of the off-diagonal term in the density matrices, and therefore the development of fast pairwise conversions, we first rely on the linear stability analysis to analytically predict the growth rate of the flavor instabilities [104, 135]. Note that, given that we intend to focus on fast pairwise conversions, we assume $\omega = 0$ in this section; such assumption is justified since $\omega \neq 0$ would mainly affect the non-linear regime of fast pairwise conversions [147].

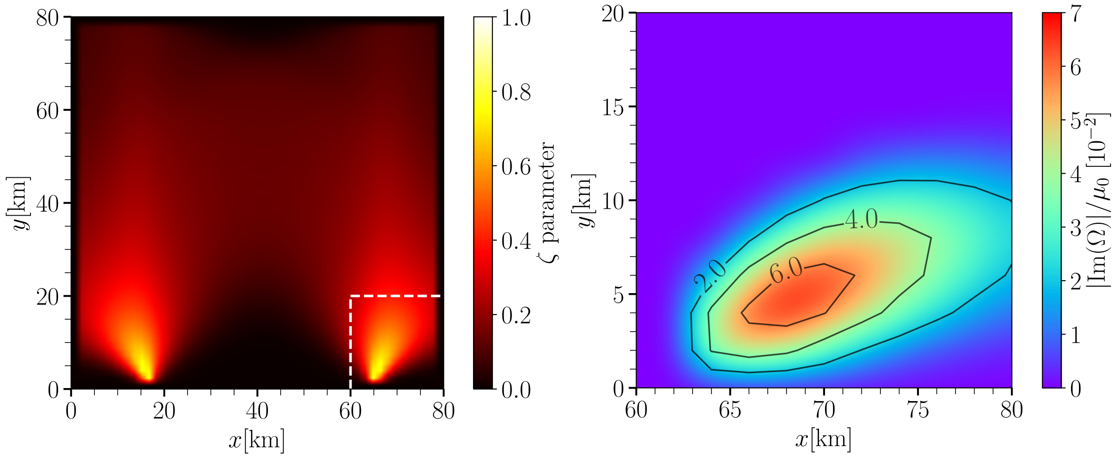

Figure 60: *Left:* Contour plot of the instability parameter ζ (see Eq. 8.10) in the 2D box in the absence of flavor conversions for the ν_e and $\bar{\nu}_e$ distributions in Fig. 57. The ELN crossings are significant just above the edges of the emitting sources. *Right:* Contour plot of $|\mathrm{Im}(\omega)|/\mu_0$ for the homogeneous mode for the benchmark NS-disk model in one of the regions where the instability parameter is the largest (see dashed lines in the left panel). A maximum growth rate $|\mathrm{Im}(\omega)| = 0.07\mu_0 \simeq 2$ ns can be achieved.

We linearize the EoM and track the evolution of the off-diagonal term through the following ansatz

$$\rho_{ex}(\theta) = Q(\theta)e^{-i\Omega t} \text{ and } \bar{\rho}_{ex}(\theta) = \bar{Q}(\theta)e^{-i\Omega t}, \tag{8.12}$$

where $\Omega = \gamma + i\kappa$ represents the collective oscillation frequency for neutrinos and antineutrinos. If $\mathrm{Im}(\Omega) \neq 0$, then the flavor instability grows exponentially with rate $|\mathrm{Im}(\Omega)|$, leading to fast pairwise conversions [133]. Note that we look for temporal instabilities for the homogeneous mode ($\vec{k} = 0$), as these are the ones possibly leading to fast pairwise conversions in extended regions [196]; by adopting a similar disk setup, Ref. [196] found that spatial instabilities occur in much smaller spatial regions than the temporal instabilities.

The off-diagonal component of Eq. 8.4 is

$$\begin{aligned} i\frac{\partial}{\partial t}\rho_{ex}(\theta) &= H_{ee}(\theta)\rho_{ex}(\theta) + H_{ex}(\theta)\rho_{xx}(\theta) - \rho_{ee}(\theta)H_{ex}(\theta) - \rho_{ex}(\theta)H_{xx}(\theta) \\ &= H_{ee}(\theta)\rho_{ex}(\theta) - \rho_{ee}(\theta)H_{ex}(\theta)\,, \end{aligned} \tag{8.13}$$

where we have assumed $\rho_{xx}(t = 0\,\mathrm{s}) = \bar{\rho}_{xx}(t = 0\,\mathrm{s}) = 0$. By substituting Eq. 8.12 in the equation above and solving for $Q(\theta)$, we obtain

$$Q(\theta) = \frac{\rho_{ee}(\theta) \int d\theta' [Q(\theta') - \bar{Q}(\theta')][1 - \cos(\theta - \theta')]}{-\frac{\Omega}{\mu} + \int d\theta' [\rho_{ee}(\theta') - \bar{\rho}_{ee}(\theta')][1 - \cos(\theta - \theta')]} \,. \tag{8.14}$$

A similar procedure follows for $\bar{Q}_\theta$ (see Eqs. 8.5 and 8.12). Then, combining the expressions for $Q(\theta)$ and $\bar{Q}(\theta)$, we have

$$Q(\theta) - \bar{Q}(\theta) = \int d\theta' \left(\frac{\rho_{ee}(\theta) - \bar{\rho}_{ee}(\theta)}{-\frac{\Omega}{\mu} + A(\theta)} \right) [Q(\theta') - \bar{Q}(\theta')][1 - \cos(\theta - \theta')] \,, \tag{8.15}$$

where $A(\theta) = \int d\theta' [\rho_{ee}(\theta') - \bar{\rho}_{ee}(\theta')][1 - \cos(\theta - \theta')]$. From the equation above, it must be true that

$$Q(\theta) - \bar{Q}(\theta) = \left[\frac{\rho_{ee}(\theta) - \bar{\rho}_{ee}(\theta)}{-\frac{\Omega}{\mu} + A(\theta)} \right] (a - b\cos\theta - c\sin\theta) \,, \tag{8.16}$$

where a, b, c are unknown coefficients. By substiting Eq. 8.16 in Eq. 8.15, we obtain a system of equations for the coefficients a, b, and c. Since the variable θ' is a dummy variable, we replace it by θ:

$$\begin{bmatrix} a \\ b \\ c \end{bmatrix} = \begin{bmatrix} \mathcal{I}[1] & -\mathcal{I}[\cos\theta] & -\mathcal{I}[\sin\theta] \\ \mathcal{I}[\cos\theta] & -\mathcal{I}[\cos\theta^2] & -\mathcal{I}[\cos\theta\sin\theta] \\ \mathcal{I}[\sin\theta] & -\mathcal{I}[\cos\theta\sin\theta] & -\mathcal{I}[\sin\theta^2] \end{bmatrix} \begin{bmatrix} a \\ b \\ c \end{bmatrix} = \mathrm{M} \begin{bmatrix} a \\ b \\ c \end{bmatrix} \,, \tag{8.17}$$

where the functional $\mathcal{I}[f]$ is

$$\mathcal{I}[f] = \int d\theta \left[\frac{\rho_{ee}(\theta) - \bar{\rho}_{ee}(\theta)}{-\frac{\Omega}{\mu} + A(\theta)} \right] f(\theta) \,. \tag{8.18}$$

The system of equations has a not trivial solution if

$$\det(\mathrm{M} - 1) = 0 \,. \tag{8.19}$$

The latter equation is polynomial in the frequency Ω. To search for instabilities, we need to look for the solutions with $\mathrm{Im}(\Omega) = \kappa \neq 0$. We then use the SciPy module [294] in Python to find the roots numerically.

The right panel of Fig. 60 shows the growth rate, $|\mathrm{Im}(\Omega)|/\mu_0$, for a region of our 2D box where the instability parameter is the largest (see the highlighted region in the left panel of Fig. 60). In the region of the 2D box corresponding to the edges of $\mathcal{S}_\nu$, $|\mathrm{Im}(\Omega)|/\mu_0 \simeq 0.01$–$0.06$; if we compare our findings to the ones reported in the top panel of Fig. 3 of Ref. [196], we obtain a roughly comparable growth rate of the flavor instability. We should highlight that we assume the ν_e and $\bar{\nu}_e$ neutrinospheres to be exactly coincident with each other (although having different widths) while a two-disk model was considered in Ref. [196]; this quantitatively affects the depth of the ELN crossings in the polar region above the remnant in the proximity of the source. We also note that we model differently the edges of the (anti)neutrino sources and the (anti)neutrino angular distributions with respect to Ref. [196] and this causes differences in the shape of the unstable regions above the NS-disk remnant.

8.4 FLAVOR EVOLUTION ABOVE THE NS-DISK REMNANT

Most of the existing work in the context of neutrino flavor conversions above the remnant disk focuses on exploring the phenomenology of slow collective oscillations and the matter-neutrino resonance [192, 194, 195, 222, 287–289]. The only existing literature on fast pairwise conversions in merger remnants relies on the linear stability analysis to explore whether favorable conditions for fast conversions exist above the remnant disk [196, 225], as also discussed in Sec. 8.3.4. In this section, we present the results of the numerical evolution in the non-linear regime of fast pairwise conversions above the NS-disk remnant and discuss the implications for the merger physics. We then generalize our findings by exploring the parameter space of the possible ν_e–$\bar{\nu}_e$ asymmetries expected above the NS-disk remnant and the relative ratio between the size of the ν_e and $\bar{\nu}_e$ sources.

8.4.1 *Numerical implementation*

We solve the EoM introduced in Sec. 8.3 for the box setup described in Sec. 8.2 by following the procedure outlined in Sec. 3.2 of Ref. [149]. In the numerical runs, we adopt $N_x = N_y = 50$ number of bins for the $x - y$ grid and $N_\theta = 300$ angular bins to ensure numerical convergence.

In order to quantify the amount of flavor mixing, we introduce the angle integrated survival probabilities

$$P(\nu_e \to \nu_e) = \frac{\int d\theta[\rho_{ee}(\vec{x}, t) - \rho_{xx}(\vec{x}, t = 0\,\mathrm{s})]}{\int d\theta[\rho_{ee}(\vec{x}, t = 0\,\mathrm{s}) - \rho_{xx}(\vec{x}, t = 0\,\mathrm{s})]}\,, \tag{8.20}$$

and similarly for $P(\bar{\nu}_e \to \bar{\nu}_e)$ with the replacement $\rho \to \bar{\rho}$. Figure 61 shows the survival probabilities of ν_e and $\bar{\nu}_e$ as functions of time for the three selected (x, y) locations (A, B, and C) in the 2D box, see Fig. 57. One can easily see that fast pairwise conversions take some time to develop, but then they reach a "steady-state" configuration and the survival probability stabilizes, despite smaller scale oscillations, without changing dramatically.

In the presence of flavor conversions, for each (x, y) point in the 2D box, flavor conversions develop on a time scale shorter than the advective time scale [149]. To take into account the (anti)neutrino drifting through the 2D box, for each (x, y) location in the 2D box, we translate the time-averaged neutrino and antineutrino density matrices from each spatial bin to the neighboring bins after a time $\Delta t \simeq \mathcal{O}(10^{-7})$ s, i.e. after the flavor conversion probability in (x, y) has reached a steady-state configuration; we keep all the parameters within each spatial bin unchanged, except for following the flavor conversions for smaller time intervals. This procedure is implemented in an automated fashion as described in Appendix C.1 and it naturally allows to recover the flavor configuration shown in Fig. 57 in the absence of flavor conversions. We stress that our procedure automatically allows to take into account the dynamical evolution of the angular distributions as a function of time, due to neutrinos streaming from the neighboring bins.

As seen in Fig. 61 the (anti)neutrino occupation numbers oscillate around an average value after the system has reached the non-linear regime. In an astrophysical system, at a given point in space, only the time-averaged occupation numbers are the relevant quantities as long as the size of the region over which neutrinos and antineutrinos are emitted is larger than the length scale over which neutrinos and antineutrinos oscillate. The aforementioned condition should always be satisfied above the remnant disk because of the short time-scales over which fast flavor conversions occur.

It is worth noticing that, while Fig. 57 represents the resultant angular distributions of ν_e and $\bar{\nu}_e$ in the absence of flavor conversions across the 2D box, by streaming the oscillated (anti)neutrinos to their neighboring bins, we also modify the angular distributions dynamically. In Ref. [149], it was shown the neutrino advection smears the ELN crossings hindering the development of fast pairwise conversions; such an effect would eventually become efficient on time scales longer than Δt, i.e. after the steady-state configuration has been reached in our 2D box. Moreover, the ELN

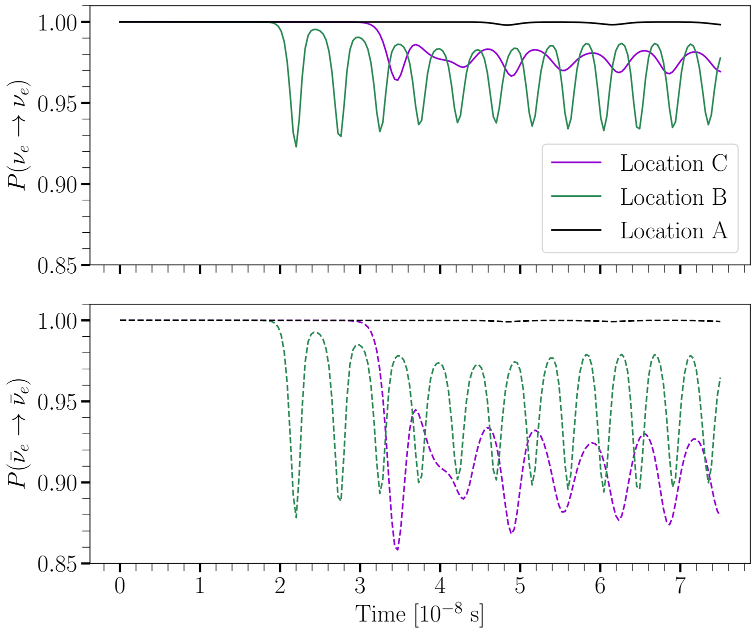

Figure 61: Temporal evolution of the survival probabilities of ν_e (top) and $\bar{\nu}_e$ (bottom) for the three selected locations A, B and C shown in Fig. 57 (see Eq. 8.20). After a certain time, $\Delta t \simeq \mathcal{O}(10^{-7})$ s, the survival probabilities have reached a steady-state configuration. Minimal flavor mixing is achieved for all three locations.

crossings in our system are assumed to be self-sustained in time because of the disk geometry and its protonization.

For a selection of points close to $\mathcal{S}_\nu$ and $\mathcal{S}_{\bar{\nu}}$, we have also tested that the growth rate obtained from the linear stability analysis in Sec. 8.3.4 perfectly matches the linear regime of the numerical solution. In particular, for the point B in Fig. 57, we find $|\mathrm{Im}(\Omega)|/\mu = 0.0489$ by numerically solving the EoM and $|\mathrm{Im}(\Omega)|/\mu = 0.049$ by relying on the stability analysis. As discussed in Ref. [147], the dependence of the linear growth rate on ω is overall negligible.

8.4.2 *Results*

Figure 61 shows the temporal evolution of the ν_e and $\bar{\nu}_e$ survival probabilities as discussed in Sec. 8.4.1. Even though flavor unstable solutions are predicted to exist almost at any location above the disk of the remnant and the linear stability analysis suggests a large growth rate, as shown in Fig. 60, our results show that fast pairwise conversions lead to a few percent variation in the flavor transition probability. At most, an average value of $P(\nu_e \to \nu_e) \simeq 0.95$ is obtained in our runs; while the survival probability for antineutrinos can reach slightly lower values, $P(\bar{\nu}_e \to \bar{\nu}_e) \simeq 0.90$, due to the lepton number conservation.

To better explore the development of fast pairwise conversions as a function of the emission angle, the top panel of Fig. 62 shows ρ_{ee} and $\bar{\rho}_{ee}$ (respectively proportional to the ν_e and $\bar{\nu}_e$ number densities) as functions of the emission angle θ for the observer located in B in Fig. 57. The angular distributions are displayed at $t = 0$ s (i, dashed lines) and at $t = 7.5 \times 10^{-8}$ s (f, solid lines) when the flavor conversions have reached a steady-state configuration (see Fig. 61 and Appendix C.1). Initially, the ELN crossings are large for $\theta \in [\pi/4, \pi/2]$; this triggers fast pairwise conversions of ν_e and $\bar{\nu}_e$. As t increases, the angular distributions of ν_e and $\bar{\nu}_e$ most prominently evolve around the angular bins in the proximity of the ELN crossing, as highlighted in the middle panel of Fig. 62, until the density matrices reach a stationary value. In the bottom panel of Fig. 62, one can see that newly formed ν_x and $\bar{\nu}_x$ angular distributions peak in a very narrow θ interval where the ELN crossings occur. As a result, ν_x ($\bar{\nu}_x$) will predominantly propagate outwards and away from the remnant symmetry axis, thus having a marginal impact on the polar region of the system.

Figure 63 summarizes our findings across the 2D box by displaying contours of the angle-integrated density matrix elements for neutrinos (on the left) and antineutrinos (on the right) for the NS-disk remnant configuration when the steady-state configuration for flavor conversions is reached. The top panels are almost identical to the ones in Fig. 57 because of the overall small amount of flavor conversions despite the large instability parameter and growth rate (see Fig. 60). From the middle and the bottom panels, we can clearly see that flavor conversions occur in the region at the edges of the emitting surfaces where ζ is larger, but they have a negligible role in the polar region above the remnant disk where the neutrino-driven wind nucleosynthesis could be affected [225].

For completeness, Appendix C.2 includes results of a high resolution run performed in the red box in Fig. 63. The overall amount of flavor conversions is comparable in the low and high resolution simulations; for this reason, we have chosen to rely on simulations with lower resolution in order to explore a larger region above the remnant disk.

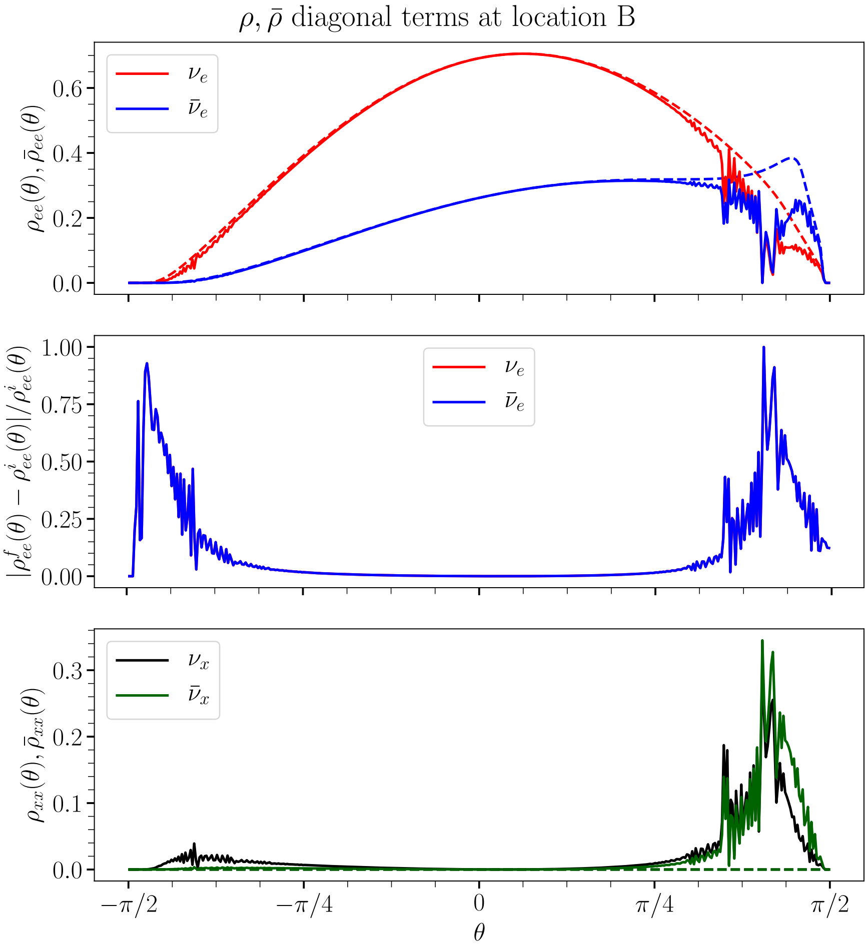

Figure 62: *Top:* Density matrix elements $\rho_{ee}(\theta)$ (in red) and $\bar{\rho}_{ee}(\theta)$ (in blue) as functions of the emission angle θ at $t = 0$ s (dashed curves, i) and at $t = 7.5 \times 10^{-8}$ s (solid curves, f) at the selected location B of Fig. 57. The density matrix elements are normalized to ρ_{tot}. *Middle:* Relative difference between the final state (f) and initial state (i) of $\rho_{ee}(\theta)$ (red) and $\bar{\rho}_{ee}(\theta)$ (blue), respectively. *Bottom:* Same as the top panel, but for the density matrix elements $\rho_{xx}(\theta)$ (black) and $\bar{\rho}_{xx}(\theta)$ (green). Fast pairwise conversions only affect the tail of the angular distributions of ν_e and $\bar{\nu}_e$ inducing minimal changes.

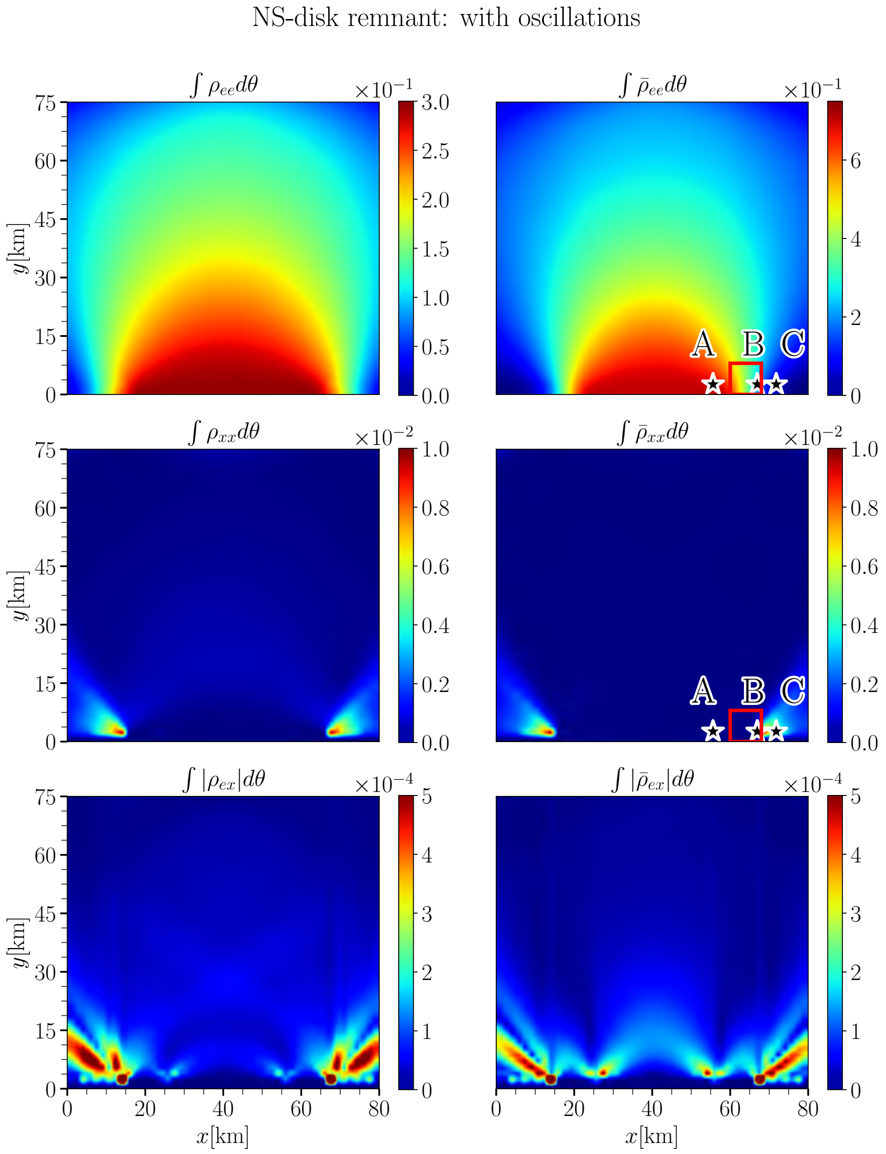

Figure 63: Contour plots of the angle-integrated elements of the density matrices $\rho(\vec{x}, \theta, t)$ (one the left) and $\bar{\rho}(\vec{x}, \theta, t)$ (on the right) for the NS-disk remnant configuration normalized to the maximum total particle number within the box i.e. $\int d\theta(\rho_{ee} + \bar{\rho}_{ee} + 2\rho_{xx})$, after $\Delta t = 10^{-7}$ s, after the flavor distribution has reached a steady-state configuration. Three selected locations (A, B, and C) are highlighted (see Fig. 57). The red box defines the region scanned with higher spatial resolution, see Appendix C.2 for details. As also shown in Fig. 60, fast pairwise conversions are more prominent near the edges of the neutrino sources. A small amount of ν_x's and $\bar{\nu}_x$'s is produced through fast pairwise conversions within the narrow opening angles at the edges of the neutrino surfaces. The ELN crossings are almost vanishing along the axis of symmetry leading to practically no flavor conversions in the polar region above the NS-disk remnant.

By comparing Figs. 60 and Fig. 63, we conclude that the high linear growth rate of fast pairwise conversions does not imply an overall large flavor conversion in the non-linear regime. However, we should stress that ours is the first numerical study of fast pairwise conversions above the merger remnant in the non-linear regime; as such, for the sake of simplicity, we have neglected the collision term in EoM. The collision term may potentially play a significant role, also because it generates a backward flux of (anti)neutrinos [134, 262], which is neglected in our setup. A better refined modeling of the neutrino conversion physics may affect the flavor outcome with implications for the r-process nucleosynthesis [196, 225].

8.4.3 *Results for other NS-disk configurations*

In order to gauge how our findings are modified for different configurations of the NS-disk remnant, in this section we vary the ν_e–$\bar{\nu}_e$ asymmetry parameter, a (see Eq. 8.3) within the range allowed from hydrodynamical simulations [287], as well as the relative ratio between the sizes of $\mathcal{S}_{\bar{\nu}}$ and $\mathcal{S}_{\nu}$ $(\bar{R}/R)$.

Figure 64 shows a contour plot of the maximum of the instability parameter ζ (Eq. 8.10, computed in the absence of flavor conversions) computed across the 2D box for each $(\bar{R}/R, a)$. The markers in Fig. 64 highlight three disk configurations that we have evolved numerically; the NS-disk configuration introduced in Sec. 8.2 is correspondent to $(\bar{R}/R, a) = (0.75, 2.4)$ (blue circle in Fig. 64). The conversion probability in the steady-state regime is $P(\nu_e \to P_{\nu_x}) \simeq 0.02$ for the NS-disk configuration introduced in Sec. 8.2 and tends to become larger for a smaller relative ratio of $\bar{R}/R$ [green diamond, $P(\nu_e \to P_{\nu_x}) \simeq 0.04$] and even more for the red triangle, where the instability parameter is maximal [$P(\nu_e \to P_{\nu_x}) \simeq 0.06$], which however probably corresponds to an extreme $\bar{R}/R$ ratio not realizable in astrophysical environments. Our findings suggest that flavor equilibration due to fast pairwise conversions is never achieved in our setup, despite the large growth rate predicted by the linear stability analysis. In addition, the regions in the 2D box that are most unstable are located in the proximity of the edges of the neutrino source, and no flavor conversions occur in the polar region above the NS-disk.

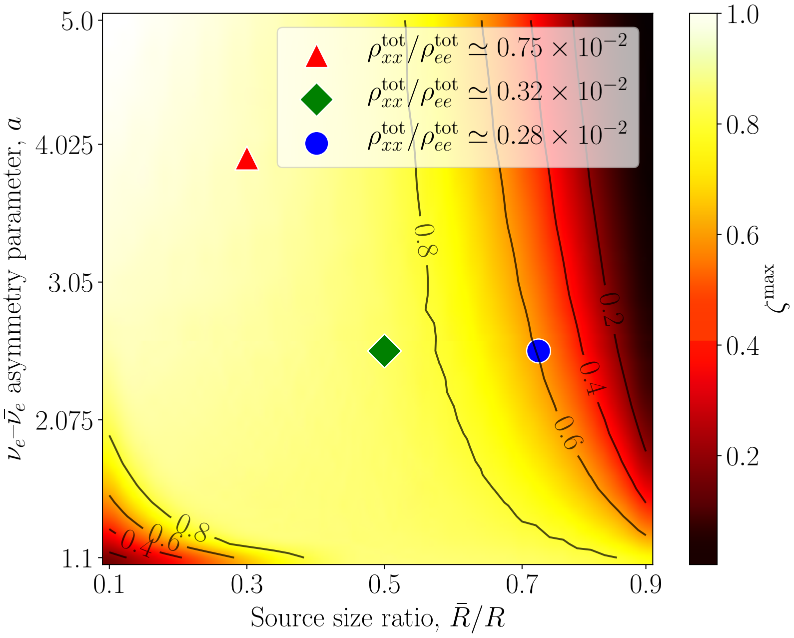

Figure 64: Contour plot of the maximal value of the instability parameter (Eq. 8.10) in the parameter space defined by the relative ratio between the $\bar{\nu}_e$ and ν_e source sizes ($\bar{R}/R$) and the ν_e–$\bar{\nu}_e$ asymmetry parameter (a). For each point in the parameter space, corresponding to a NS-disk configuration, the maximum value of ζ is computed in the absence of oscillations. In order to gauge the overall amount of flavor conversion, the three colored diamonds represent three NS-disk configurations for which we have tracked the flavor evolution numerically. The transition probability is reported in the legend for each of the three selected configurations. A slightly larger transition probability is obtained for smaller $\bar{R}/R$ ratios.

8.5 FLAVOR EVOLUTION ABOVE THE BH-DISK REMNANT

We now extend our exploration of the phenomenology of fast pairwise conversions to the BH-torus configuration. In this case, the neutrino (antineutrino) source, $\mathcal{S}_{\nu}^{\mathrm{BH}}$ ($\mathcal{S}_{\bar{\nu}}^{\mathrm{BH}}$), is identical to the NS-disk remnant case except for an inner edge located at $R_{\mathrm{BH}} = 1/3R$ [47] in correspondence of the innermost stable circular orbit, i.e. the sources do not emit particles for $x \in [L/2 - R_{\mathrm{BH}}, L/2 + R_{\mathrm{BH}}]$; all other model parameters are identical to the ones introduced in Sec. 8.2. We observe that, in the case of the BH remnant, the neutrino and antineutrinos average energies are slightly higher than in the case of the massive NS remnant, see e.g. [225, 293]. However, since minimal variations in ω do not affect the final flavor configuration [147], we keep ω unchanged for simplicity.

Figure 65 shows the resultant angle-integrated density matrices for neutrinos and antineutrinos. By comparing Figs. 63 and 65, we can see that differences appear in the proximity of the inner source edges and just above the polar region, but the flavor distributions are comparable at larger distances from the source. Also, in this case, the most unstable regions appear in the proximity of the source external edges and minimal flavor conversions take place in the polar region, although more pronounced than for the NS-disk remnant configuration (see the bottom panels of Fig. 65 and Fig. 63).

Our findings suggest that the flavor equipartition assumption adopted in Ref. [225] to explore the implications on the nucleosynthesis of the heavy elements is difficult to achieve for our BH-disk configuration, despite the large growth rate predicted by the linear stability analysis (see Sec. 8.3.4). Similarly to the NS-disk configuration, the most unstable regions are located in the proximity of the edges of the neutrino sources. However, in this case, minimal conversions occur in the polar region above the BH-disk where the neutrino wind may dominate the r-process outcome; these findings are in rough agreement with the unstable regions reported in the top panel of Fig. 7 of Ref. [225] where a growth rate of the same order of the one plotted in the right panel of Fig. 60 was obtained.

It is worth noticing that Ref. [225], by studying the evolution of the BH-torus as a function of time, reported an excess of ν_e with respect to $\bar{\nu}_e$ in the polar region at late times (e.g., after 20 ms) as a result of the dynamical evolution of the merger remnant. This effect is not taken into account in

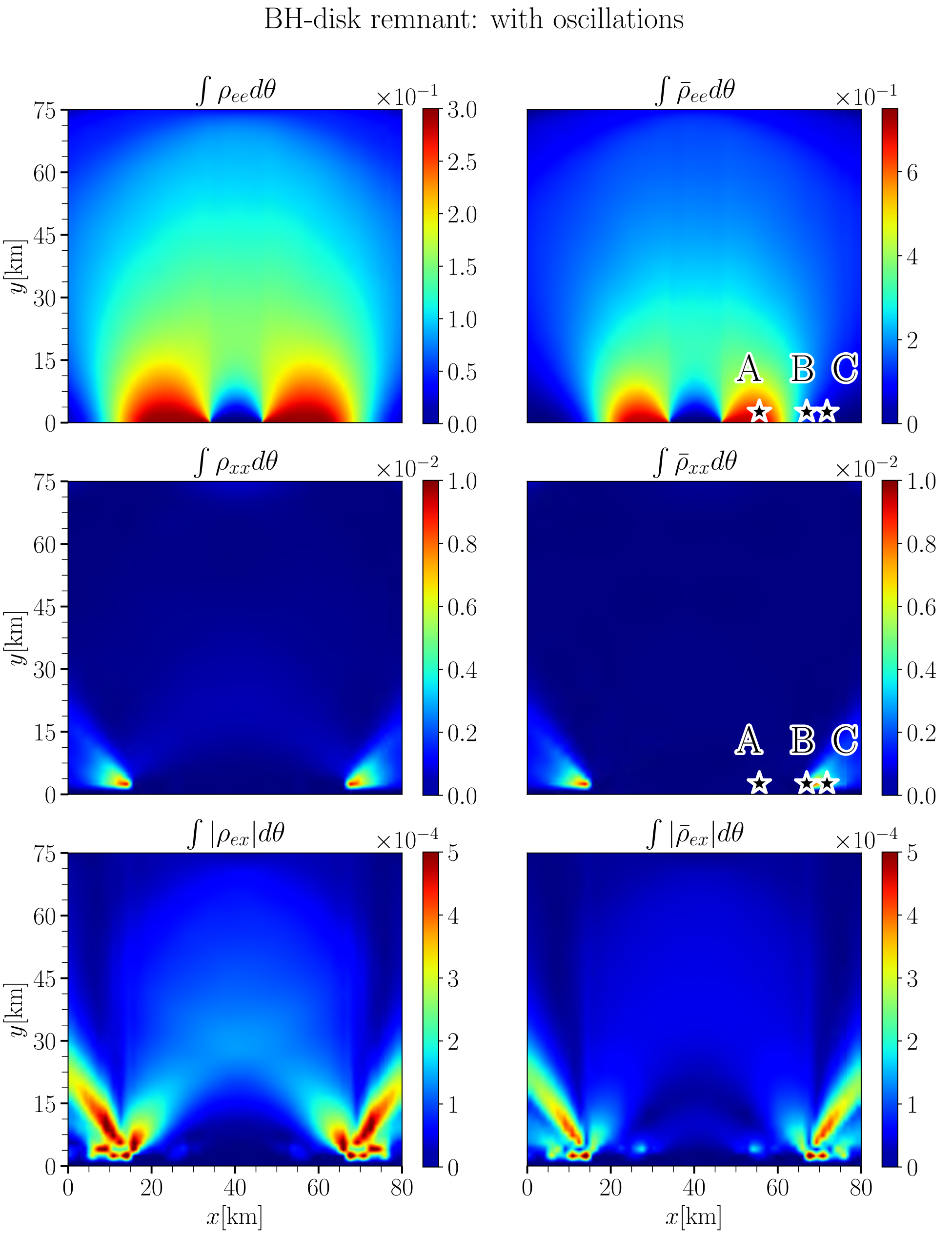

Figure 65: Same as Fig. 63 but for the BH-disk remnant configuration. Despite the differences in the source geometry, the final flavor configuration is comparable to the NS-disk remnant configuration. This suggests that the specific details of the source geometry do not lead to final state flavor configurations that are dramatically different.

our simplified BH-disk, since we focus on a smaller time interval [$\Delta t \simeq \mathcal{O}(10^{-7})$ s] and we do not take into account modifications of the neutrino emission properties due to the dynamical evolution of the remnant.

8.6 OUTLOOK AND CONCLUSIONS

Neutron star merger remnants are dense in neutrinos, and the occurrence of electron lepton number (ELN) crossings between the angular distributions of ν_e and $\bar{\nu}_e$ seem to be ubiquitous as a natural consequence of the disk protonization and the source geometry. If fast pairwise conversions of neutrinos should occur, leading to flavor equipartition, this has been shown to lead to major consequences for the synthesis of the elements heavier than iron and the related kilonova observations [196, 225]. However, the existing literature on the subject focuses on predicting the existence of eventual flavor unstable regions by relying on the linear stability analysis.

In the light of the possible major implications for the source physics, for the first time, we solve the flavor evolution above the disk remnant in a (2+1+1) dimensional setup: two spatial coordinates, one angular variable, and time. This is the first computation of fast pairwise conversions above the merger disk in the non-linear regime.

For simplicity, we adopt a two-dimensional model with two coincident ν_e and $\bar{\nu}_e$ neutrinospheres, and a different size for the two sources. We look for the final steady-state configuration in the presence of fast pairwise conversions by neglecting the collisional term in the equations of motion and by mimicking a configuration where a massive neutron star sits at the center of the remnant disk (NS-disk configuration) and a configuration with a black hole remnant (BH-disk configuration). In addition, we scan the parameter space of the possible disk model parameters predicted by hydrodynamical simulations to test the robustness of our findings.

We find that the most unstable regions favoring the occurrence of fast pairwise conversions are located in the proximity of the edges of the neutrino emitting surfaces. Only a minimal flavor change occurs in the polar region above the merger remnant in the BH-disk configuration, but flavor conversions are almost absent in the surroundings of the polar region in the NS-disk configuration. Fast pairwise flavor conversions are triggered early on and a steady-state configuration for the flavor ratio (modulo small high frequency modulations) is reached within $\mathcal{O}(10^{-7})$ s.

Even though flavor unstable solutions are predicted to exist almost at any location above the disk of the remnant with a large growth rate, as already shown in the literature, our results point towards minimal flavor changes ($< 1\%$), which would suggest a negligible impact of fast pairwise conversions on the r-process nucleosynthesis. However, our findings should be taken with caution given the approximations intrinsic to our modeling. An interplay between fast and slow ν–ν interactions in the context of the matter-neutrino resonance [192, 194, 195, 222, 287–289] may occur, and a full solution of the flavor evolution in 3D may change the flavor outcome yet again.

This work constitutes a major step forward in the exploration of fast pairwise conversions in the context of compact merger remnants from a quantitative perspective. Our findings suggest that a complete modeling of the neutrino flavor conversion physics should be taken into account in order to make robust predictions for the electromagnetic emission expected by the merger remnant and its aftermath.

8.7 CRITICAL OUTLOOK

8.7.1 *Overview and main findings*

The description of the flavor evolution of neutrinos in compact binary merger remnants is intrinsically complex (Chapter 4). Similar to core-collapse supernovae (Chapter 3), the time scale for the development of flavor conversion can be much shorter than the dynamical time scale. During the merger phase (Sec. 4.1), the NS is disrupted, ejecting material into the surroundings. This dynamical ejecta is mainly launched along the equatorial direction within the first milliseconds post-merger. Matter continues to be ejected after the dynamical phase for ~ 10 s, resulting in a wind ejecta, in which neutrinos can dominate due to the relatively lower matter densities along the polar regions. In Fig. 66 we show a schematic representation of the torus of the remnant and its ejecta. Due to the extreme neutrino densities near the neutrino decoupling regions, neutrino-neutrino interactions cannot be neglected: neutrino flavor conversion could potentially affect the neutron-to-proton ratio Y_e, the associated kilonova observations and the location of matter-neutrino resonant transitions (Sec. 4.3.1). However, the computational resources to model 3D general-relativistic, magneto-hydrodynamical simulations of compact binary mergers that include realistic neutrino transport are not yet available [87]. Thus, the flavor evolution of neutrinos is decoupled from state-of-the-art hydrodynamic simulations. Most works that attempt to "interface" neutrino flavor

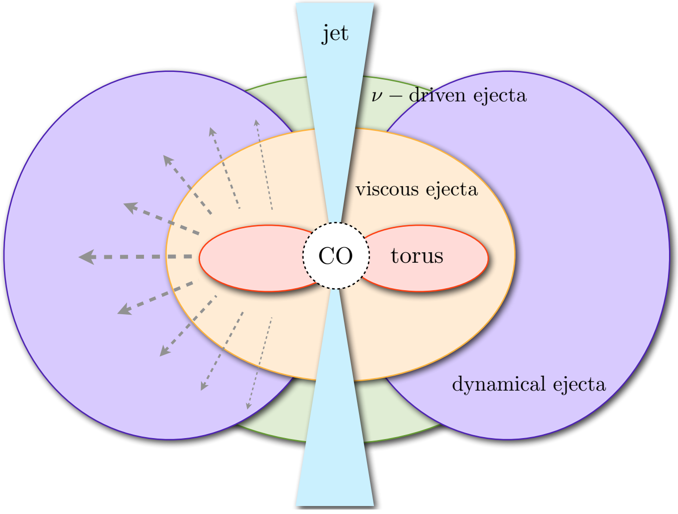

Figure 66: Schematic representation of the torus (disk) of the merger remnant and its ejecta. The compact object (CO) in the center can be a NS or a BH; as far as neutrinos are concerned, both scenarios are qualitatively very similar, with a less massive neutrino-driven wind in the case of a BH remnant. The dynamical ejecta (violet) is the first to be launched, followed by the neutrino-driven (green) and the viscously-driven (orange) ejecta. The neutrino-driven wind can dominate the ejecta in the polar region. Image taken from [87].

conversion and hydrodynamics either assume equipartition among neutrino flavors based on the existence of large growth rates of instabilities [196, 225, 226, 231] or employ an approximate treatment of neutrino transport [229, 230, 232, 295]. In Chapter 5 we have described in detail why this approach is not always correct and how it can lead to misleading conclusions.

Instead, in the work presented in this Chapter, we focus on a self-consistent multi-dimensional simulation of the neutrino flavor evolution above the disk of the remnant and look for a steady state of the system. Although this is a simplified model and does not include the many complexities involved in state-of-the-art hydrodynamical simulations, ours is the first calculation of its kind that tracks the evolution of flavor in two spatial dimensions, one angular variable and time. Moreover, we account for the (approximate) geometry of the merger, the natural excess of $\bar{\nu}_e$ over ν_e due to protonization, neutrino advection (Chapter 7) and neutrino refraction with the background medium (Chapter 5).

The NS-disk and BH-disk merger remnant configurations assume that the decoupling regions of neutrinos and antineutrinos are 1D regions with different sizes that perfectly overlap with each other, see top panel of Fig. 67 for representative neutrino emission configurations for the considered merger models. Although, in reality, the (anti)neutrino decoupling regions are expected to be spatially well-separated regions, we assume a "line model" system to focus on the neutrino flavor evolution above the disk of the remnant. We look for the final steady-state of the system in the presence of neutrino fast flavor conversion and neutrino advection (reached within 10^{-7} s of evolution), ignoring possible contributions from the collision term [150, 152, 233, 251, 252] which we leave for future work.

Our results are robust within our assumptions. We have scanned the parameter space of the possible disk model parameters predicted by hydrodynamical simulations and found similar results. As reported in Fig. 67, we find that the regions with largest growth rates ($\mathrm{Im}(\Omega/\mu_0) \simeq 10^{-2} - 10^{-1}$, with $\mu_0 = \mu(y = 0) = 10^5$ km^{-1}) are located in the vicinity of the edges of the neutrino decoupling regions ($y \simeq 5$ km), see middle and bottom panels of Fig. 67.

Notably, despite the large growth rates, we find minimal flavor conversion occurring in the polar region of the BH-disk remnant, while almost absent flavor conversion is found in the same region of the NS-disk remnant. The results for the NS- and the BH-disk systems are qualitatively very similar because the emission properties of (anti)neutrinos are almost the same in both cases, except for the emission in the polar region where, in any event, the ELN angular distributions have either tiny or no angular crossings at all.

Even though flavor unstable regions are ubiquitous above the disks of merger systems (Sec. 4.3.1), in agreement with Refs. [196, 225, 231], our results point toward minimal flavor changes ($<$ 1%), which suggests that the assumption of flavor equilibration might be unrealistic in some cases, in agreement with Ref. [233]. In other words, the final flavor outcome should be modeled appropriately in the non-linear regime, and flavor equilibration should be better motivated beyond simple arguments based on either the linear stability analysis or the presence of ELN crossings.

8.7.2 *Limitations and future perspectives*

The results presented in this Chapter should be cross-checked within a less constrained framework, including more degrees of freedom and realistic neutrino and matter profiles. Although ours is the first simulation of its kind, more work in this direction is needed to reveal new insights

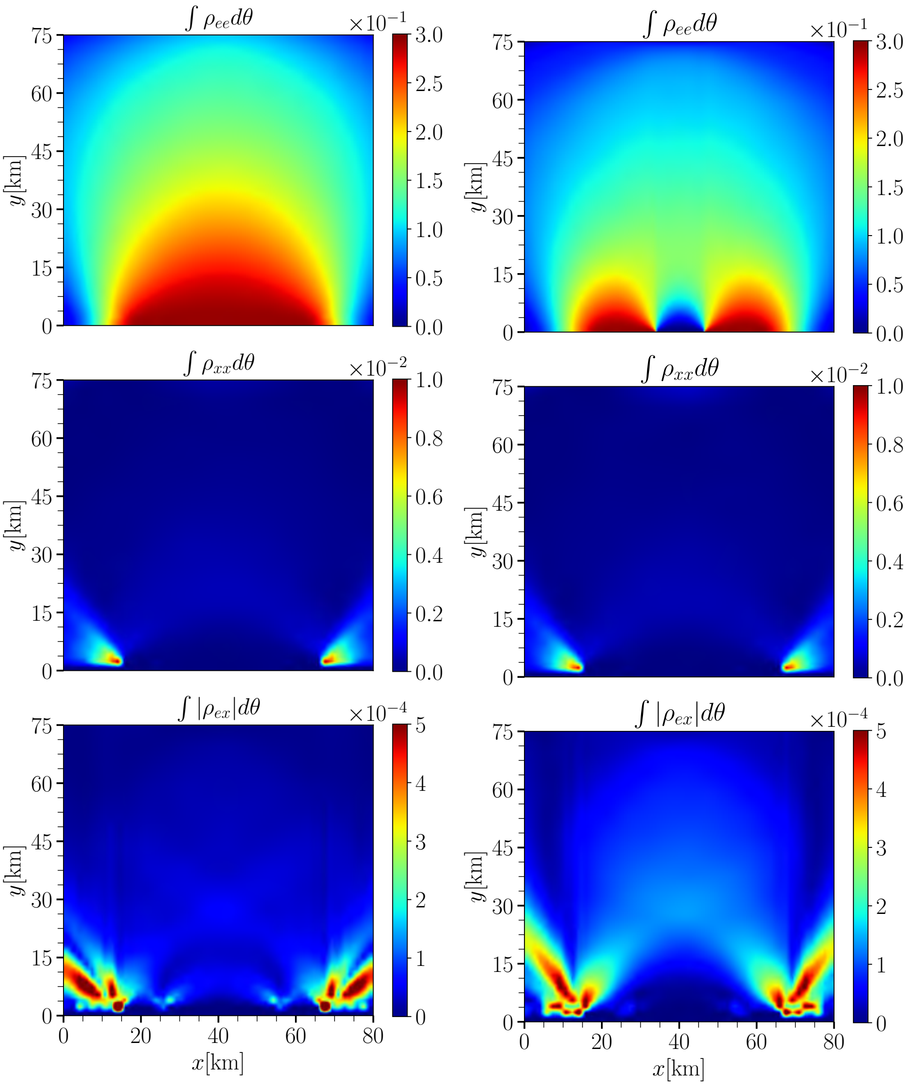

Figure 67: Contour plots of the angle-integrated entries of the density matrix for neutrinos $\rho(\vec{x}, \theta, t)$ for two compact binary merger remnant configurations. The evolution of $\bar{\rho}(\vec{x}, \theta, t)$ is very similar and described in detail later in this Chapter. We consider a NS-disk (left) and a BH-disk remnant configuration. Fast flavor conversion is more prominent near the edges of the neutrino decoupling regions (here assumed to be 1D). A small amount of ν_x's and $\bar{\nu}_x$'s is produced through fast flavor conversion within the narrow opening angles at the edges of the neutrino surfaces. The ELN angular crossings are almost vanishing along the polar axis leading to minimal flavor conversion. Both NS- and BH-disk remnants show qualitatively similar results.

into the flavor conversion in merger remnants and its impact on the associated merger remnant observations (Sec. 4.1).

8.7.2.1 *Spatially separated decoupling regions*

One of the main limitations of the merger remnant system adopted in this Chapter is the modeling of the ν_e and $\bar{\nu}_e$ decoupling regions. These are 1D dimensional regions of different lengths, both co-linear to each other. However, in reality, the (anti)neutrino decoupling surfaces are spatially well-separated regions; see, for instance, Fig. 25 or Fig. 9 of Ref. [50], where one can see the emitting surfaces varying across the spatial domain only as a function of distance. With this more realistic setup, one can no longer assume some representative ELN angular distributions as we did in the free-streaming regime, but the neutrino equations of motion should dynamically determine them. Recent works dealing with complex neutron star merger setups [225–232] can guide us in assessing possible flavor unstable regions and approximately gauge the impact of flavor conversion on the merger environment; however, they cannot conclusively answer how neutrino flavor evolves in the interior of the decoupling regions.

8.7.2.2 *Flavor transformation and decoupling*

Allowing for spatially separated decoupling regions comes with new conceptual and numerical challenges, mainly because neutrinos are still partially or entirely coupled to the plasma at these locations. Inevitably, one faces the challenge of dynamically determining the angular distributions of neutrinos as they gradually decouple from the plasma: they should come as a result of flavor evolution, neutrino propagation, and neutrino interactions with the background medium. In the context of CCSNe, the recent works in Refs. [233, 251] show that flavor conversion occurs while they are still decoupled to matter, thereby dynamically modifying the angular distributions of all other neutrinos species and affecting the location of the emitting surfaces. Such a simulation in the context of compact binary merger remnants is not available yet, and due to the less symmetric merger configurations compared to a CCSNe, it is unclear whether these results would also be valid for the merger scenario. However, these works highlight the importance of the interplay between neutrino gradual decoupling and flavor transformation and call for more work on modeling the neutrino decoupling regions.

8.7.2.3 *Dependence on neutrino energy*

Another limitation of the work in this Chapter is the assumption of mono-energetic (anti)neutrinos. Therefore, one should be careful about two essential aspects when assuming single-energy configurations. First, the on-set and the frequency of flavor conversion can be modified as a function of the neutrino energy [147]. Secondly, in connection to our previous points, the collision rates are also functions of the neutrino energy and time [295–298]. Due to the fast neutrino conversion rate in the proximity of the decoupling regions, the time dependence can be ignored; however, different neutrino energies will inevitably result in different decoupling regions among neutrino species and therefore different flavor dynamics.

8.7.2.4 *Presence of matter-neutrino resonances*

Although in our merger simulations we have included a spatially-varying neutrino interaction strength $\mu(|\vec{x}|)$ (Fig. 59), we have assumed a homogeneous and isotropic matter background that is constant across the simulation domain. In reality, the matter potential can change non-trivially as a function of distance, see for instance Figs. 23 and 23, leading to a MNR transitions (Sec. 4.2) in locations of the merger remnant where $H_{\nu\nu}(\vec{x})$ and $H_{\text{mat}}(\vec{x})$ are equal in magnitude and have opposite signs. As shown in Fig. 23, the MNR condition (Eq. 4.5) can be fulfilled around 30 km from the neutrino decoupling regions, thereby leading to almost maximum favor conversion within the radial interval $30 - 80$ km. However, in the work presented in this Chapter, we have shown that the regions very close to the neutrino decoupling regions are the most prone to convert flavor due to FFC (see Fig. 63), which means that if MNR transitions were to occur in our simulation domain, they will most likely not affect our results within the first $10 - 20$ km from the decoupling regions but further out. The latter, however, has not been verified explicitly and remains to be investigated in a dedicated study.

9

MATTER BULK VELOCITY: NON-ISOTROPIC MATTER DISTRIBUTIONS AND THEIR IMPLICATIONS

Based on: **Ian Padilla-Gay**, Shashank Shalgar, *Fast flavor conversion of neutrinos in presence of matter bulk velocity*, Phys. Rev. D **under review**, arXiv:2108.00012.

ABSTRACT A dense gas of neutrinos and antineutrinos can undergo fast pairwise conversions near the decoupling regions of core-collapse supernovae and in compact binary neutron star mergers. The flavor dependent neutrino heating can play a role in sustaining convection inside the hot and dense matter. In this paper, we study the unexplored effect of the bulk velocity of matter on fast pairwise conversions and demonstrate that neutrino flavor conversions could be significantly enhanced or suppressed depending on the direction and magnitude of the bulk velocity. The bulk velocity of matter, which is usually neglected in the context of neutrino oscillations, can reach values of one-tenth of the speed of light in astrophysical environments. We find that bulk velocities much smaller than the maximum allowed velocities can substantially change the neutrino flavor conversion rate. The demonstration of possible enhancement of neutrino flavor conversion rate due to the bulk velocity of matter also raises several important issues relevant to the supernova mechanism. Future studies with realistic velocity profiles could elucidate the possible implications on the phenomenology of core-collapse supernovae and neutron star mergers.

9.1 INTRODUCTION

Core collapse supernovae are one of the densest astrophysical objects which copiously produce neutrinos. Three flavors of neutrinos and antineutrinos are produced within about 10 seconds which carry most of the energy produced in the supernova. The neutrinos produced within this short duration play a vital in the supernova explosion mechanism according to the delayed neutrino-driven supernova explosion mechanism [299]. The neutrino-driven explosion mechanism is often invoked to explain the revival of the shock after it loses its energy photo-dissociating iron group nuclei in the outer parts of the core. The stalled shock is revived because of the nonuniform deposition of energy by neutrinos in the outer envelope of the supernova, which leads to convection, resulting in convection driven hydrodynamical instabilities [144].

The energy deposition by neutrinos is flavor dependent as the electron type neutrinos have a larger cross section with matter than non-electron type neutrinos. The presence of flavor conversion at the right time and radius can thus affect the energy deposition by neutrinos and their role in the supernova mechanism. Neutrino flavor conversions can play a role in modifying the neutrino-driven explosion mechanism only if the flavor conversions can occur relatively early and at small radii where the densities are extremely large.

However, the computation of neutrino flavor evolution in dense astrophysical environments such as supernovae is a highly challenging task. Due to the high number density of neutrinos, the neutrino flavor evolution is nonlinear due to the coherent forward scattering of neutrinos from other neutrinos [250], known as neutrino self-interactions. This phenomenon is similar to the well-known MSW effect [59, 65]; however, in the case of neutrino self-interactions, the equation of motion that governs the flavor evolution is nonlinear, and this leads to a rich and interesting phenomenology.

One of the first numerical implementations of the neutrino self-interactions in supernovae made several simplifying assumptions, like perfect spherical symmetry and instantaneous decoupling of all neutrinos at the same radius [82, 83, 89, 91]. However, the simplifying assumptions made in the earlier calculations were found to be unjustified for several reasons. First, the nonlinear evolution of neutrino flavor evolution can lead to spontaneous breaking of symmetries initially present in the system [104, 110, 261], due to which flavor transformations can occur in much denser environments. However, the numerical simulations carried out in the simplified setup demonstrated conclusively that neutrinos with different momenta evolve in a 'collective' manner in the presence of neutrino self-interactions. The term 'collective neutrino oscillations' is often used to refer to neutrino flavor evolution in the presence of neutrino self-interactions as a result.

Also, the non-instantaneous decoupling of neutrinos can lead to different angular distributions with different flavors, and in some cases, lead to angular distributions that have a crossing in the electron lepton number (ELN) [239]. A crossing in the ELN is a necessary and sufficient condition for the general case of an inhomogeneous neutrino ensemble [236]; however, in the homogeneous case, which we assume throughout this work, only a particular class of ELN crossings lead to flavor instabilities. In other words, the ELN crossing by itself is not a sufficient condition if spatial homogeneity is assumed.

Unlike the slow collective neutrino flavor evolution studied earlier [82, 83, 89, 91], which can occur only in environments for which the neutrino self-interaction potential is comparable to the vacuum frequency, the fast flavor conversions can occur in much larger densities.

The large density of neutrinos in the vicinity of the proto-neutron star (PNS) may foster fast conversions [87]. The local (anti)neutrino number density determines the timescale on which fast pairwise conversions occur. For typical values of the neutrino densities near the decoupling region, fast oscillations could take place on a scale as small as a few nanoseconds (i.e., a few meters) [155, 156, 158, 166, 265], with the possibility of pair conversions taking place in the deep interior of supernovae [172]. Although there has been a serious discussion regarding the role neutrino flavor conversions may play in instigating convection [300–302], in this paper, we focus on the converse; the effect of convection on neutrino flavor evolution. It should be noted that in the past, there have been studies of nontrivial matter profiles on collective neutrino flavor evolution, but they have been mostly limited to the study of the possible effect of turbulence and the small scale spatial variations that can induce parametric resonances [303–308].

We study the effect of the bulk velocity of matter on fast pairwise conversions. Depending on the direction of the bulk velocity and the magnitude, neutrino flavor conversions may get enhanced or suppressed. In the convective region of supernova, the bulk velocity of matter can, therefore, can lead to enhancement in some regions and suppression in other regions. This can lead to a differential in the neutrino heating rate, which could feed the convection.

However, it should be noted that the existence of large number densities of neutrinos is not restricted to the interior of supernovae. Large number densities of neutrinos are produced in the immediate aftermath of neutron star mergers, where favorable conditions for the development of fast flavor conversions may exist [196, 225]. Although the neutrino flavor evolution is not expected to play a role in the dynamics of the neutron star mergers, the synthesis of heavy elements by *r*-process can be affected by neutrino flavor evolution [226, 231]. A detailed study on the flavor evolution of neutrinos in compact binary objects [242] demonstrated that even in the presence of favorable conditions, the mixing of neutrinos might be minimal, suggesting that the assumption of flavor equipartition may overestimate the flavor conversion rate. Also, the large bulk velocities of matter are present in the region where neutrino flavor evolution occurs [287, 309, 310]. However, the geometry of neutron star mergers is typically more complicated than that of a supernova. Although the results obtained in this paper would have significant implications for neutrino flavor evolution in the context of neutron star mergers, we do not comment on the relevant phenomenological implications.

Several complications can arise even in the case of a supernova, which makes a realistic estimate of the role of the bulk velocity extremely challenging. In this paper, we thus focus on a simplified case of quantifying the effect of the bulk velocity of matter in some representative setups involving a homogeneous neutrino gas.

The paper is organized as follows: In Sec. 9.2, we introduce the equations of motion for neutrino flavor evolution in a medium that is not isotropic in nature. The source of the anisotropy of the medium is discussed and derived from the bulk velocity in Sec. 9.3. In Sec. 9.4, we demonstrate the enhancement of neutrino flavor transformation due to the presence of the bulk velocity. In Section 9.5, we demonstrate the agreement between our numerical simulations and the semianalytical technique of linear stability analysis. Section 9.6 presents the main results of this paper in the form of showing the effect of bulk velocity on the evolution of the neutrino flavor evolution by considering the evolution of a family of angular distributions parameterized in a simple manner. Finally, in Sec. 9.7 we conclude and offer an outlook.

9.2 NEUTRINO EQUATIONS OF MOTION IN DENSE MEDIA

This section describes the equations of motion governing the flavor evolution of neutrinos in the presence of a neutrino and electron background. Among other simplifications, we assume a two flavor system where ν_e is the electron flavor and ν_x represents a mixture of the ν_μ and ν_τ flavors. The flavor content of the neutrinos and antineutrinos can, therefore, be encoded by a 2×2 density matrix, which we denote by ρ and $\bar{\rho}$, respectively. However, the two flavor approximation has its limitations in the context of fast flavor conversions [148, 159, 187], the formalism used in this paper can be extended to the three flavor case, and the central premise of the results remain unchanged. It should be noted that the three flavor effect acts sequentially for the slow collective phenomenon [98, 101–103], but that is not the case for fast flavor conversions.

Fast flavor conversions can be expected to occur in dense regions of supernovae where the effect of collisions cannot be ignored. For simplicity, we also ignore the effect of momentum changing collisions, which can dramatically enhance the flavor conversions rates depending on the initial conditions used in the simulations [150].

We also assume that the angular distribution of neutrino has azimuthal symmetry with respect to the radial direction, even though the azimuthal symmetry breaking effects in the case of fast flavor conversion can have interesting consequences [183]. Because of this simplifying assumption, the angular distribution of neutrinos can be expressed in terms of a single polar angle denoted by θ. We also ignore the effect of spatial inhomogeneity that can arise in collective neutrino oscillations so that the evolution neutrino flavor only depends on the polar angle, θ, and time, t. Furthermore, for simplicity, we assume that (anti)neutrinos are of a single energy. The density matrices for neutrinos and antineutrinos are given by

$$\rho(\theta,t) = \begin{pmatrix} \rho_{ee} & \rho_{ex} \\ \rho_{ex}^* & \rho_{xx} \end{pmatrix} \quad \text{and} \quad \bar{\rho}(\theta,t) = \begin{pmatrix} \bar{\rho}_{ee} & \bar{\rho}_{ex} \\ \bar{\rho}_{ex}^* & \bar{\rho}_{xx} \end{pmatrix}, \tag{9.1}$$

where the diagonal terms are related to the occupation number of a given flavor of (anti)neutrinos while the off-diagonal terms describe the coherence between flavors. The equations of motion for a homogeneous neutrino gas can in general be written as the Heisenberg equations,

$$i\frac{\partial}{\partial t}\rho(\theta,t) = [H(\theta), \rho(\theta,t)], \tag{9.2}$$

$$i\frac{\partial}{\partial t}\bar{\rho}(\theta,t) = [\bar{H}(\theta), \bar{\rho}(\theta,t)]. \tag{9.3}$$

In the case of a homogeneous neutrino gas, the total and the partial derivative can be used interchangeably on the left-hand side. However, if the assumption of homogeneity is relaxed, the left-hand side needs to be replaced by a material derivative consisting of a time derivative and an advective term. The advective term can modify the neutrino flavor evolution for an inhomogeneous initial condition, but we ignore this effect here [149].

The Hamiltonian receives the contributions from neutrino vacuum oscillations, electron-neutrino coherent forward scattering and neutrino-neutrino coherent forward scattering,

$$H(\theta) = H_{\text{vac}} + H_{e\nu}(\theta) + H_{\nu\nu}(\theta) \ . \tag{9.4}$$

The vacuum term is proportional to the characteristic vacuum frequency $\omega = \Delta m^2/2E$,

$$H_{\text{vac}} = \frac{\omega}{2} \begin{pmatrix} -\cos 2\vartheta_V & \sin 2\vartheta_V \\ \sin 2\vartheta_V & \cos 2\vartheta_V \end{pmatrix} . \tag{9.5}$$

Here, we assume that all (anti)neutrinos have the same energy E to mimic the evolution of neutrinos with an energy distribution peaking at the value E [147]. For antineutrinos we can obtain $\bar{H}$ by replacing $\omega \to -\omega$ in H_{vac}.

The flavor transition probability is modified due to the presence of electrons in the medium. The modification of neutrino flavor conversion probability depends on the electron number density and the direction of motion. In the absence of a bulk velocity in the medium, the direction dependence of the matter effect averages out to zero. It is thus common to ignore the angle dependence of the matter term in the Hamiltonian. However, ignoring the angle dependence is an approximation and the proper expression for the matter term in the most general case is,

$$H_{e\nu}(\theta) \quad = \quad \lambda \int d(\cos\theta') \left[J_e(\theta') - \bar{J}_e(\theta') \right] \left[1 - \vec{v} \cdot \vec{v}_e \right] \ , \tag{9.6}$$

where $\lambda \equiv \sqrt{2} G_{\text{F}} n_e$ parametrizes the strength of matter potential, which is proportional to the Fermi constant, G_{F} and the number density of electrons, n_e. The quantities $J_e(\theta')$ and $\bar{J}_e(\theta')$ describe the angular distribution of the momentum of electrons and positrons, respectively, and normalized such that the $\int_{-1}^{1} J_e(\theta') d\cos\theta' = 1$. We ignore the positron density hereafter. Moreover, $\vec{v}$ and $\vec{v}_e$ are the velocities of the test neutrino and the matter background, respectively. For an homogeneous system, the momentum or angular distribution of electrons can be completely described by the bulk velocity denoted by $\vec{v}_{\text{b}}$. In other words, in the absence of spatial inhomogeneities, the only source for anisotropy in the matter distribution stems from the bulk motion of matter pointing along one preferred direction.

The standard matter effect considered in the literature is obtained by having a vanishing contribution from the term $\vec{v} \cdot \vec{v}_e$ in Eq. 9.6. However, in the interior of a supernova, the matter can flow near the neutrino decoupling region either due to the matter infall onto the proto-neutron star or due to plumes of heated matter rising radially outwards, rendering the term $\vec{v} \cdot \vec{v}_e$ angle dependent. The velocity in question is much smaller in magnitude than the speed of light but not small enough to be negligible.

The magnitude of the bulk velocity in the vicinity of the neutrino decoupling region can be as large as $|\vec{v}_{\rm b}| \simeq 0.1$ [311]. We assume that neutrinos travel at the speed of light, $|\vec{v}| = 1$, where all velocities are expressed in units of speed of light unless otherwise specified. Therefore, $H_{e\nu}$ can be written as,

$$H_{e\nu}(\theta) \quad = \quad \lambda \int d(\cos\theta') J_e(\theta') \left[1 - \cos\theta \cos\theta'\right] \ . \tag{9.7}$$

Notice that assuming an anisotropic momentum distribution of electrons, i.e., their bulk velocity is not zero, introduces a new contribution to the equations of motion, which is captured by Eq. 9.7. The angular dependence of $J_e(\theta') d(\cos\theta')$ is determined by $\vec{v}_{\rm b}$ alone as described in section 9.3.

The third term in the Hamiltonian is the neutrino self-interaction term which describes the potential experienced by neutrinos due to other neutrinos in the medium,

$$H_{\nu\nu}(\theta) \quad = \quad \mu \int d(\cos\theta') \left[\rho(\theta', t) - \bar{\rho}(\theta', t)\right] \left[1 - \cos\theta \cos\theta'\right] \ , \tag{9.8}$$

where μ parametrizes the interaction strength of neutrinos among themselves and is proportional to the number density of (anti)neutrinos. The velocity dependence for the neutrino self-interaction potential is the same as the matter potential due to the vector-vector coupling of weak interactions in both cases.

We focus on the evolution of the neutrino flavor due to the matter term and self-interaction term and set $\omega = 0$. We instead provide a seed to the off-diagonal components of the density matrices to ensure that our results do not depend on the vacuum Hamiltonian. This ensures that in the absence of the bulk velocity, the neutrino flavor evolution is bipolar in nature and thus makes a comparison between different cases easier to illustrate. Since we are interested in the interplay between $H_{e\nu}$ and $H_{\nu\nu}$ near the PNS, we assume that the neutrino self-interaction potential and the electron-neutrino interaction strength are equal to each other, i.e., $\mu = \lambda = 10^5$ km^{-1}, which is representative of the conditions realizable in a supernova in the decoupling region.

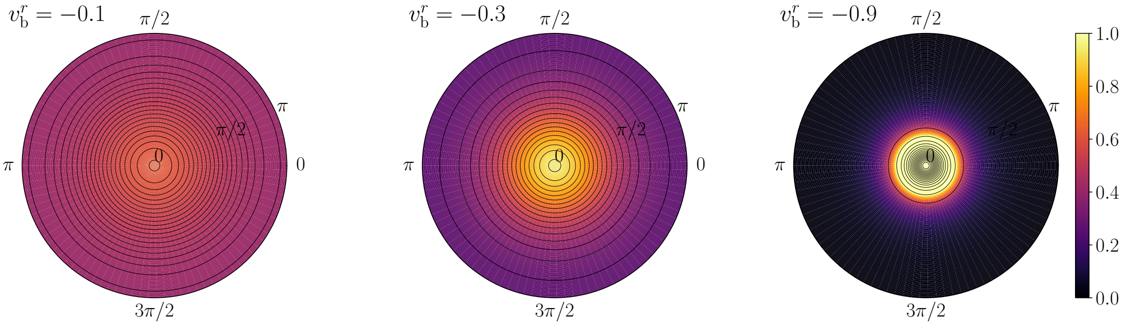

Figure 68: Two dimensional Lambert projections of the function $\widetilde{d\cos\theta}/d\cos\theta$ as shown in Eq. 9.12 for $v_b^r = -0.1$ (left), $v_b^r = -0.3$ (middle) and $v_b^r = -0.9$ (right). The solid lines are the isocontours of constant matter distribution to show the symmetry along the azimuthal direction. A non-vanishing v_b^r leads to the effect of relativistic beaming, which is clearly visible for $v_b^r = -0.9$.

It becomes more transparent that the flavor instability condition, mainly determined by crossing between ρ_{ee} and $\bar{\rho}_{ee}$, is modified by a new contribution which is proportional to the ratio λ/μ and the particular shape of $J_e(\theta)d(\cos\theta)$, which can be derived from the value of the bulk velocity. In the linear regime, there exists a symmetry between the matter term and the $\vec{K}$ wave-number vector. This is evident after accounting for a constant shift $(\Omega, \vec{K}) \to (\omega, \vec{k})$ [133]. This is expected to be the case in the linear regime, where adding a non-vanishing bulk velocity for physical $\vec{K} = 0$ maps onto a vanishing bulk velocity for some $\vec{K} \neq 0$, where the quantities $\vec{K}$, Ω, $\vec{k}$, and ω have the same meaning as in [133]. However, our aim is not to bypass a full calculation including spatial inhomogeneity but to emphasize that even conservative values of the bulk velocity could impact the fast flavor conversion and the occurrence criteria. Therefore, one should specify whether a bulk velocity is present for a particular choice of neutrino angular distributions, given that its impact on the flavor dynamics in the nonlinear regime is not negligible.

9.3 MATTER ANISOTROPY

This section describes how the angular distribution of electrons and the bulk velocity are related to each other. In the absence of bulk velocity, which is generally considered in the literature, the matter term is independent of direction. Upon introducing a non-vanishing bulk velocity, the matter term can be thought of as the Lorentz boosted version of the usual matter term. We start with an

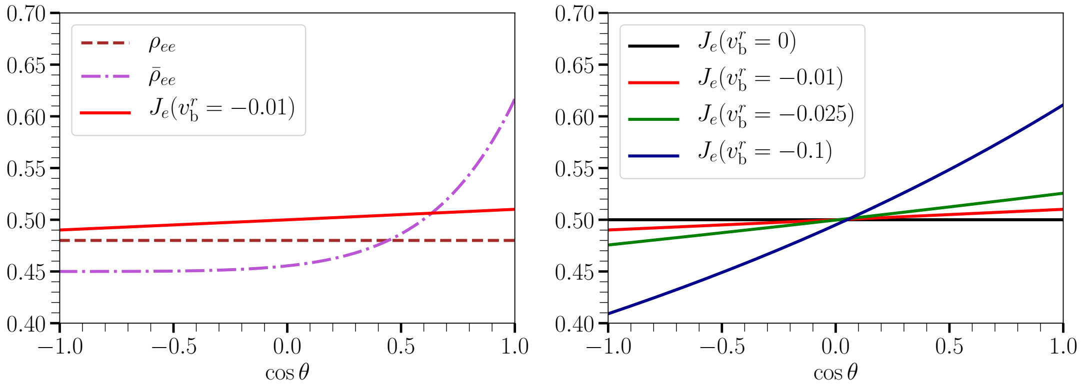

Figure 69: *Left:* (Anti)neutrino and matter angular distributions according to Eq. 9.13 with $\delta = -0.02$, $\sigma_\nu = 0.6$ and $v_b^r = -0.01$. *Right:* Various angular distributions of matter as a function of v_b^r; as the magnitude of v_b^r increases the greater is the difference between the forward ($\cos\theta = 1$) and the backward ($\cos\theta = -1$) directions.

angular distribution for electrons that would be isotropic for an observer traveling along with the fluid element. We denote this reference frame by S. On the other hand, we also consider another reference frame denoted by $\widetilde{S}$ which is fixed with respect to the center of the supernova, and in which the matter travels with a velocity $\vec{v}_b$. Throughout this paper, the bulk velocity is assumed to be in either radially outwards or inwards direction. The radial velocity of matter, denoted by v_b^r, is always the same in magnitude as $\vec{v}_b$, but v_b^r can be negative for bulk velocities that are radially outward. Obtaining the angular distribution of electrons in $\widetilde{S}$ can be done straightforwardly, as we show in this section, and provides us with a unique angular distribution for electrons once the bulk velocity is specified as long as the electrons are highly relativistic.

The starting point is to consider an isotropic distribution of electrons in reference frame S. The same isotropic distribution will be peaked along the direction of propagation for another observer in reference frame $\widetilde{S}$. Equivalently, we can calculate the angular distribution of electron momenta for a given bulk velocity $\vec{v}_b$ by boosting a relativistic isotropic gas. We denote the angular distribution in reference frame S by f_e, which by definition is independent of θ.

The angular distribution for electrons achieved after boosting f_e with a given bulk velocity serves as a good approximation for the angular distribution that can be expected in a realistic astrophysical system. In order to understand how the anisotropy arises from the inclusion of the bulk velocity, we define the parallel and perpendicular components of the velocity of electrons $\vec{v}_e$

(with respect to the bulk velocity) as $v_e^{||}$ and $v_e^{\perp}$, respectively. In the limit of vanishing bulk velocity, the velocity of electrons $\vec{v}_e$ is isotropically distributed, and the temperature scale determines the magnitude. In the interior of a supernova, the temperatures are typically much larger than the mass of the electron, and hence $|\vec{v}_e|$ almost equal to the speed of light. The Lorentz transformed quantities are denoted by a tilde i.e. $\widetilde{v}_e^{||}$ and $\widetilde{v}_e^{\perp}$. Assuming that the bulk velocity oriented along the parallel direction i.e. $\vec{v}_{\rm b} \propto v_e^{||}$, then, relativistic addition of velocities leads to the following relations,

$$\widetilde{v}_e^{||} = \frac{v_e^{||} + v_{\rm b}^r}{1 + v_e^{||} v_{\rm b}^r}, \quad \text{and} \quad \widetilde{v}_e^{\perp} = \frac{v_e^{\perp}}{\Gamma(1 + v_e^{\perp} v_{\rm b}^r)}\,, \tag{9.9}$$

where $\Gamma = 1/\sqrt{1 - [v_{\rm b}^r]^2}$ and $v_{\rm b}^r$ is the radial component of the bulk velocity as defined earlier in this section. Due to the velocity transformation the relative angle between electrons changes as a function of the direction of the bulk velocity $\vec{v}_{\rm b}$ according to

$$\widetilde{\tan\theta} = \frac{\widetilde{v}_e^{\perp}}{\widetilde{v}_e^{||}} = \frac{v_e^{\perp}}{\Gamma(v_e^{||} + v_{\rm b}^r)} = \frac{v_e \sin\theta}{\Gamma(v_e \cos\theta + v_{\rm b}^r)}\,. \tag{9.10}$$

Moreover, by substituting the definition of the boosted (unboosted) parallel components $\widetilde{v}_e^{||} = \widetilde{v}_e \widetilde{\cos\theta}$ ($v_e^{||} = v_e \cos\theta$) in Eq. 9.9 and assuming that electrons are highly relativistic i.e. $\widetilde{v}_e \simeq v_e \simeq 1$ we obtain a similar relation to Eq. 9.10 in terms of the cosine of the angle,

$$\widetilde{\cos\theta} = \frac{\cos\theta + v_{\rm b}^r}{1 + v_{\rm b}^r \cos\theta}\,. \tag{9.11}$$

Equation 9.11 can be used to derive the angular distribution of matter. The flux of electrons between $\cos\theta$ and $\cos\theta + d\cos\theta$ is given by $f_e(\theta) d\cos\theta$ in the unboosted frame. The same quantity in the boosted frame given by $\widetilde{f}_e(\theta) d\widetilde{\cos\theta}$ is related to the one in the unboosted frame by the following formula,

$$\widetilde{f}_e(\theta) d\widetilde{\cos\theta} = \widetilde{f}_e(\theta) \frac{d\widetilde{\cos\theta}}{d\cos\theta} d\cos\theta = f_e(\theta) \left(\frac{1 - [v_{\rm b}^r]^2}{(1 + v_{\rm b}^r \cos\theta)^2} \right) d\cos\theta\,, \tag{9.12}$$

where we have inserted the derivative of $\widetilde{\cos\theta}$ with respect to the unboosted variable $\cos\theta$. Moreover, in the last step, we have assumed that $\widetilde{f}_e = f_e$ because the contribution from this term to the anisotropy is a subleading contribution due to the highly relativistic velocities of individual electrons. The anisotropy of the matter potential thus generated is illustrated in Fig. 68. As the

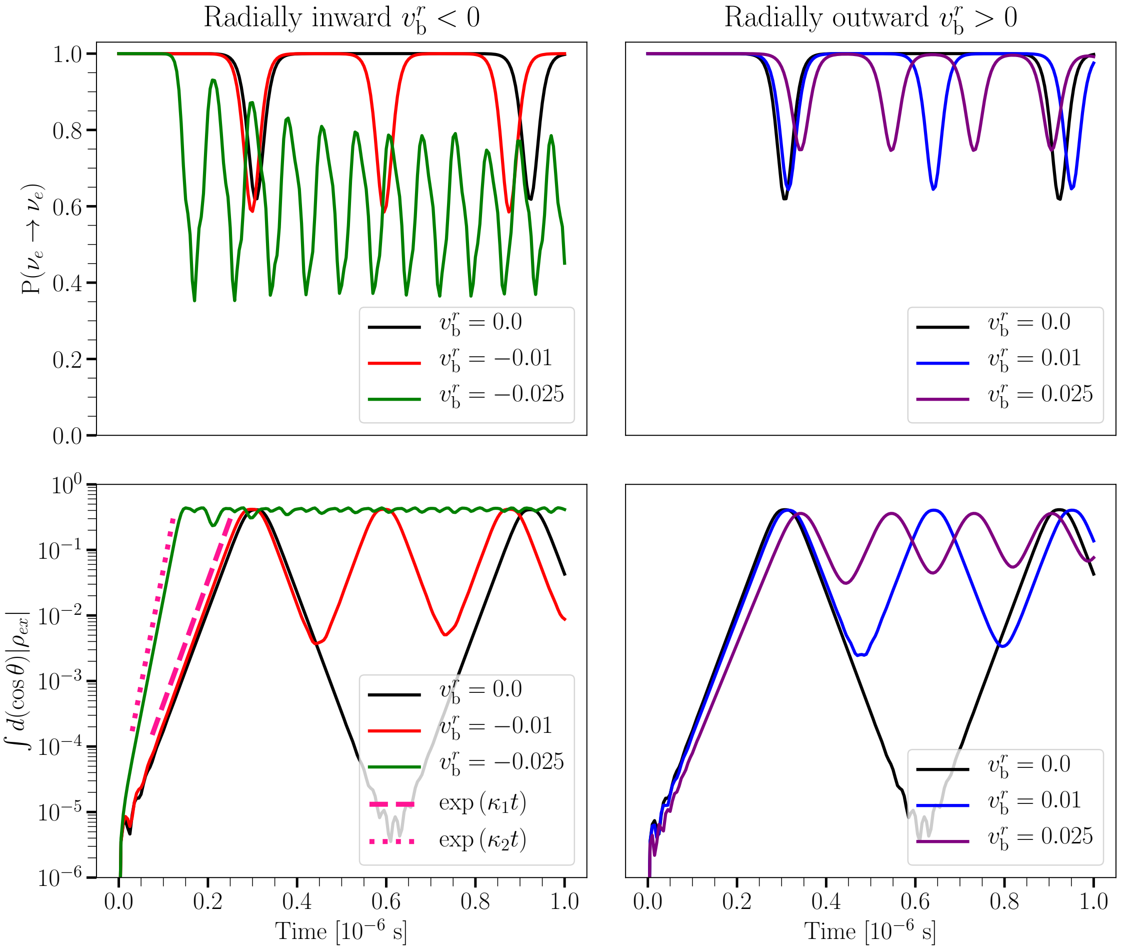

Figure 70: Angle-integrated survival probability $P(\nu_e \to \nu_e)$ (top panels) and the angle-integrated modulus of the off-diagonal term ρ_{ex} (bottom panels) for the scenarios where matter moves radially inward (left panels) and radially outward (right panels). The role of $v_b^r \neq 0$ is twofold: Firstly, there is a enhancement of conversions for $v_b^r < 0$ compared to the $v_b^r \geq 0$ cases, see top panels. Secondly, oscillations set in faster i.e., $v_b^r < 0$ leads to larger growth rates such as $\kappa_1/\mu = 0.0027$ (dotted line) and $\kappa_2/\mu = 0.0014$ (dashed line), as shown in the bottom panels.

bulk velocity increases, the matter potential becomes more and more peaked. Also, we can see that the matter potential is azimuthally symmetric around the direction of the bulk velocity as expected.

9.4 FLAVOR EVOLUTION FOR ANISOTROPIC MATTER

The angle dependent matter Hamiltonian derived in the previous section can be used in the numerical simulation of fast flavor evolution to uncover the effect of bulk velocity of matter. In this section, we specify a class of angular distributions for electron-neutrinos and electron-antineutrinos which are characterized by the parameters σ_ν and δ, which control the width of $\bar{\rho}_{ee}$ and the relative normalization between ρ_{ee} and $\bar{\rho}_{ee}$, respectively. We assume that, initially, the neutrino-dense environment is dominated by electron-flavor species i.e. $\rho_{xx}(t=0) = \bar{\rho}_{xx}(t=0) = 0$. Thus, the non-vanishing density matrix entries are

$$\begin{aligned}
\rho_{ee}(\theta) &= 0.5\,, \\
\bar{\rho}_{ee}(\theta) &= 0.45 - \delta + \frac{0.1}{\sigma_\nu}\exp\left(\frac{-\theta^2}{2\sigma_\nu^2}\right), \\
J_e(\theta) &= 0.5\frac{1-[v_{\mathrm{b}}^r]^2}{(1+v_{\mathrm{b}}^r\cos\theta)^2}\,. \qquad (9.13)
\end{aligned}$$

We implement the angular distribution for (anti)neutrinos and matter presented in Eq. 9.13 and focus on the neutrino flavor evolution as J_e transitions from the isotropic ($v_{\mathrm{b}}^r = 0$) to the anisotropic case ($v_{\mathrm{b}}^r \neq 0$). Fig. 69 shows the effect of radially inward velocity on the angular distribution of the matter term.

In Fig. 70, we show the impact of the bulk velocity on a representative angular distribution of (anti)neutrinos (shown in Fig. 69), for various values of the bulk velocity. The top panel shows the modification due to the bulk velocity that is in the radially inward direction ($v_{\mathrm{b}}^r < 0$), while the bottom panel shows the modification due to a bulk velocity in the radially outward direction ($v_{\mathrm{b}}^r > 0$). Figure 70 shows that while it is possible to get an enhancement in flavor conversion probability due to a bulk velocity that is radially inward, the radially outward bulk velocity tends to suppress the flavor conversion. The lower panels of Fig. 70 show that the effect of the bulk velocity on the flavor conversion probability is present in the linear regime of the evolution that is characterized by $\rho_{ex} \ll (\rho_{ee} + \rho_{xx})$. In the linear regime, the nonlinear equation of motion for the flavor evolution can be reliably approximated by linear equations of motion that can be solved semi-analytically. We perform linear stability analysis, characterized by an exponential growth of the off-diagonal terms of the density matrix, which serves two purposes. Firstly, the matching growth rates with our numerical simulations support the validity of our numerical simulations. Secondly, the linear stability analysis demonstrates that introducing the bulk velocity for matter in the system changes the flavor stability criteria and does not just change the magnitude of flavor conversion in the nonlinear regime. The formalism for linear stability analysis used to present the results in the lower panels of Fig. 70 is presented in the Sec. 9.5.

Figure 70 shows that favorable conditions for fast flavor depend on the interplay between $H_{\nu\nu}$ and $H_{e\nu}$ which is visible in the angle-integrated survival probability $\mathrm{P}(\nu_e \to \nu_e)$. Moreover, significant neutrino conversions are not achieved for arbitrarily large values of the bulk velocity v_b^r but are only possible when the anisotropy in the matter term is comparable with that in the neutrino-neutrino self-interaction term. In other words, significant flavor conversions are possible even for modest values of v_b^r that may be realizable in a realistic supernova environment.

9.5 LINEAR STABILITY ANALYSIS

We validate our numerical runs with semi-analytical estimates using linear stability analysis [104, 110, 129, 135, 261]. Since we are interested in fast pairwise conversions, we study the development of flavor instabilities in the linear regime and choose the scenario where $\omega = 0$ in order to focus strictly on the fast pairwise conversions i.e. $\mu \gg \omega$ [133].

We start by linearizing the EoM and tracking the evolution of the off-diagonal term

$$\rho_{ex}(\theta) = Q(\theta)e^{-i\Omega t} \text{ and } \bar{\rho}_{ex}(\theta) = \bar{Q}(\theta)e^{-i\Omega t}, \tag{9.14}$$

where $\Omega = \gamma + i\kappa$ represents the collective oscillation frequency for neutrinos and antineutrinos. If $\mathrm{Im}(\Omega) \neq 0$, then the flavor instability grows exponentially with rate $|\mathrm{Im}(\Omega)|$. We look for temporal instabilities for the homogeneous mode.

The off-diagonal component of Eq. 9.2 is

$$\begin{aligned} i\frac{\partial}{\partial t}\rho_{ex}(\theta) &= H_{ee}(\theta)\rho_{ex}(\theta) + H_{ex}(\theta)\rho_{xx}(\theta) \\ &- \rho_{ee}(\theta)H_{ex}(\theta) - \rho_{ex}(\theta)H_{xx}(\theta) \\ &= H_{ee}(\theta)\rho_{ex}(\theta) - \rho_{ee}(\theta)H_{ex}(\theta)\,, \end{aligned} \tag{9.15}$$

where we have assumed $\rho_{xx}(t = 0\text{ s}) = \bar{\rho}_{xx}(t = 0\text{ s}) = 0$. By substituting Eq. 9.14 in the equation above and solving for $Q(\theta)$, we obtain

$$Q(\theta) = \frac{\rho_{ee}(\theta) \int d(\cos\theta')[Q(\theta') - \bar{Q}(\theta')]\,[1 - \cos\theta\cos\theta']}{-\frac{\Omega}{\mu} + A(\theta)}\,, \tag{9.16}$$

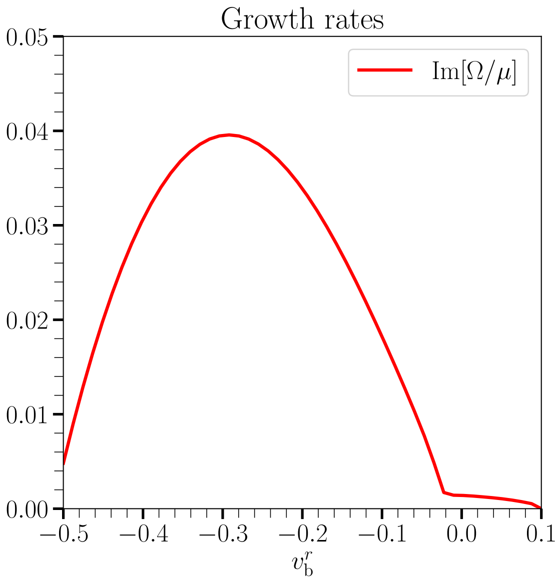

Figure 71: *Top*: Magnitude of the growth rate $\mathrm{Im}[\Omega/\mu]$ as a function of v_b^r. The angular distributions of (anti)neutrinos are fixed by choosing $\delta = -0.02$ and $\sigma_\nu = 0.6$ as specified in Eq. 9.13, while the magnitude of v_b^r is varied within the interval $v_\mathrm{b}^r \in [-0.5, 0.1]$. For positive values of v_b^r the growth rates are of order $\sim 10^{-3}$, while for negative values $v_\mathrm{b}^r \lesssim -0.025$ the growth rate increases with the bulk velocity. This continues until $v_\mathrm{b}^r \sim -0.3$ after which the trend is seen to reverse.

where we have defined the angle-dependent quantity $A(\theta)$ as

$$\begin{aligned} A(\theta) &= \int d(\cos\theta')[\rho_{ee}(\theta') - \bar{\rho}_{ee}(\theta') + \frac{\lambda}{\mu} J_e(\theta')] \\ &- \int d(\cos\theta')[\rho_{ee}(\theta') - \bar{\rho}_{ee}(\theta') + \frac{\lambda}{\mu} J_e(\theta')] \cos\theta \cos\theta' \, . \end{aligned} \tag{9.17}$$

A similar procedure follows for $\bar{Q}_\theta$ (see Eqs. 9.3 and 9.14). Then, from combining the expressions for $Q(\theta)$ and $\bar{Q}(\theta)$, it must be true that

$$Q(\theta) - \bar{Q}(\theta) = \left[\frac{\rho_{ee}(\theta) - \bar{\rho}_{ee}(\theta)}{-\frac{\Omega}{\mu} + A(\theta)}\right](a - b\cos\theta) \, , \tag{9.18}$$

where a and b are unknown coefficients. By substituting Eq. 9.18 in Eq. 9.16, we obtain a system of equations for the coefficients a and b.

$$\begin{bmatrix} a \\ b \end{bmatrix} = \begin{bmatrix} \mathcal{I}[1] & -\mathcal{I}[\cos\theta] \\ \mathcal{I}[\cos\theta] & -\mathcal{I}[\cos\theta^2] \end{bmatrix} \begin{bmatrix} a \\ b \end{bmatrix} = \mathrm{M} \begin{bmatrix} a \\ b \end{bmatrix} \, , \tag{9.19}$$

where the functional $\mathcal{I}[f]$ is

$$\mathcal{I}[f] = \int d(\cos\theta) \left[\frac{\rho_{ee}(\theta) - \bar{\rho}_{ee}(\theta)}{-\frac{\Omega}{\mu} + A(\theta)}\right] f(\theta) \, . \tag{9.20}$$

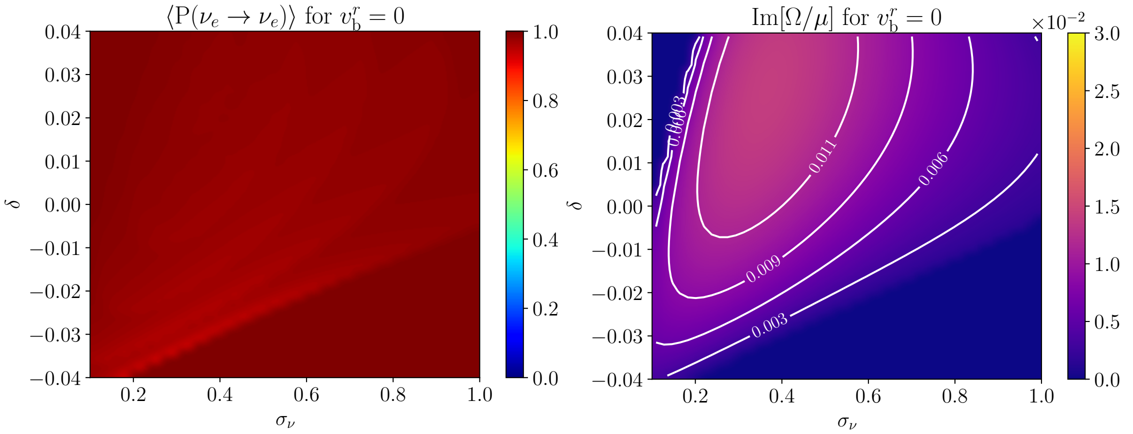

Figure 72: Isotropic case: Time averaged survival probabilities (left panel) and growth rates of the flavor instability (right panel) for the 2D parametric box. A large portion of the parameter space remains stable after 10^{-6} seconds, which is confirmed by the linear stability analysis (right panel). Moreover, for the parameter points that undergo flavor conversions, the final amount of non-electron flavor is minimal i.e. $\langle \mathrm{P}(\nu_e \to \nu_e) \rangle \simeq 0.9$.

The system of equations has a not trivial solution if and only if the following condition is met

$$\det(\mathrm{M} - 1_{2\times 2}) = 0\,. \tag{9.21}$$

Equation 9.21 is a polynomial equation in the frequency Ω. To search for instabilities, we need to look for the solutions with $\mathrm{Im}(\Omega) = \kappa \neq 0$. We find the roots of this polynomial equation using the SciPy module [294] in Python.

In Fig. 71, we show the dependence of the growth rate, $\mathrm{Im}(\Omega)$, on the bulk velocity for a representative case. For radially inward bulk velocity ($v_\mathrm{b}^r < 0$) that is not sufficiently large in magnitude, the effect of the bulk velocity is not significant. However, for larger negative values of v_b^r one can see a dramatic change in the trend around $v_\mathrm{b}^r \sim -0.025$, and the growth rate of the flavor instability increases with the magnitude of the bulk velocity. This trend continues for values of v_b^r up to ~ -0.3 after which the trend is reversed. In contrast, for an outward bulk velocity ($v_\mathrm{b}^r > 0$) growth rates are of order $\sim 10^{-3}$. It should be noted that the neutrino angular distribution in Fig. 71 is chosen to ensure that the dependence on the bulk velocity can be demonstrated. There are instances of angular distributions of neutrinos for which the effect of bulk velocity is not so dramatic.

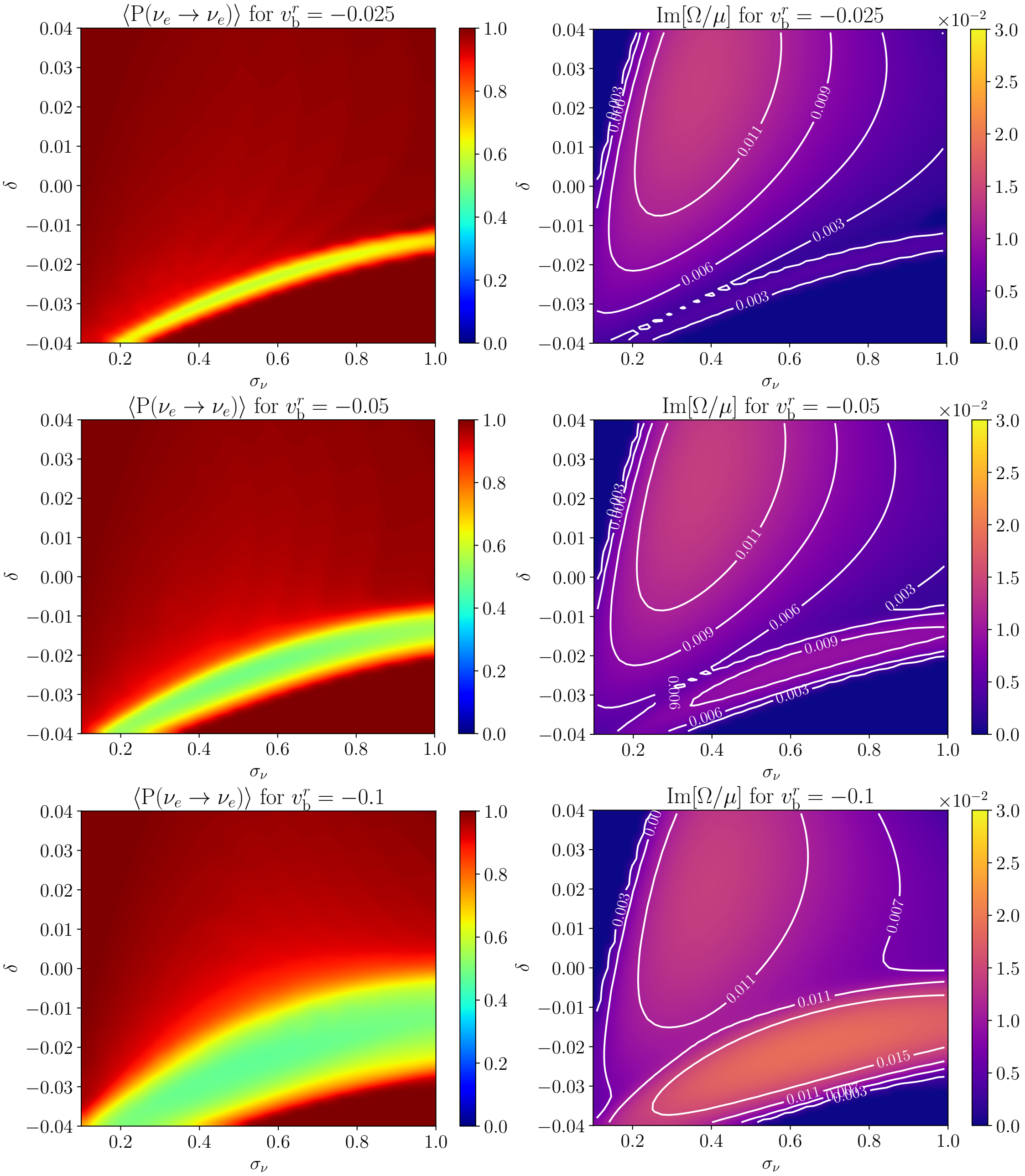

Figure 73: Time averaged survival probabilities (left panels) and growth rates of the flavor instability (right panels) for three selected values of the bulk velocity: $v_{\mathrm{b}}^{r} = -0.025$ (top panels), $v_{\mathrm{b}}^{r} = -0.05$ (middle panels) and $v_{\mathrm{b}}^{r} = -0.1$ (bottom panels). As the value of the bulk velocity reaches $v_{\mathrm{b}}^{r} \simeq -0.025$ a new unstable region emerges in the bottom of the 2D parametric box where equipartition is achieved i.e. $\langle \mathrm{P}(\nu_e \to \nu_e) \rangle \simeq 0.5$. Moreover, not only the conversions to the non-electron flavors are enhanced but also oscillations take place earlier due to larger growth rates, see left panels.

The presence of increased flavor instability as a result of the radially inward bulk velocity, as determined by the value of $\mathrm{Im}(\Omega)$, should not necessarily imply an increased flavor conversion

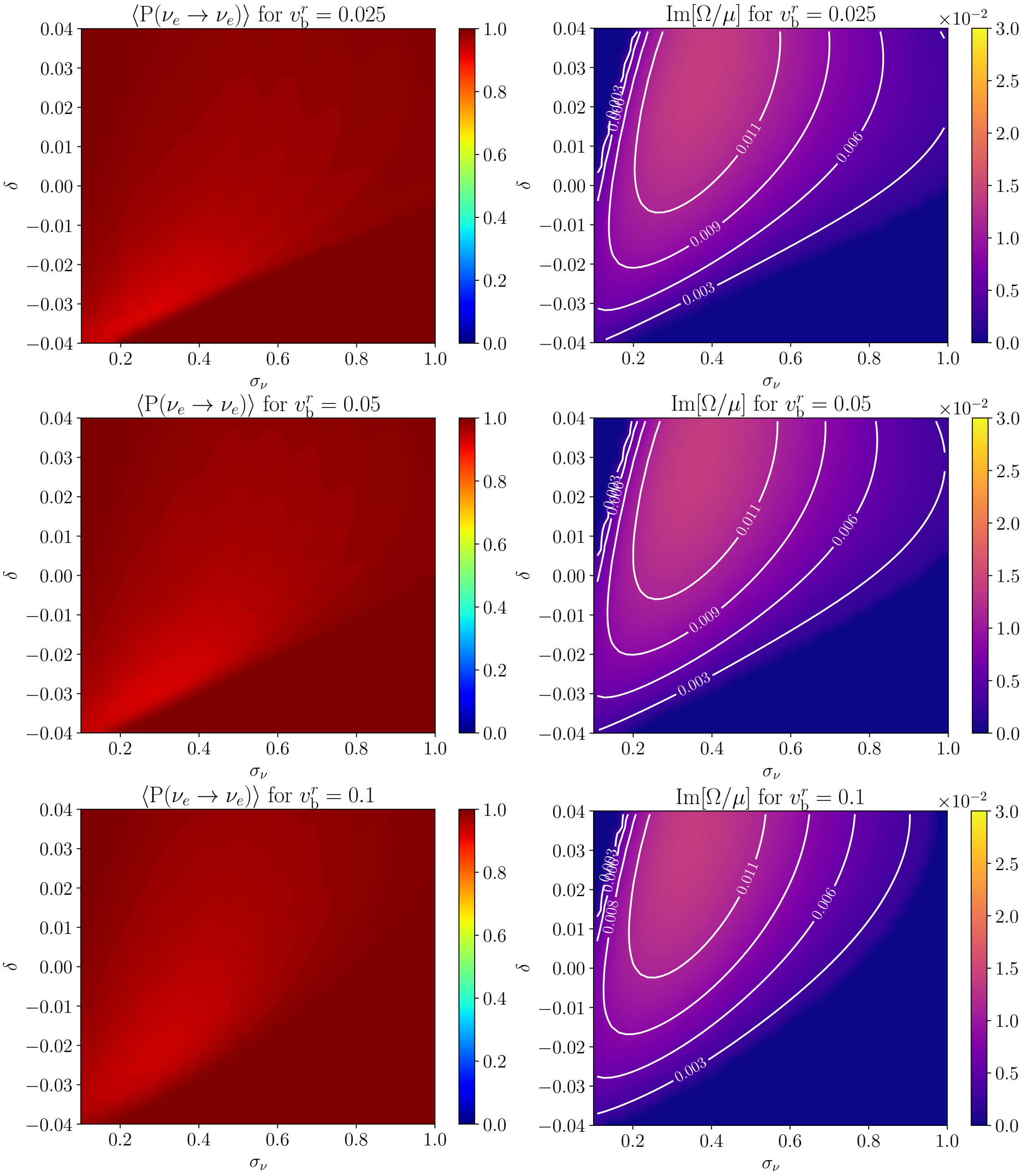

Figure 74: Time averaged survival probabilities (left panels) and growth rates of the flavor instability (right panels) for three selected values of the bulk velocity: $v_b^r = 0.025$ (top panels), $v_b^r = 0.05$ (middle panels) and $v_b^r = 0.1$ (bottom panels). Qualitatively, the radially outward case is not very sensitive to the magnitude of v_b^r since the time averaged survival probabilities and the growth rates are very similar to each other. Interestingly, a radially outward matter suppresses oscillations and resembles, at least qualitatively, the isotropic case.

rate. However, as we show in the next section, the configurations for which the bulk velocity causes an increase in the flavor instability also result in an increased flavor conversion rate. This can be demonstrated by studying the effect of the bulk velocity on several different configurations of angular distributions, as we do in the next section.

9.6 2D PARAMETRIC GRID

The results presented Fig. 70 are very general for the angular distributions of the form presented in eq. 9.13. For all possible values of δ and σ_ν, radially inward bulk velocity can enhance the neutrino flavor conversion rate, while radially outward bulk velocity always suppresses the neutrino flavor conversion rate. To demonstrate this, we calculate the growth rate of $|\rho_{ex}|$ in the linear regime with and without the inclusion of the bulk velocity. In the linear regime, the growth rate of the off-diagonal component $|\rho_{ex}|$ is exponential with time if the system is unstable, and we denote the growth rate by $\mathrm{Im}[\Omega/\mu]$.

We also calculate the angle-integrated survival probability of electron neutrinos. In some circumstances, the survival probability of neutrinos is periodic, and the time averaged survival probability is a much better representation of the amount of neutrino flavor conversion. We thus rely on the time averaged survival probability of neutrino, averaged over $t = 10^{-6}$ seconds, which we denote by $\langle \mathrm{P}(\nu_e \to \nu_e) \rangle$, as a measure of the neutrino flavor conversion rate. The time averaged survival probability underestimates the flavor conversion rate in some instances due to the significant amount of time required to reach the nonlinear regime, but it is nonetheless a fair representation for the purpose of this paper.

9.6.1 *Isotropic* ($v_\mathrm{b}^r = 0$)

In Figs. 72 we show the flavor evolution of (anti)neutrinos for a wide range of values of σ_ν and δ. Each point has a different neutrino angular distribution, while the matter angular distribution is determined by $v_\mathrm{b}^r = 0$ and kept unchanged. This provides a simple way of understanding the main differences between the isotropic and anisotropic scenarios for a wide range of (anti)neutrino angular distributions configurations and allows us to understand better which systems deviate more strongly from the isotropic scenario. In Fig. 72 we present the time averaged, angle-integrated survival probability $\langle \mathrm{P}(\nu_e \to \nu_e) \rangle$ across the grid.

In the isotropic scenario, the only dimensionful quantity is μ; neutrinos and antineutrinos oscillate in a bipolar fashion. This is explicitly shown in a particular case in the top panels of Fig. 70, but this is true for all cases in Fig. 72 where single-crossed ELN angular distributions are considered.

9.6.2 *Radially inward* ($v^r_{\mathrm{b}} < 0$)

For comparison with the isotropic case, we perform the same numerical simulations as in Fig. 72 but with $v^r_{\mathrm{b}} \neq 0$. In particular, each point on the grid has a matter angular distribution determined by $v^r_{\mathrm{b}} = -0.025, -0.05$ and -0.1, all of which peak in the forward direction i.e., more electrons are emitted in the forward direction.

In Fig. 73 we present results for the case where the matter has a negative velocity i.e., matter points along the forward direction. In a realistic supernova scenario, this would qualitatively correspond to the case where the post-shock material is pushed inward and towards the PNS with a negative radial velocity.

First of all, because the flavor evolution now depends on two dimensionful quantities μ and λ, the oscillations are no longer (entirely) bipolar, and the interference caused by the matter term depends on the ratio λ/μ. In particular, one can see that for some points on the grid, flavor conversions are unchanged, while in some others, the interference between $H_{e\nu}$ and $H_{\nu\nu}$ is very prominent. The reason for the latter is the following. As supported by the linear stability analysis, the criteria for neutrino oscillations to occur is modified through the introduction of bulk velocity; thus, one expects that stable parameter points (lower region of panels in Fig. 72) now develop a flavor instability depending on the magnitude and sign of v^r_{b}. Secondly, a much larger region of the parameter space spanned by σ_ν and δ undergoes a significant amount of flavor conversions within the considered time window compared to the isotropic case. We observe an enhancement of oscillations in Fig. 73 where $\langle \mathrm{P}(\nu_e \to \nu_e) \rangle \simeq 0.5$ for a wider range of configurations.

The panels on the right side of Fig. 73 show the growth rate of the off-diagonal components of the density matrix in the linear regime. In the regions that show an enhanced flavor conversion probability, we also see a change in the growth rate as seen by the opening of the new regions of the parameter space for which the growth rate increases with increasing magnitude of the bulk velocity in the inward direction.

9.6.3 *Radially outward* ($v_{\rm b}^r > 0$)

For completeness, we investigate the other possible scenario where the radial velocity of the post-shock material is positive. In particular, each point on the grid has a matter angular distribution determined by $v_{\rm b}^r = 0.025, 0.05$ and 0.1, all of which peak in the backward direction.

In Fig. 74 we show the same colormaps and angular distributions as in Fig. 73 but with matter pointing in the backward direction while keeping the other parameters unchanged. Interestingly, we see the opposite trend as in the former forward-peaked case. Instead of leading to flavor equipartition, an anisotropic backward matter potential leads a suppression of oscillations; even less neutrinos are converted in this case, see Fig. 74 where $\langle \mathrm{P}(\nu_e \to \nu_e) \rangle \simeq 0.9$ at most. Similarly, in the right panels of Fig. 74, we can see that the results of the linear stability analysis are also qualitatively unchanged in the case of bulk velocity that is radially outward.

9.7 CONCLUSIONS

We show that since the fast flavor evolution of neutrino depends strongly on the angle dependence of the coherent forward scattering potential, the angle dependence of the matter potential cannot be ignored. The angle dependence in the matter potential can naturally arise due to the bulk velocity of matter in astrophysical environments. In some instances, the bulk velocity of matter present in astrophysical environments can be as large as 10% of the speed of light. We find that bulk velocities much smaller than the maximum allowed velocities can substantially change the neutrino flavor conversion rate.

We obtain quantitative estimates in this paper to support our understanding. There are two alternative ways of understanding the impact of the bulk velocity of matter on neutrino flavor evolution. One, on which we heavily rely in this paper, is to consider the problem in terms of the modification in the angular dependence of the potential experienced by the neutrinos due to the bulk velocity of matter. The neutrinos traveling in the direction of the bulk velocity of the matter will see a smaller flux compared to the neutrinos in the opposite direction giving rise to the angle dependence of the matter potential. Another way to think about the problem is to consider the problem in the rest frame of the matter. Due to the change in the reference frame, the angular distribution of neutrinos is changed and could be modified in a way that either enhances or suppresses the neutrino flavor conversion rates. It should be noted that the two approaches mentioned here are two different ways of thinking about the same phenomenon; in two different reference frames.

Notwithstanding, the effect of the bulk velocity on the neutrino flavor evolution is far from negligible. The necessary condition for the existence of fast flavor instability, the presence of ELN crossings, remains unchanged. We have explored several cases of neutrino angular distribution without an ELN crossing to examine whether the anisotropic matter term can lead to fast flavor instability. However, we could not find a case in which fast flavor conversions were present in the absence of ELN crossings irrespective of the angle dependence of the matter term. This finding is not surprising since it is possible to go to a reference frame in which the matter term is isotropic, and the ELN crossings are features that are not dependent on the reference frame.

Although this paper only considers two extreme possibilities of the bulk of matter that is either radially inward or outward, this may not be the case in a realistic astrophysical system. However, we have restricted our analysis to these possibilities not to clutter the analysis with too many variables. The possible enhancement of neutrino flavor conversion rates due to the bulk velocity of matter can be demonstrated in the setup considered in this paper.

The demonstration of possible enhancement of neutrino flavor conversion rate due to the bulk velocity of matter also raises several important issues relevant to the supernova mechanism. In the widely popular delayed neutrino driven supernova mechanism, the emphasis is on investigating the role of neutrinos in triggering convection; however, the role of the convective flow of matter in triggering neutrino flavor evolution can lead to a feedback mechanism that is either positive or negative. Future analysis of the subject matter with realistic velocity profiles may be able to shed more light on the matter.

9.8 CRITICAL OUTLOOK

9.8.1 *Overview and main findings*

In this Chapter, we focus on the impact of non-isotropic matter distributions on the development of fast flavor conversion, paying particular attention to the final flavor outcome, the non-linear regime, and the long-term evolution of such non-isotropic configurations[1]. In particular, we investigate the effect of matter convection on neutrino flavor conversion. Most of the works present in the literature have focused before on implementing realistic matter profiles in neutrino flavor simulations and examined the effect of small-scale turbulence perturbations that induce parametric resonances [303–308], and the MNR transitions in the context of NS binary mergers (Sec. 4.3.1).

Our goal is to implement the non-isotropic contribution of the matter term into the neutrino EOMs (Eqs. 2.74). The motivation for including the non-isotropic matter term is the following. In astrophysical environments such as CCSNe, the matter field is not static but varies as a function of location: in some regions, the *bulk motion* of matter can be radially outward, and in some other regions, radially inward [311, 312]; see, for instance, Fig. 13 and 15 of Ref. [311]. These two regions might display different neutrino flavor conversion phenomenology because, depending on the direction of the bulk velocity, an observer at rest w.r.t. PNS might see an excess of matter either in the *backward* direction or in the *forward* direction, resulting in non-trivial (non-isotropic) angular distributions of matter.

Moreover, it is worth noting that the reason why the matter term is ignored in the EOMs is that it can be "rotated away" (Sec. 2.2.7.1) by a convenient change of basis. However, this is only possible when the matter term is isotropic, i.e., when the term in the matter Hamiltonian $[1 - \vec{v} \cdot \vec{v}_e]$

---

[1] Non-isotropy arises from considering that the matter background is not static but moving in bulk at a given velocity. If that is the case, the thermal average of the electron fields in Eq. 2.21 will receive contributions from $\mu = 1, 2, 3$.

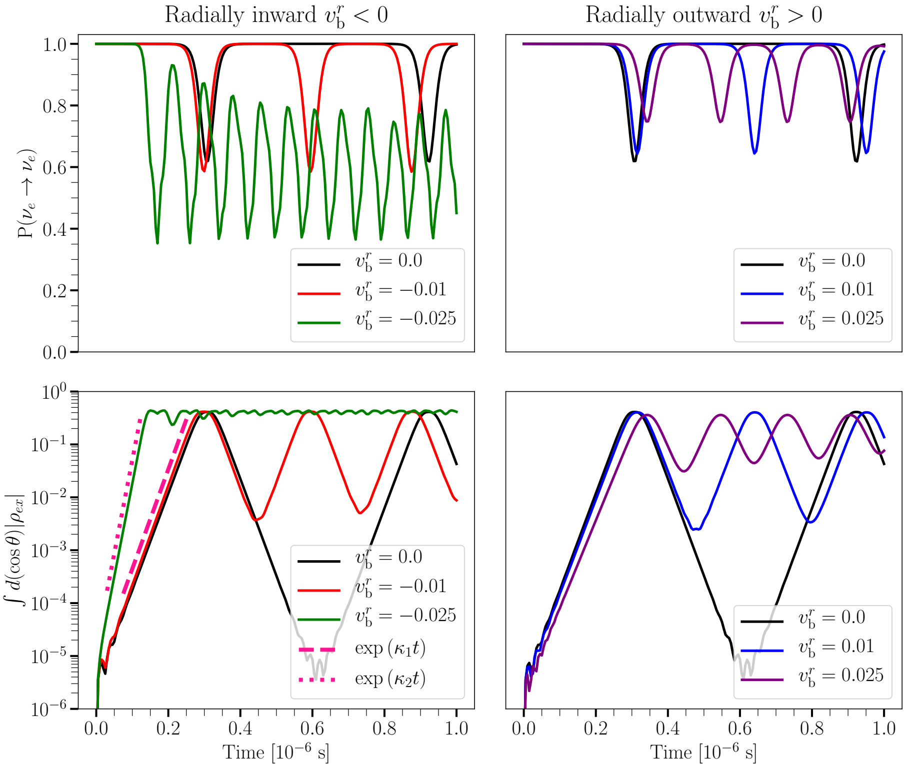

Figure 75: Angle-integrated survival probability $\mathrm{P}(\nu_e \to \nu_e)$ (top panels) and the angle-integrated modulus of the off-diagonal term ρ_{ex} (bottom panels) for the scenarios where matter moves radially inward i.e. $v_{\mathrm{b}}^{r} < 0$ (left panels) and radially outward i.e. $v_{\mathrm{b}}^{r} > 0$ (right panels), where v_{b}^{r} is the radial component of the bulk velocity vector $\vec{v}_{\mathrm{b}}$. The dashed lines correspond to the growth rates obtained from the linear stability analysis, which perfectly agrees with our numerical computations.

integrates out to 1, where $\vec{v}_e$ is the velocity of electrons in the medium and $\vec{v}$ the velocity of a test neutrino. In this work, we explore the impact of the non-isotropic contribution of the matter Hamiltonian on the non-linear behavior of fast flavor conversion.

Near the neutrino decoupling regions, the bulk velocity of matter can be as large as $|\vec{v}_{\mathrm{b}}| \simeq 0.1$ [311]. This value will determine the angular distributions of matter. If the magnitude of the bulk velocity is zero, the matter background is perfectly isotropic. Otherwise, there will be an excess of matter in the opposite direction of the matter bulk velocity vector; for instance, if the bulk velocity is radially inward, an observer at rest w.r.t to the PNS would see more matter (electrons) coming from the forward direction and less from the backward direction.

Our main findings are the flavor evolution of neutrinos in the presence of a non-isotropic matter Hamiltonian, here denoted by $H_{ev}(\theta)$, where the direction dependence (θ-dependence) is made explicit. Thus, the matter Hamiltonian resembles the structure of that of neutrino-neutrino refraction, with the exception that off-diagonal elements are completely absent in $H_{ev}(\theta)$. The matter term can be written as,

$$H_{ev}(\theta) \quad = \quad \lambda \int d(\cos\theta') J_e(\theta') \left[1 - \cos\theta \cos\theta'\right] \, . \tag{9.22}$$

Notice that assuming an anisotropic momentum distribution of electrons, i.e., their bulk velocity is not zero, introduces a new contribution to the equations of motion, which is captured by Eq. 9.22. The angular dependence of $J_e(\theta')d(\cos\theta')$ is determined by $\vec{v}_\mathrm{b}$ alone.

In Fig. 75 we summarize our main findings for our benchmark scenario. This chapter explains how these main results change by considering different initial configurations. The role of $v_\mathrm{b}^r \neq 0$ is twofold: Firstly, there is a enhancement of conversions for $v_\mathrm{b}^r < 0$ compared to the $v_\mathrm{b}^r \geq 0$ cases, see top panels. Secondly, oscillations set in faster i.e., $v_\mathrm{b}^r < 0$ leads to larger growth rates such as $\kappa_1/\mu = 0.0027$ (dotted line) and $\kappa_2/\mu = 0.0014$ (dashed line), as shown in the bottom panels.

As supported by Fig. 75, we find that bulk velocities much smaller than the maximum allowed velocities ($\simeq 0.1c$) can substantially change the neutrino flavor conversion rate and the final flavor outcome. This work demonstrates the possibility of enhancement (suppression) of neutrino flavor conversion rates depending on whether there is a region in the SN environment with a radially inward (radially outward) bulk velocity.

9.8.2 *Limitations and future perspectives*

The results presented in this Chapter assumed the most straightforward possible system to explore the role of the matter anisotropies on the flavor evolution of neutrinos. Although such a system allowed us to learn about qualitative features of the flavor evolution for the cases $v_\mathrm{b}^r > 0$ and $v_\mathrm{b}^r < 0$, more sophisticated modeling of the matter background medium is needed to gauge the impact of the bulk velocity quantitatively.

9.8.2.1 *Beyond the two-flavor framework*

One simplification of our work was the assumption of two-neutrino flavors. The question is whether our results reported in this Chapter also hold in the three-flavor framework. Direct numerical comparisons between two- and three flavors have recently shown that the flavor evolution can be qualitatively very different when including three flavors [148, 187]. The enhancement (suppression) of flavor conversion as a function of v_{b}^{r} could be affected by the inclusion of additional neutrino species, see, for instance, Fig. 2 of Ref. [148] where significantly more flavor conversion occurs in the three flavor case. Future work along this line should include extra neutrino species and study the role of v_{b}^{r} on the flavor evolution of ν_{μ}, $\bar{\nu}_{\mu}$, ν_{τ} and $\bar{\nu}_{\tau}$.

9.8.2.2 *Heavy leptons* μ, τ

In connection to the three-flavor treatment described above, one could also include heavy leptons μ and τ in the content of the matter background. Recent works (Refs. [176, 249]) have explored the role of a non-negligible abundance of muons and their impact on FFC near the SN core. These works have shown that although the muons do not affect the development of fast modes below the SN shock, they still can trigger instabilities in the $\mu - \tau$ sector. In connection to the work presented in this Chapter, this means that our matter Hamiltonian (Eq. 9.22) should not only include electron angular distributions $J_e(\theta, t)$ (see Fig. 69) but also angular distributions in the muon and tau sectors, $J_{\mu}(\theta, t)$ and $J_{\tau}(\theta, t)$, respectively. Whether there is still a qualitatively distinct flavor evolution for the $v_{\mathrm{b}}^{r} < 0$ and $v_{\mathrm{b}}^{r} > 0$ scenarios remains to be explored in future work.

Part IV

SUMMARY AND CONCLUSIONS

10

SUMMARY AND CONCLUSIONS

We summarize the main findings and conclusions of the work presented in this thesis and provide the connection to future research in the field of neutrino flavor conversion in dense astrophysical environments.

The body of work presented in this thesis has two main goals. The first one (Part ii) is to unveil new theoretical aspects of non-linear systems with a direct application to neutrino fast flavor conversion. We hope that the findings presented in that Part help bridge the gap between numerical simulations and semi-analytical treatments of the development of fast flavor instabilities. The second one (Part iii) aims to develop new numerical routines to uncover the rich phenomenology of more complicated (less symmetric) neutrino-dense environments. In the following paragraphs, we summarize the main conclusions from each work contained in Parts ii and iii.

In Chapter 5, we have explicitly shown that for a homogeneous and azimuthally symmetric two-neutrino gas, the flavor conversion physics crucially depends on the characteristic of the initial ELN distribution: similar looking ELN angular distributions can lead to entirely different flavor outcomes. Furthermore, we have shown that the amount of flavor conversion is not correlated with the growth rate of flavor instabilities from the linear stability analysis. Interestingly, the evolution of the ELN flux $\boldsymbol{D}_1(t)$ is formally equivalent to a gyroscopic pendulum in the presence of a gravitational field given by the ELN vector $\boldsymbol{D}_0$. The crucial finding of this work was the determination of the pendulum parameters (natural frequency and spin) with the real and imaginary parts of the eigenfrequency Ω from the linear stability analysis. Up to now, it was unknown that the real part of Ω could offer any valuable information on the flavor dynamics, and, to our surprise, it encodes the maximum amount of conversion that the system can display as a function of time. The latter is a novel, powerful result that could be applied for more general scenarios to gauge the impact of flavor conversion in neutrino gases.

The study presented in Chapter 6 is a follow-up work to our previous findings in Chapter 5. We investigate the role of damping due to random collisions on the final flavor outcome. When damping is included in the EOMs, the ELN vector $\boldsymbol{D}_0$ is still conserved while exerting a torque on the dynamical ELN flux vector $\boldsymbol{D}_1(t)$. Although there is no apparent gyroscopic pendulum analogy in the case of damping, some of the features of the standard gyroscopic pendulum are still preserved. Our main finding is a simple analytical formula that estimates the final steady state achieved by the system after decoherence and demonstrates that it is a linear combination of the lowest point of the pendulum of Chapter 5. Moreover, we explore the validity of this novel analytical formula and confirm that it successfully predicts the final flavor outcome for a wide variety of single-crossed ELN spectra. This work is the first next-to-minimal extension of the gyroscopic pendulum (Chapter 5) still able to predict the impact of decoherence on the evolution of the neutrino flavor.

In the work presented in Chapter 7, we explored the exciting interplay between neutrino fast flavor conversion and the propagation of the neutrino field driven by the advective term in the EOMs. Understanding this interplay is crucial for understanding compact astrophysical objects where flavor conversion (a quantum effect) is expected to manifest at macroscopic scales. In Chapter 7, we presented for the first time the neutrino flavor evolution in a multi-dimensional framework, i.e., in two spatial dimensions, one angular variable and time. To explore the non-trivial flavor dynamics of non-homogeneous systems, we relied on two benchmark scenarios that resemble two possible configurations in dense astrophysical environments: the "one dot configuration" and the "one stripe configuration." Our simulations show that the advective term inhibits the development of fast instabilities unless the spatial distribution of ELN crossings is self-sustained in time (like LESA [263]) and not stochastic (or random) in nature. Our work is the first work of its kind to conclusively show that the role of neutrino advection is decisive for the evolution of flavor. However, more advanced and sophisticated calculations are still needed to finally assess the evolution of inhomogeneities in astrophysical sources.

In Chapter 8, we model for the first time the flavor evolution of neutrinos above the disk of the remnants in a multi-dimensional framework to account not only for the angular dependence of the lepton number but also for its spatial variation. The ubiquity of flavor unstable regions was firmly established in Ref. [196]; however, their impact on synthesizing elements heavier than iron and the related kilonova observations remain under debate. As such, the work in Chapter 8 is the first numerical simulation of the non-linear regime of fast flavor conversion in the context of compact binary merger remnants. Before this study, previous work has focused only on the linear regime and the possible existence of flavor instabilities. The findings of this study show that most unstable regions favoring the occurrence of fast flavor conversion are located in the vicinity (near the edges) of the neutrino emitting regions. The crucial conclusion of this work is that minimal flavor conversion can occur in the polar regions above the merger remnant for both NS- and BH-disk configurations, whose flavor outcomes are qualitatively very similar in both scenarios. These findings hint that although flavor unstable solutions are predicted to exist almost at any locations above the disk of the remnant, minimal flavor conversion is possible, putting in question the widely implemented assumption of flavor equilibration. The work in Chapter 8 constitutes a significant step forward in the modeling of flavor evolution in compact sources; however, more sophisticated simulations should cross-check the results of this Chapter to ultimately make robust predictions for the observables expected from the merger remnant.

Last but not least, in Chapter 9 we demonstrate that the non-isotropic contribution of the matter potential cannot be neglected because fast flavor conversion sensitively depends on the angle dependence of the coherent forward scattering with the medium. The angular dependence in the matter potential arises if the electron background moves in bulk at a given velocity, which can be as large as 10 of the speed of light. As a result of the bulk motion of electrons, an observer at rest w.r.t the proto-neutron star would observe an excess of electrons in one preferred angular direction. In Chapter 9 we consider two possible directions of the bulk velocity of matter, i.e., radially inward $v_{\mathrm{b}}^{r} < 0$ and radially outward $v_{\mathrm{b}}^{r} > 0$ and explore the flavor evolution of neutrinos in the presence of electron anisotropy. Our simplified model suggests that the neutrino conversion rate due to fast modes can be enhanced in the $v_{\mathrm{b}}^{r} < 0$ scenario, while suppression of flavor conversion occurs for $v_{\mathrm{b}}^{r} > 0$. Our results motivate future work on the role of non-isotropic matter distributions in the development of fast flavor conversion and its connection to more realistic SN environments.

The work presented in this thesis (Parts ii and iii) show that the physics of fast flavor is extremely rich and sometimes even counter-intuitive. Many studies have been dedicated to solving the neutrino EOMs, and it is starting to become clear that the final flavor outcome can dramatically change when some of the symmetries imposed on the system and its solutions are relaxed. The latter resembles the case of slow flavor conversion when the spectral splits/swaps were discovered; we now understand that they can be smeared out in less symmetric systems with more degrees of freedom. In the case of fast flavor conversion, recent numerical simulations from various groups suggest a paradigm change concerning flavor equilibration.

Since the implementation of detailed neutrino transport in state-of-the-art simulations is not available yet, many open questions and issues need to be understood first [87]. These issues touch upon our conceptual understanding of collective effects and moving beyond linear stability analyses. Equally important is exploring the flavor evolution phenomenology when symmetry assumptions are relaxed; we need to quantify the impact of lifting these assumptions and develop new and faster numerical routines to simulate their flavor evolution. Moreover, throughout this thesis, we assumed Standard Model physics in the conversion of flavor, which we do not fully understand even in its "standard" version: physics beyond the Standard Model might still offer new insights. Finally, we need to gauge the impact of neutrino flavor conversion on the physics and the inner workings of astrophysical sources.

Although many of these challenges look far from today, neutrino flavor conversion physics continuously offers new insights and surprises. In the meantime, while we wait for the next galactic supernova or compact binary merger observation, new exciting manifestations of collective neutrino conversion might reveal to us, answering long-standing questions and posing new ones.

Part V

APPENDICES

A

GYROSCOPIC PENDULUM APPENDIX

In this appendix, we introduce the multipole decomposition of the EOM and show that the pendulum equations derived by truncating the multipole equations to the first few multipoles are not always predictive of the final flavor outcome. Next, we perform a discretization of the ELN angular distribution to three modes and derive a formal similarity with a pendulum characterized by its natural frequency and spin. We also outline the linear normal-mode analysis for our homogeneous system and finally provide additional details on our numerical examples.

A.1 MULTIPOLE DECOMPOSITION

One way to discretize the system of interacting Bloch vectors $\boldsymbol{D}_v$ with $v = \cos\theta$ is an expansion in Legendre polynomials $L_l(v)$ that more generally would appear in a multipole expansion of $\boldsymbol{D}_{\vec{v}}$ before assuming azimuthal symmetry [154]. Thus, we define the new functions

$$\boldsymbol{D}_l(t) = \int_{-1}^{+1} dv\, L_l(v)\, \boldsymbol{D}_v(t) \tag{A.1}$$

that obey the co-rotating EOMs

$$\dot{\boldsymbol{D}}_l = \frac{\mu}{2}\big(a_l \boldsymbol{D}_{l-1} + b_l \boldsymbol{D}_{l+1}\big) \times \boldsymbol{D}_1\,, \tag{A.2}$$

where $a_l = 2l/(2l+1)$ and $b_l = 2(l+1)/(2l+1)$. The EOMs for the first few multipoles are explicitly:

$$\dot{\boldsymbol{D}}_0 = 0\,, \tag{A.3a}$$

$$\dot{\boldsymbol{D}}_1 = \mu\,\frac{\boldsymbol{D}_0 + 2\boldsymbol{D}_2}{3} \times \boldsymbol{D}_1\,, \tag{A.3b}$$

$$\dot{\boldsymbol{D}}_2 = \frac{3\mu}{5}\,\boldsymbol{D}_3 \times \boldsymbol{D}_1\,, \tag{A.3c}$$

$$\dot{\boldsymbol{D}}_3 = \mu\,\frac{3\boldsymbol{D}_2 + 4\boldsymbol{D}_4}{7} \times \boldsymbol{D}_1\,. \tag{A.3d}$$

$\boldsymbol{D}_0$ is conserved and $\boldsymbol{D}_1$ is the only one that evolves instantaneously like a precession, i.e., its length is conserved. The equation for $\boldsymbol{D}_3$ is the first one clearly showing the general structure that a given $\boldsymbol{D}_l$ is driven by one higher and one lower multipole.

This infinite tower of equations can be closed by truncation, assuming that the spectrum has no fine-grained information. In this case, high multipoles should be considered to be negligible. Actually, this is a nontrivial point because it looks like lower multipoles impact higher ones in the EOMs, so higher multipoles should get excited from lower ones, even if they were small at first, as also discussed in Refs. [154, 156].

Johns et al. [155] have observed that, if we truncate Eqs. (A.2) by setting $\dot{\boldsymbol{D}}_3 = 0$, the lowest multipole equations in the comoving frame are equivalent to the ones of a pendulum in the flavor space. Comparing Eqs. (A.3) with Eqs. (5.7) reveals that we should identify $\boldsymbol{R} = \boldsymbol{D}_1$ as usual and $\boldsymbol{J} = (\boldsymbol{D}_0 + 2\boldsymbol{D}_2)/3$, implying $\dot{\boldsymbol{J}} = 2\dot{\boldsymbol{D}}_2/3$. In turn, this implies that we may identify $\boldsymbol{G} = 2\boldsymbol{D}_3/5$ and $\gamma = \mu$. We now denote with $D_n = D_n^z|_{t=0}$ the initial values that are not conserved except for $\boldsymbol{D}_0$ and $\boldsymbol{D}_1$. With this notation, one finds for the spin $S = (D_0 + 2D_2)/3$ and finally

$$\lambda^2 = \frac{2}{5} D_3 D_1 \,, \tag{A.4a}$$

$$\sigma^2 = \frac{S^2}{4\lambda^2} = \frac{(1/9)\,(D_0 + 2D_2)^2}{(8/5)\,D_1 D_3} \,. \tag{A.4b}$$

With these identifications, our interpretations agree with the ones in Ref. [155], noting that they used the symbol σ for what we call S. Hence, the condition for an instability $\sigma < 1$ reads

$$\frac{(D_0 + 2D_2)^2}{D_1 D_3} < \frac{72}{5} \,. \tag{A.5}$$

Or, equivalently, the pendulum is locked in its initial configuration if

$$\xi = \frac{S^2}{(2/5)\,D_1^z D_3^z} > 4 \,. \tag{A.6}$$

From the relations $\Gamma = \mu\lambda\sqrt{1-\sigma^2}$ and $\cos\vartheta_{\rm min} = -1 + 2\sigma^2$ provided in the main text, these results imply

$$\Gamma = \mu\sqrt{\frac{2D_1D_3}{5} - \frac{(D_0 + 2D_2)^2}{36}} \,, \tag{A.7a}$$

$$\cos\vartheta_{\rm min} = -1 + \frac{5\,(D_0 + 2D_2)^2}{36\,D_1 D_3} \tag{A.7b}$$

for the initial growth rate and depth of conversion. These predictions can be compared with those of our numerical examples, or equivalently, with those from the normal-mode analysis.

Actually, as a starting point for their pendulum discussion, the authors of Ref. [155] used the second-order equation

$$\frac{\boldsymbol{r} \times \ddot{\boldsymbol{r}}}{\mu} + S\dot{\boldsymbol{r}} = \mu D_1 \boldsymbol{G} \times \boldsymbol{r} \,, \tag{A.8}$$

where $\boldsymbol{R} = \boldsymbol{D}_1$, $\boldsymbol{r} = \boldsymbol{R}/R$, the spin of the pendulum is $S = \boldsymbol{r} \cdot (\frac{1}{3}\boldsymbol{D}_0 + \frac{2}{3}\boldsymbol{D}_2)$, and $\boldsymbol{G} = \frac{2}{5}\boldsymbol{D}_3$.

To show that this second-order equation follows from our two first-order ones, we write the latter in the form $\dot{\boldsymbol{r}} = \boldsymbol{J} \times \boldsymbol{r}$ and $\dot{\boldsymbol{J}} = \boldsymbol{G} \times \boldsymbol{r}$ where μ was absorbed in the definition of time and all other coefficients in the definition of $\boldsymbol{G}$. Taking another derivative of the first equation yields $\ddot{\boldsymbol{r}} = \dot{\boldsymbol{J}} \times \boldsymbol{r} + \boldsymbol{J} \times \dot{\boldsymbol{r}}$ and inserting the second equation for $\dot{\boldsymbol{J}}$ gives $\ddot{\boldsymbol{r}} = (\boldsymbol{G} \times \boldsymbol{r}) \times \boldsymbol{r} + \boldsymbol{J} \times \dot{\boldsymbol{r}} = (\boldsymbol{G} \cdot \boldsymbol{r})\boldsymbol{r} - \boldsymbol{G} + \boldsymbol{J} \times \dot{\boldsymbol{r}}$, where we have used $\boldsymbol{r}^2 = 1$. Now we consider $\boldsymbol{r} \times \ddot{\boldsymbol{r}}$ and see that the first term disappears and the second is $\boldsymbol{G} \times \boldsymbol{r}$; the third is $\boldsymbol{r} \times (\boldsymbol{J} \times \dot{\boldsymbol{r}}) = (\boldsymbol{r} \cdot \dot{\boldsymbol{r}})\boldsymbol{J} - (\boldsymbol{r} \cdot \boldsymbol{J})\dot{\boldsymbol{r}}$. Noting that $\dot{\boldsymbol{r}}$ is perpendicular to $\boldsymbol{r}$ and $\boldsymbol{r} \cdot \boldsymbol{J} = S$ is the conserved spin, we find $\boldsymbol{r} \times \ddot{\boldsymbol{r}} + S\,\dot{\boldsymbol{r}} = \boldsymbol{G} \times \boldsymbol{r}$. Reinstating the original meaning of the variables leads to Eq. (A.8). The advantage is that $\boldsymbol{J}$ no longer appears, but only the conserved spin.

As already discussed in the main text, for sufficiently large S, the pendulum is locked in its initial stable configuration and cannot swing away from the flavor axis. Hence, the pendulum is stable, and we expect that FFC cannot take place. The pendulum is also in a stable configuration when it is oriented in the same direction as the gravity vector $\boldsymbol{G}$.

Figure 76 shows the contour plot of the minimum value of the lepton-number flux $D_1^z(t)$ in the plane spanned by a and b. We can see from Fig. 76 (see also Fig. 30) that we expect a different flavor outcome as a function of a and b, with regions of no flavor mixing despite the existence of an ELN crossing.

In agreement with Ref. [155], our results support that the outcome of the neutrino flavor qualitatively changes depending on the relative signs of the $l = 0$–3 multipoles. The relative sign of $\boldsymbol{D}_0|_{t=0}$ and $\boldsymbol{D}_2|_{t=0}$ determines the magnitude of S. Secondly, the relative sign of $\boldsymbol{D}_1|_{t=0}$ and $\boldsymbol{D}_3|_{t=0}$ also determines whether the pendulum is initially in a stable (unstable) equilibrium configuration, before it is perturbed. Our results are also in agreement with the ones of Ref. [155] for the configurations when gravity plays a role in stabilizing the pendulum (results not shown here). Qualitatively, these findings are in agreement with Fig. 3 of Ref. [155] where the relative signs of the multipoles lead to different growth rates of the flavor instability.

This suggests that it may be enough to rely on the $l = 0$–3 multipoles of $\boldsymbol{D}_v$ in order to predict the stability of the flavor pendulum and gauge the amount of flavor mixing. However, it is important to stress that the errors induced by truncating the angular-moment expansion at an arbitrary small l propagate back to large scale with major consequences on the overall flavor evolution in the nonlinear regime [156].

The $\xi = 4$ isocontour (dashed blue line) in Fig. 76 shows unstable regions predicted by the pendulum analysis. We find that in the stable (bottom) part of the parameter space in Fig. 76, the spin is large enough to lock the flavor pendulum, not letting it swing away from the flavor axis. Conversely, in the unstable (top) region in Fig. 76, S is smaller, allowing $\boldsymbol{r}$ to oscillate. However, we also find that fast flavor mixing does not occur for all configurations below the black dashed line representing the locus where $D_0^z = 0$ and the unstable regions do not coincide with the $\xi = 4$ contour.

This discrepancy is due to the fact that, for very forward-peaked distributions, the ξ criterion worsens, see the lower region below the $D_0^z = 0$ line. Moreover, we can see a sudden transition

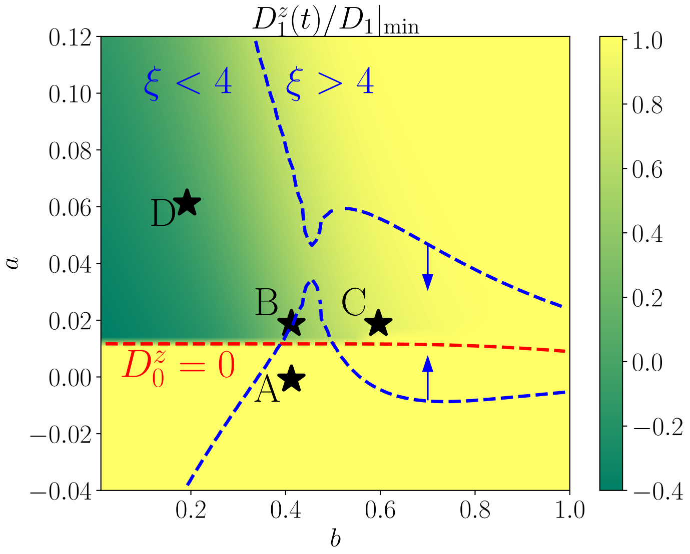

Figure 76: Contour plot of the minimum value of the lepton-number flux $D_1^z(t)/D_1^z|_{t=0}$ in the plane spanned by a and b (see Eqs. 5.6a, 5.6b and Fig. 30). The isocontour of the configurations with $\xi = 4$ (obtained by truncating the multipole expansion of the EOM at $l = 3$) is marked by dashed blue lines, where the arrows point into the unstable region ($\xi \lesssim 4$). Due to the limited number of multipoles, this criterion worsens for very peaked angular distributions and does not allow one to reliably predict the flavor outcome for a general ELN configuration.

to large flavor mixing in the proximity of the $D_0^z = 0$ line, not predictable by the ξ criterion. These deviations of the numerical results from the $\xi = 4$ constraints are due to the fact the high-l multipoles (with $l > 3$) are relevant and do affect the flavor stability. As a consequence, it is difficult to asses, a priori, when the pendulum approximation proposed in Ref. [156] should hold.

A.2 FLAVOR PENDULUM OF THREE MODES

The coherence of all modes suggests a small number of underlying degrees of freedom that can be diagnosed using the Gram matrix $G_{ij} = \int_{t_1}^{t_2} dt\, \boldsymbol{D}_{v_i}(t) \cdot \boldsymbol{D}_{v_j}(t)$ [234]. It is calculated for our discrete set of numerical $\boldsymbol{D}_{v_i}(t)$ with $i = 1, \ldots, n$ for a convenient, but arbitrary, time interval. The rank of G that we call $N+1$ reveals the number of independent functions. The system always has one time-independent solution in the form of $\boldsymbol{D}_0 = \sum_{i=1}^{n} \boldsymbol{D}_{v_i}(t)$, thus N is the number of independent *dynamical* functions. For our single-crossed examples we always find $N = 2$. Hence, we conjecture that single-crossed ELN spectra provide solutions that are equivalent to two dynamical degrees of freedom, equivalent to three discrete angle modes.

To study a system of three discrete modes we note that another way to combine the $\boldsymbol{D}_v$ is to use angular moments of the $v = \cos\theta$ distribution defined as

$$\boldsymbol{M}_n = \int_{-1}^{+1} dv\, v^n \boldsymbol{D}_v \,. \tag{A.9}$$

Here $\boldsymbol{M}_0$ is the same as $\boldsymbol{D}_0$ and $\boldsymbol{M}_1 = \boldsymbol{D}_1$ is the flux. The EOM is

$$\dot{\boldsymbol{M}}_n = \mu\, \boldsymbol{M}_{n+1} \times \boldsymbol{M}_1 \,. \tag{A.10}$$

Once more we see immediately that $\boldsymbol{M}_0$ is conserved, whereas the dipole $\boldsymbol{M}_1$ performs an instantaneous precession around the second moment and thus its length $M_1 = |\boldsymbol{M}_1|$ is conserved. The length of the other moments is not conserved. The Legendre polynomials (see Appendix A) are one combination of the moments that is based on an orthogonal set of functions, whereas the v^n are linearly independent, but not orthogonal.

The EOMs should be discretized to be solved numerically. We will see that the evolution is coherent among the $\boldsymbol{D}_v$, meaning that neighboring modes have similar evolution and do not develop large differences over time. In this sense, representing the spectrum with a small discrete set of modes v_i with $i = 1, \ldots, N$ should provide a good proxy to the true solution. Moreover, in our axially symmetric case, there are no spurious instabilities [243, 244].

Notice, however, that we need a minimum of three discrete bins (or "beams") to obtain nontrivial results. As in the continuous case, the overall lepton number $\boldsymbol{D}_0 = \sum_{i=1}^{N} \boldsymbol{D}_{v_i}$ is conserved and $\boldsymbol{D}_1 = \sum_{i=1}^{N} v_i \boldsymbol{D}_{v_i}$ has conserved length. So if $N = 2$ the only possible solution is a precession of $\boldsymbol{D}_1$ around $\boldsymbol{D}_0$. For $N \geq 3$, there exist instabilities and pendulum-like solutions.

Next we consider the simplest homogeneous case that can provide an instability, i.e., the general three-mode case consisting of three Bloch vectors $\boldsymbol{D}_{v_i}$ with velocities v_i with $i = 1$, 2 or 3. The corresponding angular moments are $\boldsymbol{M}_n = \sum_{i=1}^{3} v_i^n \boldsymbol{D}_{v_i}$. In turn, we can express the three $\boldsymbol{D}_{v_i}$ in terms of the moments. We have only three $\boldsymbol{D}_{v_i}$ modes, so there are only three linearly independent moments.

We can express any moment in terms of three others. We use the lowest ones and close the tower of EOMs with

$$\begin{aligned}\boldsymbol{M}_3 &= v_1 v_2 v_3 \boldsymbol{M}_0 + (v_1 + v_2 + v_3)\boldsymbol{M}_2 \\ &\qquad - (v_1 v_2 + v_1 v_3 + v_2 v_3)\boldsymbol{M}_1 \,. \end{aligned} \tag{A.11}$$

To find this result, we first expressed the three $\boldsymbol{D}_{v_i}$ in terms of the first three moments, and then inserted these expressions in the definition of $\boldsymbol{M}_3$. Then the tower of EOMs for the moments is

$$\dot{\boldsymbol{M}}_0 = 0\,, \tag{A.12a}$$

$$\dot{\boldsymbol{M}}_1 = \mu \boldsymbol{M}_2 \times \boldsymbol{M}_1\,, \tag{A.12b}$$

$$\begin{aligned}\dot{\boldsymbol{M}}_2 &= \mu \boldsymbol{M}_3 \times \boldsymbol{M}_1 \\ &= \mu\big[v_1 v_2 v_3 \boldsymbol{M}_0 + (v_1 + v_2 + v_3)\boldsymbol{M}_2\big] \times \boldsymbol{M}_1\,. \end{aligned} \tag{A.12c}$$

We see that we can add any multiple of $\boldsymbol{M}_1$ to $\boldsymbol{M}_2$ without changing the second equation. Specifically we use

$$\begin{aligned}\boldsymbol{M}_2' &= \boldsymbol{M}_2 - (v_1 + v_2 + v_3)\boldsymbol{M}_1 \\ &= -(v_2 + v_3) v_1 \boldsymbol{D}_{v_1} - (v_1 + v_3) v_2 \boldsymbol{D}_{v_2} \\ &\qquad - (v_1 + v_2) v_3 \boldsymbol{D}_{v_3}\,, \end{aligned} \tag{A.13}$$

providing the EOMs

$$\begin{aligned} \dot{\boldsymbol{M}}_0 &= 0\,, && \text{(A.14a)} \\ \dot{\boldsymbol{M}}_1 &= \mu \boldsymbol{M}_2' \times \boldsymbol{M}_1\,, && \text{(A.14b)} \\ \dot{\boldsymbol{M}}_2' &= \mu\, v_1 v_2 v_3 \boldsymbol{M}_0 \times \boldsymbol{M}_1\,. && \text{(A.14c)} \end{aligned}$$

These are the pendulum equations in the form of Eq. (5.7) with the identification $\boldsymbol{G} = \boldsymbol{M}_0$ (gravity), $\boldsymbol{R} = \boldsymbol{M}_1$ (pendulum radius), $\boldsymbol{J} = \boldsymbol{M}_2'$ (angular momentum), and the coupling constant $\gamma = \mu v_1 v_2 v_3$. If $v_1 v_2 v_3$ of the chosen beams is negative, we instead identify $\boldsymbol{G} = -\boldsymbol{M}_0$ to ensure a positive γ.

These results imply $\lambda^2 = v_1 v_2 v_3 M_0 M_1$ for the square of the natural pendulum frequency, whereas the spin is $S = J_z = M_2 - (v_1 + v_2 + v_3) M_1$, where we use $M_2 = M_2^z|_{t=0}$, recalling that the length of $\boldsymbol{M}_2$ is not conserved. The condition for instability is $S^2 < 4\lambda^2$ or explicitly

$$\left[M_2 - (v_1 + v_2 + v_3) M_1\right]^2 < 4 |v_1 v_2 v_3 M_0 M_1|\,. \qquad \text{(A.15)}$$

So none of v_i must vanish and, of course, the lepton number M_0 and lepton-number flux M_1 both must be nonzero. To have three modes in the first place, all three $D^z_{v_i}$ must be nonzero, so all six parameters of our model must be nonzero. The quantity representing the angular momentum is complicated and does not suggest any simple extension to a continuous spectrum.

For given pendulum parameters we can find an equivalent three-mode system. The reverse transformation applied to the initial configuration provides

$$\begin{aligned} g_{v_1} &= \frac{S + v_1 M_1 + v_2 v_3 M_0}{(v_1 - v_2)(v_1 - v_3)}\,, && \text{(A.16a)} \\ g_{v_2} &= \frac{S + v_2 M_1 + v_1 v_3 M_0}{(v_2 - v_1)(v_2 - v_3)}\,, && \text{(A.16b)} \\ g_{v_3} &= \frac{S + v_3 M_1 + v_1 v_2 M_0}{(v_3 - v_1)(v_3 - v_2)}\,, && \text{(A.16c)} \end{aligned}$$

where we have used $J_z = S$ and the spectrum of discrete modes is $g_{v_i} = D^z_{v_i}|_{t=0}$.

As discussed in the main text, from a single-crossed spectrum g_v we can obtain the pendulum parameters σ and λ and thus the corresponding spin $S = 2\sigma\lambda$ as well as the coupling parameter γ, defined to be positive, and we have $M_0 = \int dv g_v$ and $M_1 = \int dv v g_v$. In this way, four of the six parameters are given that determine a three-mode realization of the same pendular motion. The natural pendulum frequency (in units of μ) is given by $\lambda^2 = \omega_{\rm P}^2 + \Gamma^2$ and in our three-mode case $\lambda^2 = v_1 v_2 v_3 M_0 M_1$, implying $v_1 v_2 v_3 = (\omega_{\rm P}^2 + \Gamma^2)/(M_0 M_1)$. On the l.h.s., $|v_1 v_2 v_3| < 1$, suggesting that $\omega_{\mathrm{P}}^2 + \Gamma^2 < |M_0 M_1|$. In our numerical examples this condition is certainly fulfilled, but it is not mathematically obvious if this is generally true for any single-crossed spectrum that exhibits an instability. If it were not the case, a three-mode realization of the motion would not be possible.

Assuming this to be the case for a given g_v we can choose the three-mode representation such that $v_1 = -1$, $v_3 = +1$, and $v_2 = u$ with $-1 < u < +1$. Then the equivalent three-mode system is given by

$$S = 2\omega_{\mathrm{P}} \quad \text{and} \quad u = -\frac{\omega_{\mathrm{P}}^2 + \Gamma^2}{M_0 M_1} \tag{A.17}$$

and

$$\begin{aligned} g_{v=-1} &= \frac{S - M_1 + uM_0}{2(1+u)}\,, & \text{(A.18a)} \\ g_{v=u} &= \frac{-S - uM_1 + M_0}{1-u^2}\,, & \text{(A.18b)} \\ g_{v=+1} &= \frac{S + M_1 - uM_0}{2(1-u)}\,. & \text{(A.18c)} \end{aligned}$$

In summary, we have found that three discrete modes behave like a stable or unstable flavor pendulum, the latter being described by only two parameters, the natural frequency λ and spin S. Conversely, for a given pendulum with these parameters we can identify a two-parameter family of three-mode realizations.

A.3 EXPLICIT SOLUTION FOR CONTINUOUS SPECTRUM

If a single-crossed spectrum g_v produces a coherent pendulum-like solution, we have seen that the motion of $\boldsymbol{D}_1(t)$ can be understood as a pendulum with parameters that can be extracted from g_v without solving the EOMs. We have also seen that in this case the Bloch vectors $\boldsymbol{D}_v(t)$ are functions that one should be able to express as linear combinations of only three independent functions. We have seen in Supplement B that we can identify three functions that we now call $\boldsymbol{P}_{v_i}(t)$ that reproduce the same pendulum with $\boldsymbol{D}_1(t) = \boldsymbol{P}_1(t)$. (In the corresponding discussion for slow modes these functions were called “carrier modes” [234].) These three functions solve the EOM

$$\dot{\boldsymbol{P}}_{v_i} = \mu\, v_i \boldsymbol{P}_{v_i} \times \boldsymbol{P}_1\,. \tag{A.19}$$

We now transform the three functions to produce a continuous spectrum by virtue of

$$\bar{\boldsymbol{P}}_v = \prod_{i=1}^{3}(v_i - v) \sum_{i=1}^{3} \frac{\boldsymbol{P}_{v_i}}{v_i - v} \,. \tag{A.20}$$

The first factor was included to avoid a singularity when v equals one of the discrete velocities. These new functions fulfill the original EOM

$$\partial_t \bar{\boldsymbol{P}}_v = \mu\, v \bar{\boldsymbol{P}}_v \times \boldsymbol{P}_1 \tag{A.21}$$

as one can easily verify by inserting the definition of $\bar{\boldsymbol{P}}_v$ and using Eq. (A.19). We may further define the unit vectors

$$\boldsymbol{p}_v = \pm \frac{\bar{\boldsymbol{P}}_v}{|\bar{\boldsymbol{P}}_v|} \tag{A.22}$$

with a possible sign change such that $p_v^z|_{t=0} = 1$. Therefore, the solutions for the original modes are simply $\boldsymbol{D}_v(t) = g_v \boldsymbol{p}_v(t)$.

To summarize, if the spectrum g_v reveals, in the linear regime, an instability we can construct the nonlinear solution for $\boldsymbol{D}_1(t)$ in the form of a pendulum, obtain three modes that produce the same pendulum motion, and construct the explicit solution for $\boldsymbol{D}_v(t)$ and any other Bloch vector that follows the same EOM as $\boldsymbol{D}_v(t)$. In other words, the pendulum solution suggested by the information from the linear equations indeed fulfills the original EOMs also in the nonlinear regime.

A.4 NORMAL-MODE ANALYSIS

In the main text, we have briefly sketched the normal-mode analysis in the homogeneous case, leading to an eigenvalue equation that is very simple. However, it is also instructive to arrive at this result beginning with the inhomogeneous equations and taking the homogeneous limit in the end. The final result is the same, but it is nevertheless reassuring that there is no hidden issue of non-commuting limits. In principle, of course, this is just a step-by-step account of what can be found in the literature in various forms.

Our starting point is the two-flavor EOM, assuming axial symmetry, before taking the homogeneous limit:

$$i\,(\partial_t + v\partial_z)\mathsf{D}_v = \mu[\mathsf{D}_0, \mathsf{D}_v] - \mu[\mathsf{D}_1, v\mathsf{D}_v] \,. \tag{A.23}$$

Here $\mathsf{D}_0 = \int dv\, \mathsf{D}_v$ and $\mathsf{D}_1 = \int dv\, v\mathsf{D}_v$ and we use the notation $\int dv = \int_{-1}^{+1} dv$ as in the main text. We here keep explicitly the first term on the r.h.s. without going to a co-rotating frame because we are interested in the real part of the dispersion relation that should be carefully distinguished from the overall precession caused by this neutrino-neutrino matter term which we follow carefully.

We recall that, in terms of the Bloch vector components, the lepton-number density matrices are

$$\mathsf{D}_v = \frac{1}{2}\begin{pmatrix} D_v^z & D_v^{xy} \\ D_v^{yx} & -D_v^z \end{pmatrix} = \frac{g_v}{2}\begin{pmatrix} s_v & S_v \\ S_v^* & -s_v \end{pmatrix}, \tag{A.24}$$

where $D_v^{xy} = D_v^x + iD_v^y$ and the complex conjugate $D_v^{yx} = D_v^x - iD_v^y$. The ELN spectrum is the initial $g_v = D_v^z|_{t=0}$ and is assumed not to depend on space. In other words, we assume the initial setup to be homogeneous, but the solutions are allowed to be inhomogeneous. The diagonal and off-diagonal normalized components s_v and S_v follow our older notation and are not related to the particle-number matrices.

The linear regime consists of the off-diagonal elements being small compared with the diagonal ones, in normalized form meaning that $|S_v| \ll 1$ and the expansion is in powers of S_v. Taking the z-components at their initial value, the off-diagonal EOM is

$$\left[i\left(\partial_t + v\partial_z\right) - \left(\Lambda_0 - v\Lambda_1\right)\right] S_v = -\mu \int du\, g_u \left(S_u - vuS_u\right), \tag{A.25}$$

where $\Lambda_0 = \mu D_0$ and $\Lambda_1 = \mu D_1 = \mu D_1^z|_{t=0}$.

For a normal-mode analysis we seek plane-wave solutions of the form $S_v(t,z) = Q_v\, e^{-i(\Omega t - Kz)}$, where Q_v depends on the wave vector (Ω, K) and K is the wavevector in the z direction. The EOM in Fourier space thus is

$$[\underbrace{(\Omega - \Lambda_0)}_{\omega} - v\underbrace{(K - \Lambda_1)}_{k}]\, Q_v = -\mu \int du\, g_u \left(Q_u - vuQ_u\right). \tag{A.26}$$

In the absence of interactions ($\mu = 0$) the only solutions are $\omega = vk$, which are "under the light cone" defined by $\omega = k$, and have eigenfunctions $Q_v = \delta(\omega - vk)$. For nonzero μ, these non-collective modes continue to exist with a more complicated singular Q_v [158].

In addition, collective modes appear which either have a real $\omega > k$ or a complex ω without restrictions on k. As a function of v, the r.h.s. of Eq. (A.26) has the form $a - bv$, where a and

b are numbers that depend on the spectrum and on the solution, but not on v. Therefore, the eigenfunction is of the form

$$Q_v = \frac{a - bv}{\omega - vk}, \tag{A.27}$$

implying

$$a - bv = -\int du\, G_u \frac{a - bu - vu(a - bu)}{\omega - uk}, \tag{A.28}$$

where we have now absorbed μ in $G_v = \mu\, g_v$.

This equation must be true for all v, so we have two equations that can be written as

$$\underbrace{\begin{pmatrix} I_0 + 1 & -I_1 \\ -I_1 & I_2 - 1 \end{pmatrix}}_{\Pi} \begin{pmatrix} a \\ b \end{pmatrix} = 0. \tag{A.29}$$

Here the "moments" are

$$I_n(\omega, k) = \int du\, G_u \frac{u^n}{\omega - uk}. \tag{A.30}$$

The dispersion relation follows from

$$\det \Pi = (I_0 + 1)(I_2 - 1) - I_1^2 = 0. \tag{A.31}$$

Once we have found $\omega(k)$ we can determine the eigenfunction up to an overall factor, i.e., for a chosen a we can find b or the other way around.

There is a nontrivial relation between the moments defined in Eq. (A.30) as can be seen by the following manipulations:

$$\Lambda_0 = \int du\, G_u = \int du\, G_u \frac{\omega - uk}{\omega - uk} = \omega I_0 - k I_1 \tag{A.32}$$

and likewise

$$\Lambda_1 = \int du\, G_u\, u = \omega I_1 - k I_2. \tag{A.33}$$

Therefore, two of I_0, I_1 and I_2 can be eliminated from the determinant condition Eq. (A.31) which thus can be written in three alternative forms in terms of only one of them. One case is

$$I_0(\omega, k) = \frac{\Lambda_0(\omega + \Lambda_0) + k(k + \Lambda_1)}{\omega(\omega + \Lambda_0) - k(k + \Lambda_1)}. \tag{A.34}$$

The physically homogeneous case $K = 0$ implies that $k = -\Lambda_1$. Therefore, the determinant condition simplifies to

$$\omega I_0(\omega, -\Lambda_1) = \Lambda_0 \tag{A.35a}$$

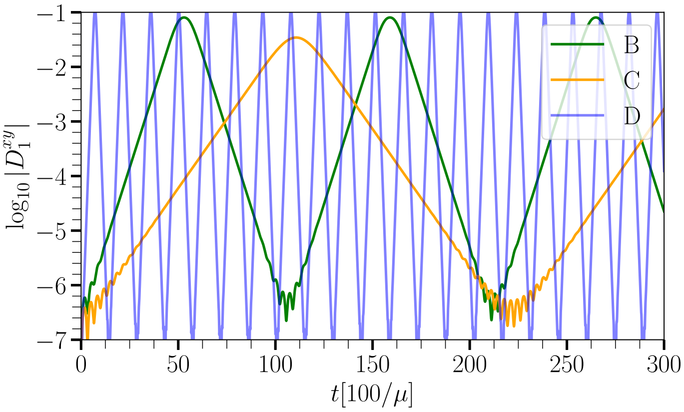

Figure 77: Same as Fig. 28, but for the evolution of the transverse components (flavor direction) of the lepton-number flux, $|D_1^{xy}| = \sqrt{(D_1^x)^2 + (D_1^y)^2}$ for the unstable cases B–D.

and with Eqs. (A.32) and (A.33) implies

$$I_1(\omega, -\Lambda_1) = 0, \tag{A.35b}$$

$$I_2(\omega, -\Lambda_1) = 1. \tag{A.35c}$$

If we insert these results in Eq. (A.29) we see that the second equation is fulfilled for any a and b, whereas the first equation requires $a = 0$. Therefore, we conclude that in the physically homogeneous case, the eigenfunction has $a = 0$ and thus is proportional to v with an arbitrary coefficient $b \neq 0$.

We thus recover the result derived in the main text where we started directly from the homogeneous EOM. In terms of physical variables, the eigenvalue is determined by $(\Omega - \Lambda_0) I_0(\Omega - \Lambda_0, -\Lambda_1) = \Lambda_0$. Here as always going to the co-moving frame in flavor space amounts to absorbing Λ_0 in $\Omega \to \omega = \Omega - \Lambda_0$ and not setting $\Lambda_0 = 0$.

A.5 FURTHER ANALYSIS OF OUR NUMERICAL EXAMPLES

The solutions for the complex eigenfrequencies for our examples A–D (see main text) are summarized in Table 3. The analytical results are in excellent agreement with the numerical ones, as was already shown in Fig. 28 in the main text. In Fig. 77, we show the evolution of the xy component that grows exponentially until the nonlinear regime is reached. The “wiggles” around the lowest

Table 3: Solutions for the complex eigenfrequencies of our benchmark ELN configurations A–D (see main text).

Case	Λ_0 $[\mu/100]$	Λ_1 $[\mu/100]$	$\omega_\pm = \omega_{\rm P} \pm i\Gamma$ $[\mu/100]$	σ	$\cos\vartheta_{\rm min}$
A	-1.2666	-4.2666	stable	—	—
B	$+0.7334$	-4.2666	$0.1828 \pm 0.1291\,i$	0.817	$+0.335$
C	$+0.7388$	-3.2728	$0.2047 \pm 0.0584\,i$	0.962	$+0.849$
D	$+4.7334$	-5.2665	$1.0743 \pm 1.1121\,i$	0.694	-0.034

points reflect the initial conditions (the small seeds) that excite all modes, but only the unstable one subsequently grows exponentially.

In order to highlight the periodic nature of the motion, we show in the upper panel of Fig. 78 a phase diagram $(\dot\vartheta, \vartheta)$ derived from our solutions $\vartheta(t)$ and $\dot\vartheta(t)$. The motions continue to trace out their respective tracks.

To illustrate the pendulum motion quantitatively, we show $\dot\vartheta^2$ as a function of ϑ in the bottom panel, once more derived from the numerical solutions $\vartheta(t)$ and $\dot\vartheta(t)$. From Eq. (5.8b) we glean that the motion is equivalent to a mass point with kinetic energy $\dot\vartheta^2$ that moves in a potential which is the negative of the r.h.s., so the numerically found $\dot\vartheta^2$ as a function of ϑ maps out the potential given on the r.h.s. of Eq. (5.8b). With the pendulum parameters shown in Table 3, the predicted curves are plotted as dashed lines, once more confirming the perfect agreement.

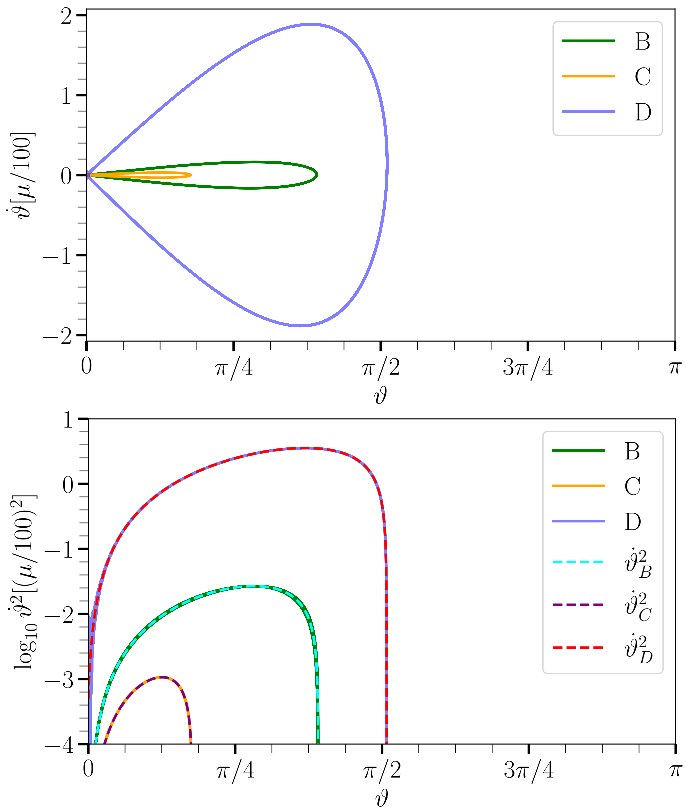

Figure 78: Parametric plots of $\dot{\vartheta}$ (top) and $\dot{\vartheta}^2$ (bottom) as functions of ϑ for our unstable examples B–D. In order to favor a comparison, the bottom panel includes the numerical results for our three unstable examples B–D (solid lines) and the analytical ones (dashed lines). The agreement between the two is excellent.

B

GYROSCOPIC PENDULUM WITH DAMPING APPENDIX

B.1 NORMAL MODE ANALYSIS IN THE PRESENCE OF DAMPING

In this appendix, we carry out the normal mode analysis in the presence of collisional damping. We start by linearizing the EOMs and tracking the evolution of the off-diagonal terms:

$$\varrho_{ex}(v) = Q(v)e^{-i\Omega t} \text{ and } \bar{\varrho}_{ex}(v) = \bar{Q}(v)e^{-i\Omega t}, \tag{B.1}$$

where Ω represents the collective oscillation frequency for neutrinos and antineutrinos. We look for temporal instabilities for the homogeneous mode ($\vec{k} = 0$). The off-diagonal component of the EOM for neutrinos and antineutrinos are

$$\begin{aligned} i\dot{\varrho}_{ex}(v) &= H_{ee}(v)\varrho_{ex}(v) - \varrho_{ee}(v)H_{ex}(v) - i\Gamma\varrho_{ex}(v)\,, & \text{(B.2)} \\ i\dot{\bar{\varrho}}_{ex}(v) &= H_{ee}(v)\bar{\varrho}_{ex}(v) - \bar{\varrho}_{ee}(v)H_{ex}(v) - i\alpha\Gamma\bar{\varrho}_{ex}(v) & \text{(B.3)} \end{aligned}$$

where we have assumed $\varrho_{xx}(t_0) = \bar{\varrho}_{xx}(t_0) = 0$. Again, here Γ is the damping rate, and α allows for a difference in the damping rates of neutrinos and antineutrinos. By substituting Eq. B.1 in the equation above and solving for $Q(v)$, we obtain

$$Q(v) = \frac{\varrho_{ee}(v)\int dv'[Q(v') - \bar{Q}(v')]\,[1 - vv']}{-\Omega - i\Gamma + A(v)}\,, \tag{B.4}$$

where we express Ω and Γ in units of μ. Also, we have defined the angle-dependent quantity $A(v)$ as

$$A(v) \equiv \int dv'[\varrho_{ee}(v') - \bar{\varrho}_{ee}(v')][1 - vv']\,. \tag{B.5}$$

A similar procedure follows for $\bar{Q}(v)$:

$$\bar{Q}(v) = \frac{\bar{\varrho}_{ee}(v)\int dv'[Q(v') - \bar{Q}(v')]\,[1 - vv']}{-\Omega - i\alpha\Gamma + A(v)}\,. \tag{B.6}$$

Combining the expressions for $Q(v)$ and $\bar{Q}(v)$, we have

$$Q(v) - \bar{Q}(v) = \int dv' \left[\frac{\varrho_{ee}(v)}{-\Omega - i\Gamma + A(v)} - \frac{\bar{\varrho}_{ee}(v)}{-\Omega - i\alpha\Gamma + A(v)} \right] [Q(v') - \bar{Q}(v')] \left[1 - vv'\right] \ . \tag{B.7}$$

From the equation above, it must be true that

$$\begin{aligned} Q(v) - \bar{Q}(v) \quad &= \quad \left[\frac{\varrho_{ee}(v)}{-\Omega - i\Gamma + A(v)} - \frac{\bar{\varrho}_{ee}(v)}{-\Omega - i\alpha\Gamma + A(v)} \right] \\ &\quad (\beta_1 - \beta_2 v) \ , \end{aligned} \tag{B.8}$$

where β_1 and β_2 are unknown coefficients.

Substituting Eq. B.8 in Eq. B.7, we obtain a system of equations for the coefficients β_1 and β_2:

$$\begin{bmatrix} \beta_1 \\ \beta_2 \end{bmatrix} = \begin{bmatrix} \mathcal{I}[1] & -\mathcal{I}[v] \\ \mathcal{I}[v] & -\mathcal{I}[v^2] \end{bmatrix} \begin{bmatrix} \beta_1 \\ \beta_2 \end{bmatrix} = \mathrm{M} \begin{bmatrix} \beta_1 \\ \beta_2 \end{bmatrix} \ , \tag{B.9}$$

where the functional $\mathcal{I}[f]$ is

$$\mathcal{I}[f] = \int dv \left[\frac{\varrho_{ee}(v)}{-\Omega - i\Gamma + A(v)} - \frac{\bar{\varrho}_{ee}(v)}{-\Omega - i\alpha\Gamma + A(v)} \right] f(v) \ . \tag{B.10}$$

The system of equations has a not trivial solution if and only if the following condition is met

$$\det(\mathrm{M} - 1_{2\times 2}) = 0 \ . \tag{B.11}$$

The latter equation is polynomial in the frequency Ω. To search for instabilities, we need to look for the solutions with $\mathrm{Im}[\Omega] \neq 0$.

If $\alpha = 1$, the functional $\mathcal{I}[f]$ simplifies to

$$\mathcal{I}[f] = \int dv \left[\frac{\varrho_{ee}(v) - \bar{\varrho}_{ee}(v)}{-\Omega - i\Gamma + A(v)} \right] f(v) \ . \tag{B.12}$$

C

COMPACT BINARY MERGER REMNANT APPENDIX

C.1 THE EVOLUTION ALGORITHM

In order to explore the flavor configuration achieved in our 2D box after a certain time Δt, we take into account neutrino advection in the EoM and aim to look for a "steady-state" flavor configuration, i.e. for a configuration where the survival probability of (anti)neutrinos has reached a constant value as a function of time except for small oscillations around that value. In this Appendix, we describe the algorithm adopted to transport the (anti)neutrino gas through the advective operator $(\vec{v} \cdot \vec{\nabla})$ in the EoM.

As sketched in Fig. 79, we evolve in time the flavor content in the different $\mathcal{S}_i$ regions in the box, individually and sequentially. We start from the one closest to the (anti)neutrino sources, $\mathcal{S}_\nu$ and $\mathcal{S}_{\bar{\nu}}$, through $\mathcal{S}_{N_y}$ at the opposite edge of the box.

In our algorithm, the time-averaged density matrices are transported from $\mathcal{S}_i$ to $\mathcal{S}_{i+1}$, if a steady-state configuration of flavor conversions has been reached, e.g. when the average values of $|\rho_{ex}|, |\bar{\rho}_{ex}|$ do not change more than a few percent ($\simeq 1\%$), as shown in Fig. 80. This procedure is repeated in our algorithm to simulate the free streaming of neutrinos and antineutrinos through the box until the last region S_{N_y} is reached.

The sequential and pixel-by-pixel time evolution of the box is well motivated by physical arguments, namely, by the fact that ν–ν interactions occur locally. A neutrino located at (x, y) can only affect its nearest-neighbouring background neutrinos at $(x \pm \delta x, y \pm \delta y)$, where $\delta x, \delta y$ are infinitesimal displacements (the length of $\delta x, \delta y$ being set by the pixel length). In addition, the fact that we only stream neutrinos from the sources towards the opposite edges of the simulation box, and do not propagate them backwards, guarantees that a steady-state configuration is always achieved throughout the box.

C.2 SPATIAL RESOLUTION

In this appendix, we discuss the convergence of our results, especially regarding the spatial resolution adopted in this work. In order to do this, we solve the EoMs in a smaller box of 8×8 km^2 (high resolution run), corresponding to the red box in Fig. 63, while maintaining the same number of grid points and all other input quantities unchanged. We follow the flavor evolution for 5×10^{-7} s by including neutrino advection at each time step. The red box has been located in one of the most unstable regions above the emitting surfaces, hence we expect that our test on the convergence of our results will provide an estimation of the largest possible error in the prediction of the flavor conversion probability.

Figure 81 shows a contour plot of the angle integrated density matrix elements, $\rho_{ee}(\vec{x}, \theta, t)$ and $\bar{\rho}_{ee}(\vec{x}, \theta, t)$, at 5×10^{-7} s for the region highlighted by the red box in Fig. 63. The top panels have been obtained by using higher spatial resolution in the 8×8 km^2 box, while the bottom panels represent the red box in Fig. 63. The overall amount of flavor conversion is comparable in the low and high resolution cases. However, due to the better spatial resolution, small scale structures develop across a small patch in the high-resolution run (see green patches in the top left panel of Fig. 81) in correspondence of the unstable regions found in the right panel of Fig. 60. It is important to notice that the occurrence of a relatively larger conversion rate in a smaller spatial region in Fig. 81 does not lead to a spread of the flavor instability to nearby spatial bins. The overall flavor conversion rate averaged over a large area is thus unaffected by the presence of small scale structures.

Figure 82 shows the time evolution of the angle-integrated ρ_{ex} for point B in the high resolution run (in red) and in the low resolution run (in green), and for point D in the high resolution run (in orange, see Fig. 82). Location D has been chosen as representative of the most unstable region in the top panels of Fig. 81. One can see that the error in predicting the amount of flavor conversions in our low resolution runs is less than 1% across the region inspected in Fig. 81 and up to 10% for the small stripe showing the largest flavor conversions. Our findings are not surprising as the angular distributions for nearby bins are very similar to each other.

Importantly, any spatial correlation between nearby spatial cells is averaged out by the advective term in the non-linear regime, as discussed in Ref. [149]. Hence, the small localized region with slightly larger flavor conversions surrounding point D, in the high resolution run in Fig. 81, does not affect our overall conclusions. We stress that the red box in Fig. 63 corresponds to the region with the largest amount of flavor conversions, hence our spatial resolution allows to obtain even more accurate results for any remaining location above the remnant disk. Given the negligible difference in the overall flavor outcome between the two runs with different spatial resolution, we choose to adopt the coarser grid throughout the paper since it allow us to explore a larger region above the remnant disk and better gauge the role of neutrinos in compact binary mergers.

Our results thus show the limitation of intuitive conclusions that can be drawn by relying on the linear stability analysis which imply a strong correlation between various spatial points. The collective nature of the flavor evolution is less manifest in the non-linear regime; this allows to perform numerical simulations over a coarser simulation grid than one may anticipate.

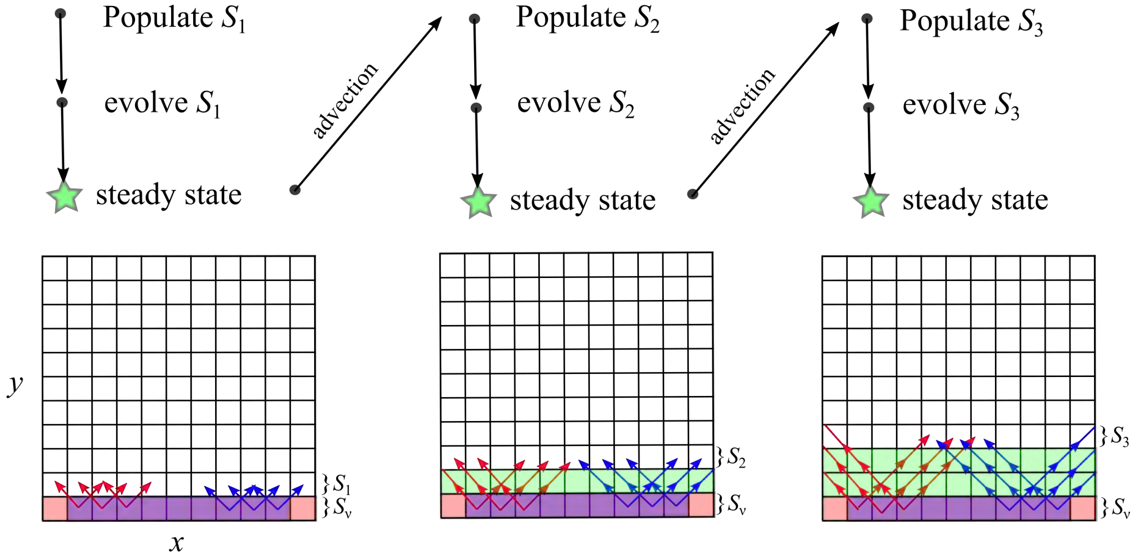

Figure 79: Schematic representation of the algorithm implemented to determine the final steady-state configuration reached in our 2D system The neutrino and antineutrino decoupling regions, $\mathcal{S}_\nu$ and $\mathcal{S}_{\bar{\nu}}$, are plotted in red and blue, respectively. The regions $\mathcal{S}_i$ $(i = 1, 2, ..., N_y)$ that reach a steady-state flavor configuration as a function of time are shown in green.

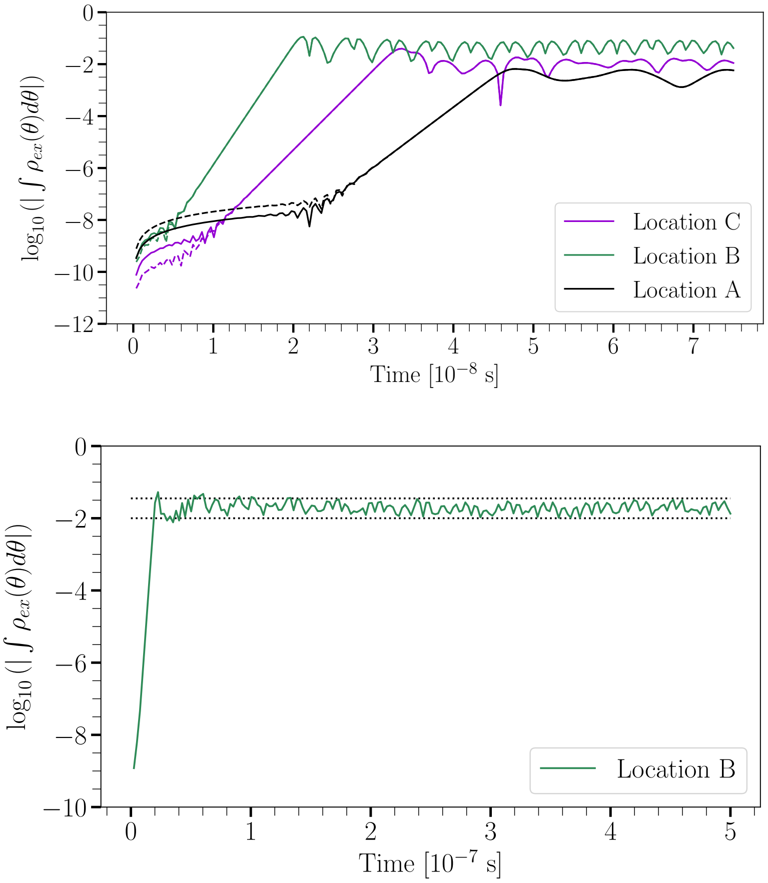

Figure 80: *Top:* Temporal evolution of $|\int \rho_{ex} d\theta|$ (solid) and $|\int \bar{\rho}_{ex} d\theta|$ (dashed) matrix elements at the locations A, B and C, see Figs. 57 and 61. The exponential growth of the off-diagonal terms, and therefore, of the flavor instabilities, develops within a few ns. At a later stage, the system becomes highly non-linear and reaches an approximate steady-state. *Bottom*: Temporal evolution of $|\int \rho_{ex} d\theta|$ (location B), but tracking its temporal evolution for almost an order of magnitude longer. The dashed lines highlight the small variation of the transition probability, which allows to compute a steady-state flavor configuration.

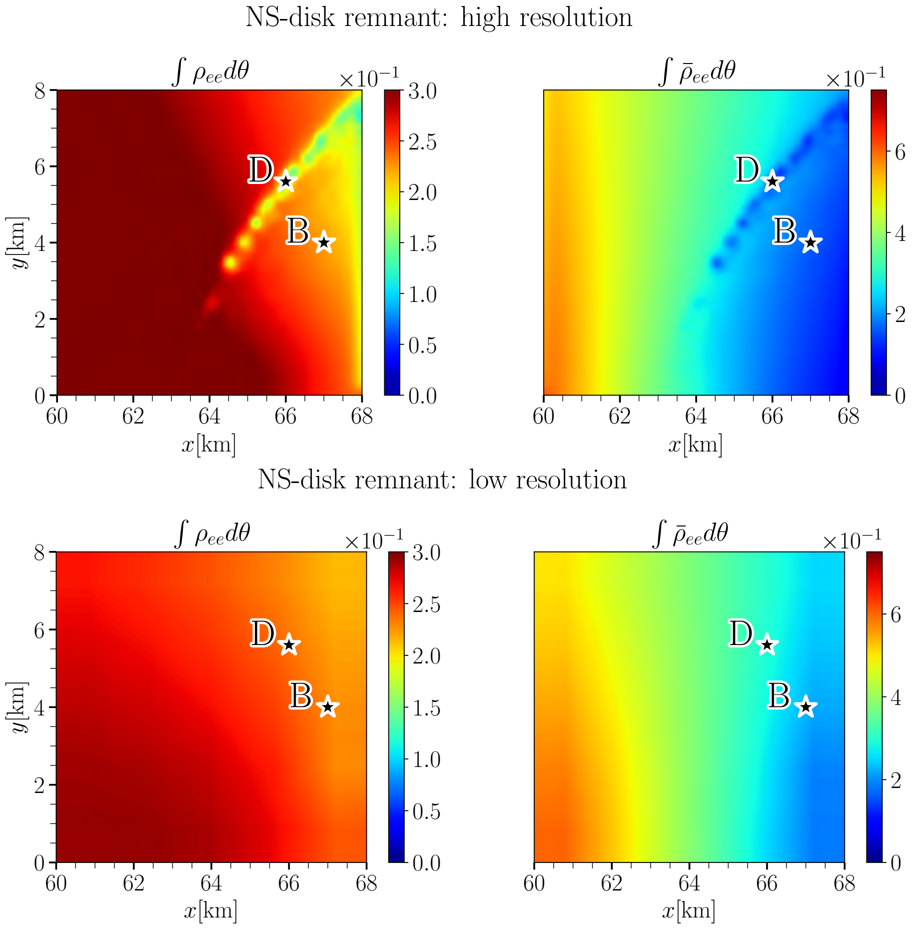

Figure 81: Analogous to Fig. 63, contour plots of the angle-integrated elements of the density matrices, $\rho_{ee}(\vec{x}, \theta, t)$ (on the left) and $\bar{\rho}_{ee}(\vec{x}, \theta, t)$ (on the right) for the NS-disk configuration. The simulation domain is defined through a 8×8 km^2 spatial grid for the top panels (high resolution run) and a 80×80 km^2 grid for the bottom panels (low resolution run, adopted throughout the paper); in both cases, the plotted region corresponds to the red box in Fig. 63. Two selected locations (B and D) are used to inspect the temporal evolution of the survival probability, see Fig. 82. The presence of small spatial structure does not affect the overall flavor evolution in the neighboring regions.

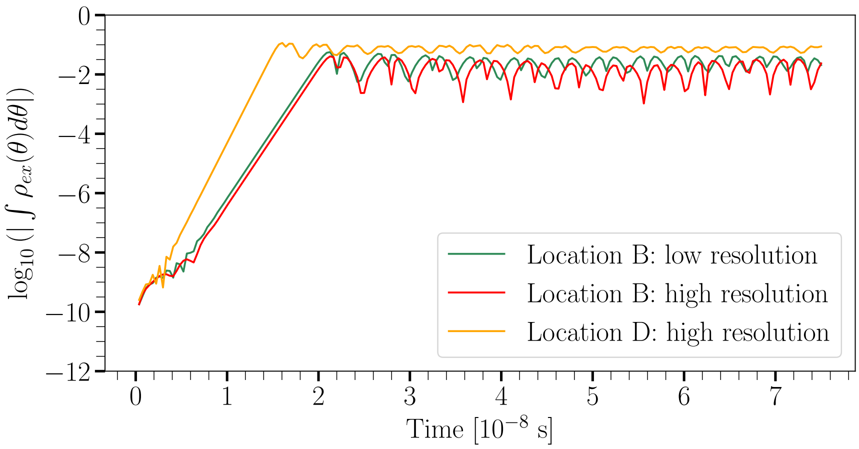

Figure 82: Same as in Fig. 80, but here we compare the temporal evolution of the angle-integrated ρ_{ex} elements of the low (80×80 km^2, green) and high (8×8 km^2, red and orange) spatial resolution grids for points B and D, see also Fig. 81. The different spatial resolution negligibly affects the steady-state flavor configuration.

BIBLIOGRAPHY

---

[1] C. L. Cowan et al. “Detection of the Free Neutrino: a Confirmation”. In: *Science* 124.3212 (1956), pp. 103–104. DOI: `10.1126/science.124.3212.103`. eprint: `https://www.science.org/doi/pdf/10.1126/science.124.3212.103`. URL: `https://www.science.org/doi/abs/10.1126/science.124.3212.103`.

[2] John Charles Street and E. C. Stevenson. “New Evidence for the Existence of a Particle of Mass Intermediate Between the Proton and Electron”. In: *Physical Review* 52 (1937), pp. 1003–1004.

[3] G. Danby et al. “Observation of High-Energy Neutrino Reactions and the Existence of Two Kinds of Neutrinos”. In: *Phys. Rev. Lett.* 9 (1 July 1962), pp. 36–44. DOI: `10.1103/PhysRevLett.9.36`. URL: `https://link.aps.org/doi/10.1103/PhysRevLett.9.36`.

[4] M. L. Perl et al. “Evidence for Anomalous Lepton Production in $e^+ - e^-$ Annihilation”. In: *Phys. Rev. Lett.* 35 (22 Dec. 1975), pp. 1489–1492. DOI: `10.1103/PhysRevLett.35.1489`. URL: `https://link.aps.org/doi/10.1103/PhysRevLett.35.1489`.

[5] K. Kodama et al. “Observation of tau neutrino interactions”. In: *Physics Letters B* 504.3 (2001), pp. 218–224. ISSN: 0370-2693. DOI: `https://doi.org/10.1016/S0370-2693(01)00307-0`. URL: `https://www.sciencedirect.com/science/article/pii/S0370269301003070`.

[6] Raymond Davis, Don S. Harmer, and Kenneth C. Hoffman. “Search for Neutrinos from the Sun”. In: *Phys. Rev. Lett.* 20 (21 May 1968), pp. 1205–1209. DOI: `10.1103/PhysRevLett.20.1205`. URL: `https://link.aps.org/doi/10.1103/PhysRevLett.20.1205`.

[7] John N. Bahcall and M. H. Pinsonneault. “Standard solar models, with and without helium diffusion and the solar neutrino problem”. In: *Rev. Mod. Phys.* 64 (1992), pp. 885–926. DOI: `10.1103/RevModPhys.64.885`.

[8] K.S. Hirata et al. “Observation of a small atmospheric v/ve ratio in Kamiokande”. In: *Physics Letters B* 280.1 (1992), pp. 146–152. ISSN: 0370-2693. DOI: https://doi.org/10.1016/0370-2693(92)90788-6. URL: https://www.sciencedirect.com/science/article/pii/0370269392907886.

[9] R. Becker-Szendy et al. “Search for muon neutrino oscillations with the Irvine-Michigan-Brookhaven detector”. In: *Phys. Rev. Lett.* 69 (7 Aug. 1992), pp. 1010–1013. DOI: 10.1103/PhysRevLett.69.1010. URL: https://link.aps.org/doi/10.1103/PhysRevLett.69.1010.

[10] D. Casper et al. “Measurement of atmospheric neutrino composition with the IMB-3 detector”. In: *Phys. Rev. Lett.* 66 (20 May 1991), pp. 2561–2564. DOI: 10.1103/PhysRevLett.66.2561. URL: https://link.aps.org/doi/10.1103/PhysRevLett.66.2561.

[11] Y. Fukuda et al. “Evidence for Oscillation of Atmospheric Neutrinos”. In: *Phys. Rev. Lett.* 81 (8 Aug. 1998), pp. 1562–1567. DOI: 10.1103/PhysRevLett.81.1562. URL: https://link.aps.org/doi/10.1103/PhysRevLett.81.1562.

[12] A. Bellerive et al. “The Sudbury Neutrino Observatory”. In: *Nuclear Physics B* 908 (2016). Neutrino Oscillations: Celebrating the Nobel Prize in Physics 2015, pp. 30–51. ISSN: 0550-3213. DOI: https://doi.org/10.1016/j.nuclphysb.2016.04.035. URL: https://www.sciencedirect.com/science/article/pii/S0550321316300736.

[13] Y. Fukuda et al. “Evidence for oscillation of atmospheric neutrinos”. In: *Phys. Rev. Lett.* 81 (1998), pp. 1562–1567. DOI: 10.1103/PhysRevLett.81.1562. arXiv: hep-ex/9807003.

[14] Y. Ashie et al. “Evidence for an oscillatory signature in atmospheric neutrino oscillation”. In: *Phys. Rev. Lett.* 93 (2004), p. 101801. DOI: 10.1103/PhysRevLett.93.101801. arXiv: hep-ex/0404034.

[15] Raymond Davis. “A review of the homestake solar neutrino experiment”. In: *Progress in Particle and Nuclear Physics* 32 (1994), pp. 13–32. ISSN: 0146-6410. DOI: https://doi.org/10.1016/0146-6410(94)90004-3. URL: https://www.sciencedirect.com/science/article/pii/0146641094900043.

[16] Q. R. Ahmad et al. "Direct evidence for neutrino flavor transformation from neutral current interactions in the Sudbury Neutrino Observatory". In: *Phys. Rev. Lett.* 89 (2002), p. 011301. DOI: 10.1103/PhysRevLett.89.011301. arXiv: nucl-ex/0204008.

[17] K. Eguchi et al. "First results from KamLAND: Evidence for reactor anti-neutrino disappearance". In: *Phys. Rev. Lett.* 90 (2003), p. 021802. DOI: 10.1103/PhysRevLett.90.021802. arXiv: hep-ex/0212021.

[18] T. Araki et al. "Measurement of neutrino oscillation with KamLAND: Evidence of spectral distortion". In: *Phys. Rev. Lett.* 94 (2005), p. 081801. DOI: 10.1103/PhysRevLett.94.081801. arXiv: hep-ex/0406035.

[19] E. Aliu et al. "Evidence for muon neutrino oscillation in an accelerator-based experiment". In: *Phys. Rev. Lett.* 94 (2005), p. 081802. DOI: 10.1103/PhysRevLett.94.081802. arXiv: hep-ex/0411038.

[20] D. G. Michael et al. "Observation of muon neutrino disappearance with the MINOS detectors and the NuMI neutrino beam". In: *Phys. Rev. Lett.* 97 (2006), p. 191801. DOI: 10.1103/PhysRevLett.97.191801. arXiv: hep-ex/0607088.

[21] Edoardo Vitagliano, Irene Tamborra, and Georg Raffelt. "Grand Unified Neutrino Spectrum at Earth: Sources and Spectral Components". In: *Rev. Mod. Phys.* 92 (2020), p. 45006. DOI: 10.1103/RevModPhys.92.045006. arXiv: 1910.11878 [astro-ph.HE].

[22] R. Abbasi et al. "IceCube high-energy starting event sample: Description and flux characterization with 7.5 years of data". In: *Phys. Rev. D* 104 (2 July 2021), p. 022002. DOI: 10.1103/PhysRevD.104.022002. URL: https://link.aps.org/doi/10.1103/PhysRevD.104.022002.

[23] M. G. Aartsen et al. "All-sky Search for Time-integrated Neutrino Emission from Astrophysical Sources with 7 yr of IceCube Data". In: *The Astrophysical Journal* 835.2 (Jan. 2017), p. 151. DOI: 10.3847/1538-4357/835/2/151. URL: https://doi.org/10.3847/1538-4357/835/2/151.

[24] M. G. Aartsen et al. “Searches for Extended and Point-like Neutrino Sources with Four Years of IceCube Data”. In: *Astrophys. J.* 796.2 (2014), p. 109. DOI: `10.1088/0004-637X/796/2/109`. arXiv: `1406.6757 [astro-ph.HE]`.

[25] K. Hirata et al. “Observation of a neutrino burst from the supernova SN1987A”. In: *Phys. Rev. Lett.* 58 (14 Apr. 1987), pp. 1490–1493. DOI: `10.1103/PhysRevLett.58.1490`. URL: `https://link.aps.org/doi/10.1103/PhysRevLett.58.1490`.

[26] R. M. Bionta et al. “Observation of a neutrino burst in coincidence with supernova 1987A in the Large Magellanic Cloud”. In: *Phys. Rev. Lett.* 58 (14 Apr. 1987), pp. 1494–1496. DOI: `10.1103/PhysRevLett.58.1494`. URL: `https://link.aps.org/doi/10.1103/PhysRevLett.58.1494`.

[27] E.N. Alexeyev et al. “Detection of the neutrino signal from SN 1987A in the LMC using the INR Baksan underground scintillation telescope”. In: *Physics Letters B* 205.2 (1988), pp. 209–214. ISSN: 0370-2693. DOI: `https://doi.org/10.1016/0370-2693(88)91651-6`. URL: `https://www.sciencedirect.com/science/article/pii/0370269388916516`.

[28] M. R. Krishnaswamy et al. “The Kolar Gold Fields Neutrino Experiment. II. Atmospheric Muons at a Depth of 7000 hg cm-2 (Kolar)”. In: *Proceedings of the Royal Society of London. Series A, Mathematical and Physical Sciences* 323.1555 (1971), pp. 511–522. ISSN: 00804630. URL: `http://www.jstor.org/stable/78071` (visited on 08/06/2022).

[29] M. G. Aartsen et al. “Multimessenger observations of a flaring blazar coincident with high-energy neutrino IceCube-170922A”. In: *Science* 361.6398 (2018), eaat1378. DOI: `10.1126/science.aat1378`. arXiv: `1807.08816 [astro-ph.HE]`.

[30] A. Franckowiak et al. “Patterns in the Multiwavelength Behavior of Candidate Neutrino Blazars”. In: *Astrophys. J.* 893.2 (2020), p. 162. DOI: `10.3847/1538-4357/ab8307`. arXiv: `2001.10232 [astro-ph.HE]`.

[31] P. Giommi et al. “3HSP J095507.9+355101: a flaring extreme blazar coincident in space and time with IceCube-200107A”. In: *Astron. Astrophys.* 640 (2020), p. L4. DOI: `10.1051/0004-6361/202038423`. arXiv: `2003.06405 [astro-ph.HE]`.

[32] S. Garrappa et al. "Investigation of two Fermi-LAT gamma-ray blazars coincident with high-energy neutrinos detected by IceCube". In: *Astrophys. J.* 880.2 (2019), 880:103. DOI: `10.3847/1538-4357/ab2ada`. arXiv: `1901.10806 [astro-ph.HE]`.

[33] M. Kadler et al. "Coincidence of a high-fluence blazar outburst with a PeV-energy neutrino event". In: *Nature Phys.* 12.8 (2016), pp. 807–814. DOI: `10.1038/NPHYS3715`. arXiv: `1602.02012 [astro-ph.HE]`.

[34] Robert Stein et al. "A tidal disruption event coincident with a high-energy neutrino". In: *Nature Astron.* 5.5 (2021), pp. 510–518. DOI: `10.1038/s41550-020-01295-8`. arXiv: `2005.05340 [astro-ph.HE]`.

[35] A. Albert et al. "Search for Neutrinos from the Tidal Disruption Events AT2019dsg and AT2019fdr with the ANTARES Telescope". In: *Astrophys. J.* 920.1 (2021), p. 50. DOI: `10.3847/1538-4357/ac16d6`. arXiv: `2103.15526 [astro-ph.HE]`.

[36] Claire Guépin et al. "Ultra-High Energy Cosmic Rays and Neutrinos from Tidal Disruptions by Massive Black Holes". In: *Astron. Astrophys.* 616 (2018). [Erratum: Astron.Astrophys. 636, C3 (2020)], A179. DOI: `10.1051/0004-6361/201732392`. arXiv: `1711.11274 [astro-ph.HE]`.

[37] Tetyana Pitik et al. "Is the High-energy Neutrino Event IceCube-200530A Associated with a Hydrogen-rich Superluminous Supernova?" In: *Astrophys. J.* 929.2 (2022), p. 163. DOI: `10.3847/1538-4357/ac5ab1`. arXiv: `2110.06944 [astro-ph.HE]`.

[38] B. P. Abbott et al. "Multi-messenger Observations of a Binary Neutron Star Merger". In: *Astrophys. J. Lett.* 848.2 (2017), p. L12. DOI: `10.3847/2041-8213/aa91c9`. arXiv: `1710.05833 [astro-ph.HE]`.

[39] M. G. Aartsen et al. "The IceCube Neutrino Observatory: Instrumentation and Online Systems". In: *JINST* 12.03 (2017), P03012. DOI: `10.1088/1748-0221/12/03/P03012`. arXiv: `1612.05093 [astro-ph.IM]`.

[40] M. Ageron et al. "ANTARES: The first undersea neutrino telescope". In: *Nuclear Instruments and Methods in Physics Research Section A: Accelerators, Spectrometers, Detectors and Associated Equipment* 656.1 (2011), pp. 11–38. ISSN: 0168-9002. DOI: `https://doi.org/10.1016/`

j.nima.2011.06.103. URL: https://www.sciencedirect.com/science/article/pii/S0168900211013994.

[41] "The Pierre Auger Cosmic Ray Observatory". In: *Nuclear Instruments and Methods in Physics Research Section A: Accelerators, Spectrometers, Detectors and Associated Equipment* 798 (2015), pp. 172–213. ISSN: 0168-9002. DOI: https://doi.org/10.1016/j.nima.2015.06.058. URL: https://www.sciencedirect.com/science/article/pii/S0168900215008086.

[42] A. Albert et al. "Search for High-energy Neutrinos from Binary Neutron Star Merger GW170817 with ANTARES, IceCube, and the Pierre Auger Observatory". In: *Astrophys. J. Lett.* 850.2 (2017), p. L35. DOI: 10.3847/2041-8213/aa9aed. arXiv: 1710.05839 [astro-ph.HE].

[43] Y. Hayato et al. "Search for Neutrinos in Super-Kamiokande Associated with the GW170817 Neutron-star Merger". In: *Astrophys. J. Lett.* 857.1 (2018), p. L4. DOI: 10.3847/2041-8213/aabaca. arXiv: 1802.04379 [astro-ph.HE].

[44] Aswathi Balagopal V. et al. "IceCube search for neutrinos coincident with gravitational wave events from LIGO/Virgo run O3". In: (Aug. 2022). arXiv: 2208.09532 [astro-ph.HE].

[45] G. G. Raffelt. *Stars as laboratories for fundamental physics: The astrophysics of neutrinos, axions, and other weakly interacting particles*. May 1996. ISBN: 978-0-226-70272-8.

[46] M. Ruffert et al. "Coalescing neutron stars: A Step towards physical models. 2. Neutrino emission, neutron tori, and gamma-ray bursts". In: *Astron. Astrophys.* 319 (1997), pp. 122–153. arXiv: astro-ph/9606181.

[47] Francois Foucart et al. "Post-merger evolution of a neutron star-black hole binary with neutrino transport". In: *Phys. Rev. D* 91.12 (2015), p. 124021. DOI: 10.1103/PhysRevD.91.124021. arXiv: 1502.04146 [astro-ph.HE].

[48] S. R. Kulkarni. "Modeling supernova-like explosions associated with gamma-ray bursts with short durations". In: (Oct. 2005). arXiv: astro-ph/0510256.

[49] B. D. Metzger et al. “Electromagnetic counterparts of compact object mergers powered by the radioactive decay of r-process nuclei”. In: 406.4 (Aug. 2010), pp. 2650–2662. DOI: `10.1111/j.1365-2966.2010.16864.x`. arXiv: `1001.5029 [astro-ph.HE]`.

[50] A. Perego et al. “Neutrino-driven winds from neutron star merger remnants”. In: *Mon. Not. Roy. Astron. Soc.* 443.4 (2014), pp. 3134–3156. DOI: `10.1093/mnras/stu1352`. arXiv: `1405.6730 [astro-ph.HE]`.

[51] Hans-Thomas Janka et al. “Theory of Core-Collapse Supernovae”. In: *Phys. Rept.* 442 (2007), pp. 38–74. DOI: `10.1016/j.physrep.2007.02.002`. arXiv: `astro-ph/0612072`.

[52] P. A. Zyla et al. “Review of Particle Physics”. In: *PTEP* 2020.8 (2020), p. 083C01. DOI: `10.1093/ptep/ptaa104`.

[53] Scott Willenbrock. “Symmetries of the standard model”. In: *Theoretical Advanced Study Institute in Elementary Particle Physics: Physics in* $D \geqq 4$. Oct. 2004, pp. 3–38. arXiv: `hep-ph/0410370`.

[54] B. Pontecorvo. “Neutrino Experiments and the Problem of Conservation of Leptonic Charge”. In: *Zh. Eksp. Teor. Fiz.* 53 (1967), pp. 1717–1725.

[55] B. Pontecorvo. “Mesonium and anti-mesonium”. In: *Sov. Phys. JETP* 6 (1957), p. 429.

[56] B. Pontecorvo. “Inverse beta processes and nonconservation of lepton charge”. In: *Zh. Eksp. Teor. Fiz.* 34 (1957), p. 247.

[57] A. Bellerive et al. “The Sudbury Neutrino Observatory”. In: *Nucl. Phys. B* 908 (2016), pp. 30–51. DOI: `10.1016/j.nuclphysb.2016.04.035`. arXiv: `1602.02469 [nucl-ex]`.

[58] Ziro Maki, Masami Nakagawa, and Shoichi Sakata. “Remarks on the Unified Model of Elementary Particles”. In: *Progress of Theoretical Physics* 28.5 (Nov. 1962), pp. 870–880.

[59] S. P. Mikheyev and A. Yu. Smirnov. “Resonance Amplification of Oscillations in Matter and Spectroscopy of Solar Neutrinos”. In: *Sov. J. Nucl. Phys.* 42 (1985). [,305(1986)], pp. 913–917.

[60] P. F. de Salas et al. “2020 global reassessment of the neutrino oscillation picture”. In: *JHEP* 02 (2021), p. 071. DOI: `10.1007/JHEP02(2021)071`. arXiv: `2006.11237 [hep-ph]`.

[61] P. F. De Salas et al. "Neutrino Mass Ordering from Oscillations and Beyond: 2018 Status and Future Prospects". In: *Front. Astron. Space Sci.* 5 (2018), p. 36. DOI: `10.3389/fspas.2018.00036`. arXiv: `1806.11051 [hep-ph]`.

[62] Stefano Gariazzo et al. "Neutrino mass and mass ordering: No conclusive evidence for normal ordering". In: (May 2022). arXiv: `2205.02195 [hep-ph]`.

[63] Blair Jamieson. "Future Neutrino Experiments". In: *20th Conference on Flavor Physics and CP Violation*. July 2022. arXiv: `2207.05044 [hep-ex]`.

[64] R. L. Workman et al. "Review of Particle Physics". In: *PTEP* 2022 (2022), p. 083C01. DOI: `10.1093/ptep/ptac097`.

[65] L. Wolfenstein. "Neutrino Oscillations in Matter". In: *Phys. Rev.* D17 (1978). [,294(1977)], pp. 2369–2374. DOI: `10.1103/PhysRevD.17.2369`.

[66] E. Fermi. "Versuch einer Theorie der β-Strahlen. I". In: *Zeitschrift fur Physik* 88.3-4 (Mar. 1934), pp. 161–177. DOI: `10.1007/BF01351864`.

[67] Fred L. Wilson. "Fermi's Theory of Beta Decay". In: *American Journal of Physics* 36.12 (1968), pp. 1150–1160. DOI: `10.1119/1.1974382`. eprint: `https://doi.org/10.1119/1.1974382`. URL: `https://doi.org/10.1119/1.1974382`.

[68] Markus Fierz. "Zur Fermischen Theorie des β-Zerfalls". In: *Zeitschrift fur Physik* 104.7-8 (July 1937), pp. 553–565. DOI: `10.1007/BF01330070`.

[69] Michael Edward Peskin and Daniel V. Schroeder. *An Introduction to Quantum Field Theory*. Reading, USA: Addison-Wesley (1995) 842 p. Westview Press, 1995.

[70] C. W. Kim and A. Pevsner. *Neutrinos in physics and astrophysics*. Vol. 8. 1993.

[71] Dirk Notzold and Georg Raffelt. "Neutrino Dispersion at Finite Temperature and Density". In: *Nucl. Phys. B* 307 (1988), pp. 924–936. DOI: `10.1016/0550-3213(88)90113-7`.

[72] Carlo Giunti and Chung W. Kim. *Fundamentals of Neutrino Physics and Astrophysics*. Oxford University Press, Mar. 2007. ISBN: 9780198508717. DOI: `10.1093/acprof:oso/9780198508717.001.0001`. URL: `https://doi.org/10.1093/acprof:oso/9780198508717.001.0001`.

[73] G. Sigl and G. G. Raffelt. "General kinetic description of relativistic mixed neutrinos". In: *Nucl. Phys. B* 406 (1993), pp. 423–451. DOI: 10.1016/0550-3213(93)90175-O.

[74] James Pantaleone. "Neutrino oscillations at high densities". In: *Physics Letters B* 287.1 (1992), pp. 128–132. ISSN: 0370-2693. DOI: https://doi.org/10.1016/0370-2693(92)91887-F. URL: https://www.sciencedirect.com/science/article/pii/037026939291887F.

[75] L. Stodolsky. "Treatment of neutrino oscillations in a thermal environment". In: *Phys. Rev. D* 36 (8 Oct. 1987), pp. 2273–2277. DOI: 10.1103/PhysRevD.36.2273. URL: https://link.aps.org/doi/10.1103/PhysRevD.36.2273.

[76] R. A. Harris and Leo Stodolsky. "Two State Systems in Media and 'Turing's Paradox'". In: *Phys. Lett. B* 116 (1982), pp. 464–468. DOI: 10.1016/0370-2693(82)90169-1.

[77] H. Nunokawa et al. "Supernova bounds on resonant active sterile neutrino conversions". In: *Phys. Rev. D* 56 (1997), pp. 1704–1713. DOI: 10.1103/PhysRevD.56.1704. arXiv: hep-ph/9702372.

[78] Charles J. Stapleford et al. "Nonstandard Neutrino Interactions in Supernovae". In: *Phys. Rev. D* 94.9 (2016), p. 093007. DOI: 10.1103/PhysRevD.94.093007. arXiv: 1605.04903 [hep-ph].

[79] Yvonne Y. Y. Wong. "Analytical treatment of neutrino asymmetry equilibration from flavor oscillations in the early universe". In: *Phys. Rev. D* 66 (2002), p. 025015. DOI: 10.1103/PhysRevD.66.025015. arXiv: hep-ph/0203180.

[80] A. D. Dolgov et al. "Cosmological bounds on neutrino degeneracy improved by flavor oscillations". In: *Nucl. Phys. B* 632 (2002), pp. 363–382. DOI: 10.1016/S0550-3213(02)00274-2. arXiv: hep-ph/0201287.

[81] Lucas Johns et al. "Neutrino flavor transformation in the lepton-asymmetric universe". In: *Phys. Rev. D* 94.8 (2016), p. 083505. DOI: 10.1103/PhysRevD.94.083505. arXiv: 1608.01336 [hep-ph].

[82] Huaiyu Duan, George M. Fuller, and Yong-Zhong Qian. “Collective Neutrino Oscillations”. In: *Ann. Rev. Nucl. Part. Sci.* 60 (2010), pp. 569–594. DOI: `10.1146/annurev.nucl.012809.104524`. arXiv: `1001.2799 [hep-ph]`.

[83] Huaiyu Duan, George M. Fuller, and Yong-Zhong Qian. “Collective neutrino flavor transformation in supernovae”. In: *Phys. Rev.* D74 (2006), p. 123004. DOI: `10.1103/PhysRevD.74.123004`. arXiv: `astro-ph/0511275 [astro-ph]`.

[84] C. W. Kim, Jewan Kim, and W. K. Sze. “Geometrical representation of neutrino oscillations in vacuum and matter”. In: *Phys. Rev. D* 37 (4 Feb. 1988), pp. 1072–1075. DOI: `10.1103/PhysRevD.37.1072`. URL: `https://link.aps.org/doi/10.1103/PhysRevD.37.1072`.

[85] James Pantaleone. “Dirac neutrinos in dense matter”. In: *Phys. Rev. D* 46 (2 July 1992), pp. 510–523. DOI: `10.1103/PhysRevD.46.510`. URL: `https://link.aps.org/doi/10.1103/PhysRevD.46.510`.

[86] Christian Y. Cardall. “Liouville equations for neutrino distribution matrices”. In: *Phys. Rev. D* 78 (2008), p. 085017. DOI: `10.1103/PhysRevD.78.085017`. arXiv: `0712.1188 [astro-ph]`.

[87] Irene Tamborra and Shashank Shalgar. “New Developments in Flavor Evolution of a Dense Neutrino Gas”. In: *Ann. Rev. Nucl. Part. Sci.* 71 (2021), pp. 165–188. DOI: `10.1146/annurev-nucl-102920-050505`. arXiv: `2011.01948 [astro-ph.HE]`.

[88] Alessandro Mirizzi et al. “Supernova Neutrinos: Production, Oscillations and Detection”. In: *Riv. Nuovo Cim.* 39.1-2 (2016), pp. 1–112. DOI: `10.1393/ncr/i2016-10120-8`. arXiv: `1508.00785 [astro-ph.HE]`.

[89] Huaiyu Duan et al. “Simulation of Coherent Non-Linear Neutrino Flavor Transformation in the Supernova Environment. 1. Correlated Neutrino Trajectories”. In: *Phys. Rev.* D74 (2006), p. 105014. DOI: `10.1103/PhysRevD.74.105014`. arXiv: `astro-ph/0606616 [astro-ph]`.

[90] Gianluigi L. Fogli et al. "Collective neutrino flavor transitions in supernovae and the role of trajectory averaging". In: *JCAP* 0712 (2007), p. 010. DOI: `10.1088/1475-7516/2007/12/010`. arXiv: `0707.1998 [hep-ph]`.

[91] Huaiyu Duan et al. "Coherent Development of Neutrino Flavor in the Supernova Environment". In: *Phys. Rev. Lett.* 97 (2006), p. 241101. DOI: `10.1103/PhysRevLett.97.241101`. arXiv: `astro-ph/0608050 [astro-ph]`.

[92] Steen Hannestad et al. "Self-induced conversion in dense neutrino gases: Pendulum in flavour space". In: *Phys. Rev.* D74 (2006). [Erratum: Phys. Rev.D76,029901(2007)], p. 105010. DOI: `10.1103/PhysRevD.74.105010, 10.1103/PhysRevD.76.029901`. arXiv: `astro-ph/0608695 [astro-ph]`.

[93] Huaiyu Duan et al. "Analysis of collective neutrino flavor transformation in supernovae". In: *Phys. Rev. D* 75 (2007), p. 125005. DOI: `10.1103/PhysRevD.75.125005`. arXiv: `astro-ph/0703776`.

[94] Alessandro Mirizzi and Ricard Tomas. "Multi-angle effects in self-induced oscillations for different supernova neutrino fluxes". In: *Phys. Rev. D* 84 (2011), p. 033013. DOI: `10.1103/PhysRevD.84.033013`. arXiv: `1012.1339 [hep-ph]`.

[95] John F. Cherry et al. "Multi-Angle Simulation of Flavor Evolution in the Neutrino Neutronization Burst From an O-Ne-Mg Core-Collapse Supernova". In: *Phys. Rev. D* 82 (2010), p. 085025. DOI: `10.1103/PhysRevD.82.085025`. arXiv: `1006.2175 [astro-ph.HE]`.

[96] Alessandro Mirizzi and Pasquale D. Serpico. "Instability in the Dense Supernova Neutrino Gas with Flavor-Dependent Angular Distributions". In: *Phys. Rev. Lett.* 108 (2012), p. 231102. DOI: `10.1103/PhysRevLett.108.231102`. arXiv: `1110.0022 [hep-ph]`.

[97] Alessandro Mirizzi and Pasquale Dario Serpico. "Flavor Stability Analysis of Dense Supernova Neutrinos with Flavor-Dependent Angular Distributions". In: *Phys. Rev. D* 86 (2012), p. 085010. DOI: `10.1103/PhysRevD.86.085010`. arXiv: `1208.0157 [hep-ph]`.

[98] Basudeb Dasgupta and Amol Dighe. "Collective three-flavor oscillations of supernova neutrinos". In: *Phys. Rev. D* 77 (2008), p. 113002. DOI: `10.1103/PhysRevD.77.113002`. arXiv: `0712.3798 [hep-ph]`.

[99] Huaiyu Duan, George M. Fuller, and Yong-Zhong Qian. “Stepwise spectral swapping with three neutrino flavors”. In: *Phys. Rev. D* 77 (2008), p. 085016. DOI: `10.1103/PhysRevD.77.085016`. arXiv: `0801.1363 [hep-ph]`.

[100] Gianluigi Fogli et al. “Supernova neutrino three-flavor evolution with dominant collective effects”. In: *JCAP* 04 (2009), p. 030. DOI: `10.1088/1475-7516/2009/04/030`. arXiv: `0812.3031 [hep-ph]`.

[101] Basudeb Dasgupta, Georg G. Raffelt, and Irene Tamborra. “Triggering collective oscillations by three-flavor effects”. In: *Phys. Rev. D* 81 (2010), p. 073004. DOI: `10.1103/PhysRevD.81.073004`. arXiv: `1001.5396 [hep-ph]`.

[102] Alexander Friedland. “Self-refraction of supernova neutrinos: mixed spectra and three-flavor instabilities”. In: *Phys. Rev. Lett.* 104 (2010), p. 191102. DOI: `10.1103/PhysRevLett.104.191102`. arXiv: `1001.0996 [hep-ph]`.

[103] Basudeb Dasgupta et al. “Neutrino mass hierarchy and three-flavor spectral splits of supernova neutrinos”. In: *Phys. Rev. D* 81 (2010), p. 093008. DOI: `10.1103/PhysRevD.81.093008`. arXiv: `1002.2943 [hep-ph]`.

[104] Georg G. Raffelt, Srdjan Sarikas, and David de Sousa Seixas. “Axial Symmetry Breaking in Self-Induced Flavor Conversion of Supernova Neutrino Fluxes”. In: *Phys. Rev. Lett.* 111.9 (2013). [Erratum: Phys. Rev. Lett.113,no.23,239903(2014)], p. 091101. DOI: `10.1103/PhysRevLett.113.239903, 10.1103/PhysRevLett.111.091101`. arXiv: `1305.7140 [hep-ph]`.

[105] Georg Raffelt and David de Sousa Seixas. “Neutrino flavor pendulum in both mass hierarchies”. In: *Phys. Rev. D* 88 (2013), p. 045031. DOI: `10.1103/PhysRevD.88.045031`. arXiv: `1307.7625 [hep-ph]`.

[106] Huaiyu Duan. “Flavor Oscillation Modes In Dense Neutrino Media”. In: *Phys. Rev. D* 88 (2013), p. 125008. DOI: `10.1103/PhysRevD.88.125008`. arXiv: `1309.7377 [hep-ph]`.

[107] Alessandro Mirizzi. “Multi-azimuthal-angle effects in self-induced supernova neutrino flavor conversions without axial symmetry”. In: *Phys. Rev. D* 88.7 (2013), p. 073004. DOI: `10.1103/PhysRevD.88.073004`. arXiv: `1308.1402 [hep-ph]`.

[108] Sovan Chakraborty and Alessandro Mirizzi. "Multi-azimuthal-angle instability for different supernova neutrino fluxes". In: *Phys. Rev. D* 90.3 (2014), p. 033004. DOI: `10.1103/PhysRevD.90.033004`. arXiv: `1308.5255 [hep-ph]`.

[109] Gianpiero Mangano, Alessandro Mirizzi, and Ninetta Saviano. "Damping the neutrino flavor pendulum by breaking homogeneity". In: *Phys. Rev. D* 89.7 (2014), p. 073017. DOI: `10.1103/PhysRevD.89.073017`. arXiv: `1403.1892 [hep-ph]`.

[110] Huaiyu Duan and Shashank Shalgar. "Flavor instabilities in the neutrino line model". In: *Phys. Lett.* B747 (2015), pp. 139–143. DOI: `10.1016/j.physletb.2015.05.057`. arXiv: `1412.7097 [hep-ph]`.

[111] Alessandro Mirizzi, Gianpiero Mangano, and Ninetta Saviano. "Self-induced flavor instabilities of a dense neutrino stream in a two-dimensional model". In: *Phys. Rev. D* 92.2 (2015), p. 021702. DOI: `10.1103/PhysRevD.92.021702`. arXiv: `1503.03485 [hep-ph]`.

[112] Alessandro Mirizzi. "Breaking the symmetries in self-induced flavor conversions of neutrino beams from a ring". In: *Phys. Rev. D* 92.10 (2015), p. 105020. DOI: `10.1103/PhysRevD.92.105020`. arXiv: `1506.06805 [hep-ph]`.

[113] Huaiyu Duan. "Collective neutrino oscillations and spontaneous symmetry breaking". In: *Int. J. Mod. Phys. E* 24.09 (2015), p. 1541008. DOI: `10.1142/S0218301315410086`. arXiv: `1506.08629 [hep-ph]`.

[114] Sajad Abbar and Huaiyu Duan. "Neutrino flavor instabilities in a time-dependent supernova model". In: *Phys. Lett. B* 751 (2015), pp. 43–47. DOI: `10.1016/j.physletb.2015.10.019`. arXiv: `1509.01538 [astro-ph.HE]`.

[115] Sovan Chakraborty et al. "Self-induced flavor conversion of supernova neutrinos on small scales". In: *JCAP* 01 (2016), p. 028. DOI: `10.1088/1475-7516/2016/01/028`. arXiv: `1507.07569 [hep-ph]`.

[116] Basudeb Dasgupta and Alessandro Mirizzi. "Temporal Instability Enables Neutrino Flavor Conversions Deep Inside Supernovae". In: *Phys. Rev. D* 92.12 (2015), p. 125030. DOI: `10.1103/PhysRevD.92.125030`. arXiv: `1509.03171 [hep-ph]`.

[117] Francesco Capozzi, Basudeb Dasgupta, and Alessandro Mirizzi. “Self-induced temporal instability from a neutrino antenna”. In: *JCAP* 04 (2016), p. 043. DOI: `10.1088/1475-7516/2016/04/043`. arXiv: `1603.03288 [hep-ph]`.

[118] Sovan Chakraborty et al. “No collective neutrino flavor conversions during the supernova accretion phase”. In: *Phys. Rev. Lett.* 107 (2011), p. 151101. DOI: `10.1103/PhysRevLett.107.151101`. arXiv: `1104.4031 [hep-ph]`.

[119] Sovan Chakraborty et al. “Analysis of matter suppression in collective neutrino oscillations during the supernova accretion phase”. In: *Phys. Rev. D* 84 (2011), p. 025002. DOI: `10.1103/PhysRevD.84.025002`. arXiv: `1105.1130 [hep-ph]`.

[120] Basudeb Dasgupta, Evan P. O’Connor, and Christian D. Ott. “The Role of Collective Neutrino Flavor Oscillations in Core-Collapse Supernova Shock Revival”. In: *Phys. Rev. D* 85 (2012), p. 065008. DOI: `10.1103/PhysRevD.85.065008`. arXiv: `1106.1167 [astro-ph.SR]`.

[121] Srdjan Sarikas et al. “Suppression of Self-Induced Flavor Conversion in the Supernova Accretion Phase”. In: *Phys. Rev. Lett.* 108 (2012), p. 061101. DOI: `10.1103/PhysRevLett.108.061101`. arXiv: `1109.3601 [astro-ph.SR]`.

[122] Ninetta Saviano et al. “Stability analysis of collective neutrino oscillations in the supernova accretion phase with realistic energy and angle distributions”. In: *Phys. Rev. D* 85 (2012), p. 113002. DOI: `10.1103/PhysRevD.85.113002`. arXiv: `1203.1484 [hep-ph]`.

[123] Sovan Chakraborty et al. “Suppression of the multi-azimuthal-angle instability in dense neutrino gas during supernova accretion phase”. In: *Phys. Rev. D* 89.9 (2014), p. 093001. DOI: `10.1103/PhysRevD.89.093001`. arXiv: `1402.1767 [hep-ph]`.

[124] Francesco Capozzi and Ninetta Saviano. “Neutrino Flavor Conversions in High-Density Astrophysical and Cosmological Environments”. In: *Universe* 8.2 (2022), p. 94. DOI: `10.3390/universe8020094`. arXiv: `2202.02494 [hep-ph]`.

[125] V. Alan Kostelecky and Stuart Samuel. “Selfmaintained coherent oscillations in dense neutrino gases”. In: *Phys. Rev. D* 52 (1995), pp. 621–627. DOI: `10.1103/PhysRevD.52.621`. arXiv: `hep-ph/9506262`.

[126] Stuart Samuel. “Bimodal coherence in dense selfinteracting neutrino gases”. In: *Phys. Rev. D* 53 (1996), pp. 5382–5393. DOI: 10.1103/PhysRevD.53.5382. arXiv: hep-ph/9604341.

[127] Georg G. Raffelt and Alexei Yu. Smirnov. “Adiabaticity and spectral splits in collective neutrino transformations”. In: *Phys. Rev. D* 76 (2007), p. 125008. DOI: 10.1103/PhysRevD.76.125008. arXiv: 0709.4641 [hep-ph].

[128] R. F. Sawyer. “Speed-up of neutrino transformations in a supernova environment”. In: *Phys. Rev. D* 72 (2005), p. 045003. DOI: 10.1103/PhysRevD.72.045003. arXiv: hep-ph/0503013.

[129] R. F. Sawyer. “The multi-angle instability in dense neutrino systems”. In: *Phys. Rev. D* 79 (2009), p. 105003. DOI: 10.1103/PhysRevD.79.105003. arXiv: 0803.4319 [astro-ph].

[130] R. F. Sawyer. “Neutrino cloud instabilities just above the neutrino sphere of a supernova”. In: *Phys. Rev. Lett.* 116.8 (2016), p. 081101. DOI: 10.1103/PhysRevLett.116.081101. arXiv: 1509.03323 [astro-ph.HE].

[131] A. Esteban-Pretel et al. “Role of dense matter in collective supernova neutrino transformations”. In: *Phys. Rev. D* 78 (2008), p. 085012. DOI: 10.1103/PhysRevD.78.085012. arXiv: 0807.0659 [astro-ph].

[132] Sovan Chakraborty et al. “Collective neutrino flavor conversion: Recent developments”. In: *Nucl. Phys.* B908 (2016), pp. 366–381. DOI: 10.1016/j.nuclphysb.2016.02.012. arXiv: 1602.02766 [hep-ph].

[133] Ignacio Izaguirre, Georg G. Raffelt, and Irene Tamborra. “Fast Pairwise Conversion of Supernova Neutrinos: A Dispersion-Relation Approach”. In: *Phys. Rev. Lett.* 118.2 (2017), p. 021101. DOI: 10.1103/PhysRevLett.118.021101. arXiv: 1610.01612 [hep-ph].

[134] Sajad Abbar and Huaiyu Duan. “Fast neutrino flavor conversion: roles of dense matter and spectrum crossing”. In: *Phys. Rev. D* 98.4 (2018), p. 043014. DOI: 10.1103/PhysRevD.98.043014. arXiv: 1712.07013 [hep-ph].

[135] Arka Banerjee, Amol Dighe, and Georg Raffelt. “Linearized flavor-stability analysis of dense neutrino streams”. In: *Phys. Rev. D* 84 (2011), p. 053013. DOI: 10.1103/PhysRevD.84.053013. arXiv: 1107.2308 [hep-ph].

[136] Hans-Thomas Janka. "Explosion Mechanisms of Core-Collapse Supernovae". In: *Ann. Rev. Nucl. Part. Sci.* 62 (2012), pp. 407–451. DOI: 10.1146/annurev-nucl-102711-094901. arXiv: 1206.2503 [astro-ph.SR].

[137] R. Bollig et al. "Muon Creation in Supernova Matter Facilitates Neutrino-driven Explosions". In: *Phys. Rev. Lett.* 119.24 (2017), p. 242702. DOI: 10.1103/PhysRevLett.119.242702. arXiv: 1706.04630 [astro-ph.HE].

[138] T. Fischer et al. "Neutrino spectra evolution during protoneutron star deleptonization". In: 85.8, 083003 (Apr. 2012), p. 083003. DOI: 10.1103/PhysRevD.85.083003. arXiv: 1112.3842 [astro-ph.HE].

[139] Adam Burrows, John Hayes, and Bruce A. Fryxell. "On the nature of core collapse supernova explosions". In: *Astrophys. J.* 450 (1995), p. 830. DOI: 10.1086/176188. arXiv: astro-ph/9506061.

[140] H. -T. Janka and E. Mueller. "Neutrino heating, convection, and the mechanism of Type-II supernova explosions." In: 306 (Feb. 1996), p. 167.

[141] John M. Blondin, Anthony Mezzacappa, and Christine DeMarino. "Stability of standing accretion shocks, with an eye toward core collapse supernovae". In: *Astrophys. J.* 584 (2003), pp. 971–980. DOI: 10.1086/345812. arXiv: astro-ph/0210634.

[142] Irene Tamborra et al. "SELF-SUSTAINED ASYMMETRY OF LEPTON-NUMBER EMISSION: A NEW PHENOMENON DURING THE SUPERNOVA SHOCK-ACCRETION PHASE IN THREE DIMENSIONS". In: *The Astrophysical Journal* 792.2 (Aug. 2014), p. 96. DOI: 10.1088/0004-637x/792/2/96. URL: https://doi.org/10.1088/0004-637x/792/2/96.

[143] G. M. Fuller and W. C. Haxton. "Neutrinos in Stellar Astrophysics". In: (Aug. 2022). arXiv: 2208.08050 [nucl-th].

[144] H. -Thomas Janka, Tobias Melson, and Alexander Summa. "Physics of Core-Collapse Supernovae in Three Dimensions: a Sneak Preview". In: *Ann. Rev. Nucl. Part. Sci.* 66 (2016), pp. 341–375. DOI: 10.1146/annurev-nucl-102115-044747. arXiv: 1602.05576 [astro-ph.SR].

[145] Sherwood Richers and Manibrata Sen. “Fast Flavor Transformations”. In: (July 2022). arXiv: `2207.03561 [astro-ph.HE]`.

[146] Irene Tamborra et al. “Flavor-dependent neutrino angular distribution in core-collapse supernovae”. In: *Astrophys. J.* 839 (2017), p. 132. DOI: `10.3847/1538-4357/aa6a18`. arXiv: `1702.00060 [astro-ph.HE]`.

[147] Shashank Shalgar and Irene Tamborra. “Dispelling a myth on dense neutrino media: fast pairwise conversions depend on energy”. In: *JCAP in press* (). arXiv: `2007.07926 [astro-ph.HE]`.

[148] Shashank Shalgar and Irene Tamborra. “Three flavor revolution in fast pairwise neutrino conversion”. In: *Phys. Rev. D* 104.2 (2021), p. 023011. DOI: `10.1103/PhysRevD.104.023011`. arXiv: `2103.12743 [hep-ph]`.

[149] Shashank Shalgar, Ian Padilla-Gay, and Irene Tamborra. “Neutrino propagation hinders fast pairwise flavor conversions”. In: *JCAP* 06 (2020), p. 048. DOI: `10.1088/1475-7516/2020/06/048`. arXiv: `1911.09110 [astro-ph.HE]`.

[150] Shashank Shalgar and Irene Tamborra. “A change of direction in pairwise neutrino conversion physics: The effect of collisions”. In: *Phys. Rev. D* 103 (2021), p. 063002. DOI: `10.1103/PhysRevD.103.063002`. arXiv: `2011.00004 [astro-ph.HE]`.

[151] Lucas Johns. “Collisional flavor instabilities of supernova neutrinos”. In: (Apr. 2021). arXiv: `2104.11369 [hep-ph]`.

[152] Joshua D. Martin et al. “Fast flavor oscillations in dense neutrino media with collisions”. In: *Phys. Rev. D* 103 (2021), p. 063001. DOI: `10.1103/PhysRevD.103.063001`. arXiv: `2101.01278 [hep-ph]`.

[153] Francesco Capozzi et al. “Collisional triggering of fast flavor conversions of supernova neutrinos”. In: *Phys. Rev. Lett.* 122.9 (2019), p. 091101. DOI: `10.1103/PhysRevLett.122.091101`. arXiv: `1808.06618 [hep-ph]`.

[154] G. G. Raffelt and G. Sigl. “Self-induced decoherence in dense neutrino gases”. In: *Phys. Rev. D* 75 (2007), p. 083002. DOI: `10.1103/PhysRevD.75.083002`. arXiv: `hep-ph/0701182`.

[155] Lucas Johns et al. "Neutrino oscillations in supernovae: angular moments and fast instabilities". In: *Phys. Rev.* D101.4 (2020), p. 043009. DOI: `10.1103/PhysRevD.101.043009`. arXiv: `1910.05682 [hep-ph]`.

[156] Lucas Johns et al. "Fast oscillations, collisionless relaxation, and spurious evolution of supernova neutrino flavor". In: *Phys. Rev. D* 102.10 (2020), p. 103017. DOI: `10.1103/PhysRevD.102.103017`. arXiv: `2009.09024 [hep-ph]`.

[157] Sagar Airen et al. "Normal-mode analysis for collective neutrino oscillations". In: *JCAP* 12 (2018), p. 019. DOI: `10.1088/1475-7516/2018/12/019`. arXiv: `1809.09137 [hep-ph]`.

[158] Francesco Capozzi, Georg Raffelt, and Tobias Stirner. "Fast Neutrino Flavor Conversion: Collective Motion vs. Decoherence". In: *JCAP* 09 (2019), p. 002. DOI: `10.1088/1475-7516/2019/09/002`. arXiv: `1906.08794 [hep-ph]`.

[159] Madhurima Chakraborty and Sovan Chakraborty. "Three flavor neutrino conversions in supernovae: slow \& fast instabilities". In: *JCAP* 01 (2020), p. 005. DOI: `10.1088/1475-7516/2020/01/005`. arXiv: `1909.10420 [hep-ph]`.

[160] Francesco Capozzi et al. "Fast flavor conversions of supernova neutrinos: Classifying instabilities via dispersion relations". In: *Phys. Rev.* D96.4 (2017), p. 043016. DOI: `10.1103/PhysRevD.96.043016`. arXiv: `1706.03360 [hep-ph]`.

[161] Changhao Yi et al. "Dispersion relation of the fast neutrino oscillation wave". In: *Phys. Rev.* D99.6 (2019), p. 063005. DOI: `10.1103/PhysRevD.99.063005`. arXiv: `1901.01546 [hep-ph]`.

[162] Hiroki Nagakura et al. "Where, when, and why: Occurrence of fast-pairwise collective neutrino oscillation in three-dimensional core-collapse supernova models". In: *Phys. Rev. D* 104.8 (2021), p. 083025. DOI: `10.1103/PhysRevD.104.083025`. arXiv: `2108.07281 [astro-ph.HE]`.

[163] Basudeb Dasgupta and Manibrata Sen. "Fast Neutrino Flavor Conversion as Oscillations in a Quartic Potential". In: *Phys. Rev. D* 97.2 (2018), p. 023017. DOI: `10.1103/PhysRevD.97.023017`. arXiv: `1709.08671 [hep-ph]`.

[164] Ian Padilla-Gay, Irene Tamborra, and Georg G. Raffelt. “Neutrino Flavor Pendulum Reloaded: The Case of Fast Pairwise Conversion”. In: *Phys. Rev. Lett.* 128.12 (2022), p. 121102. DOI: `10.1103/PhysRevLett.128.121102`. arXiv: `2109.14627 [astro-ph.HE]`.

[165] Milad Delfan Azari et al. “Linear Analysis of Fast-Pairwise Collective Neutrino Oscillations in Core-Collapse Supernovae based on the Results of Boltzmann Simulations”. In: *Phys. Rev. D* 99.10 (2019), p. 103011. DOI: `10.1103/PhysRevD.99.103011`. arXiv: `1902.07467 [astro-ph.HE]`.

[166] Basudeb Dasgupta, Alessandro Mirizzi, and Manibrata Sen. “Simple method of diagnosing fast flavor conversions of supernova neutrinos”. In: *Phys. Rev. D* 98.10 (2018), p. 103001. DOI: `10.1103/PhysRevD.98.103001`. arXiv: `1807.03322 [hep-ph]`.

[167] Sajad Abbar. “Searching for Fast Neutrino Flavor Conversion Modes in Core-collapse Supernova Simulations”. In: *JCAP* 05 (2020), p. 027. DOI: `10.1088/1475-7516/2020/05/027`. arXiv: `2003.00969 [astro-ph.HE]`.

[168] Hiroki Nagakura and Lucas Johns. “Constructing angular distributions of neutrinos in core-collapse supernovae from zeroth and first moments calibrated by full Boltzmann neutrino transport”. In: *Phys. Rev. D* 103.12 (2021), p. 123025. DOI: `10.1103/PhysRevD.103.123025`. arXiv: `2104.05729 [astro-ph.HE]`.

[169] Hiroki Nagakura and Lucas Johns. “New method for detecting fast neutrino flavor conversions in core-collapse supernova models with two-moment neutrino transport”. In: *Phys. Rev. D* 104.6 (2021), p. 063014. DOI: `10.1103/PhysRevD.104.063014`. arXiv: `2106.02650 [astro-ph.HE]`.

[170] Milad Delfan Azari et al. “Fast collective neutrino oscillations inside the neutrino sphere in core-collapse supernovae”. In: *Phys. Rev.* D101.2 (2020), p. 023018. DOI: `10.1103/PhysRevD.101.023018`. arXiv: `1910.06176 [astro-ph.HE]`.

[171] Sajad Abbar et al. “Fast Neutrino Flavor Conversion Modes in Multidimensional Core-collapse Supernova Models: the Role of the Asymmetric Neutrino Distributions”. In: *Phys. Rev.* D101.4 (2020), p. 043016. DOI: `10.1103/PhysRevD.101.043016`. arXiv: `1911.01983 [astro-ph.HE]`.

[172] Robert Glas et al. “Fast Neutrino Flavor Instability in the Neutron-star Convection Layer of Three-dimensional Supernova Models”. In: *Phys. Rev. D* 101.6 (2020), p. 063001. DOI: `10.1103/PhysRevD.101.063001`. arXiv: `1912.00274 [astro-ph.HE]`.

[173] Sajad Abbar et al. “On the occurrence of fast neutrino flavor conversions in multidimensional supernova models”. In: *Phys. Rev. D* 100.4 (2019), p. 043004. DOI: `10.1103/PhysRevD.100.043004`. arXiv: `1812.06883 [astro-ph.HE]`.

[174] Hiroki Nagakura et al. “Fast-pairwise collective neutrino oscillations associated with asymmetric neutrino emissions in core-collapse supernova”. In: (Oct. 2019). DOI: `10.3847/1538-4357/ab4cf2`. arXiv: `1910.04288 [astro-ph.HE]`.

[175] Taiki Morinaga et al. “Fast neutrino-flavor conversion in the preshock region of core-collapse supernovae”. In: *Phys. Rev. Res.* 2.1 (2020), p. 012046. DOI: `10.1103/PhysRevResearch.2.012046`. arXiv: `1909.13131 [astro-ph.HE]`.

[176] Francesco Capozzi et al. “Fast neutrino flavor conversions in one-dimensional core-collapse supernova models with and without muon creation”. In: *Phys. Rev. D* 103.6 (2021), p. 063013. DOI: `10.1103/PhysRevD.103.063013`. arXiv: `2012.08525 [astro-ph.HE]`.

[177] Sajad Abbar et al. “On the characteristics of fast neutrino flavor instabilities in three-dimensional core-collapse supernova models”. In: *Phys. Rev. D* 103.6 (2021), p. 063033. DOI: `10.1103/PhysRevD.103.063033`. arXiv: `2012.06594 [astro-ph.HE]`.

[178] Masamichi Zaizen and Taiki Morinaga. “Nonlinear evolution of fast neutrino flavor conversion in the preshock region of core-collapse supernovae”. In: *Phys. Rev. D* 104.8 (2021), p. 083035. DOI: `10.1103/PhysRevD.104.083035`. arXiv: `2104.10532 [hep-ph]`.

[179] Sajad Abbar and Francesco Capozzi. “Suppression of fast neutrino flavor conversions occurring at large distances in core-collapse supernovae”. In: *JCAP* 03.03 (2022), p. 051. DOI: `10.1088/1475-7516/2022/03/051`. arXiv: `2111.14880 [astro-ph.HE]`.

[180] Meng-Ru Wu et al. “Collective fast neutrino flavor conversions in a 1D box: Initial conditions and long-term evolution”. In: *Phys. Rev. D* 104.10 (2021), p. 103003. DOI: `10.1103/PhysRevD.104.103003`. arXiv: `2108.09886 [hep-ph]`.

[181] Sherwood Richers et al. “Particle-in-cell Simulation of the Neutrino Fast Flavor Instability”. In: *Phys. Rev. D* 103.8 (2021), p. 083013. DOI: `10.1103/PhysRevD.103.083013`. arXiv: `2101.02745 [astro-ph.HE]`.

[182] Sherwood Richers, Donald Willcox, and Nicole Ford. “Neutrino fast flavor instability in three dimensions”. In: *Phys. Rev. D* 104.10 (2021), p. 103023. DOI: `10.1103/PhysRevD.104.103023`. arXiv: `2109.08631 [astro-ph.HE]`.

[183] Shashank Shalgar and Irene Tamborra. “Symmetry breaking induced by pairwise conversion of neutrinos in compact sources”. In: *Phys. Rev. D* 105.4 (2022), p. 043018. DOI: `10.1103/PhysRevD.105.043018`. arXiv: `2106.15622 [hep-ph]`.

[184] Hirokazu Sasaki and Tomoya Takiwaki. “Dynamics of fast neutrino flavor conversions with scattering effects: a detailed analysis”. In: (Sept. 2021). DOI: `10.1093/ptep/ptac082`. arXiv: `2109.14011 [hep-ph]`.

[185] Günter Sigl. “Simulations of fast neutrino flavor conversions with interactions in inhomogeneous media”. In: *Phys. Rev. D* 105.4 (2022), p. 043005. DOI: `10.1103/PhysRevD.105.043005`. arXiv: `2109.00091 [hep-ph]`.

[186] Soumya Bhattacharyya and Basudeb Dasgupta. “Fast flavor oscillations of astrophysical neutrinos with 1, 2, . . . , ∞ crossings”. In: *JCAP* 07 (2021), p. 023. DOI: `10.1088/1475-7516/2021/07/023`. arXiv: `2101.01226 [hep-ph]`.

[187] Francesco Capozzi et al. “Fast flavor conversions in supernovae: the rise of mu-tau neutrinos”. In: (May 2020). arXiv: `2005.14204 [hep-ph]`.

[188] Eric Burns. “Neutron Star Mergers and How to Study Them”. In: *Living Rev. Rel.* 23.1 (2020), p. 4. DOI: `10.1007/s41114-020-00028-7`. arXiv: `1909.06085 [astro-ph.HE]`.

[189] Joshua A. Faber and Frederic A. Rasio. “Binary Neutron Star Mergers”. In: *Living Rev. Rel.* 15 (2012), p. 8. DOI: `10.12942/lrr-2012-8`. arXiv: `1204.3858 [gr-qc]`.

[190] Luca Baiotti and Luciano Rezzolla. “Binary neutron star mergers: a review of Einstein’s richest laboratory”. In: *Reports on Progress in Physics* 80.9 (July 2017), p. 096901. DOI: `10.1088/1361-6633/aa67bb`. URL: `https://doi.org/10.1088/1361-6633/aa67bb`.

[191] Claire Guépin, Kumiko Kotera, and Foteini Oikonomou. "High-energy neutrino transients and the future of multi-messenger astronomy". In: (July 2022). arXiv: `2207.12205 [astro-ph.HE]`.

[192] A. Malkus, A. Friedland, and G. C. McLaughlin. "Matter-Neutrino Resonance Above Merging Compact Objects". In: (Mar. 2014). arXiv: `1403.5797 [hep-ph]`.

[193] A. Malkus, G. C. McLaughlin, and R. Surman. "Symmetric and Standard Matter-Neutrino Resonances Above Merging Compact Objects". In: *Phys. Rev. D* 93.4 (2016), p. 045021. DOI: `10.1103/PhysRevD.93.045021`. arXiv: `1507.00946 [hep-ph]`.

[194] Meng-Ru Wu, Huaiyu Duan, and Yong-Zhong Qian. "Physics of neutrino flavor transformation through matter–neutrino resonances". In: *Phys. Lett. B* 752 (2016), pp. 89–94. DOI: `10.1016/j.physletb.2015.11.027`. arXiv: `1509.08975 [hep-ph]`.

[195] A. Malkus et al. "Neutrino oscillations above black hole accretion disks: disks with electron-flavor emission". In: *Phys. Rev. D* 86 (2012), p. 085015. DOI: `10.1103/PhysRevD.86.085015`. arXiv: `1207.6648 [hep-ph]`.

[196] Meng-Ru Wu and Irene Tamborra. "Fast neutrino conversions: Ubiquitous in compact binary merger remnants". In: *Phys. Rev.* D95.10 (2017), p. 103007. DOI: `10.1103/PhysRevD.95.103007`. arXiv: `1701.06580 [astro-ph.HE]`.

[197] Stephan Rosswog and M. Liebendoerfer. "High resolution calculations of merging neutron stars. 2: Neutrino emission". In: *Mon. Not. Roy. Astron. Soc.* 342 (2003), p. 673. DOI: `10.1046/j.1365-8711.2003.06579.x`. arXiv: `astro-ph/0302301`.

[198] Yuichiro Sekiguchi et al. "Gravitational Waves and Neutrino Emission from the Merger of Binary Neutron Stars". In: *Phys. Rev. Lett.* 107 (5 July 2011), p. 051102. DOI: `10.1103/PhysRevLett.107.051102`. URL: `https://link.aps.org/doi/10.1103/PhysRevLett.107.051102`.

[199] Koutarou Kyutoku and Kazumi Kashiyama. "Detectability of thermal neutrinos from binary-neutron-star mergers and implication to neutrino physics". In: *Phys. Rev. D* 97.10 (2018), p. 103001. DOI: `10.1103/PhysRevD.97.103001`. arXiv: `1710.05922 [astro-ph.HE]`.

[200] Rodrigo Fernández and Brian D. Metzger. “Electromagnetic Signatures of Neutron Star Mergers in the Advanced LIGO Era”. In: *Ann. Rev. Nucl. Part. Sci.* 66 (2016), pp. 23–45. DOI: `10.1146/annurev-nucl-102115-044819`. arXiv: `1512.05435 [astro-ph.HE]`.

[201] Aleksander Sadowski et al. “The Total Merger Rate of Compact Object Binaries In The Local Universe”. In: *Astrophys. J.* 676 (2008), p. 1162. DOI: `10.1086/528932`. arXiv: `0710.0878 [astro-ph]`.

[202] André da Silva Schneider et al. “Equation of State and Progenitor Dependence of Stellar-mass Black Hole Formation”. In: *The Astrophysical Journal* 894.1 (Apr. 2020), p. 4. DOI: `10.3847/1538-4357/ab8308`. URL: `https://doi.org/10.3847/1538-4357/ab8308`.

[203] T. M. Tauris et al. “Formation of Double Neutron Star Systems”. In: *Astrophys. J.* 846.2 (2017), p. 170. DOI: `10.3847/1538-4357/aa7e89`. arXiv: `1706.09438 [astro-ph.HE]`.

[204] R. A. Hulse and J. H. Taylor. “Discovery of a pulsar in a binary system.” In: 195 (Jan. 1975), pp. L51–L53. DOI: `10.1086/181708`.

[205] J. H. Taylor and J. M. Weisberg. “A new test of general relativity - Gravitational radiation and the binary pulsar PSR 1913+16”. In: 253 (Feb. 1982), pp. 908–920. DOI: `10.1086/159690`.

[206] Benjamin P. Abbott et al. “Upper Limits on the Rates of Binary Neutron Star and Neutron Star–black Hole Mergers From Advanced Ligo’s First Observing run”. In: *Astrophys. J. Lett.* 832.2 (2016), p. L21. DOI: `10.3847/2041-8205/832/2/L21`. arXiv: `1607.07456 [astro-ph.HE]`.

[207] E. Troja, S. Rosswog, and N. Gehrels. “Precursors of Short Gamma-ray Bursts”. In: 723.2 (Nov. 2010), pp. 1711–1717. DOI: `10.1088/0004-637X/723/2/1711`. arXiv: `1009.1385 [astro-ph.HE]`.

[208] B. P. Abbott et al. “GW170814: A Three-Detector Observation of Gravitational Waves from a Binary Black Hole Coalescence”. In: *Phys. Rev. Lett.* 119 (14 Oct. 2017), p. 141101. DOI: `10.1103/PhysRevLett.119.141101`. URL: `https://link.aps.org/doi/10.1103/PhysRevLett.119.141101`.

[209] Francesco Zappa et al. “Gravitational-wave luminosity of binary neutron stars mergers”. In: *Phys. Rev. Lett.* 120.11 (2018), p. 111101. DOI: 10.1103/PhysRevLett.120.111101. arXiv: 1712.04267 [gr-qc].

[210] Daniel M. Siegel and Brian D. Metzger. “Three-Dimensional General-Relativistic Magnetohydrodynamic Simulations of Remnant Accretion Disks from Neutron Star Mergers: Outflows and r-Process Nucleosynthesis”. In: *Phys. Rev. Lett.* 119 (23 Dec. 2017), p. 231102. DOI: 10.1103/PhysRevLett.119.231102. URL: https://link.aps.org/doi/10.1103/PhysRevLett.119.231102.

[211] B. D. Metzger, A. L. Piro, and E. Quataert. “Time-Dependent Models of Accretion Disks Formed from Compact Object Mergers”. In: *Mon. Not. Roy. Astron. Soc.* 390 (2008), p. 781. DOI: 10.1111/j.1365-2966.2008.13789.x. arXiv: 0805.4415 [astro-ph].

[212] L. Dessart et al. “Neutrino signatures and the neutrino-driven wind in Binary Neutron Star Mergers”. In: *Astrophys. J.* 690 (2009), p. 1681. DOI: 10.1088/0004-637X/690/2/1681. arXiv: 0806.4380 [astro-ph].

[213] Wen-fai Fong et al. “A Decade of Short-duration Gamma-ray Burst Broadband Afterglows: Energetics, Circumburst Densities, and jet Opening Angles”. In: *Astrophys. J.* 815.2 (2015), p. 102. DOI: 10.1088/0004-637X/815/2/102. arXiv: 1509.02922 [astro-ph.HE].

[214] R. Oechslin and Hans-Thomas Janka. “Torus Formation in Neutron Star Mergers and Well-Localized Short Gamma-Ray Bursts”. In: *Mon. Not. Roy. Astron. Soc.* 368 (2006), pp. 1489–1499. DOI: 10.1111/j.1365-2966.2006.10238.x. arXiv: astro-ph/0507099.

[215] S. E. Woosley and Robert D. Hoffman. “The alpha -Process and the r-Process”. In: 395 (Aug. 1992), p. 202. DOI: 10.1086/171644.

[216] Kenta Hotokezaka et al. “Radioactive decay products in neutron star merger ejecta: heating efficiency and γ-ray emission”. In: *Mon. Not. Roy. Astron. Soc.* 459.1 (2016), pp. 35–43. DOI: 10.1093/mnras/stw404. arXiv: 1511.05580 [astro-ph.HE].

[217] Jennifer Barnes et al. “Radioactivity and thermalization in the ejecta of compact object mergers and their impact on kilonova light curves”. In: *Astrophys. J.* 829.2 (2016), p. 110. DOI: 10.3847/0004-637X/829/2/110. arXiv: 1605.07218 [astro-ph.HE].

[218] Jennifer Barnes and Daniel Kasen. “Effect of a High Opacity on the Light Curves of Radioactively Powered Transients from Compact Object Mergers”. In: *Astrophys. J.* 775 (2013), p. 18. DOI: `10.1088/0004-637X/775/1/18`. arXiv: `1303.5787 [astro-ph.HE]`.

[219] Meng-Ru Wu et al. “Finding the remnants of the Milky Way’s last neutron star mergers”. In: *Astrophys. J.* 880.1 (2019), p. 23. DOI: `10.3847/1538-4357/ab2593`. arXiv: `1905.03793 [astro-ph.HE]`.

[220] Oleg Korobkin et al. “Gamma-rays from kilonova: a potential probe of r-process nucleosynthesis”. In: (May 2019). DOI: `10.3847/1538-4357/ab64d8`. arXiv: `1905.05089 [astro-ph.HE]`.

[221] A. Malkus et al. “Neutrino oscillations above black hole accretion disks: Disks with electron-flavor emission”. In: *Phys. Rev. D* 86 (8 Oct. 2012), p. 085015. DOI: `10.1103/PhysRevD.86.085015`. URL: `https://link.aps.org/doi/10.1103/PhysRevD.86.085015`.

[222] Yong-Lin Zhu, Albino Perego, and Gail C. McLaughlin. “Matter Neutrino Resonance Transitions above a Neutron Star Merger Remnant”. In: *Phys. Rev. D* 94.10 (2016), p. 105006. DOI: `10.1103/PhysRevD.94.105006`. arXiv: `1607.04671 [hep-ph]`.

[223] A. Malkus, G. C. McLaughlin, and R. Surman. “Symmetric and standard matter neutrino resonances above merging compact objects”. In: *Phys. Rev. D* 93 (4 Feb. 2016), p. 045021. DOI: `10.1103/PhysRevD.93.045021`. URL: `https://link.aps.org/doi/10.1103/PhysRevD.93.045021`.

[224] D. Väänänen and G. C. McLaughlin. “Uncovering the matter-neutrino resonance”. In: *Phys. Rev. D* 93 (10 May 2016), p. 105044. DOI: `10.1103/PhysRevD.93.105044`. URL: `https://link.aps.org/doi/10.1103/PhysRevD.93.105044`.

[225] Meng-Ru Wu et al. “Imprints of neutrino-pair flavor conversions on nucleosynthesis in ejecta from neutron-star merger remnants”. In: *Phys. Rev.* D96.12 (2017), p. 123015. DOI: `10.1103/PhysRevD.96.123015`. arXiv: `1711.00477 [astro-ph.HE]`.

[226] Manu George et al. “Fast neutrino flavor conversion, ejecta properties, and nucleosynthesis in newly-formed hypermassive remnants of neutron-star mergers”. In: *Phys. Rev. D*

102.10 (2020), p. 103015. DOI: 10.1103/PhysRevD.102.103015. arXiv: 2009.04046 [astro-ph.HE].

[227] Oliver Just et al. "Fast neutrino conversion in hydrodynamic simulations of neutrino-cooled accretion disks". In: *Phys. Rev. D* 105.8 (2022), p. 083024. DOI: 10.1103/PhysRevD.105.083024. arXiv: 2203.16559 [astro-ph.HE].

[228] Sherwood Richers. "Evaluating Approximate Flavor Instability Metrics in Neutron Star Mergers". In: (June 2022). arXiv: 2206.08444 [astro-ph.HE].

[229] Evan Grohs et al. "Neutrino Fast Flavor Instability in three dimensions for a Neutron Star Merger". In: (June 2022). arXiv: 2207.02214 [hep-ph].

[230] Rodrigo Fernández et al. "The Fast Flavor Instability in Hypermassive Neutron Star Disk Outflows". In: (July 2022). arXiv: 2207.10680 [astro-ph.HE].

[231] Xinyu Li and Daniel M. Siegel. "Neutrino Fast Flavor Conversions in Neutron-Star Post-merger Accretion Disks". In: *Phys. Rev. Lett.* 126.25 (2021), p. 251101. DOI: 10.1103/PhysRevLett.126.251101. arXiv: 2103.02616 [astro-ph.HE].

[232] Sherwood Richers et al. "Monte Carlo Neutrino Transport Through Remnant Disks from Neutron Star Mergers". In: *Astrophys. J.* 813.1 (2015), p. 38. DOI: 10.1088/0004-637X/813/1/38. arXiv: 1507.03606 [astro-ph.HE].

[233] Shashank Shalgar and Irene Tamborra. "Neutrino Flavor Conversion, Advection, and Collisions: The Full Solution". In: (July 2022). arXiv: 2207.04058 [astro-ph.HE].

[234] Georg G. Raffelt. "N-mode coherence in collective neutrino oscillations". In: *Phys. Rev. D* 83 (2011). See the post-publication version arXiv:1103.2891v4 for the corrected equations (B4) and (B5)., p. 105022. DOI: 10.1103/PhysRevD.83.105022. arXiv: 1103.2891 [hep-ph].

[235] Lucas Johns and George M. Fuller. "Strange mechanics of the neutrino flavor pendulum". In: *Phys. Rev. D* 97.2 (2018), p. 023020. DOI: 10.1103/PhysRevD.97.023020. arXiv: 1709.00518 [hep-ph].

[236] Taiki Morinaga. "Fast neutrino flavor instability and neutrino flavor lepton number crossings". In: (Mar. 2021). arXiv: 2103.15267 [hep-ph].

[237] Basudeb Dasgupta et al. “Multiple spectral splits of supernova neutrinos”. In: *Phys. Rev. Lett.* 103 (2009), p. 051105. DOI: 10.1103/PhysRevLett.103.051105. arXiv: 0904.3542 [hep-ph].

[238] Lucas Johns and Hiroki Nagakura. “Fast flavor instabilities and the search for neutrino angular crossings”. In: *Phys. Rev. D* 103.12 (2021), p. 123012. DOI: 10.1103/PhysRevD.103.123012. arXiv: 2104.04106 [hep-ph].

[239] Shashank Shalgar and Irene Tamborra. “On the Occurrence of Crossings Between the Angular Distributions of Electron Neutrinos and Antineutrinos in the Supernova Core”. In: *Astrophys. J.* 883 (2019), p. 80. DOI: 10.3847/1538-4357/ab38ba. arXiv: 1904.07236 [astro-ph.HE].

[240] Milad Delfan Azari et al. “Linear Analysis of Fast-Pairwise Collective Neutrino Oscillations in Core-Collapse Supernovae based on the Results of Boltzmann Simulations”. In: *Phys. Rev.* D99.10 (2019), p. 103011. DOI: 10.1103/PhysRevD.99.103011. arXiv: 1902.07467 [astro-ph.HE].

[241] Zewei Xiong et al. “Potential impact of fast flavor oscillations on neutrino-driven winds and their nucleosynthesis”. In: *Astrophys. J.* 900.2 (2020), p. 144. DOI: 10.3847/1538-4357/abac5e. arXiv: 2006.11414 [astro-ph.HE].

[242] Ian Padilla-Gay, Shashank Shalgar, and Irene Tamborra. “Multi-Dimensional Solution of Fast Neutrino Conversions in Binary Neutron Star Merger Remnants”. In: (Sept. 2020). arXiv: 2009.01843 [astro-ph.HE].

[243] Srdjan Sarikas, David de Sousa Seixas, and Georg G. Raffelt. “Spurious instabilities in multi-angle simulations of collective flavor conversion”. In: *Phys. Rev. D* 86 (2012), p. 125020. DOI: 10.1103/PhysRevD.86.125020. arXiv: 1210.4557 [hep-ph].

[244] Taiki Morinaga and Shoichi Yamada. “Linear stability analysis of collective neutrino oscillations without spurious modes”. In: *Phys. Rev. D* 97.2 (2018), p. 023024. DOI: 10.1103/PhysRevD.97.023024. arXiv: 1803.05913 [hep-ph].

[245] A. B. Balantekin. “Quantum Entanglement and Neutrino Many-Body Systems”. In: *J. Phys. Conf. Ser.* 2191.1 (2022), p. 012004. DOI: 10.1088/1742-6596/2191/1/012004.

[246] Amol V. Patwardhan, Michael J. Cervia, and A. B. Balantekin. "Spectral splits and entanglement entropy in collective neutrino oscillations". In: *Phys. Rev. D* 104.12 (2021), p. 123035. DOI: `10.1103/PhysRevD.104.123035`. arXiv: `2109.08995 [hep-ph]`.

[247] Michael J. Cervia et al. "Collective neutrino oscillations with tensor networks using a time-dependent variational principle". In: *Phys. Rev. D* 105 (2022), p. 123025. DOI: `10.1103/PhysRevD.105.123025`. arXiv: `2202.01865 [hep-ph]`.

[248] Alessandro Roggero, Ermal Rrapaj, and Zewei Xiong. "Entanglement and correlations in fast collective neutrino flavor oscillations". In: (Mar. 2022). arXiv: `2203.02783 [astro-ph.HE]`.

[249] Francesco Capozzi et al. "Supernova Fast Flavor Conversions in 1+1 D : Influence of Mu-tau neutrinos". In: (May 2022). arXiv: `2205.06272 [hep-ph]`.

[250] James T. Pantaleone. "Neutrino oscillations at high densities". In: *Phys. Lett. B* 287 (1992), pp. 128–132. DOI: `10.1016/0370-2693(92)91887-F`.

[251] Shashank Shalgar and Irene Tamborra. "Supernova Neutrino Decoupling Is Altered by Flavor Conversion". In: (June 2022). arXiv: `2206.00676 [astro-ph.HE]`.

[252] Rasmus S. L. Hansen, Shashank Shalgar, and Irene Tamborra. "Enhancement or damping of fast neutrino flavor conversions due to collisions". In: *Phys. Rev. D* 105.12 (2022), p. 123003. DOI: `10.1103/PhysRevD.105.123003`. arXiv: `2204.11873 [astro-ph.HE]`.

[253] Chinami Kato and Hiroki Nagakura. "Effects of energy-dependent scatterings on fast neutrino flavor conversions". In: (July 2022). arXiv: `2207.09496 [astro-ph.HE]`.

[254] Hiroki Nagakura and Masamichi Zaizen. "Time-dependent, quasi-steady, and global features of fast neutrino-flavor conversion". In: (June 2022). arXiv: `2206.04097 [astro-ph.HE]`.

[255] Ian Padilla-Gay and Shashank Shalgar. "Fast flavor conversion of neutrinos in presence of matter bulk velocity". In: (July 2021). arXiv: `2108.00012 [astro-ph.HE]`.

[256] Eve Armstrong. "Inference solves a boundary-value collision problem with relevance to neutrino flavor transformation". In: *Phys. Rev. D* 105.8 (2022), p. 083012. DOI: `10.1103/PhysRevD.105.083012`. arXiv: `2111.07412 [physics.comp-ph]`.

[257] Francesco Capozzi et al. "Collisional Triggering of Fast Flavor Conversions of Supernova Neutrinos". In: *Phys. Rev. Lett.* 122 (9 Mar. 2019), p. 091101. DOI: `10.1103/PhysRevLett.122.091101`. URL: `https://link.aps.org/doi/10.1103/PhysRevLett.122.091101`.

[258] Vincenzo Cirigliano, Mark W. Paris, and Shashank Shalgar. "Effect of collisions on neutrino flavor inhomogeneity in a dense neutrino gas". In: *Physics Letters B* 774 (2017), pp. 258–267. ISSN: 0370-2693. DOI: `https://doi.org/10.1016/j.physletb.2017.09.039`. URL: `https://www.sciencedirect.com/science/article/pii/S0370269317307505`.

[259] Lucas Johns and Zewei Xiong. "Collisional instabilities of neutrinos and their interplay with fast flavor conversion in compact objects". In: (Aug. 2022). arXiv: `2208.11059 [hep-ph]`.

[260] G. L. Fogli et al. "Low-energy spectral features of supernova (anti)neutrinos in inverted hierarchy". In: *Phys. Rev.* D78 (2008), p. 097301. DOI: `10.1103/PhysRevD.78.097301`. arXiv: `0808.0807 [hep-ph]`.

[261] Sajad Abbar, Huaiyu Duan, and Shashank Shalgar. "Flavor instabilities in the multiangle neutrino line model". In: *Phys. Rev.* D92.6 (2015), p. 065019. DOI: `10.1103/PhysRevD.92.065019`. arXiv: `1507.08992 [hep-ph]`.

[262] Basudeb Dasgupta, Alessandro Mirizzi, and Manibrata Sen. "Fast neutrino flavor conversions near the supernova core with realistic flavor-dependent angular distributions". In: *JCAP* 1702.02 (2017), p. 019. DOI: `10.1088/1475-7516/2017/02/019`. arXiv: `1609.00528 [hep-ph]`.

[263] Irene Tamborra et al. "Self-sustained asymmetry of lepton-number emission: A new phenomenon during the supernova shock-accretion phase in three dimensions". In: *Astrophys. J.* 792.2 (2014), p. 96. DOI: `10.1088/0004-637X/792/2/96`. arXiv: `1402.5418 [astro-ph.SR]`.

[264] A. Esteban-Pretel et al. "Role of dense matter in collective supernova neutrino transformations". In: *Phys. Rev.* D78 (2008), p. 085012. DOI: `10.1103/PhysRevD.78.085012`. arXiv: `0807.0659 [astro-ph]`.

[265] Joshua D. Martin, Changhao Yi, and Huaiyu Duan. “Dynamic fast flavor oscillation waves in dense neutrino gases”. In: *Phys. Lett.* B800 (2020), p. 135088. DOI: `10.1016/j.physletb.2019.135088`. arXiv: `1909.05225 [hep-ph]`.

[266] Boost. *Boost C++ Libraries*. `http://www.boost.org/`. 2019.

[267] OpenMP.org. *The OpenMP API specification for parallel programming*. `http://openmp.org`. 2013.

[268] Huaiyu Duan, Joshua D. Martin, and Sivaprasad Omanakuttan. “Flavor isospin waves in one-dimensional axisymmetric neutrino gases”. In: *Phys. Rev. D* 104.12 (2021), p. 123026. DOI: `10.1103/PhysRevD.104.123026`. arXiv: `2110.02286 [hep-ph]`.

[269] Soumya Bhattacharyya and Basudeb Dasgupta. “Fast Flavor Depolarization of Supernova Neutrinos”. In: *Phys. Rev. Lett.* 126.6 (2021), p. 061302. DOI: `10.1103/PhysRevLett.126.061302`. arXiv: `2009.03337 [hep-ph]`.

[270] B.P. Abbott et al. “GW170817: Observation of Gravitational Waves from a Binary Neutron Star Inspiral”. In: *Phys. Rev. Lett.* 119.16 (2017), p. 161101. DOI: `10.1103/PhysRevLett.119.161101`. arXiv: `1710.05832 [gr-qc]`.

[271] B.P. Abbott et al. “Gravitational Waves and Gamma-rays from a Binary Neutron Star Merger: GW170817 and GRB 170817A”. In: *Astrophys. J. Lett.* 848.2 (2017), p. L13. DOI: `10.3847/2041-8213/aa920c`. arXiv: `1710.05834 [astro-ph.HE]`.

[272] B.P. Abbott et al. “Multi-messenger Observations of a Binary Neutron Star Merger”. In: *Astrophys. J. Lett.* 848.2 (2017), p. L12. DOI: `10.3847/2041-8213/aa91c9`. arXiv: `1710.05833 [astro-ph.HE]`.

[273] J. M. Lattimer and D. N. Schramm. “Black-Hole-Neutron-Star Collisions”. In: *apjl* 192 (Sept. 1974), p. L145. DOI: `10.1086/181612`.

[274] David Eichler et al. “Nucleosynthesis, Neutrino Bursts and Gamma-Rays from Coalescing Neutron Stars”. In: *Nature* 340 (1989), pp. 126–128. DOI: `10.1038/340126a0`.

[275] Li-Xin Li and Bohdan Paczynski. “Transient events from neutron star mergers”. In: *Astrophys. J. Lett.* 507 (1998), p. L59. DOI: `10.1086/311680`. arXiv: `astro-ph/9807272`.

[276] B.D. Metzger et al. “Electromagnetic Counterparts of Compact Object Mergers Powered by the Radioactive Decay of R-process Nuclei”. In: *Mon. Not. Roy. Astron. Soc.* 406 (2010), p. 2650. DOI: `10.1111/j.1365-2966.2010.16864.x`. arXiv: `1001.5029 [astro-ph.HE]`.

[277] Brian D. Metzger. “Kilonovae”. In: *Living Rev. Rel.* 20.1 (2017), p. 3. DOI: `10.1007/s41114-017-0006-z`. arXiv: `1610.09381 [astro-ph.HE]`.

[278] Shinya Wanajo et al. “Production of all the *r*-process nuclides in the dynamical ejecta of neutron star mergers”. In: *Astrophys. J. Lett.* 789 (2014), p. L39. DOI: `10.1088/2041-8205/789/2/L39`. arXiv: `1402.7317 [astro-ph.SR]`.

[279] Yuichiro Sekiguchi et al. “Dynamical mass ejection from binary neutron star mergers: Radiation-hydrodynamics study in general relativity”. In: *Phys. Rev. D* 91.6 (2015), p. 064059. DOI: `10.1103/PhysRevD.91.064059`. arXiv: `1502.06660 [astro-ph.HE]`.

[280] David Radice et al. “Dynamical Mass Ejection from Binary Neutron Star Mergers”. In: *Mon. Not. Roy. Astron. Soc.* 460.3 (2016), pp. 3255–3271. DOI: `10.1093/mnras/stw1227`. arXiv: `1601.02426 [astro-ph.HE]`.

[281] Jonah M. Miller et al. “Full Transport Model of GW170817-Like Disk Produces a Blue Kilonova”. In: *Phys. Rev. D* 100.2 (2019), p. 023008. DOI: `10.1103/PhysRevD.100.023008`. arXiv: `1905.07477 [astro-ph.HE]`.

[282] S. E. Woosley. “Gamma-ray bursts from stellar mass accretion disks around black holes”. In: *Astrophys. J.* 405 (1993), p. 273. DOI: `10.1086/172359`.

[283] M. Ruffert and H.-T. Janka. “Gamma-ray bursts from accreting black holes in neutron star mergers”. In: *Astron. Astrophys.* 344 (1999), pp. 573–606. arXiv: `astro-ph/9809280`.

[284] Ivan Zalamea and Andrei M. Beloborodov. “Neutrino heating near hyper-accreting black holes”. In: *Mon. Not. Roy. Astron. Soc.* 410.4 (Feb. 2011), pp. 2302–2308. DOI: `10.1111/j.1365-2966.2010.17600.x`. arXiv: `1003.0710 [astro-ph.HE]`.

[285] Oliver Just et al. “Neutron-star merger ejecta as obstacles to neutrino-powered jets of gamma-ray bursts”. In: *Astrophys. J. Lett.* 816.2 (2016), p. L30. DOI: `10.3847/2041-8205/816/2/L30`. arXiv: `1510.04288 [astro-ph.HE]`.

[286] Francois Foucart et al. “Monte-Carlo Neutrino Transport in Neutron Star Merger Simulations”. In: *Astrophys. J. Lett.* 902.1, L27 (Oct. 2020), p. L27. DOI: `10.3847/2041-8213/abbb87`. arXiv: `2008.08089 [astro-ph.HE]`.

[287] Maik Frensel et al. “Neutrino Flavor Evolution in Binary Neutron Star Merger Remnants”. In: *Phys. Rev. D* 95.2 (2017), p. 023011. DOI: `10.1103/PhysRevD.95.023011`. arXiv: `1607.05938 [astro-ph.HE]`.

[288] James Y. Tian, Amol V. Patwardhan, and George M. Fuller. “Neutrino Flavor Evolution in Neutron Star Mergers”. In: *Phys. Rev. D* 96.4 (2017), p. 043001. DOI: `10.1103/PhysRevD.96.043001`. arXiv: `1703.03039 [astro-ph.HE]`.

[289] Shashank Shalgar. “Multi-angle calculation of the matter-neutrino resonance near an accretion disk”. In: *JCAP* 02 (2018), p. 010. DOI: `10.1088/1475-7516/2018/02/010`. arXiv: `1707.07692 [hep-ph]`.

[290] Sajad Abbar and Maria Cristina Volpe. “On Fast Neutrino Flavor Conversion Modes in the Nonlinear Regime”. In: *Phys. Lett. B* 790 (2019), pp. 545–550. DOI: `10.1016/j.physletb.2019.02.002`. arXiv: `1811.04215 [astro-ph.HE]`.

[291] Soumya Bhattacharyya and Basudeb Dasgupta. “Late-time behavior of fast neutrino oscillations”. In: *Phys. Rev. D* 102.6 (2020), p. 063018. DOI: `10.1103/PhysRevD.102.063018`. arXiv: `2005.00459 [hep-ph]`.

[292] Ricard Ardevol-Pulpillo et al. “Improved Leakage-Equilibration-Absorption Scheme (ILEAS) for Neutrino Physics in Compact Object Mergers”. In: *Mon. Not. Roy. Astron. Soc.* 485.4 (2019), pp. 4754–4789. DOI: `10.1093/mnras/stz613`. arXiv: `1808.00006 [astro-ph.HE]`.

[293] Oliver Just et al. “Comprehensive nucleosynthesis analysis for ejecta of compact binary mergers”. In: *Mon. Not. Roy. Astron. Soc.* 448.1 (2015), pp. 541–567. DOI: `10.1093/mnras/stv009`. arXiv: `1406.2687 [astro-ph.SR]`.

[294] Jones E., Oliphant T., Peterson P., *et al.*, SciPy: Open source scientific tools for Python (2001–). `http://www.scipy.org/`.

[295] Sherwood A. Richers et al. “Neutrino Quantum Kinetics in Compact Objects”. In: *Phys. Rev. D* 99.12 (2019), p. 123014. DOI: `10.1103/PhysRevD.99.123014`. arXiv: `1903.00022 [astro-ph.HE]`.

[296] R. L. Bowers and J. R. Wilson. “A numerical model for stellar core collapse calculations.” In: 50 (Nov. 1982), pp. 115–159. DOI: `10.1086/190822`.

[297] Evan O’Connor. “An Open-Source Neutrino Radiation Hydrodynamics Code for Core-Collapse Supernovae”. In: *Astrophys. J. Suppl.* 219.2 (2015), p. 24. DOI: `10.1088/0067-0049/219/2/24`. arXiv: `1411.7058 [astro-ph.HE]`.

[298] Anthony Mezzacappa et al. “Physical, numerical, and computational challenges of modeling neutrino transport in core-collapse supernovae”. In: *Liv. Rev. Comput. Astrophys.* 6 (2020), p. 4. DOI: `10.1007/s41115-020-00010-8`. arXiv: `2010.09013 [astro-ph.HE]`.

[299] Hans A. Bethe and James R. Wilson. “Revival of a stalled supernova shock by neutrino heating”. In: *Astrophys. J.* 295 (1985), pp. 14–23. DOI: `10.1086/163343`.

[300] Ondrej Pejcha, Basudeb Dasgupta, and Todd A. Thompson. “Effect of Collective Neutrino Oscillations on the Neutrino Mechanism of Core-Collapse Supernovae”. In: *Mon. Not. Roy. Astron. Soc.* 425 (2012), p. 1083. DOI: `10.1111/j.1365-2966.2012.21443.x`. arXiv: `1106.5718 [astro-ph.HE]`.

[301] Yudai Suwa et al. “Impacts of collective neutrino oscillations on core-collapse supernova explosions”. In: *Astrophys. J.* 738 (2011), p. 165. DOI: `10.1088/0004-637X/738/2/165`. arXiv: `1106.5487 [astro-ph.HE]`.

[302] Else Pllumbi et al. “Impact of neutrino flavor oscillations on the neutrino-driven wind nucleosynthesis of an electron-capture supernova”. In: *Astrophys. J.* 808.2 (2015), p. 188. DOI: `10.1088/0004-637X/808/2/188`. arXiv: `1406.2596 [astro-ph.SR]`.

[303] Alexander Friedland and Andrei Gruzinov. “Neutrino signatures of supernova turbulence”. In: (July 2006). arXiv: `astro-ph/0607244`.

[304] James P. Kneller and Cristina Volpe. “Turbulence effects on supernova neutrinos”. In: *Phys. Rev. D* 82 (2010), p. 123004. DOI: `10.1103/PhysRevD.82.123004`. arXiv: `1006.0913 [hep-ph]`.

[305] Sandhya Choubey, N. P. Harries, and G. G. Ross. “Turbulent supernova shock waves and the sterile neutrino signature in megaton water detectors”. In: *Phys. Rev. D* 76 (2007), p. 073013. DOI: `10.1103/PhysRevD.76.073013`. arXiv: `hep-ph/0703092`.

[306] Evgeny K. Akhmedov. “Parametric resonance in neutrino oscillations in matter”. In: *Pramana* 54 (2000). Ed. by Anjan S. Joshipura and Palash B. Pal, pp. 47–63. DOI: `10.1007/s12043-000-0006-4`. arXiv: `hep-ph/9907435`.

[307] J. P. Kneller, G. C. McLaughlin, and K. M. Patton. “Stimulated Neutrino Transformation in Supernovae”. In: *J. Phys. G* 40 (2013), p. 055002. DOI: `10.1088/0954-3899/40/5/055002`. arXiv: `1202.0776 [hep-ph]`.

[308] Lei Ma, Shashank Shalgar, and Huaiyu Duan. “Matter parametric neutrino flavor transformation through Rabi resonances”. In: *Phys. Rev. D* 98.10 (2018), p. 103011. DOI: `10.1103/PhysRevD.98.103011`. arXiv: `1807.10219 [hep-ph]`.

[309] Kenta Hotokezaka et al. “Mass ejection from the merger of binary neutron stars”. In: *Phys. Rev. D* 87 (2013), p. 024001. DOI: `10.1103/PhysRevD.87.024001`. arXiv: `1212.0905 [astro-ph.HE]`.

[310] Koutarou Kyutoku, Kunihito Ioka, and Masaru Shibata. “Anisotropic mass ejection from black hole-neutron star binaries: Diversity of electromagnetic counterparts”. In: *Phys. Rev. D* 88.4 (2013), p. 041503. DOI: `10.1103/PhysRevD.88.041503`. arXiv: `1305.6309 [astro-ph.HE]`.

[311] Oliver Just et al. “Core-collapse supernova simulations in one and two dimensions: comparison of codes and approximations”. In: *Mon. Not. Roy. Astron. Soc.* 481.4 (2018), pp. 4786–4814. DOI: `10.1093/mnras/sty2578`. arXiv: `1805.03953 [astro-ph.HE]`.

[312] W. Raphael Hix et al. “Essential ingredients in core-collapse supernovae”. In: *AIP Advances* 4.4 (2014), p. 041013. DOI: `10.1063/1.4870009`. eprint: `https://doi.org/10.1063/1.4870009`. URL: `https://doi.org/10.1063/1.4870009`.